POLITECNICO DI TORINO
Repository ISTITUZIONALE

Variable Kinematic Finite Element Formulations Applied to Multi-layered Structures and Multi-field Problems

Original
Variable Kinematic Finite Element Formulations Applied to Multi-layered Structures and Multi-field Problems / Li, Guohong. - (2019 Mar 08), pp. 1-230.

Availability:
This version is available at: 11583/2729361 since: 2019-03-26T16:08:46Z

Publisher:
Politecnico di Torino

Published
DOI:10.6092/polito/porto/2729361

Terms of use:
openAccess

This article is made available under terms and conditions as specified in the corresponding bibliographic description in the repository

Publisher copyright

(Article begins on next page)

04 August 2020

Doctoral Dissertation
Doctoral Program in Mechanical Engineering (31st cycle)

Variable Kinematic Finite Element Formulations Applied to Multi-layered Structures and Multi-field Problems

By

Guohong Li

* * * * * *

Supervisors
Prof. Erasmo Carrera, Supervisor
Assoc. Prof. Maria Cinefra, Supervisor
Dr. Enrico Zappino, Supervisor

Politecnico di Torino
February 8, 2019

This thesis is licensed under a Creative Commons License, Attribution - Noncommercial-NoDerivative Works 4.0 International: see `www.creativecommons.org`. The text may be reproduced for non-commercial purposes, provided that credit is given to the original author.

I hereby declare that, the contents and organisation of this dissertation constitute my own original work and does not compromise in any way the rights of third parties, including those relating to the security of personal data.

. . . .
Guohong Li
Turin, February 8, 2019

Abstract

The thesis presents variable kinematic finite element (FE) formulations for the numerical simulation of laminated structures considering multi-field effects. In the weak-form governing equations, couplings among hygroscopic, thermal, electrical, and mechanical fields are accounted for. The development of refined beam, plate, and shell FE models in the framework of Carrera Unified Formulation (CUF) is presented. Various refined approximation theories (employing Taylor series, trigonometric series, exponential functions, Lagrange and Chebyshev polynomials) are implemented in either Equivalent-Single-Layer (ESL) or Layer-Wise (LW) approach and numerically assessed. Node-Dependent Kinematics (NDK), a versatile tool to construct FE models with variable nodal kinematic capabilities, is introduced. Adoption of hierarchical Legendre polynomial functions as beam cross-section functions and plate/shell shape functions is demonstrated.

Application of the proposed FE approach in pure mechanical and multi-field modeling is discussed through a variety of numerical examples. Construction of global-local beam, plate, and shell FE models with NDK is demonstrated. FE solutions for angle-ply laminates, which can be used as new benchmarks, are proposed. An evaluation of membrane and shear locking phenomena in hierarchical shell elements in the analysis of multi-layered structures is presented, and it is concluded that the *p*-refinement can effectively alleviate the locking effects. The solution of thermo-mechanical, hygro-mechanical, and electro-mechanical problems with refined FE models is discussed through numerical cases.

The used FE approaches lead to results agreeing well with the available reference solutions. Three-dimensional accuracy can be achieved with high numerical efficiency. It is demonstrated that CUF provides a powerful framework for the development of advanced FE approaches.

Keywords: *finite elements, composite laminates, beam models, plate models, shell models, Carrera Unified Formulation, node-dependent kinematics, global-local analysis, thermal stress, hygroscopic stress, piezo-electric components.*

Summary

The heterogeneity of composite structures and the complexity of multi-field coupling effects raise the demands for advanced numerical simulation techniques. This work presents refined beam, plate, and shell finite element (FE) models for the modeling of multi-layered structures accounting for multi-field effects.

Carrera Unified Formulation (CUF) is a framework for the development of refined 1D and 2D numerical models. Based on CUF, various and miscellaneous kinematics of an arbitrary order can be implemented in either Equivalent-Single-Layer (ESL) or Layer-Wise (LW) approach. Through the FNs (*fundamental nuclei*), whose form is independent of the kinematic assumptions and the type of shape functions, FE formulation can be expressed compactly. The FE models presented in the current work are developed in the framework of CUF.

This dissertation contains four parts: variable kinematic FE models developed in the CUF framework for the multi-field modeling of multi-layered structures; an adaptable refinement approach which can lead to FE models with optimal numerical efficiency; the application of the presented beam, plate, and shell models in multi-field simulations; two special topics for the elastic plate and shell models.

The first part presents refined beam, plate, and shell models built in the CUF framework. Traditional theories of structures are reviewed, and the use of various basis functions in constructing advanced FE models based on CUF is described. The coupled hygro-thermo-electro-mechanical governing equations and their forms for beam, plate, and shell models are presented. The weak-form governing equations are derived by extending the Principle of Virtual Displacements to multi-field problems. The FNs (*fundamental nuclei*), core units of the stiffness matrix in multi-field FE models, are presented. Node-Dependent Kinematics, a versatile tool to construct finite element models with variable nodal kinematic capabilities, is introduced. The component-wise assembly technique of stiffness matrices and load vectors is explained. Decomposition of strain energy in beam and plate/shell models is discussed.

In the second part, the adaptable refinement approach is applied to the global-local modeling with refined beam, plate, and shell FE models. In the CUF framework, the FE refinement can be conducted on two mathematical levels: the enrichment of the shape functions, and the enhancement of the kinematic models. With Node-Dependent Kinematics (NDK), variable ESL/LW nodal kinematics can be carried out on the FE

nodes. These features enable one to determine the refinements according to the needs of the analysis, and FE models with optimal efficiency can be obtained. The building of numerically efficient global-local models with NDK is demonstrated through examples. Adoption of hierarchical Legendre polynomials as beam cross-section functions and plate/shell shape functions is presented.

The third part is devoted to the multi-field modeling accounting for temperature, moisture, and electric fields. Partially coupled thermo-mechanical and hygro-mechanical models with various kinematics (adopting Lagrange polynomials, Taylor series, exponential functions, and trigonometric functions, separately) assumptions are used in the analysis of multi-layered plates and shells. Fully coupled electro-mechanical models are applied to the simulations of beams with surface-mounted and embedded piezo-patches, and NDK is adopted to improve the numerical efficiency.

In the last part, two special topics are addressed. Solutions for angle-ply composite plates with arbitrary stacking sequence under various boundary conditions, which can be used as new benchmarks, are obtained through refined plate FE models employing Chebyshev polynomials in LW approach and trigonometric series as ESL kinematics. The shear and membrane locking phenomena in hierarchical shell elements for the analysis of laminated structures are numerically evaluated through proper energy decomposition. Efficient integration scheme for hierarchical shell elements is also discussed.

Acknowledgements

First, I would like to express my gratitude to Prof. Carrera for his continuous and timely supervision during the Ph.D. program. I must express my thanks to other supervisors of mine, Assoc. Prof. Cinefra and Dr. Zappino, for their patience and guidance when I was faced with challenges. I am also grateful to Dr. Petrolo, Dr. Alfonso, and Dr. Filippi, for their kind help whenever I turned to them.

I want express my thanks to MUL2 group and all the colleagues. It is my honor to have been a member of this vibrant and creative team. I have benefited a lot from the inspiring discussions, unreserved sharing, and cooperation. Special thanks to my dear colleagues and friends, Ibrahim Kaleel and Alberto Garcia de Miguel, for their support and encouragement during the last three years.

I would also like to thank Prof. Rolfes and Dr. Jansen for hosting me during the academic visit to Leibniz University Hannover.

Finally, I would like to acknowledge the FULLCOMP project (FULLy analysis, design, manufacturing, and health monitoring of COMPosite structures) which is funded by the European Commission under a Marie Sklodowska-Curie Innovative Training Networks grant. The professionalism, kind sharing, and close collaboration of all the supervisors and Ph.D. students in FULLCOMP have made FULLCOMP fruitful and successful.

To those who have been supportive and
encouraging to me

Contents

List of Tables **xii**

List of Figures **xv**

1 Introduction **1**
- 1.1 Theories of structures 1
- 1.2 Carrera Unified Formulation 3
- 1.3 Global-local modeling 4
- 1.4 Multi-field modeling 6
  - 1.4.1 Hygro-thermo-mechanical modeling 6
  - 1.4.2 Electro-mechanical modeling 8
- 1.5 An overview of the present work 9

I Variable Kinematic Finite Element Formulations 11

2 Refined beam, plate, and shell theories of structures **13**
- 2.1 A unified form of theories of structures 13
- 2.2 Beam models 15
  - 2.2.1 Euler–Bernoulli Beam Theory (EBBT) 15
  - 2.2.2 Timoshenko Beam Theory (TBT) 17
  - 2.2.3 A linear beam model 18
  - 2.2.4 Higher-order beam models using Taylor Expansions (TE) 19
  - 2.2.5 Beam models using trigonometric, hyperbolic, and exponential series 20
  - 2.2.6 Beam models using Lagrange Expansions (LE) 20
  - 2.2.7 Beam models using hierarchical functions (HLE) 21
- 2.3 Plate and shell models 23
  - 2.3.1 Classical Plate Theory (CPT) 23
  - 2.3.2 First-order Shear Deformation Theory (FSDT) 24
  - 2.3.3 A linear plate model 26
  - 2.3.4 Higher-order plate models using Taylor Expansions (TE) 26

2.3.5 Plate models using trigonometric, hyperbolic, and exponential series . . . 27
2.3.6 Plate models using Lagrange Expansions (LE) . . . 27
2.3.7 Plate models using orthogonal polynomials . . . 28
2.4 Theories of multi-layered structures . . . 29
2.4.1 Equivalent-Single Layer (ESL) approach . . . 30
2.4.2 Layer-Wise (LW) approach . . . 30
2.4.3 Examples of ESL and LW models . . . 32

3 Hygro-thermo-electro-mechanical basic equations 35
3.1 Tensor form of the basic equations . . . 35
3.1.1 Strain-displacement relations and gradient equations . . . 35
3.1.2 Constitutive equations . . . 36
3.1.3 Equilibrium and conservation equations . . . 36
3.1.4 Boundary conditions . . . 37
3.1.5 Free energy density . . . 37
3.2 Matrix form of the basic equations for beam, plate, and shell models . . . 37
3.2.1 Strain-displacement relations . . . 37
3.2.2 Gradient equations . . . 39
3.2.3 Constitutive equations . . . 40
3.2.4 Equilibrium and conservation equations . . . 45
3.2.5 Boundary conditions . . . 45
3.2.6 Free energy density . . . 46

4 Variable kinematic finite element formulations 47
4.1 Variable kinematic assumptions . . . 47
4.2 Various finite element shape functions . . . 48
4.2.1 1D shape functions for beam elements . . . 48
4.2.2 2D shape functions for plate and shell elements . . . 49
4.3 Node-Dependent Kinematics (NDK) . . . 50
4.3.1 Beam elements with NDK . . . 50
4.3.2 Plate and shell elements with NDK . . . 51
4.4 Weak form of governing equations . . . 52
4.4.1 Linear system of equations . . . 52
4.4.2 FNs of beam models . . . 55
4.4.3 FNs of plate and shell models . . . 56
4.5 Assembly of stiffness matrix and load vector . . . 57
4.5.1 Characteristics of assembly procedure for NDK FE models . . . 57
4.5.2 Mixing ESL and LW nodal kinematics . . . 57
4.5.3 Consideration of patches . . . 58
4.6 Decomposition of strain energy . . . 59
4.6.1 Strain energy decomposition in beam models . . . 61

4.6.2 Strain energy decomposition in plate and shell models 63

II Adaptable Refinement Approach 67

5 Refined beam FE models with Node-Dependent Kinematics 69
5.1 Case 1: A simply supported sandwich beam under local pressure 69
5.2 Case 2: A two-layered cantilever beam under four points loads 74
5.3 Conclusions 75

6 Refined plate FE models with Node-Dependent Kinematics 79
6.1 Case 1: Simply-supported cross-ply plates under bi-sinusoidal pressure 79
6.2 Case 2: Simply supported three-layered plates subjected to a point load 83
6.3 Case 3: Three-layered cross-ply composite plate under local pressure . 86
6.4 Conclusions 86

7 Refined shell FE models with Node-Dependent Kinematics 89
7.1 Case 1: Two-layered cylindrical shells under distributed pressure 89
7.2 Case 2: Simply-supported cross-ply spherical shells under sinusoidal distributed pressure 93
7.3 Case 3: Simply-supported three-layered cross-ply spherical shells under local distributed pressure 94
7.4 Conclusions 103

III Multi-field Modeling 105

8 Thermo-mechanical plate and shell FE models with various kinematics 107
8.1 Various kinematic assumptions 107
8.2 Three-layered square plates under thermal load 108
8.3 Two-layered cylindrical shells under thermal load 117
8.4 Conclusions 120

9 Hygro-mechanical plate and shell models with variable kinematics 125
9.1 Three-layered square plates with (0°/90°/0°) under hygroscopic fields . 125
9.2 Two-layered cylindrical shells with (0°/90°) under hygroscopic fields . . 129
9.3 Conclusions 131

10 Piezoelectric modeling with beam models 135
10.1 Cantilever beams containing piezo-patches with variable locations . . . 135
10.2 A cantilever beam with a top-mounted piezo-patch on the clamped end 141
10.3 Conclusions 143

IV Special Topics **147**

11 Refined finite element solutions for anisotropic laminated plates **149**
11.1 Definitions of simply supported boundary conditions 149
11.2 Numerical cases 151
  11.2.1 Case 1: Simply supported thick square plates with $(-15^\circ/15^\circ)$ and $(-30^\circ/30^\circ/-30^\circ/-30^\circ)$ 152
  11.2.2 Case 2: Simply supported square plates with $(0^\circ/30^\circ)$ 152
  11.2.3 Case 3: Simply supported square plates with $(-45^\circ/45^\circ)$ 155
  11.2.4 Case 4: Simply supported square plates with $(-45^\circ/0^\circ/90^\circ/45^\circ)$. 157
  11.2.5 Case 5: Square plates with $(0^\circ/60^\circ)$ under mixed clamped-free boundary conditions 158
11.3 Conclusions 159

12 Evaluation of shear and membrane locking in hierarchical shell elements **161**
12.1 Integration schemes for hierarchical elements 162
  12.1.1 Full integration scheme 163
  12.1.2 Reduced integration scheme 163
  12.1.3 Selectively reduced integration scheme 164
  12.1.4 Properties of the stiffness matrix of hierarchical elements with reduced and selective integration 166
12.2 Results and discussion 167
  12.2.1 Shear locking: cylindrical shells under distributed pressure . . . 167
  12.2.2 Membrane locking: cylindrical panels under bending 174
12.3 Conclusions 179

Concluding remarks **181**

Bibliography **187**

List of Tables

5.1 Elastic constants of materials used on the sandwich beam. 70
5.2 Displacement and stress evaluation on the sandwich beam under local pressure. 71
5.3 Elastic properties of the materials used in the two-layered cantilever beam. 75
5.4 Deflection and stress evaluations on the two-layered cantilever beam. . 76
6.1 Deflection and stresses on the three-layered cross-ply plate with $a/h = 2$ under bi-sinusoidal pressure, obtained with LE4 as thickness functions. 81
6.2 Deflection and stresses on the three-layered cross-ply plate with $a/h = 100$ under bi-sinusoidal pressure, obtained with LE4 as thickness functions. 82
6.3 $\bar{w}$ at $(\frac{a}{2}, \frac{b}{2}, 0)$ on the simply-supported cross-ply plates under a point load. 85
6.4 Deflection and stresses on the layered plate under uniform local pressure. 87
7.1 Deflection and stresses on the two-layered cylindrical shell with $R_\beta/h = 2$. 91
7.2 Deflection and stresses on the two-layered cylindrical shell with $R_\beta/h = 100$. 92
7.3 Deflection and stresses on the two-layered cylindrical shell with $R_\beta/h = 500$. 92
7.4 Spherical shells with (0°/90°) and $R/h = 5$ under bi-sinusoidal pressure. 94
7.5 spherical shells with (0°/90°/90°/0°) and $a/h = 100$ under bi-sinusoidal distributed pressure. 95
7.6 Aspect-ratios of C3D20R elements in the 3D models for the three-layered spherical shells under local pressure. 97
7.7 Deflection and stress evaluation on the three-layered spherical shells under local pressure, $R/h = 10$. 98
7.8 Deflection and stress evaluation on the three-layered spherical shells under local pressure, $R/h = 100$. 98
7.9 Deflection and stress evaluation on the three-layered spherical shells under local pressure, $R/h = 1000$. 99
7.10 A comparison between uniformly refined models and NDK models for the three-layered spherical shells under local pressure regarding computational costs. 102
8.1 Acronyms of various ESL kinematic models. 108

8.2 Material properties of the lamina used on the three-layered square plates. 109
8.3 Mesh convergence study with LE4 on the three-layered plate with $a/h = 100$ subjected to assumed linear temperature profiles. 109
8.4 Deflections and stresses obtained with LW models for the three-layer square plates with various a/h under thermal fields. 111
8.5 Deflections and stresses on three-layer square plates with various a/h under calculated temperature profiles, obtained with ESL models ET*n* and ET*n*Z. 112
8.6 Deflections and stresses on the three-layered plates under calculated temperature profiles, obtained with ESL models EExp*n*Z and ET1Exp*n*Z. 114
8.7 Deflections and stresses on the three-layer plates calculated temperature profiles, obtained with ESL models ES*n*C*n*Z and ET1S*n*C*n*Z. 115
8.8 Mechanical properties of T300/5208 composite lamina. 117
8.9 Mesh convergence study with LE4 on the cylindrical shells with $R_\alpha/h = 500$ under assumed temperature filed. 117
8.10 Deflection and stresses obtained with LW models for the two-layer cylindrical shells under thermal fields. 118
8.11 Deflections and stresses on the two-layer cylindrical shells under calculated temperature fields, obtained with ESL models EExp*n*Z and ES*n*C*n*Z. 120
8.12 Deflections and stresses on the two-layer cylindrical shells under calculated temperature fields, obtained with ESL models ET*n*Z and ET1S*n*C*n*Z. 121
9.1 Mechanical and hygroscopic properties of T300/5208 lamina. 126
9.2 Deflection and stresses on the three-layered plates under hygroscopic fields, obtained with LW models. 126
9.3 Deflections and stresses on the three-layered plates under calculated moisture field obtained with ESL models ET*n*Z and ET1S*n*C*n*Z. 127
9.4 Deflections and stresses on the two-layered cylindrical shells under hygroscopic fields, obtained with LW models. 130
9.5 Deflections and stresses on the two-layered cylindrical shells under calculated moisture fields, obtained with ESL models ET*n*Z and ET1S*n*C*n*Z. 132
10.1 Material properties of PZT-5H 136
10.2 Deflections on the free end of the beams in *Case A*. 138
10.3 Deflections at the center of the free-end cross-section of EAM beams with variable locations in *Case B*. 139
10.4 Material coefficients of PZT-4. 141
10.5 Deflections and stresses on the cantilever beam with a top-mounted piezoelectric actuator. 143
11.1 Edge displacement boundary conditions on laminated plates. 151
11.2 Deflection and stresses on the simply supported square plates with (0°/30°) under bi-sinusoidal distributed pressure on top and bottom surfaces. . . 154
11.3 Deflection and stresses on the simply supported square plates with (−45°/45°) under constant pressure on the top surface. 156

11.4 Deflection and stresses on the simply supported square plates with $(-45°/0°/90°/45°)$ under bi-sinusoidal distributed pressure on the top surface. 157
11.5 Deflection and stresses on the square plates with $(0°/60)$ under constant pressure on the top and bottom surfaces respectively and mixed boundary conditions CFCC. 159
12.1 Displacement and stress evaluation on the three-layered cylindrical shells with various R_β/h under distributed pressure. 168
12.2 Displacement and energy evaluation of the three-layered cylindrical panel under bending, obtained through hierarchical elements with $p = 7$. 175

List of Figures

2.1 A one-dimensional structure. 13
2.2 A two-dimensional structure. 14
2.3 Euler–Bernoulli Beam Theory. 16
2.4 Timoshenko Beam Theory. 17
2.5 Cross-section functions F_τ with different polynomial orders. 19
2.6 Isoparametric mapping on the beam cross-section. 21
2.7 2D hierarchical functions [224]. 23
2.8 First-order Shear Deformation Theory. 25
2.9 Multi-layered structures. 29
2.10 Two types of models for multi-layered structures. 30
2.11 Displacement-based ESL plate models with TE, through-thickness variation of deflection and transverse normal strain and stress. 32
2.12 Displacement-based LW plate models with LE, through thickness variation of deflection and transverse normal strain and stress. 33
3.1 Geometry of doubly curved shells. 38
3.2 Actuation mechanisms of piezoelectric components. 42
4.1 A B4 element with node-dependent kinematics. 50
4.2 A FE model consists of four-node Lagrangian elements (Q4) with Node-Dependent Kinematics (NDK). 51
4.3 Assignment of nodal kinematics in 2D hierarchical elements. 52
4.4 Assembly of stiffness matrix and load vector of FE models with node-dependent kinematics. 58
4.5 Assembly of the stiffness matrix and load vector of elements with various nodal kinematics. 59
4.6 Assembly of the stiffness matrix and load vector of a beam model with a piezo patch. 60
4.7 Axial strains on the cross-section of a beam model. 62
5.1 Geometry, boundary conditions and FE model for the sandwich beam. . 70
5.2 Evaluation of σ_{yz} on the sandwich beam under local pressure. 71
5.3 Through-the-thickness variation of $\bar{\sigma}_{yz}$ and $\bar{\sigma}_{yy}$ on the sandwich beam under local pressure. 72

5.4 Variation of w, σ_{yy}, and σ_{yz} along the axial direction of the sandwich beam. 73
5.5 Contour plot of σ_{yz} on surface $(\frac{a}{2}, y, z)$ of the sandwich beam under local pressure. 74
5.6 Contour plot of σ_{zz} on surface $(\frac{a}{2}, y, z)$ of the sandwich beam under local pressure. 74
5.7 The two-layered cantilever beam under four points loads. 75
5.8 Distribution of σ_{yz} along $(0, \frac{8b}{9}, \bar{z})$ on the two-layered cantilever beam, obtained with HLEp kinematics. 76
5.9 Variation of σ_{yy} and σ_{yz} through $(0, \frac{8b}{9}, \bar{z})$ on the two-layered cantilever beam. 77
6.1 FE model for the composite laminated plate under bi-sinusoidal pressure. 80
6.2 Relative error of $\bar{\sigma}_{yz}$ on the three-layered cross-ply plates under pressure load, obtained with LE4 as thickness functions. 81
6.3 Distribution of the transverse shear stresses through the thickness of the plates under bi-sinusoidal pressure. 82
6.4 Distribution of σ_{xz} obtained with hierarchical plate elements employing LE4 as thickness functions. 83
6.5 Simply-supported cross-ply composite plates subjected to a point load. 83
6.6 Assignment of nodal kinematics on the NDK FE models for the laminated plates under a point load. 84
6.7 Variation of $\bar{w}$ through $(a/2, b/2, \bar{z})$ on the three-layered plates under a point load. 85
6.8 The three-layered cross-ply composite plate under uniform local pressure. 86
6.9 Assignment of nodal kinematics on the FE model for the three-layered cross-ply composite plate under local pressure. 87
6.10 Distribution of transverse shear stresses through the thickness of the layered plate under local uniform pressure. 88
7.1 Simply-supported cylindrical shells under inner distributed pressure. . 90
7.2 Distribution of transverse stresses through the thickness of the two-layered cylindrical shells ($R_\beta/h = 2$: p8-LE7, mesh 1×2; $R_\beta/h = 100$: p8-LE3, mesh 2×4; $R_\beta/h = 500$: p8-LE3, mesh 2×4). 93
7.3 Three-layered cross-ply spherical shells under local bi-sinusoidal distributed pressure. 95
7.4 NDK FE models with variable TE/LE nodal capabilities for the three-layered spherical shells under local pressure. 99
7.5 Through-the-thickness distribution of $\bar{\sigma}_{\alpha z}$ through $(\frac{a}{25}, 0, \bar{z})$ in the three-layered spherical shells under local pressure. 100
7.6 Through-the-thickness distribution of $\bar{\sigma}_{\beta z}$ through $(0, \frac{2b}{25}, \bar{z})$ in the three-layered spherical shells under local pressure. 100
7.7 $\sigma_{\alpha z}$ on the three-layered spherical shell ($R/h = 10$) under local pressure. 101
7.8 $\sigma_{\alpha z}$ on the three-layered spherical shell ($R/h = 100$) under local pressure. 101

7.9 $\sigma_{\alpha z}$ on the three-layered spherical shell ($R/h = 1000$) under local pressure. 101
7.10 Numerical efficiency of various FE models in the analysis of the three-layered spherical shells under local pressure. 102
8.1 $\bar{\sigma}_{xz}$ through the thickness of the composite plates under assumed linear temperature profile, obtained with LW models. 110
8.2 Through-the-thickness temperature profiles $\bar{\theta}_A$ for the three-layered composite plates with various thickness ratios (a/h). 110
8.3 Through-the-thickness variation of deflections and stresses on the three-layered plates with various a/h ratios under thermal load, obtained with LW models. 111
8.4 Variation of $\bar{\sigma}_{xz}$ through the thickness of the three-layered plates under calculated temperature profiles, obtained with ESL models ET*n* and ET*n*Z. 113
8.5 $\bar{\sigma}_{xz}$ through the thickness of the three-layered plates under calculated temperature profiles, obtained with EExp*n*Z and ET1Exp*n*Z. 113
8.6 $\bar{\sigma}_{xz}$ through the thickness of the three-layered plates under calculated temperature profiles, obtained with ES*n*C*n*Z and ET1S*n*C*n*Z. 116
8.7 $\bar{\sigma}_{xz}$ through the thickness of the three-layered plates under calculated temperature profiles, obtained by ESL models with various thickness functions. 116
8.8 Temperature profiles $\theta_A(z)$ for composite cylindrical shells with various thickness ratios (R_α/h). 118
8.9 Distribution of deflections and stresses through the thickness of the two-layered cylindrical shells under assumed and calculated temperature fields obtained with LW kinematics. 119
8.10 $\sigma_{\alpha z}$ through the thickness of the two-layered cylindrical shells under calculated temperature field, obtained with ET*n*Z kinematics. 122
8.11 Transverse shear stress $\sigma_{\alpha z}$ through the thickness of the composite shells with various R_α/h ratios, obtained with EExp*n*Z kinematics. 122
8.12 $\sigma_{\alpha z}$ through the thickness of the two-layered cylindrical shells under calculated temperature fields, obtained with ES*n*C*n*Z kinematics. 123
8.13 $\sigma_{\alpha z}$ through the thickness of the two-layered cylindrical shells under calculated temperature fields, obtained with ET1S*n*C*n*Z kinematics. . . 123
9.1 Moisture concentration profiles on the three-layered plates with various a/h. 126
9.2 Through-the-thickness variation of deflection and stresses on the three-layered plates under calculated moisture fields. 128
9.3 σ_{xz} through the thickness of the three-layered plates under calculated moisture fields, obtained with ESL models with ET*n*Z and ET1S*n*C*n*Z. . 129
9.4 Moisture profiles on the two-layered cylindrical shells. 130
9.5 Transverse displacement w and stresses through the thickness of the composite cylindrical shells with various R_α/h ratios under hygroscopic fields, LE4 solutions with both linear and calculated moisture profiles. . 131

9.6 $\sigma_{\alpha z}$ through the thickness of the two-layered cylindrical shells under calculated moisture fields. 133
10.1 Cantilever beams with surface-mounted and embedded piezo-patches. 136
10.2 Cross-section discretization with 12LE9 for the beam structures in *Case A*. 137
10.3 Variation of w along the beam axis of the beams in *Case A*. 138
10.4 Deflections on the free end of the cantilever beams with piezo-patches with variable locations in *Case B*. 139
10.5 Deflection on the free-end of the SAM beam with $d = 0.01$m in *Case B*. 140
10.6 Deflection and stress evaluation on the SAM configuration with $d = 0.01$m in *Case B*. 140
10.7 The cantilever beam with a top-mounted piezo-patch on the clamped end. 142
10.8 Variation of w and σ_{yy} along the axis of the beam with a surface-mounted piezo-patch. 144
10.9 σ_{yz} on cross-section $y = c/2$ of the beam with a top-mounted piezo-patch obtained with model 16LE9. 144
10.10 Variation of σ_{yz} on cross-section $y = c/2$ of the beam with a top-mounted piezo-patch. 145
11.1 Simply supported edge boundary conditions for a plate, Figure 5-7 in [114]. 150
11.2 Through-the-thickness variation of stresses on the simply supported square plate with (−15°/15°) under distributed pressure on top and bottom surfaces. 153
11.3 Through-the-thickness variation of stresses on the simply supported square plate with (−30°/30°/ − 30°/30°) under distributed pressure on top and bottom surfaces. 153
11.4 Distribution of stresses through the thickness of the simply supported square plates with (0°/30°) under bi-sinusoidal distributed load on top and bottom surfaces. 154
11.5 σ_{yz} on the simply supported thick ($a/h = 4$) plate with (0°/30°), $z \times 1$. . 155
11.6 σ_{yz} on the simply supported thin ($a/h = 50$) plate with (0°/30°), $z \times 12.5$. 155
11.7 Through-the-thickness distribution of stresses on the simply supported square plate with (−45°/45°) under constant pressure on the top surface. 156
11.8 Through-the-thickness distribution of stresses on the simply supported plates with (−45°/0°/90°/45°) under bi-sinusoidal distributed pressure on the top surface. 157
11.9 σ_{xz} on the simply supported plates with (−45°/0°/90°/45) under bi-sinusoidal distributed pressure on the top surface. 158
11.10 Through-the-thickness variation of stresses on the plates with (0°/60°) under constant pressure on the top and bottom surfaces and mixed boundary conditions. 159

12.1 Gauss points used for the full integration of hierarchical shell elements. "FULL" represents the adoption of the full integration approach. 164
12.2 Gauss points used for the reduced integration of hierarchical shell elements with $p = 4$. "RX" and "RY" indicate reduced integration in the ξ and η directions, respectively. 165
12.3 Reduced integration scheme for an hierarchical element with $p = 4$. "RX": reduced integration in the ξ direcion; "RY": reduced integration in the η direction; "FULL": full integration in both directions. 165
12.4 Eigenvalues of hierarchical elements with reduced integration (REDI) and selective integration (SELI). 166
12.5 Convergence regarding the normalized deflection of FE models for the three-layered cylindrical shells under distributed pressure. 169
12.6 Convergence regarding the strain energy of FE models for the three-layered cylindrical shells under distributed pressure. 170
12.7 Variation of strain energy components with respect to the polynomial degree on the three-layered cylindrical shells under distributed pressure. 172
12.8 Energy components versus radius-to-thickness ratio R_β/h on the three-layered cylindrical shells under distributed pressure. 173
12.9 Three-layered cylindrical panel under simple supports on two ends. . . 174
12.10 Convergence regarding the normalized deflection of FE models for the simply supported cylindrical panels under bending, for various radius-to-thickness ratio R_β/h. 176
12.11 Convergence regarding the strain energy of FE models for the simply supported cylindrical panels under bending, for various radius-to-thickness ratio R_β/h. 177
12.12 Variation of relevant energy components with respect to the polynomial degree of FE models for the three-layered cylindrical panel under bending. 178
12.13 Ratio of different energy components versus radius-to-thickness ratio on the three-layered cylindrical panel under bending. 178

Chapter 1

Introduction

Beams are slender structures, and plates/shells are thin-walled structures with thickness dimension comparatively much smaller than the other two in-plane dimensions. Shells have curvatures, and plates can be seen as flat shells. Due to the high structural efficiency, multi-layered structures, such as composite laminated beams, plates, and shells are widely used in modern engineering, especially in the aerospace industry. Smart structures with surface-mounted or embedded piezoelectric components are also drawing significant attention.

A great variety of theories of structures have been suggested, some of which have been broadly adopted in structural analyses, for example, finite element (FE) simulations. Nevertheless, due to the heterogeneous properties and complex arrangements of multi-layered structures, conventional FE models soon reach their limits, which has boosted the demands for structural analysis methods, especially the sophisticated local effects that cause stress concentration.

1.1 Theories of structures

In history, a variety of 1D models for the modeling of slender structures have been proposed. Classical theories such as Euler-Bernoulli Beam Theory [88] and Timoshenko Beam Theory [234, 233] have been broadly applied in numerical analyses, though they fail in accurately capturing the transverse shear stresses over the beam cross-sections. Refined beam theories were then proposed to overcome this drawback. Warping functions were suggested to account for the cross-sectional warping of thin-walled structures by Vlasov [250]. A Generalized Beam Theory (GBT), in which the warping deformation can be considered through the introduction of cross-section deformation modes, was suggested for thin-walled beam structures [209]. A class of Higher-order Theories (HOT) was proposed by introducing higher-order terms to the displacement field in the axial direction [256, 119, 262].

Classical Plate Theory (CPT) is the simplest 2D model, which is based on Kirchoff-Love hypothesis [152]. Since the transverse shear effects are ignored, only in-plane strains are accounted for. CPT is extensively used on thin plate and shell structures. Some examples can be found in [230, 251, 168]. First-Order Shear Deformation Theory (FSDT) based on the Mindlin–Reissner assumption [198, 162] considers the transverse shear effects but can only approximate the transverse shear stresses through the thickness as constants. Plate and shell finite elements (FE) using FSDT were developed by Hughes and Tezduyar [109], Ferreira et al. [92], and Rolfes and Rohwer [204], among others. To further improve the solution accuracy of plate models, Higher-Order Theories (HOT) [103, 5, 190, 197, 120, 118] were presented, which have been widely adopted in structural analyses of plates and shells. A comprehensive discussion of HOT and the FE suitability was presented by Tessler [232]. Some of these models were reviewed by Kapania and Raciti [121, 122]. A systematic summary of HOT for laminated plates and shells can be found in the work of Reddy [194].

The use of trigonometric terms in beam models was reported by various authors, such as the works of Shimpi and Ghugal [212], Arya, Shimpi, and Naik [9], and Vidal and Polit [248, 249]. Polit and Touratier [184] adopted cosine functions for the approximation of transverse shear strains in laminated plates to avoid using shear correction factors. Dau, Polit, and Touratier [80] used trigonometric functions to capture transverse shear stresses in multi-layered shells. Ferreira, Roque, and Jorge [90] suggested a trigonometric shear deformation theory for symmetrically laminated plates. An extension, a sinusoidal shear deformation model, was applied to laminated shell structures by Ferreira et al. [91]. Mantari, Oktem, and Soares [155] suggested a trigonometric shear deformation theory and demonstrated the effectiveness on laminated composite and sandwich plates. Mantari, Oktem, and Soares [153] and Mantari, Bonilla, and Soares [154] presented trigonometric-exponential higher order shear deformation theories for composite plates. Karama, Afaq, and Mistou [129, 128] developed a refined shear deformation beam model by introducing the exponential functions to the displacement assumptions.

As summarized by Carrera [41] and Reddy [194], models for multi-layered structures can be built in two approaches, namely the Equivalent Single Layer (ESL) and Layer-Wise (LW) approaches. In ESL models, displacements are assumed over the whole cross-sectional domain of the structure, while LW considers the displacement field on the cross-section of each layer and accounts for the displacement continuity at layer interfaces. ESL approach does not require the description of layer interfaces and suits a wide range of basis functions. Traditional models and higher-order models can be categorized into the ESL class. Differently, LW models require a proper representation of displacements at interfaces between neighboring layers. LW approach was used extensively by many researchers, such as Noor and Burton [170], Reddy [191], Mawenya and Davies [158], Chaudhuri and Seide [64], and Rammerstorfer, Dorninger, and Starlinger [187].

1.2 Carrera Unified Formulation

Carrera Unified Formulation (CUF) is a general framework for the development of refined beam, plate, and shell models proposed by Carrera [41, 40, 59]. Starting from a compact form of displacement assumptions, weak form governing equations can be expressed through the *fundamental nuclei* (FNs) [59]. The expressions of FNs are independent of the kinematic assumptions and are widely applicable to a variety of structural models. Traditional theories and higher-order theories can be implemented as particular cases of refined *cross-section functions*, in both 1D (beam) and 2D (plate and shell) cases. CUF framework facilitates the development of advanced FE models, in which both shape function enrichment and kinematic refinement can be implemented conveniently. Beam, plate, and shells problems can be solved in a unified manner. A great variety of basis functions can be integrated in either ESL or LW approach to formulating refined structural theories [59].

In numerical analyses, improved accuracy can be reached through the refinement of the models. CUF provides the convenience to conduct mathematical refinements through the FNs. In CUF-based structural models, the type of basis functions adopted and the number of cross-section functions are both variable and can be treated as model input parameters. The refinement of the model can be gradually conducted until prescribed accuracy is achieved. The works of Cinefra and Carrera [68], Cinefra and Valvano [69], and Cinefra, Valvano, and Carrera [70] are examples of variable kinematics approach for mechanical problems.

Various approximation functions can be employed to build refined beam, plate, and shell models, in either ESL or LW approach. In refined multi-layered beam models, Carrera, Filippi, and Zappino [48, 47] tested various basis functions, including Taylor series, trigonometric series, and exponential functions together with a zig-zag term suggested by Murakami [166]. Application of Chebyshev polynomials in beam models was reported by Filippi et al. [95]. 2D hierarchical Legendre polynomials were used as the cross-section functions of beam element by Pagani et al. [176]. Implementation of trigonometric, exponential, and miscellaneous functions as the cross-section functions in ESL refined plate FE models for composite laminates and sandwich structures was reported by Filippi et al. [94]. Legendre polynomials were adopted to build refined LW kinematics in multi-layered shell FE models by Carrera, Büttner, and Nali [36], Cinefra and Carrera [68], and Cinefra and Valvano [69]. The optimal structural models are problem-dependent. A best-theory diagram method was presented to choose the most suitable theory for specific structural problems [180, 72, 261].

Based on CUF, Carrera and Zappino [56, 57] introduced the dependence of cross-section functions on the shape functions in beam elements. This approach was named as Node-dependent Kinematics (NDK). Trough NDK, various kinematic models can coexist in a beam element and be blended by the shape functions over the beam axial domain. More importantly, NDK allows for the local kinematic refinement in the critical region with local effects to be captured. The features make NDK feasible in the construction of simultaneous global-local models with multiple kinematic models. Since no additional coupling or modification of mesh is needed, NDK is convenient to use in FE analyses. NDK technique was later extended to plate models for mechanical [242] and piezo-elastic [55] problems. In general, the solution accuracy can be improved by enriching the assumptions of the displacement field. Meanwhile, the increased number of model variables leads to raised computational costs in FE analyses. With NDK technique, accuracy in the local area can be kept with lower computational efforts.

The FE models can be refined on two levels, namely the refinement of cross-section functions and the enhancement of shape functions (p-refinement). p-refinement is more efficient than h-refinement due to its high convergence rate [224, 226]. Also, the avoidance of re-meshing can shorten the pre-processing time consumption. Application of 2D hierarchical functions in the refinement of beam models in the CUF framework was reported by Pagani et al. [176] and Carrera, Miguel, and Pagani [49]. It is reported that 2D hierarchical elements are not sensitive to locking phenomena when the polynomial order is sufficiently high [224, 226, 222, 221, 86, 1]. The shear and membrane locking of hierarchical functions in refined multi-layered shell finite elements remains to be assessed.

With NDK, nodal ESL/LW capabilities can be switched when required, as elaborated by Zappino et al. [263]. The combination of mathematical refinements and NDK leads to a broad spectrum of FE models on the same set of FE meshes. Such capabilities enable analyzers to fully exploit the potential of FE models.

1.3 Global-local modeling

In FE models, the refinement of mathematical assumptions can improve the solution accuracy, but also leads to an increased number of degrees of freedom, even makes the solution computationally expensive. To reach a compromise between the desired accuracy and solution expenses, a local refinement is often needed to improve solution accuracy in critical regions where local effects occur.

The most direct refinement approach is the h-version refinement [13, 266], which increases the mesh refinement for a better approximation. An adaptive h-version method was suggested to regenerate the mesh in local zones based on an error estimator [270, 266]. The p-refinement approach [223, 12, 220, 226] enhances the order of shape functions. The $h-p$-version method combines these two methods [10, 173, 271, 192]. In the s-version refinement (mesh superposition technique) [96, 97], an additional set of meshes is overlapped on the existing FE grid to improve the local accuracy. It should be pointed out that these techniques do not deal with the kinematic assumptions.

In the analysis of multi-layered structures, kinematic refinements can be carried out on specific layers through superimposing an LW displacement field of a layer onto the global ESL field [148, 149]. Similar methods based on the idea of multiple assumed displacement fields were further adopted by Chen and Wu [66], Chen and Si [65], Khalili, Shariyat, and Rajabi [131], and Lezgy-Nazargah, Beheshti-Aval, and Shariyat [146]. Such approaches were applied to the modeling of delaminations [259, 164, 246, 247]. A variable kinematic theory based on the superposition of an ESL and an LW displacement fields was suggested by Reddy and Robbins [196] and Robbins and Reddy [202]. Carrera, Pagani, and Valvano [51] presented variable kinematic shell models in which the displacement assumptions of specific layers can be directly set in LW approach while other layers are grouped and modeled as equivalent single layers. A similar concept, Sublaminate Generalized Unified Formulation (S-GUF), was suggested by D'Ottavio et al. [78]. A ply-grouping approach was adopted by Chang, Perez, and Chang [63] when analyzing composite laminates with 3D brick elements. Jones et al. [115] suggested 3D super-elements to reduce the computational consumption of 3D FE model in the modeling of laminated structures.

Various approaches for the coupling between a locally refined model and a global model were proposed. The displacement compatibility at global-local domain interfaces can be enforced by using Lagrangian multipliers [185, 6, 33, 50]. The Arlequin method couples two domains with incompatible kinematics by using Lagrangian multipliers in an overlapping zone [82, 83]. Application of Arlequin method in the modeling of multilayered structures was reported by many researchers, such as Biscani et al. [28, 29, 27], He et al. [101], Hu, Belouettar, Potier-Ferry, et al. [106], and Hu et al. [105]. Blanco, Feijóo, and Urquiza [31] and Wenzel et al. [253] presented eXtended Variational Formulation (XVF) with two Lagrange multiplier fields to couple non-overlapping domains with different mathematical assumptions.

In a typical one-way sequential global-local approach, a separate local model is driven on its boundaries by the displacement field taken from a previously solved global model [165], while the influence of the local model on the global displacement is discarded. As an improvement, iterative procedures were presented to ensure the compatibility and equilibrium at global-local interfaces [254, 255, 156], yet extra computational resources will be consumed in the iterative process.

Some coupling techniques are also implemented in commercial software. Multi-Point Constraints (MPCs) and Rigid Beam Element (RBE) use linear functions to relate the displacements of the independent and dependent nodes. Shell-to-solid coupling connects the edge nodes on a 2D model to those on a 3D model through distribution coupling constraints. Sub-modeling is based on the one-way sequential global-local method.

1.4 Multi-field modeling

In engineering applications, smart structures containing piezoelectric components might be exposed to thermal and hygroscopic environments. Coupled multi-field modeling will provide a better understanding of structural behavior in such cases. The capturing of multi-field effects is vital for the modeling and design of smart structures.

The consistent constitutive equations can be derived on a thermodynamic basis as demonstrated by Ikeda [112] and Sih et al.[214]. Variational principles for a series of multi-field couplings were discussed by Dökmeci [84], Sung and Thompson [219], Altay and Dökmecí [3], and Yang [260]. Altay and Dökmeci [4] proposed a hygro-thermo-electro-mechanical variational principle together with the fundamental equations for corresponding four-field problems. Smittakorn and Heyliger [215] presented a hygro-thermo-electro-mechanical model for laminated plate structures under steady-state and transient conditions.

1.4.1 Hygro-thermo-mechanical modeling

Heat conduction is governed by Fourier law of conduction [98]. The resultant temperature variation causes strains in structures. Due to the thermo-mechanical coupling, straining of structures also generates heat in transient and dynamic processes. In steady-state conditions, thermo-mechanical problems are partially coupled, which means only the deformation due to temperature change is considered.

Some works available in the literature adopted assumed temperature field. Das and Rath [79] considered the transverse shear effects in the bending of a thick plate under assumed temperature field. Tungikar and Rao [239] presented exact three-dimensional closed-form solutions for steady-state heat conduction and the resultant thermal stresses in cross-ply laminated plates. Kant and Khare [117] used a higher-order model in FE modeling of multi-layered plates under assumed linear temperature profile through the thickness. Adopting Reddy's higher-order theory [190, 197], Khdeir and Reddy [135] studied the response of cross-ply laminated plates under thermal field with linear distribution through the thickness and presented exact solutions. Miller, Kicher, and Millavec [161] reported the use of Kirchoff-Love hypothesis in layered shell models and the temperature variation was taken as input to the analysis. By using higher-order theories, Khare, Kant, and Garg [132] presented closed-form solutions for cross-ply shell laminates under linearly varying temperature through the thickness. Khdeir [134] suggested closed-form solutions for circular cylindrical shells under temperature field that has assumed uniform or linear variation through the thickness. Based on a higher-order theory [195], Khdeir, Rajab, and Reddy [133] proposed exact solutions for cylindrical and doubly curved shells under assumed thermal loads and various boundary conditions.

Temperature field can be obtained in a separate step by solving Fourier's equation and then be used in a subsequent step on the structure as input data. Dumir et al. [85]

used an improved efficient zig-zag theory and a third order theory for cylindrical laminated shells, and the exact temperature profile described in a sub-layerwise manner was the input to the partially-coupled thermo-mechanical model.

Various refined thermoelastic plate models based on ESL or LW approaches are implemented in the CUF framework. The works of Carrera [38] and Robaldo and Carrera [200] remarked the superiority of the mixed approach to displacement-based models in the thermoelastic analysis of laminated plates under assumed thermal field. Carrera [39] compared the structural response of multi-layered plates under assumed linear and exact temperature profiles through the thickness and pointed out that the exact temperature field is essential for thick plates. Cinefra, Valvano, and Carrera [70] developed shell finite elements for the thermoelastic analysis of multi-layered structures under exact temperature field obtained in a separate step. Nali, Carrera, and Calvi [167] presented fully-coupled thermo-mechanical laminated plate models which allow for the calculation of instantaneous temperature field.

Fick's diffusion law was derived by Fick [93]. The Fick's law is analogous to the Fourier law mathematically. An attempt to extend this analogy to moisture convection and cross-coupled moisture diffusion was made by Szekeres [228]. The coupling effects between the temperature and moisture fields are known as the Dufour (diffusion-thermal) and Soret (thermal-diffusion) effects [130, 214]. Sih, Shih, and Chou [213] conducted transient hygrothermal analyses on composite plates which demonstrated that coupled effects are significant in some cases. Tambour [231] also illustrated that the moisture-heat coupling effects might cause local temperature overshoots thus cannot be neglected. Szekeres and Engelbrecht [229] considered the Dufour and Soret effects and presented coupled hygro-thermal models for composites.

Patel, Ganapathi, and Makhecha [178] presented finite elements adopting a higher-order theory for laminated plates and used temperature and moisture fields with assumed linear distribution in numerical analyses. By using a higher-order shear deformation theory together with Murakami's zig-zag function [166], Alsubari, Ali, and Aminanda [2] investigated the response of cylindrical laminated shells under combined assumed temperature and moisture fields. It was reported that temperature increase and moisture concentration lead to a reduction of mechanical properties in composite materials [182, 238, 214]. Hyer et al. [111] investigated the dependence of elastic and thermal expansion properties on temperature in T300/5208 graphite/epoxy. Lo et al. [150] considered the change of material properties due to temperature variation and moisture concentration in the partially coupled hygrothermal analysis of laminated plates, and a finite element adopting global-local higher-order theory was developed.

Shen and Springer [211] and Benkeddad, Grediac, and Vautrin [25, 24] investigated transient one-dimensional diffusion through the thickness in composite plates. The same approach was extended to the computation of transient hygroscopic stresses in composite laminated plates under asymmetrical and cyclic environmental conditions

[237, 236]. Jacquemin and Vautrin [113] presented a semi-analytical model for the assessment of stresses in cylindrical laminated shells under cyclic temperature and moisture environmental conditions, and the calculated transient moisture concentration field was substituted into a partially coupled hygro-thermo-mechanical model.

1.4.2 Electro-mechanical modeling

Electro-mechanical coupling is a reversible process that an electrical field causes straining (direct effect) and deformation causes an electric potential (reverse effect). Such coupling effects are the main characteristics of various piezoelectric materials, which have been used on sensors and actuators in a great variety of smart structures. Piezoelectric components, either patches or layers, are usually bonded to the surfaces or embedded in the structures.

Crawley and De Luis [77] and Crawley and Anderson [76] numerically modeled and experimentally studied surface-bonded and embedded piezo actuators on beam structures. A refined layer-wise model was suggested by Robbins and Reddy [201] to capture the interaction between the substrate structure and piezoelectric components. A refined sinus beam model was presented by Beheshti-Aval et al. [20] for laminated beam structures with piezoelectric layers. Based on CUF, Miglioretti, Carrera, and Petrolo [160] used Lagrange polynomials as cross-section functions in refined beam element for electro-mechanical modeling. Zappino et al. [264] considered thermal loads in the refined electro-mechanical beam models.

An extensive variety of electro-mechanical models are based on traditional theories CPT or FSDT. The works of Wang and Rogers [251], Lee [144], Hwang and Park [110], and Piefort [181] are examples of the application of CPT in building electro-mechanical plate models. Plate models based on FSDT were presented by Chandrashekhara and Agarwal [62], Batra [18], Suleman and Venkayya [217], and Huang and Wu [107], among many other researchers. Jonnalagadda, Blandford, and Tauchert [116] developed a thermo-electro-mechanical model with FSDT for composite plate structures with piezoelectric layers. Rogacheva [203] presented shell formulations for electro-mechanical modeling. Tzou and Gadre [240] applied CPT in the analysis of laminated shell structure with piezoelectric components. A triangle shell element using a layer-wise constant shear angle theory was proposed by Tzou and Ye [241] for laminates with piezoelectric actuators and sensors.

A hybrid ESL-LW plate model, in which ESL and LW assumptions were respectively used for displacements and electric potential, was suggested by Mitchell and Reddy [163]. A beam model with third-order zig-zag functions combining LW approximation of electric field was suggested by Kapuria [125]. This approach was later extended into an electro-mechanical plate model by the same author [123]. Brick elements was used by Batra and Liang [19] and Hauch [99]. However, it is widely agreed that solid elements are comparatively computational expensive in the simulation of thin piezoelectric components.

A series of higher-order plate theories for piezoelectric problems, including representations based on trigonometric series, power series, and Legendre polynomials, were reviewed by Wang and Yang [252]. The work of Saravanos and Heyliger [205] consists of an extensive review of the beam, plate, and shell models for piezoelectric modeling developed till the end of the 1990s. Benjeddou [22] compared a variety of piezoelectric finite element implementations reported in the literature before the 2000s. The review made by Kapuria, Kumari, and Nath [124] reports more recent advances of modeling methods for piezoelectric composite laminates.

Based on CUF, mixed plate models developed through the Reissner Mixed Variational Theorem (RMVT) for piezoelectric modeling were proposed by Carrera and Fagiano [46] and Carrera, Büttner, and Nali [36]. Cinefra et al. [71] suggested an axiomatic/asymptotic technique for the detection of the optimal plate model to capture the static response of composite laminates with piezoelectric components. Variable kinematic shell models for laminated structures with embedded piezoelectric components were implemented by Carrera and Valvano [54] in the CUF framework. NDK was also applied to the FE simulation of structures with piezo-patches by Carrera, Valvano, and Kulikov [55]. A comprehensive discussion of the modeling of smart plate and shell structures through CUF can be found in the work of Carrera, Brischetto, and Nali [42].

1.5 An overview of the present work

Rigorous and efficient modeling techniques are essential for engineers to better exploit the potential of engineering structures. The present work is aimed at the development of variable kinematic finite element approaches for the modeling of multi-layered structures accounting for multi-field effects. The refined FE models are developed in the CUF framework, and the discussions are confined to the linear static problems. The following topics are considered:

1. Various and miscellaneous kinematic assumptions for plate and shell models are implemented and compared regarding the numerical accuracy and efficiency.

2. New static benchmark cases for angle-ply laminated plates are proposed through refined 2D FE modeling.

3. The shear and membrane locking phenomena in refined hierarchical shell elements for laminated structures are numerically evaluated.

4. An adaptable refinement approach for FE models based on the combination of Node-Dependent Kinematics and two-level mathematical refinements is presented. Application of this technique in efficient global-local analyses is demonstrated.

5. Refined beam, plate, and shell models accounting for hygroscopic, thermal, and electric effects are presented. The models are verified through thermo-mechanical, hygro-mechanical, and electro-mechanical benchmark cases.

Part I

Variable Kinematic Finite Element Formulations

Chapter 2

Refined beam, plate, and shell theories of structures

In this chapter, refined beam, plate, and shell models are outlined. First, a unified formulation of continuum-based reduced beam, plate, and shell theories of structures is introduced. Second, classical theories of structures are reviewed and examined through this unified formulation. Third, various refined models are discussed.

2.1 A unified form of theories of structures

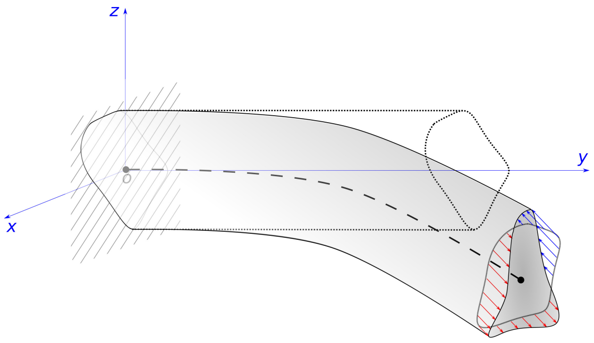

Figure 2.1: A one-dimensional structure.

A 1D structural component has the axial dimension much larger than the other two cross-section dimensions. As illustrated in Fig. 2.1, The deformation of such slender structures can be described through the deformation of the neutral axis, the rotation of the cross-section around the neutral axis, and the deformation on the cross-section. A *bar* refers to a 1D structure that can only carry the axial load. *Beams* refer to structural components that can also bear bending. Plenty of 1D theories have been suggested for the modeling of slender structures. Classical beam theories include Euler–Bernoulli Beam Theory (EBBT) [88] and Timoshenko Beam Theory (TBT) [234, 233].

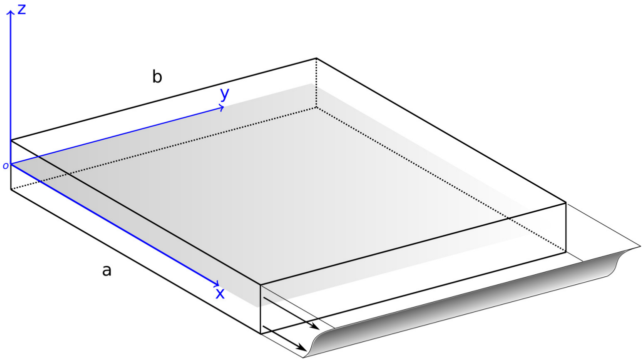

Figure 2.2: A two-dimensional structure.

2D structures have a thin thickness dimension and greater spans in the two directions along the neutral surface. Deformation of 2D structures consists of the membrane deformation on the neutral surface, the rotation of the cross-section concerning the neutral surface, and the stretch of the cross-section along the thickness direction. *Membranes* can only withstand biaxial tractions perpendicular to their normal directions. Sometimes, the concept *plate* is used to indicate structures that can carry only in-plane loads [157]. In the current work, *plates* and *shells* are 2D structures able to hold both membrane and bending loads, and the difference is that plates are flat structures while shells have single or double curvatures. Traditional 2D theories of structures include the Kirchhoff–Love Plate Theory (also known as Classical Plate Theory, CPT) [152], and the First-order Shear Deformation Theory (FSDT) [198, 162].

In a unified manner, the displacement field $\boldsymbol{u} = \{u, v, w\}^\top$ of 1D and 2D continuum-based reduced theories of structures can be assumed as:

$$\begin{aligned} u &= F_\tau^u \, u_\tau \\ v &= F_\tau^v \, v_\tau \\ w &= F_\tau^w \, w_\tau \end{aligned} \tag{2.1}$$

which in fact is a linear combination of the unknown functions (u_τ, v_τ, and w_τ) and the cross-section functions (F_τ^u, F_τ^v, and F_τ^w). Similar expressions have been used by many researchers, for example, Reddy [194]. If the same set of F_τ are applied to all the displacement components, the above expression can be written into:

$$\begin{Bmatrix} u \\ v \\ w \end{Bmatrix} = F_\tau \begin{Bmatrix} u_\tau \\ v_\tau \\ w_\tau \end{Bmatrix} \tag{2.2}$$

A more compact form reads [40]:

$$\boldsymbol{u} = F_\tau \, \boldsymbol{u}_\tau \tag{2.3}$$

in which F_τ describes the deformation of the cross-section and $\boldsymbol{u}_\tau$ represents the displacement vector along the neutral line or the neutral surface. The repeated index τ implies the application of Einstein's summation convention.

For 1D (beam) structures, the displacements assumptions take the following form:

$$\boldsymbol{u}(x,y,z) = F_\tau(x,z)\ \boldsymbol{u}_\tau(y) \tag{2.4}$$

in which $F_\tau(x,z)$ are defined on the cross-sectional domain.

For plate structures, the displacement field can be approximated through:

$$\boldsymbol{u}(x,y,z) = F_\tau(z)\ \boldsymbol{u}_\tau(x,y) \tag{2.5}$$

The geometry of shells are often described in the orthogonal curvilinear reference system (α, β, z). A general form of shell theories reads:

$$\boldsymbol{u}(\alpha,\beta,z) = F_\tau(z)\ \boldsymbol{u}_\tau(\alpha,\beta) \tag{2.6}$$

For plates and shells, F_τ are defined on the thickness domain, and they are also referred to as the thickness functions. The same plate displacement models can be applied to shells by simply transforming the coordinates through the following rule:

$$x \to \alpha, \quad y \to \beta, \quad z \to z. \tag{2.7}$$

Conversely, a shell becomes a plate when the curvature radii are infinite. Transformation of shell coordinates to plate coordinates reads:

$$\alpha \to x, \quad \beta \to y, \quad z \to z. \tag{2.8}$$

This chapter is focused on the formulation and the construction of 1D and 2D theories through F_τ, which is a fundamental part of CUF.

2.2 Beam models

A series of beam theories are reviewed and interpreted in the CUF framework.

2.2.1 Euler–Bernoulli Beam Theory (EBBT)

The EBBT model is based on the assumptions that each cross-section keeps rigid and rotates with the neutral line while remaining perpendicular to the neutral line. Accordingly, the displacement functions describing the EBBT model read:

$$\begin{aligned} u(y) &= u_1(y) \\ v(x,y,z) &= v_1(y) - u_{1,y}(y)\ x + w_{1,y}(y)\ z \\ w(y) &= w_1(y) \end{aligned} \tag{2.9}$$

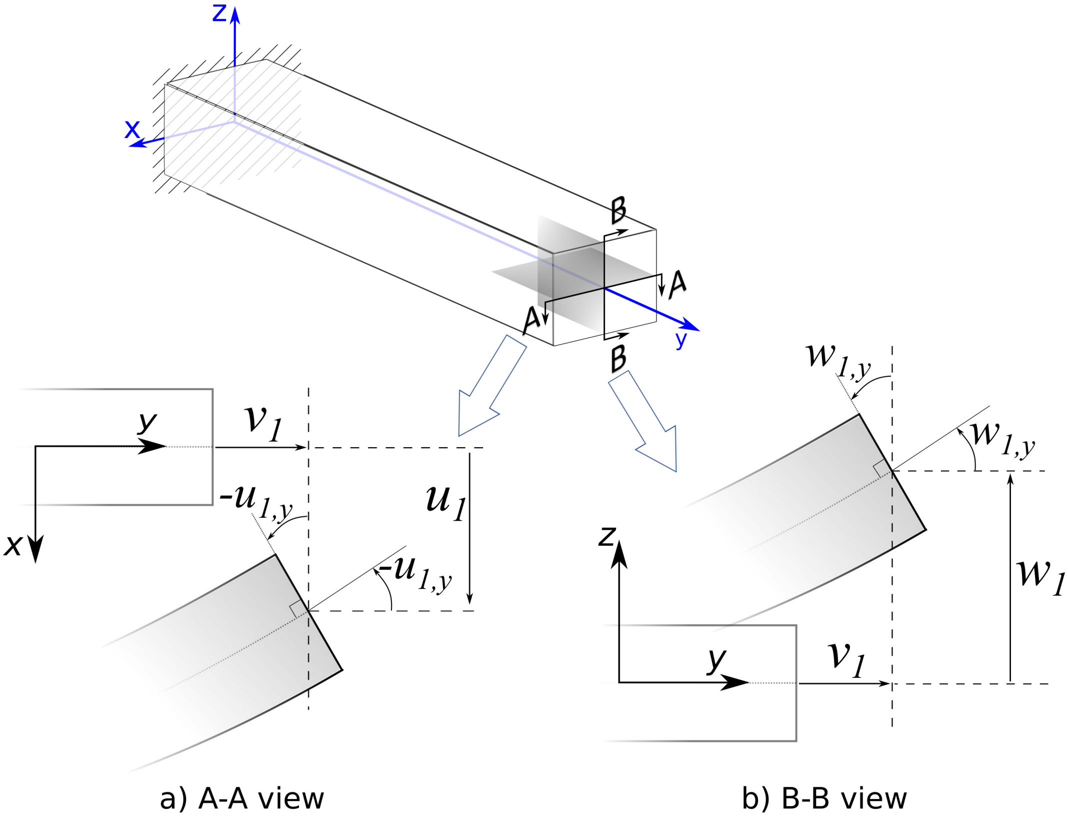

Figure 2.3: Euler–Bernoulli Beam Theory.

By recalling Eqn. (2.1), the above expression is a particular case of the following linear beam theory:

$$\begin{aligned} u(x,y,z) &= u_1(y) + u_2(y)\, x + u_3(y)\, z \\ v(x,y,z) &= v_1(y) + v_2(y)\, x + v_3(y)\, z \\ w(x,y,z) &= w_1(y) + w_2(y)\, x + w_3(y)\, z \end{aligned} \tag{2.10}$$

by using the following cross-section functions:

$$\begin{aligned} F_1^u &= 1; \quad F_2^u = 0; \quad F_3^u = 0; \\ F_1^v &= 1; \quad F_2^v = x; \quad F_3^v = z; \\ F_1^w &= 1; \quad F_2^w = 0; \quad F_3^w = 0. \end{aligned} \tag{2.11}$$

In addition, v_2 and v_3 depend on u_1 and w_1, respectively:

$$v_2 = -u_{1,y}, \quad v_3 = w_{1,y}. \tag{2.12}$$

which means that there are three independent unknowns in the model (u_1, v_1, w_1). The coefficients u_1, v_1, and w_1, correspond to the translation of the neutural line in the three directions, separately. As shown in Fig. 2.3, $u_{1,y}$ and $-w_{1,y}$ are the rotations of the cross-section around z and x axes, respectively.

EBBT considers only the axial strain ε_{yy}:

$$\varepsilon_{yy} = \frac{dv}{dy} = \frac{dv_1}{\partial y} - \frac{d^2u_1}{dy^2}x + \frac{d^2w_1}{dy^2}z \tag{2.13}$$

in which there exist the second derivatives of $u_1(y)$ and $w_1(y)$. This requires that $u_1(y)$ and $w_1(y)$ have C^1 continuity.

2.2.2 Timoshenko Beam Theory (TBT)

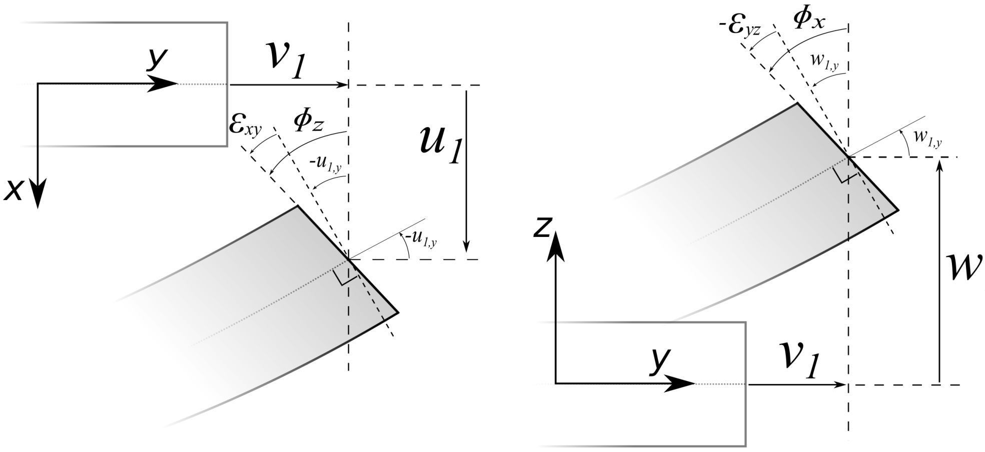

(a) Top view (A-A view in Fig. 2.3)   (b) Side view (B-B view in Fig. 2.3)

Figure 2.4: Timoshenko Beam Theory.

The Timoshenko beam model is formulated by assuming that the cross-section remains rigid but not necessarily perpendicular to the neutral line when deforming, as shown in Fig. 2.4. TBT assumes the displacement field as:

$$\begin{aligned} u(x,y,z) &= u_1(y) \\ v(x,y,z) &= v_1(y) + \phi_z(y)\,x - \phi_x(y)\,z \\ w(x,y,z) &= w_1(y) \end{aligned} \tag{2.14}$$

where ϕ_z and ϕ_x represent the rotations of the cross-section around z and y axes, respectively.

In the unified form (Eqn. 2.1), the same set of cross-sections as in the EBBT case can be used in the current model:

$$\begin{aligned} F_1^u &= 1; \quad F_2^u = 0; \quad F_3^u = 0; \\ F_1^v &= 1; \quad F_2^v = x; \quad F_3^v = z; \\ F_1^w &= 1; \quad F_2^w = 0; \quad F_3^w = 0. \end{aligned} \tag{2.15}$$

Differently, there are two additional independent coefficients:

$$v_2 = \phi_z, \quad v_3 = -\phi_x. \tag{2.16}$$

Thus, there are five independent unknowns in TBT.

TBT allows for the transverse shear deformations γ_{xy} and γ_{yz}. By recalling the geometrical relations, the strains are obtained as:

$$\begin{aligned} \varepsilon_{yy} &= \frac{\partial v}{\partial y} && = v_{1,y} + \phi_{z,y}\ x - \phi_{x,y}\ z \\ \varepsilon_{xy} &= \frac{\partial v}{\partial x} + \frac{\partial u}{\partial y} && = \phi_z + u_{1,y} \\ \varepsilon_{yz} &= \frac{\partial v}{\partial z} + \frac{\partial w}{\partial y} && = -\phi_x + w_{1,y} \end{aligned} \tag{2.17}$$

Note that the above expression leads to constant shear strains on a cross-section. A shear correction factor, determined by the geometry features of the cross-section geometry, can be introduced as a remedy. The calculation of this factor has been discussed extensively by many researchers, such as Timoshenko [234], Cowper [75], and Carrera et al. [53]. Most of the correction methods are based on the equivalence of energy.

2.2.3 A linear beam model

Eqn. (2.10) represents a complete linear beam model with nine unknowns in which F_τ is uniformly applied to u, v, and w components. By recalling Eqn. (2.2), Eqn. (2.10) can be obtained by taking:

$$F_1 = 1; \quad F_2 = x; \quad F_3 = z. \tag{2.18}$$

This linear model results in linear axial strain ε_{yy}, linear transverse shear strains ε_{xy} and ε_{yz}, and constant cross-sectional strains ε_{xx}, ε_{zz}, and ε_{xz}:

$$\begin{aligned} \varepsilon_{yy} &= \frac{\partial v}{\partial y} && = v_{1,y} + v_{2,y}\ x + v_{3,y}\ z \\ \varepsilon_{xy} &= \frac{\partial u}{\partial y} + \frac{\partial v}{\partial x} && = u_{1,y} + u_{2,y}\ x + u_{3,y}\ z + v_2 \\ \varepsilon_{yz} &= \frac{\partial v}{\partial z} + \frac{\partial w}{\partial y} && = v_3 + w_{1,y} + w_{2,y}\ x + w_{3,y}\ z \\ \varepsilon_{xx} &= \frac{\partial u}{\partial x} && = u_2 \\ \varepsilon_{zz} &= \frac{\partial w}{\partial w} && = w_3 \\ \varepsilon_{xz} &= \frac{\partial u}{\partial z} + \frac{\partial w}{\partial x} && = u_3 + w_2 \end{aligned} \tag{2.19}$$

Compared to TBT, the in-plane deformation on the cross-section is considered, and the transverse shear deforming capability is increased.

It should be noted that in EBBT, TBT, and this linear beam model there exist Poisson Locking, which can be overcome by either adopting higher-order beam theories or modifying the elastic coefficients (see Carrera et al. [59]).

2.2.4 Higher-order beam models using Taylor Expansions (TE)

The displacement assumptions can be further enriched by increasing the order of F_τ. For a higher-order beam theory based on the Taylor (Maclaurin) series, the cross-section functions can be constructed as follows:

$$\begin{gathered} F_1 = 1, \\ F_2 = x, \quad F_3 = z, \\ F_4 = x^2, \quad F_5 = xz, \quad F_6 = z^2; \\ F_7 = x^3, \quad F_8 = x^2 z, \quad F_9 = xz^2; \quad F_{10} = z^3; \\ \dots \end{gathered} \tag{2.20}$$

in which the polynomial expansions are obtained from Pascal's triangle. Note that the expansions for the $(N-1)$-th order model are included in those for the N-th order model through this hierarchical definition. Thickness functions based on Taylor series can be denoted as "TEn", wherein n indicates the highest order of the used polynomials.

Fig. 2.5 compares the cross-section functions of different orders. Different approximations can lead to similar strain energy solutions, yet the strain fields might be quite different. With the refinement of the models, the deformation can be captured more accurately, and the stress-free natural boundary conditions can be approached. The cost of the improved accuracy is the increased number of unknowns in the model. In applications, lower-order beam models can be sufficient for very slender structures, while accurate strain/stress solutions require higher-order models than displacements.

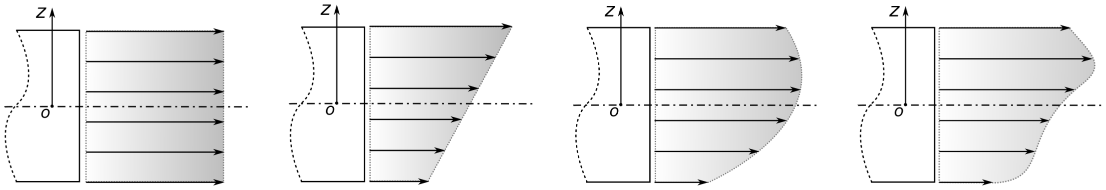

(a) Constant (b) First-order (c) Second-order (d) Higher-orders

Figure 2.5: Cross-section functions F_τ with different polynomial orders.

Under the hypothesis of small strains and rotations, the unknowns corresponding to $F_1 = 1$ are the translational displacements of the neutural line, those for the first-order therms $F_2 = x$ and $F_3 = z$ the rotational angles of the cross-section, the second-order unknowns the curvatures caused by the deformation. The physical meanings of the unknowns for even higher-order expansions are not explicit. A discussion can be found in the work of Li and Liu [149, 30].

2.2.5 Beam models using trigonometric, hyperbolic, and exponential series

Various series expansions can be adopted to formulate refined beam models. Trigonometric series can be incorporated through [47]:

$$\begin{aligned} &F_1 = \sin(\frac{\pi x}{a}), \quad &&F_2 = \cos(\frac{\pi x}{a}), \quad &&F_3 = \sin(\frac{\pi z}{b}), \quad &&F_4 = \cos(\frac{\pi z}{b}); \\ &F_5 = \sin(\frac{2\pi x}{a}), \quad &&F_6 = \cos(\frac{2\pi x}{a}), \quad &&F_7 = \sin(\frac{2\pi z}{b}), \quad &&F_8 = \cos(\frac{2\pi z}{b}); \\ &\dots \end{aligned} \tag{2.21}$$

in which a and b are the dimensions of the cross-section in x and y directions, respectively.

Hyperbolic functions can be used accordingly:

$$\begin{aligned} &F_1 = \sinh(\frac{\pi x}{a}), \quad &&F_2 = \cosh(\frac{\pi x}{a}), \quad &&F_3 = \sinh(\frac{\pi z}{b}), \quad &&F_4 = \cosh(\frac{\pi z}{b}); \\ &F_5 = \sinh(\frac{2\pi x}{a}), \quad &&F_6 = \cosh(\frac{2\pi x}{a}), \quad &&F_7 = \sinh(\frac{2\pi z}{b}), \quad &&F_8 = \cosh(\frac{2\pi z}{b}); \\ &\dots \end{aligned} \tag{2.22}$$

Exponential expansions can be introduced as follows [47]:

$$\begin{aligned} &F_1 = e^{(\frac{x}{a})}, \quad &&F_2 = e^{(\frac{z}{b})}; \\ &F_3 = e^{(\frac{2x}{a})}, \quad &&F_4 = e^{(\frac{2z}{b})}; \\ &\dots \end{aligned} \tag{2.23}$$

For such models, the unknowns are merely mathematical weighting coefficients. Generally, these types of thickness functions are hierarchical. In addition, combinations of different types of expansions will lead to miscellaneous models.

2.2.6 Beam models using Lagrange Expansions (LE)

Lagrange interpolation polynomials can better describe the geometrical features of the cross-section than the Taylor series do. In the present work, such type of cross-section functions is referred to as Lagrange Expansions (LE). The construction of LE functions is analogous to that of Lagrangian shape functions for 2D finite elements.

Defined on a quadrilateral domain in the natural coordinate system (ξ, η), LE functions on four interpolation points (LE4) read:

$$F_\tau = \frac{1}{4}(1 + \xi\xi_\tau)(1 + \eta\eta_\tau) \qquad \tau = 1,2,3,4 \tag{2.24}$$

in which $(\xi, \eta) \in [-1,1]$, and (ξ_τ, η_τ) are the coordinates of point τ.

LE functions on nine points (LE9) can be defined similarly as:

$$F_\tau = [\frac{1}{2}\xi\xi_\tau(1 + \xi\xi_\tau) + (1 - \xi^2)(1 - \xi_\tau^2)][\frac{1}{2}\eta\eta_\tau(1 + \eta\eta_\tau) + (1 - \eta^2)(1 - \eta_\tau^2)] \tag{2.25}$$

Through isoparametric mapping, the functions defined in the natural coordinate system (ξ, η) can be transformed to a domain on the cross-section in the Cartesian coordinate system (x, y), as illustrated in Fig. 2.6. The mapping from the natural coordinates to global coordinates read:

$$\begin{aligned} x &= x_\tau \; F_\tau(\xi, \eta) \\ z &= z_\tau \; F_\tau(\xi, \eta) \end{aligned} \tag{2.26}$$

where (x_τ, z_τ) indicate the local coordinates of a interpolation point τ.

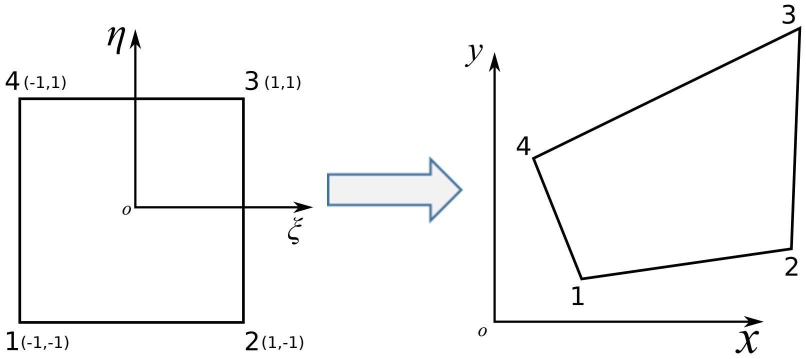

Figure 2.6: Isoparametric mapping on the beam cross-section.

Refined beam models with LE cross-sections can also be classified into the 3D category with an invariant cross-section. LE beam kinematic models are rigorous but computationally expensive in general. Their another feature is that the unknowns (u_τ, v_τ, w_τ) naturally represent translations of a line parallel to the neutral line on the beam body.

2.2.7 Beam models using hierarchical functions (HLE)

Szabó and Babuška [224] and Szabó, Düster, and Rank [226] suggested a series of hierarchical p-version functions for the approximation of deformation on quadrilateral domains. Such hierarchical functions can also be adopted as the cross-section functions. Pagani et al. [176] reported the efficiency of hierarchical functions in refined beam elements and referred to them as Hierarchical Legendre Expansions (HLE). In this type of functions, polynomial degree p is treated as an independent variable. The functions for a quadrilateral domain (ξ, η) can be classified into vertex modes, side modes, and internal modes, as shown in Fig. 2.7. The hierarchical functions can be expressed in a unified manner as:

$$F_\tau(\xi, \eta) = \phi_m(\xi)\ \phi_n(\eta) \quad (\xi, \eta) \in [-1,1] \tag{2.27}$$

where $\phi_m(\xi)$ are defined as:

$$\phi_m(\xi) = \begin{cases} \frac{1}{2}(1-\xi) & m = 0 \\ \frac{1}{2}(1+\xi) & m = 1 \\ \sqrt{\frac{2m-1}{2}} \int_{-1}^{\xi} P_{m-1}(x)dx = \frac{P_m(\xi) - P_{m-2}(\xi)}{\sqrt{4m-2}} & m = 2,3,\cdots \end{cases} \tag{2.28}$$

in which P_m represents the Legendre polynomials. $\phi_n(\eta)$ can be obtained accordingly.

Vertex modes are linear interpolations on the four vertex points:

$$\begin{aligned} F_1(\xi, \eta) &= \phi_0(\xi)\ \phi_0(\eta) \\ F_2(\xi, \eta) &= \phi_1(\xi)\ \phi_0(\eta) \\ F_3(\xi, \eta) &= \phi_1(\xi)\ \phi_1(\eta) \\ F_4(\xi, \eta) &= \phi_0(\xi)\ \phi_1(\eta) \end{aligned} \tag{2.29}$$

Side modes correspond to deformation modes dominated by the side edges:

$$F_\tau(\xi, \eta) = \begin{cases} \phi_m(\xi)\ \phi_0(\eta) & m \geqslant 2; \quad \tau = 5,9,13,18,\cdots \\ \phi_1(\xi)\ \phi_n(\eta) & n \geqslant 2; \quad \tau = 6,10,14,19,\cdots \\ \phi_m(\xi)\ \phi_1(\eta) & m \geqslant 2; \quad \tau = 7,11,15,20,\cdots \\ \phi_0(\xi)\ \phi_n(\eta) & n \geqslant 2; \quad \tau = 8,12,16,21,\cdots \end{cases} \tag{2.30}$$

Internal modes describe the deformation shapes happening on the internal surface and vanishing on the four edges:

$$F_\tau(\xi, \eta) = \phi_m(\xi)\ \phi_n(\eta) \qquad m, n \geqslant 2; \quad \tau = 17, 22, 23, 28, 29, 30, \cdots \tag{2.31}$$

An isoparametric mapping of coordinates is also required (see Eqn. 2.26). It should be noted that only the vertex modes will be accounted for in the isoparametric mapping since only they possess specific coordinates, see Eqn. (2.29).

This type of functions is *hierarchical* since the set of functions for $p-1$ are included in those for p. When the polynomial degree is increased by one order, only the newly added functions and the resultant matrices need to be introduced to the formulation. In addition to the high numerical efficiency and convenience in numerical applications, geometric mapping is also supported through the blending functions in such elements [226]. Application of this mapping technique in modeling beams with geometrically exact cross-sections was reported by Pagani et al. [175].

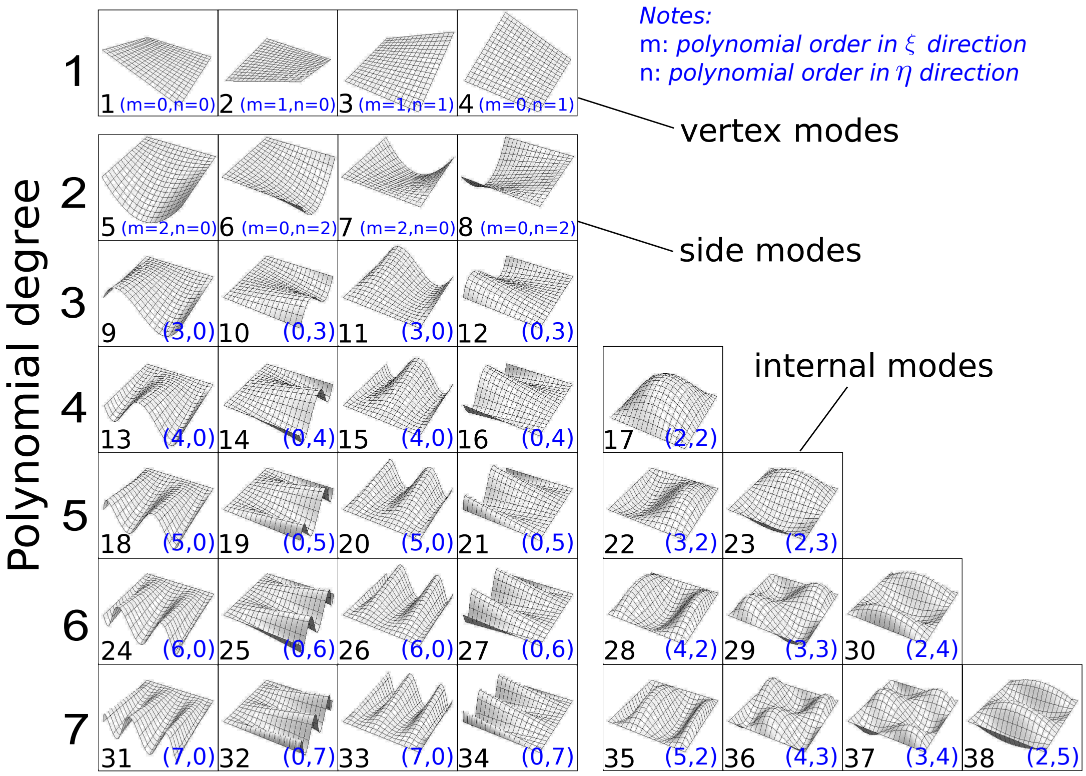
Notes:
m: polynomial order in ξ direction
n: polynomial order in η direction
vertex modes
side modes
internal modes
Polynomial degree
1
2
3
4
5
6
7
1 (m=0,n=0)
2 (m=1,n=0)
3 (m=1,n=1)
4 (m=0,n=1)
5 (m=2,n=0)
6 (m=0,n=2)
7 (m=2,n=0)
8 (m=0,n=2)
9 (3,0)
10 (0,3)
11 (3,0)
12 (0,3)
13 (4,0)
14 (0,4)
15 (4,0)
16 (0,4)
17 (2,2)
18 (5,0)
19 (0,5)
20 (5,0)
21 (0,5)
22 (3,2)
23 (2,3)
24 (6,0)
25 (0,6)
26 (6,0)
27 (0,6)
28 (4,2)
29 (3,3)
30 (2,4)
31 (7,0)
32 (0,7)
33 (7,0)
34 (0,7)
35 (5,2)
36 (4,3)
37 (3,4)
38 (2,5)

Figure 2.7: 2D hierarchical functions [224].

2.3 Plate and shell models

This section summarizes a variety of 2D theories, which are demonstrated with plate models and can be extended to shells by transforming the coordinates by referring to Eqn. (2.7).

2.3.1 Classical Plate Theory (CPT)

Classical Plate Theory (CLT) was presented by Love [152] based on the assumptions proposed by Kirchhoff. CLT is also referred to as Kirchhoff–Love Plate Theory. In this model, it is assumed that the straight lines normal to the neutral surface are rigid in the thickness direction, and keep straight and normal to the neutral surface under deformation. This theory is an extension of EBBT to 2D structures, and its deformation form can also be demonstrated through Fig. 2.3. Kirchhoff–Love hypothesis assumes the displacement field to be:

$$\begin{aligned} u(x,y,z) &= u_1(x,y) - z\, w_{1,x}(x,y) \\ v(x,y,z) &= v_1(x,y) - z\, w_{1,y}(x,y) \\ w(x,y,z) &= w_1(x,y) \end{aligned} \tag{2.32}$$

in which u_1, v_1, and w_1 are the translations on the neutural surface, $-w_{1,x}$ and $w_{1,y}$ the rotations of the corss-section around y and x axes, respectively (see Fig. 2.8). The thickness functions corresponding to this model are:

$$\begin{aligned} F_1^u &= 1; \quad F_2^u = z; \\ F_1^v &= 1; \quad F_2^v = z; \\ F_1^w &= 1; \quad F_2^w = 0. \end{aligned} \tag{2.33}$$

and the unknowns have the following relations:

$$u_2 = -w_{1,x}, \quad v_2 = -w_{1,y}. \tag{2.34}$$

In total, there are three independent unknowns in this model.

The above displacements result in a strain field with three in-plane strain components, namely ε_{xx}, ε_{yy}, and ε_{xy}:

$$\begin{aligned} \varepsilon_{xx} &= \frac{\partial u}{\partial x} && = u_{1,x} - z\frac{\partial^2 w_1}{\partial x^2} \\ \varepsilon_{yy} &= \frac{\partial v}{\partial y} && = v_{1,y} - z\frac{\partial^2 w_1}{\partial y^2} \\ \varepsilon_{xy} &= \frac{\partial u}{\partial y} + \frac{\partial v}{\partial x} && = u_{1,y} + v_{1,x} - 2z\frac{\partial^2 w_1}{\partial x \partial y} \end{aligned} \tag{2.35}$$

which are linearly distributed through the thickness direction. Note that $w_1(x, y)$ requires C^1 continuity in numerical analyses. The transverse shear strains ε_{xz}, ε_{yz} and transverse normal strain ε_{zz} are neglected. Finite elements based on CLT are usually called *thin plate/shell elements* intended for the modeling of structures with a high span-to-thickness ratio.

2.3.2 First-order Shear Deformation Theory (FSDT)

Suggested by Reissner [198] and Mindlin [162], the First-order Shear Deformation Theory (FSDT) assumes that the lines normal to the middle surface remain straight but are not constrained to be perpendicular to the middle surface of the plate. The FSDT is also referred to as the Mindlin–Reissner Theory. Different from Kirchhoff–Love hypothesis, FSDT accounts for the transverse shear effects and is intended for relatively thickness 2D structures. The displacement field of FSDT reads:

$$\begin{aligned} u(x, y, z) &= u_1(x, y) + z\ \phi_y(x, y) \\ v(x, y, z) &= v_1(x, y) - z\ \phi_x(x, y) \\ w(x, y, z) &= w_1(x, y) \end{aligned} \tag{2.36}$$

in which ϕ_y and ϕ_x designate the rotations of the cross-section around the y and x axes [194], respectively (see Fig. 2.8). In the FSDT model there exist five unknowns, and its corresponding thickness functions are:

$$\begin{aligned} F_1^u &= 1; \quad F_2^u = z; \\ F_1^v &= 1; \quad F_2^v = z; \\ F_1^w &= 1; \quad F_2^w = 0. \end{aligned} \tag{2.37}$$

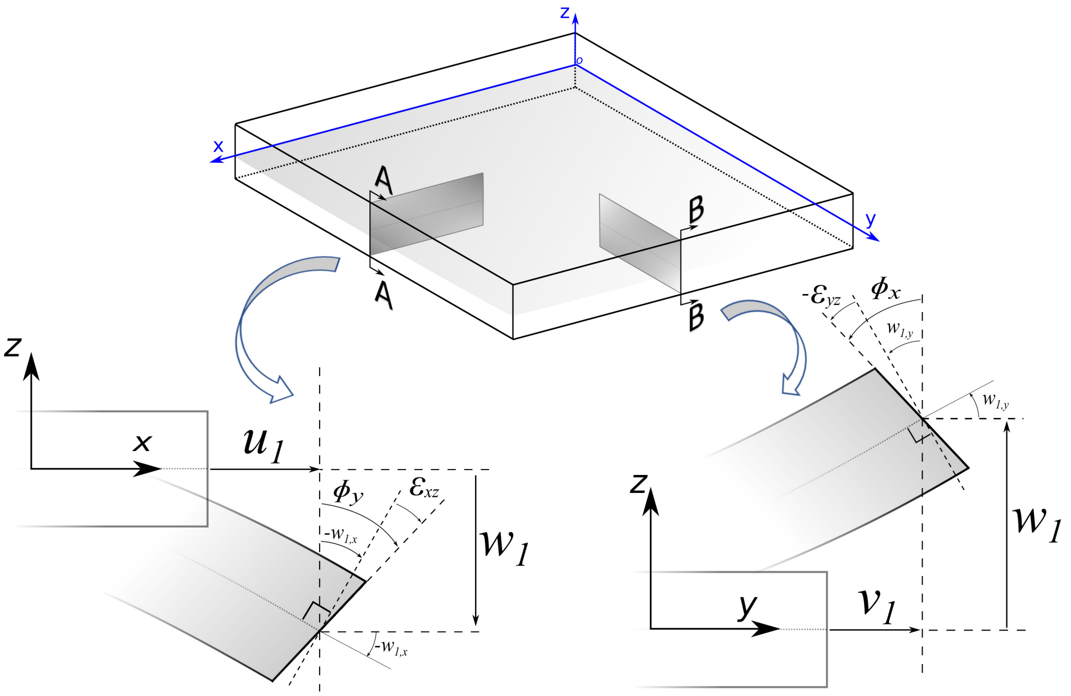

a) A-A view b) B-B view

Figure 2.8: First-order Shear Deformation Theory.

By applying the linear geometrical equations, the strain components obtained are:

$$\begin{aligned} \varepsilon_{xx} &= \frac{\partial u}{\partial x} && = u_{1,x} + z\,\phi_{y,x} \\ \varepsilon_{yy} &= \frac{\partial v}{\partial y} && = v_{1,y} - z\,\phi_{x,y} \\ \varepsilon_{xy} &= \frac{\partial u}{\partial y} + \frac{\partial v}{\partial x} && = u_{1,y} + z\,\phi_{y,y} + v_{1,x} - z\,\phi_{x,x} \\ \varepsilon_{xz} &= \frac{\partial u}{\partial z} + \frac{\partial w}{\partial x} && = \phi_y + w_{1,x} \\ \varepsilon_{yz} &= \frac{\partial v}{\partial z} + \frac{\partial w}{\partial y} && = -\phi_x + w_{1,y} \end{aligned} \tag{2.38}$$

Note that the in-plane strains vary linearly through the thickness, while the transverse shear stresses are constant in the thickness direction. Since this model assumes the 2D structure to be unable to stretch through the thickness, the transverse normal strain ε_{zz} is absent.

2.3.3 A linear plate model

A linear model with thickness extensibility reads:

$$\begin{aligned} u(x,y,z) &= u_1(x,y) + z\, u_2(x,y) \\ v(x,y,z) &= v_1(x,y) + z\, v_2(x,y) \\ w(x,y,z) &= w_1(x,y) + z\, w_2(x,y) \end{aligned} \tag{2.39}$$

in which there exist six independent unknowns. It can be observed that the CLT and FSDT are particular cases of this linear model. By considering Eqn. (2.5), this linear model can be obtained by taking:

$$F_1 = 1; \quad F_2 = z. \tag{2.40}$$

This linear model leads to the following set of strain components:

$$\begin{aligned} \varepsilon_{xx} &= \frac{\partial u}{\partial x} && = u_{1,x} + z\, u_{2,x} \\ \varepsilon_{yy} &= \frac{\partial v}{\partial y} && = v_{1,y} + z\, v_{2,y} \\ \varepsilon_{xy} &= \frac{\partial u}{\partial y} + \frac{\partial v}{\partial x} && = u_{1,y} + z\, u_{2,y} + v_{1,x} + z\, v_{2,x} \\ \varepsilon_{xz} &= \frac{\partial u}{\partial z} + \frac{\partial w}{\partial x} && = u_2 + w_{1,x} + z\, w_{2,x} \\ \varepsilon_{yz} &= \frac{\partial v}{\partial z} + \frac{\partial w}{\partial y} && = v_2 + w_{1,y} + z\, w_{2,y} \\ \varepsilon_{zz} &= \frac{\partial w}{\partial z} && = w_2 \end{aligned} \tag{2.41}$$

which means that in terms of through-thickness variation, the in-plane and transverse shear strains are linear, and the transverse normal strain is constant. Also, the newly introduced unknown w_2 signifies the stretching gradient of the thickness.

CPT, FSDT, and linear plate theories suffer from the Poisson locking phenomenon (also known as thickness locking) which can be contrasted by using modified elastic coefficients. Detailed discussion on this topic can be found in [59].

2.3.4 Higher-order plate models using Taylor Expansions (TE)

In the above discussion on several models, the gradual refinement of plate models through enriching the thickness functions has been demonstrated. Further refined theories can be formulated by substituting Taylor series into Eqn. (2.5), which means the adoption of the following thickness functions:

$$F_1 = 1, \quad F_2 = z^1, \quad \dots, \quad F_\tau = z^{\tau-1}, \dots \tag{2.42}$$

This type of thickness-functions is denoted as Taylor Expansions (TE), and TEn represents thickness functions adopting the full series of Taylor series from the 0-th order to the n-th order. The higher-order thickness functions improve the deformation capabilities of the cross-section (see Fig. 2.5). About the interpretation of model unknowns, one can refer to Section 2.2.4. TE-type theories are most widely adopted due to their inherent simplicity. Reddy's third-order plate theory [190, 189] is a successful example.

2.3.5 Plate models using trigonometric, hyperbolic, and exponential series

Trigonometric series together with a constant term form the following set of thickness functions [60]:

$$F_1 = 1, \quad F_2 = \sin(\frac{\pi z}{h}), \quad F_3 = \cos(\frac{\pi z}{h}), \quad F_4 = \sin(\frac{2\pi z}{h}), \quad F_5 = \cos(\frac{2\pi z}{h}), \quad \cdots \tag{2.43}$$

where h is the plate thickness.

Thickness functions based on hyperbolic series can be taken as:

$$F_1 = 1, \quad F_2 = \sinh(\frac{\pi z}{h}), \quad F_3 = \cosh(\frac{\pi z}{h}), \quad F_4 = \sinh(\frac{2\pi z}{h}), \quad F_5 = \cosh(\frac{2\pi z}{h}), \quad \cdots \tag{2.44}$$

Exponential expansions can be employed through [43, 60]:

$$F_1 = 1, \quad F_2 = e^{(\frac{z}{h})}, \quad F_3 = e^{(\frac{2z}{h})}, \quad F_4 = e^{(\frac{3z}{h})}, \quad F_5 = e^{(\frac{4z}{h})}, \quad \cdots \tag{2.45}$$

Different types of expansions can be used in combination to formulate miscellaneous thickness functions [60, 74, 73].

2.3.6 Plate models using Lagrange Expansions (LE)

Thickness functions based on Lagrange interpolation polynomials read:

$$F_\tau(\zeta) = \prod_{i=0, i\neq\tau}^{N} \frac{\zeta - \zeta_i}{\zeta_\tau - \zeta_i} \tag{2.46}$$

where ζ_τ are located at the prescribed interpolation points, and $\zeta_0 = -1$ and $\zeta_N = 1$ represent the bottom and top surfaces of the plate, respectively. The interpolation points are usually equally distributed through the shell thickness. Bias points, such as Chebyshev nodes, are also reported to be used by Kulikov and Plotnikova [139, 142].

A one-dimensional isoparametric mapping from $\zeta \in [-1,1]$ to $z \in [-\frac{h}{2}, \frac{h}{2}]$ reads:

$$z = z_\tau \, F_\tau(\zeta) \tag{2.47}$$

in which z_τ is the coordinate of point ζ_τ in the thickness direction in the global reference system.

In the present work, thickness functions based on Lagrange interpolation polynomials are referred to as Lagrange Expansions (LE). Different from the beam case, LEn as thickness functions of plate or shell models indicates the use of n-th order Lagrange polynomials. Similar to the beam case discussed in Section 2.2.6, unknowns in refined plate models with LE represent the translational freedoms of a surface in parallel with the middle surface. The resultant plate models are also classified into 3D-type models [194].

2.3.7 Plate models using orthogonal polynomials

Legendre polynomials are widely used orthogonal polynomials. They can be employed to construct thickness functions directly by taking $F_n = P_{n-1}$ (P_n indicates Legendre polynomials) as follows:

$$\begin{aligned}
&F_1 = 1;\\
&F_2 = z;\\
&F_3 = \frac{1}{2}(3z^2 - 1);\\
&F_4 = \frac{1}{2}(5z^3 - 3z);\\
&F_5 = \frac{1}{8}(35z^4 - 30z^2 + 3);\\
&\dots
\end{aligned} \tag{2.48}$$

Alternatively, one can use Legendre polynomials defined in the natural coordinate system $\zeta \in [-1,1]$ by considering the following expressions of the displacements:

$$\boldsymbol{u} = F_t \, \boldsymbol{u}_t + F_b \, \boldsymbol{u}_b + F_r \, \boldsymbol{u}_r = F_s \, \boldsymbol{u}_s, \qquad s = t, b, r \;, \quad r = 2, \dots, N. \tag{2.49}$$

in which the sub-indexes t and b indicate the top and bottom surfaces of the plate. The thickness functions are set by utilizing:

$$F_t = \frac{P_0 + P_1}{2} = \frac{1 + \zeta}{2}, \quad F_b = \frac{P_0 - P_1}{2} = \frac{1 - \zeta}{2}, \quad F_r = P_r - P_{r-2}. \tag{2.50}$$

In such models, $\boldsymbol{u}_b$ and $\boldsymbol{u}_t$ are the translations of the top and bottom surfaces, respectively. The other unknowns may not have specific physical meanings. Note that F_t and F_b represent a linear interpolation of displacements on the top and bottom surfaces, which is also reported to be used in the formulation of thick or solid shell elements [272, 100, 227]. In a sense, Eqn. (2.49) results in a series of refined solid shell models.

Regarding the isoparametric mapping of coordinates (see Eqn. 2.47), only the linear interpolation functions (F_t and F_b in Eqn. 2.50) will be used since there exist only coordinates of the top and bottom surfaces in this type of models.

A third approach to include Legendre polynomials in thickness functions is to use the one-dimensional hierarchical functions proposed by Szabó and Babuška [224] and Szabó, Düster, and Rank [226]. This type of hierarchical functions can be treated as a further development of Eqn. (2.49) by considering the norm of Legendre polynomials over the interval $[-1,1]$ (see Eqn. 2.28).

The advantages of hierarchical functions, mainly due to their orthogonality and hierarchal characteristics, have been discussed exclusively by Szabó, Düster, and Rank [226] and briefly explained in Section 2.2.7. It should be noted that some other types of polynomials have similar properties to Legendre polynomials. A variety of other orthogonal polynomials can be adopted to build thickness functions accordingly, including, but not limited to, Chebyshev polynomials and Hermite polynomials.

2.4 Theories of multi-layered structures

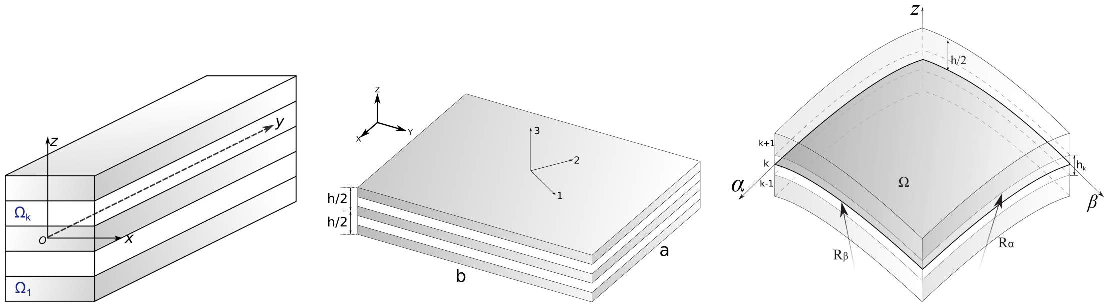

(a) Multi-layered beams (b) Multi-layered plates (c) Multi-layered shells

Figure 2.9: Multi-layered structures.

Many engineering structures consist of multiple layers such as laminated beams, plates, and shells, as shown in Fig. 2.9. The beam and plate/shell theories described in the previous sections in this chapter can be extended to multi-layered structures with perfect interfacial bonds in two frameworks, namely Equivalent-Single Layer (ESL) approach and Layer-Wise (LW) approach (see Fig. 2.10).

For a unit elastic body in the k-th layer, by referring to Eqn. (2.3), the displacements can be expressed as:

$$\boldsymbol{u}^k = F_\tau{}^k \, \boldsymbol{u}_\tau^{(k)} \tag{2.51}$$

where for ESL models $\boldsymbol{u}_\tau^{(k)} = \boldsymbol{u}_\tau$, for LW models $\boldsymbol{u}_\tau^{(k)} = \boldsymbol{u}_\tau^k$. The key difference between

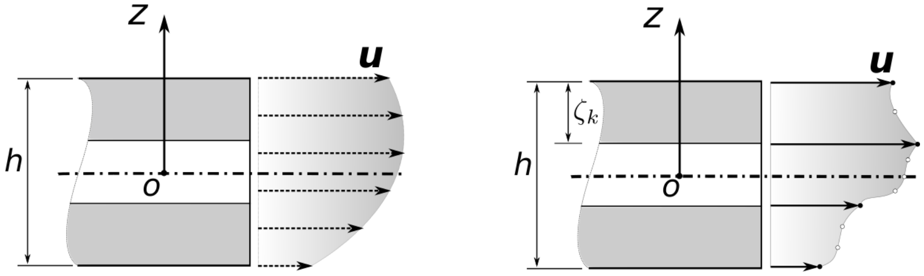

(a) Equivalent Single-Layer (ESL) (b) Layer-Wise (LW)

Figure 2.10: Two types of models for multi-layered structures.

ESL and LW approach lies in the construction of cross-section functions ${F_\tau}^k$, which leads to the difference regarding the form of $\boldsymbol{u}_\tau$.

2.4.1 Equivalent-Single Layer (ESL) approach

In the ESL approach, F_τ are defined on the whole cross-sectional domain of the multi-layered structure, as demonstrated by Fig. 2.10a. The main feature of ESL is that the cross-section is treated as a single domain in which the cross-section functions F_τ are defined, and the stresses are calculated by considering the resultant strains in each layer in displacement-based models. All the above-introduced theories of structures can be used in ESL approach.

Due to the heterogeneity of multi-layered structures, ESL models lead to continuous transverse strains through the thickness and discontinuous transverse stresses at layer interfaces. Given such a defect, ESL models are still most widely used due to their intrinsic simplicity and fairly good performance in modeling many slender and thin-walled structures.

To improve the interfacial continuity of transverse stresses, Murakami [166] suggested a zig-zag function that reads:

$$F_Z^k(z) = (-1)^k \zeta_k \tag{2.52}$$

where $\zeta_k = 2z_k/h_k$ is the non-dimensional thickness coordinate in the kth layer, and h_k the layer thickness. In Eqn. (2.52), the subscript Z signifies the zig-zag term. This zig-zag function can be appended to the expansions of refined ESL models to further improve the solution accuracy.

2.4.2 Layer-Wise (LW) approach

In the LW approach, the displacement field in each layer is individually assumed (see Fig. 2.10b), and ${F_\tau}^k$ are usually defined in the natural coordinate system and will be mapped to the cross-section of the k-th layer. To impose the interfacial continuity of displacements, the following constraints are necessary:

$$\boldsymbol{u}_t^k = \boldsymbol{u}_b^{k+1} \qquad k = 1, \cdots, N_l - 1. \tag{2.53}$$

in which the subscripts t and b represent the top and bottom surfaces of the k-th layer, and N_l the total number of layers. In fact, if $\boldsymbol{u}_t^k$ and $\boldsymbol{u}_b^k$ are also unknowns of the model, namely, $\boldsymbol{u}_\tau^k$ in Eqn. (2.51), the enforcement of the interfacial displacement continuity will become convenient. In Sections 2.2.6 and 2.3.6, it has been explained that in models with LE, the unknowns represent the translational displacements. Thus, LE can be applied to construct LW models conveniently. The hierarchical functions (see Sections 2.2.7 and 2.3.7) also suit the LW approach. Also, in the construction of plate and shell models, by replacing the first two terms with linear interpolation functions for the top and bottom surfaces of a layer (see Eqn. 2.50), some orthogonal polynomials such as Legendre, Chebyshev, and Hermite polynomials can also be used in the LW approach. In a sense, LW models have multiple reference surfaces but ESL models have only one. The existence of these physical interfaces facilitates the modeling of piezoelectric layers and patches. Such applications will be discussed in Chapters 10 in Part III.

In structural analyses, when the displacement field is obtained, the strains and stresses can be calculated subsequently in each layer. In LW models, the interlaminar continuity of transverse stresses are not guaranteed but can be numerically approached by refining the thickness functions [60]. Empirically, for linear mechanical analyses of multilayered plates and shells with a wide range of span-to-thickness ratio, fourth-order polynomials in each layer can lead to continuous transverse stresses through the thickness [60]. Sufficiently refined LW models are capable of giving accurate 3D solutions. LW models are also classified into the 3D category [194].

For multi-layered beams, Eqn. (2.51) can be written into:

$$\boldsymbol{u}^k(x, y, z) = \boldsymbol{u}_\tau(y)\ {F_\tau}^k(x, z) \tag{2.54}$$

in which ${F_\tau}^k(x, z)$ are mapped from $F_\tau(\xi, \zeta)$, which are defined in the natural coordinate system. This relation can be represented by:

$${F_\tau}^k(\xi, \zeta) \rightarrow {F_\tau}^k(x, z) \tag{2.55}$$

where $(\xi, \eta) \in [-1{,}1]$ are the coordinates in the natural reference system. The mapping of coordinates is given by:

$$\begin{aligned} x &= {x_\tau}^k\ {F_\tau}^k(\xi, \eta) \\ z &= {z_\tau}^k\ {F_\tau}^k(\xi, \eta) \end{aligned} \tag{2.56}$$

In the case of multi-layered plates, Eqn. (2.51) is further expressed as:

$$\boldsymbol{u}^k(x, y, z) = \boldsymbol{u}_\tau(x, y)\ {F_\tau}^k(z) \tag{2.57}$$

Accordingly, $F^k(z)$ defined in the global coordinate system is obtained from $F^k(\zeta)$ defined over the isoparametric domain $-1 \leq \zeta \leq 1$:

$${F_\tau}^k(\zeta) \rightarrow {F_\tau}^k(z) \tag{2.58}$$

Similar to Eqn. (2.47), the mapping relation of coordinates in the multi-layered plates is:

$$z = z_{\tau}{}^{k}\ F_{\tau}{}^{k}(\zeta) \tag{2.59}$$

For multi-layered shells which are defined in the curvilinear coordinate system (α, β, z), Eqn. (2.51) becomes:

$$\boldsymbol{u}^{k}(\alpha, \beta, z) = \boldsymbol{u}_{\tau}(\alpha, \beta)\ F_{\tau}{}^{k}(z) \tag{2.60}$$

Eqn. (2.58) also applies to multi-layered shell models.

2.4.3 Examples of ESL and LW models

Fig. 2.11 shows examples of ESL plate models adopting TE as thickness functions for approximations of displacements and the subsequent through-thickness distribution of deflection, transverse normal strain and stress. Note that TE*n* indicates the adoption of full Taylor series until the *n*th order. Fig. 2.11 demonstrates the continuity of strains and discontinuity of interfacial stress.

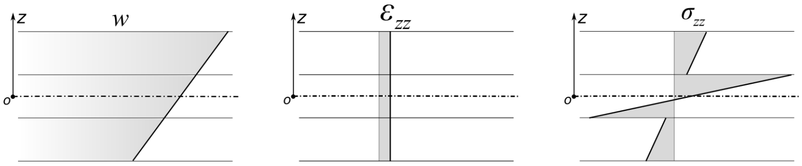

(a) TE1

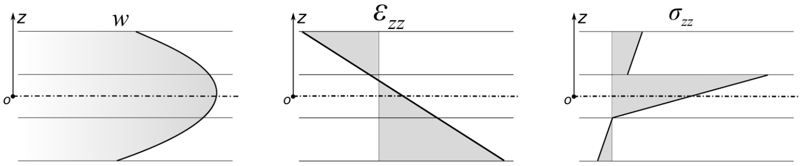

(b) TE2

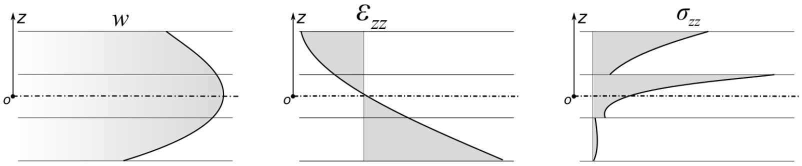

(c) TE4

Figure 2.11: Displacement-based ESL plate models with TE, through-thickness variation of deflection and transverse normal strain and stress.

Fig. 2.12 presents examples of displacement-based plate models in which LE are used as thickness functions uniformly in each layer. In Fig. 2.12, LE*n* signifies the *n*-th order Lagrange polynomials. With the increase of the order of the thickness functions, the solution accuracy can be improved gradually, and continuous transverse stresses variation through the thickness can be obtained. Compared to ESL models, LW models are generally more accurate yet comparatively heavy in computation.

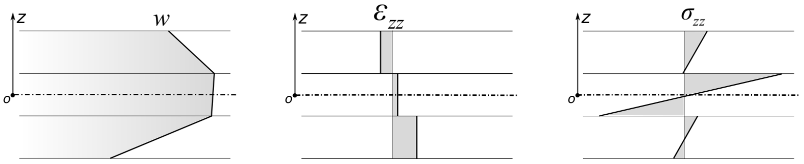
z
w
o
z
ε_{zz}
o
z
σ_{zz}
o

(a) LE1

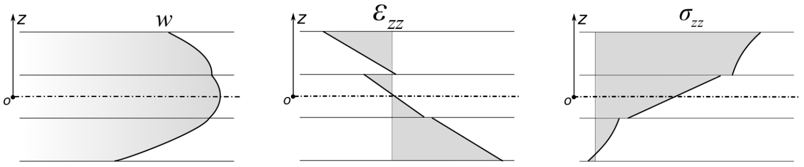
z
w
o
z
ε_{zz}
o
z
σ_{zz}
o

(b) LE2

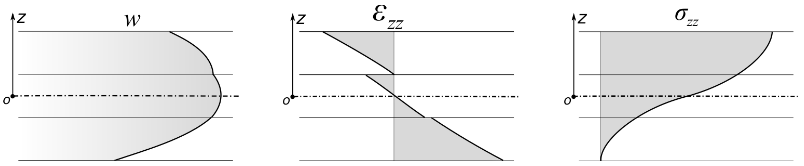
z
w
o
z
ε_{zz}
o
z
σ_{zz}
o

(c) LE4

Figure 2.12: Displacement-based LW plate models with LE, through thickness variation of deflection and transverse normal strain and stress.

Chapter 3

Hygro-thermo-electro-mechanical basic equations

This section consists of the fundamental equations of the steady-state hygro-thermo-electro-mechanical problems.

3.1 Tensor form of the basic equations

The considered primary variables include displacements u_i, electric potential ϕ, temperature increment θ, and change of moisture concentration c.

3.1.1 Strain-displacement relations and gradient equations

The strain tensor ε_{ij} can be obtained through the strain-displacement relations:

$$\varepsilon_{ij} = \frac{1}{2}(u_{i,j} + u_{j,i}) \tag{3.1}$$

The electrical field E_i, temperature gradients ϑ_i, and moisture gradients Υ_i are given by the following gradient equations:

$$E_i = -\phi_{,i} \tag{3.2}$$

$$\vartheta_i = -\theta_{,i} \tag{3.3}$$

$$\Upsilon_i = -c_{,i} \tag{3.4}$$

where $i, j = 1,2,3$.

3.1.2 Constitutive equations

The linear constitutive relations take the following form [4, 215]:

$$\sigma_{ij} = C_{ijkl}\epsilon_{kl} - e_{kij}E_k - \lambda_{ij}\theta - \psi_{ij}c \tag{3.5}$$

$$D_i = e_{ikl}\epsilon_{kl} + \chi_{ik}E_k + r_i\theta + \iota_i c \tag{3.6}$$

$$q_i = \kappa_{ik}\vartheta_k + \varphi_{ik}\Upsilon_k \tag{3.7}$$

$$h_i = \gamma_{ik}\vartheta_k + \xi_{ik}\Upsilon_k \tag{3.8}$$

wherein σ_{ij} indicates the stress tensor, D_i the electric displacement vector, q_i the heat flux vector, and h_i the moisture flux vector. In the above equations, $i, j, k, l = 1,2,3$.

The related material coefficients include the elastic constants C_{ijkl} (Hooke's law), dielectric permittivity coefficients χ_{ij}, thermal stress coefficients λ_{ij}, hygroscopic stress coefficients ψ_{ij}, piezoelectric coefficients e_{ikl}, pyroelectric coefficients r_i, hygro-electric coupling coefficient ι_i, thermal-hygroscopic coupling coefficient ζ, thermal conductivity coefficients κ_{ik}, moisture diffusivity coefficients ξ_{ik}, moisture flux due to the thermal gradients γ_{ik} (the thermodiffusion or Soret effect), and heat flux caused by the moisture gradients φ_{ik} (Dufour effect).

Note that λ_{ij} and ψ_{ij} can be considered as:

$$\lambda_{ij} = C_{ijkl}\ \alpha_{kl} \tag{3.9}$$

$$\psi_{ij} = C_{ijkl}\ \beta_{kl} \tag{3.10}$$

where α_{kl} and β_{kl} are the thermal and hygroscopic expansion coefficients, respectively.

3.1.3 Equilibrium and conservation equations

The equilibrium equations take the following form when body forces are absent:

$$\sigma_{ij,j} = 0 \tag{3.11}$$

In the absence of free charge, internal heat source, and internal moisture source, the conservation equations read:

$$D_{i,i} = 0 \tag{3.12}$$

$$q_{i,i} = 0 \tag{3.13}$$

$$h_{i,i} = 0 \tag{3.14}$$

which represent the conservation of charge (Gauss's law), heat conduction equation (Fourier's law), and moisture diffusion equation (Fick's law), separately.

3.1.4 Boundary conditions

The boundary conditions on the external surfaces of the elastic body are:

$$\begin{aligned} u_i &= \bar{u}_i \quad \text{on } \Gamma_u, & \phi &= \bar{\phi} \quad \text{on } \Gamma_\phi, \\ \theta &= \bar{\theta} \quad \text{on } \Gamma_\theta, & c &= \bar{c} \quad \text{on } \Gamma_c. \end{aligned} \tag{3.15}$$

$$\begin{aligned} \sigma_{ij}\, n_j &= \bar{p}_i \quad \text{on } \Gamma_p, & -D_i\, n_i &= \bar{D}_n \quad \text{on } \Gamma_D, \\ -q_i\, n_i &= \bar{q}_n \quad \text{on } \Gamma_q, & -h_i\, n_i &= \bar{h}_n \quad \text{on } \Gamma_h. \end{aligned} \tag{3.16}$$

in which n_i is the outward unit normal vector of the bounding surface, $\bar{u}_i$, $\bar{\phi}$, $\bar{\theta}$, and $\bar{c}$ are the essential boundary conditions, and $\bar{p}_i$, $\bar{D}_n$, $\bar{q}_n$, and $\bar{h}_n$ the natural boundary conditions. The overbar symbol ($\bar{\ }$) denotes prescribed values.

3.1.5 Free energy density

Based on the above governing equations, the free energy density G for static cases can be written into:

$$\begin{aligned} G =& \frac{1}{2}C_{ijkl}\varepsilon_{ij}\varepsilon_{kl} - \frac{1}{2}\chi_{ik}E_iE_k - \frac{1}{2}\kappa_{ik}\vartheta_i\vartheta_k - \frac{1}{2}\xi_{ik}\Upsilon_i\Upsilon_k - e_{ikl}E_i\varepsilon_{kl} - \frac{1}{2}\iota_iE_ic - \frac{1}{2}r_iE_i\theta \\ & - \frac{1}{2}\gamma_{ik}\vartheta_k\Upsilon_i - \frac{1}{2}\varphi_{ik}\vartheta_i\Upsilon_k - \frac{1}{2}\Psi_{ij}\varepsilon_{ij}c - \frac{1}{2}\lambda_{ij}\varepsilon_{ij}\theta \end{aligned} \tag{3.17}$$

3.2 Matrix form of the basic equations for beam, plate, and shell models

Beam and plate models without curvatures are defined in the Cartesian coordinate system (x, y, z), see Figs. 2.9a and 2.9b. Doubly curved shells with uniform thickness can be described in the orthogonal curvilinear system (α, β, z), see Fig. 2.9c.

3.2.1 Strain-displacement relations

Beams and plates

The relation between the engineering strain vector $\boldsymbol{\varepsilon}$ and displacement vector $\boldsymbol{u}(x, y, z) = \{u, v, w\}^\top$ reads:

$$\boldsymbol{\varepsilon} = \mathbf{b}\,\boldsymbol{u} \tag{3.18}$$

in which the strain vector is arranged as:

$$\boldsymbol{\varepsilon}(x, y, z) = \{\varepsilon_{xx}, \varepsilon_{yy}, \varepsilon_{zz}, \varepsilon_{yz}, \varepsilon_{xz}, \varepsilon_{xy}\}^\top \tag{3.19}$$

For beams and plates, the strain-displacement relations for 3D continuum bodies can be directly used, which means:

$$\mathbf{b} = \begin{bmatrix} \frac{\partial}{\partial x} & 0 & 0 \\ 0 & \frac{\partial}{\partial y} & 0 \\ 0 & 0 & \frac{\partial}{\partial z} \\ 0 & \frac{\partial}{\partial z} & \frac{\partial}{\partial y} \\ \frac{\partial}{\partial z} & 0 & \frac{\partial}{\partial x} \\ \frac{\partial}{\partial y} & \frac{\partial}{\partial x} & 0 \end{bmatrix} \tag{3.20}$$

Doubly curved shells

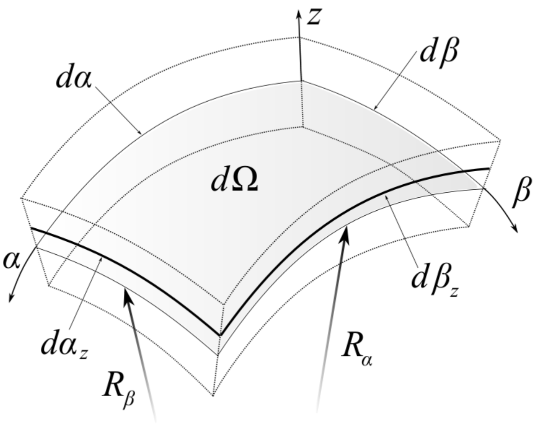

Figure 3.1: Geometry of doubly curved shells.

Geometric properties of shells are comparatively complicated than flat plates. Fig. 3.1 shows a differential element of a shell [194], in which α and β indicate the lines of curvature on the middle surface and z the thickness direction. The infinitesimal area dS parallel to the middle surface at z is:

$$dS = H_\alpha\, H_\beta\, d\alpha\, d\beta\, = H_\alpha\, H_\beta\, d\Omega \tag{3.21}$$

in which $d\Omega$ is the infinitesimal area on the middle surface of the shell. An elemental volume dV is given by:

$$dV = H_\alpha\, H_\beta\, H_z\, d\alpha\, d\beta\, dz\ . \tag{3.22}$$

For shells with constant radii of curvature, the metric coefficients H_α, H_β, and H_z read:

$$H_\alpha = (1 + z/R_\alpha), \quad H_\beta = (1 + z/R_\beta), \quad H_z = 1\ . \tag{3.23}$$

where R_α and R_β are the principal radii of curvature of the middle surface. For more details about shell theories, the reader is referred to [145, 194].

For doubly curved shells, corresponding to the displacement vector $\boldsymbol{u}(\alpha, \beta, z) = \{u, v, w\}^\top$, the strain vector is arranged as follows:

$$\boldsymbol{\varepsilon}(\alpha, \beta, z) = \{\varepsilon_{\alpha\alpha}, \varepsilon_{\beta\beta}, \varepsilon_{zz}, \varepsilon_{\beta z}, \varepsilon_{\alpha z}, \varepsilon_{\alpha\beta}\}^\top \tag{3.24}$$

and the differential operators matrix $\mathbf{b}$ becomes:

$$\mathbf{b} = \begin{bmatrix} \frac{\partial_\alpha}{H_\alpha} & 0 & \frac{1}{H_\alpha R_\alpha} \\ 0 & \frac{\partial_\beta}{H_\beta} & \frac{1}{H_\beta R_\beta} \\ 0 & 0 & \partial_z \\ 0 & \partial_z - \frac{1}{H_\beta R_\beta} & \frac{\partial_\beta}{H_\beta} \\ \partial_z - \frac{1}{H_\alpha R_\alpha} & 0 & \frac{\partial_\alpha}{H_\alpha} \\ \frac{\partial_\beta}{H_\beta} & \frac{\partial_\alpha}{H_\alpha} & 0 \end{bmatrix} \tag{3.25}$$

Note that when $H_\alpha = H_\beta = 1$ ($R_\alpha \to \infty$, $R_\beta \to \infty$), a shell becomes a plate which is flat in geometry.

3.2.2 Gradient equations

The electric field vector $\boldsymbol{E}$, temperature gradient vector $\boldsymbol{\vartheta}$, and moisture gradient vector $\boldsymbol{\Upsilon}$ can be obtained through:

$$\boldsymbol{E} = -\nabla\phi \tag{3.26}$$

$$\boldsymbol{\vartheta} = -\nabla\theta \tag{3.27}$$

$$\boldsymbol{\Upsilon} = -\nabla c \tag{3.28}$$

where ∇ is the gradient operator vector.

For beams and plates, ∇ reads:

$$\nabla = \{\partial_x, \partial_y, \partial_z\}^\top \tag{3.29}$$

For doubly curved shells, ∇ takes the following form:

$$\nabla = \{\frac{\partial_\alpha}{H_\alpha}, \frac{\partial_\beta}{H_\beta}, \partial_z\}^\top \tag{3.30}$$

3.2.3 Constitutive equations

For a homogeneous medium, the linear constitutive relations in matrix form read:

$$\boldsymbol{\sigma} = \boldsymbol{C}\boldsymbol{\varepsilon} - \boldsymbol{e}^{\top}\boldsymbol{E} - \boldsymbol{\lambda}^{\top}\theta - \boldsymbol{\psi}^{\top}c \tag{3.31}$$

$$\boldsymbol{D} = \boldsymbol{e}\boldsymbol{\varepsilon} + \boldsymbol{\chi}\boldsymbol{E} + \boldsymbol{r}^{\top}\theta + \boldsymbol{\iota}^{\top}c \tag{3.32}$$

$$\boldsymbol{q} = \boldsymbol{\kappa}\boldsymbol{\vartheta} + \boldsymbol{\varphi}\boldsymbol{\Upsilon} \tag{3.33}$$

$$\boldsymbol{h} = \boldsymbol{\gamma}\boldsymbol{\vartheta} + \boldsymbol{\xi}\boldsymbol{\Upsilon} \tag{3.34}$$

wherein $\boldsymbol{\sigma}$ is the stress vector, $\boldsymbol{D}$ the electric displacements vector, $\boldsymbol{q}$ the heat flux vector, and $\boldsymbol{h}$ the moisture vector.

For straight beams and plates, the stress vector reads:

$$\boldsymbol{\sigma}(x, y, z) = \{\sigma_{xx}, \sigma_{yy}, \sigma_{zz}, \sigma_{yz}, \sigma_{xz}, \sigma_{xy}\}^{\top} \tag{3.35}$$

For shells with double curvatures, $\boldsymbol{\sigma}$ is arranged as:

$$\boldsymbol{\sigma}(\alpha, \beta, z) = \{\sigma_{\alpha\alpha}, \sigma_{\beta\beta}, \sigma_{zz}, \sigma_{\beta z}, \sigma_{\alpha z}, \sigma_{\alpha\beta}\}^{\top} \tag{3.36}$$

The orthotropic material properties and some multi-field coupling effects are briefly discussed in this section. Detailed discussion on the Dufour and Soret effects can be found in the literature such as [213, 231, 229, 130, 214].

Elastic constants of orthotropic materials

In orthotropic materials, there exist three orthogonal planes of symmetry. In the material coordinate system (1,2,3), the material coefficients matrix $\boldsymbol{C}_m$ takes the following form:

$$\boldsymbol{C}_m = \begin{bmatrix} C_{11} & C_{12} & C_{13} & 0 & 0 & 0 \\ C_{21} & C_{22} & C_{23} & 0 & 0 & 0 \\ C_{31} & C_{32} & C_{33} & 0 & 0 & 0 \\ 0 & 0 & 0 & C_{44} & 0 & 0 \\ 0 & 0 & 0 & 0 & C_{55} & 0 \\ 0 & 0 & 0 & 0 & 0 & C_{66} \end{bmatrix} \tag{3.37}$$

which is characterized by nine independent material constants, namely the Young's moduli (E_1, E_2, E_3), the shear moduli (G_{23}, G_{13}, G_{12}), and the Poisson ratios (ν_{12}, ν_{13}, ν_{23}). For more details, one is referred to the work of Reddy [194].

Heat conduction and thermal expansions

The heat conduction coefficients matrix $\boldsymbol{\kappa}_m$ in the material coordinates reads:

$$\boldsymbol{\kappa}_m = \begin{bmatrix} \kappa_{11} & 0 & 0 \\ 0 & \kappa_{22} & 0 \\ 0 & 0 & \kappa_{33} \end{bmatrix} \tag{3.38}$$

Temperature increase causes the structure to expand and results in the change of stresses. This effect is captured by the thermal stress coefficients vector $\boldsymbol{\lambda}$. Expressed in the material coordinate system (1,2,3), λ_m has the following relation with the thermal expansion coefficients $\boldsymbol{\alpha}_m$:

$$\boldsymbol{\lambda}_m = \boldsymbol{C}_m\, \boldsymbol{\alpha}_m \tag{3.39}$$

wherein:

$$\boldsymbol{\alpha}_m = \begin{Bmatrix} \alpha_1 & \alpha_2 & \alpha_0 & 0 & 0 & 0 \end{Bmatrix}^\top \tag{3.40}$$

Moisture diffusion and hygroscopic expansions

The material moisture diffusivity matrix $\boldsymbol{\xi}_m$ takes the following form:

$$\boldsymbol{\xi}_m = \begin{bmatrix} \xi_{11} & 0 & 0 \\ 0 & \xi_{22} & 0 \\ 0 & 0 & \xi_{33} \end{bmatrix} \tag{3.41}$$

Moisture concentration increment also leads to mechanical expansions and subsequent hygroscopic stresses. Similar to the thermal case, the hygroscopic stress coefficients vector $\boldsymbol{\psi}_m$ is related to the hygroscopic expansions coefficients vector $\boldsymbol{\beta}$ through:

$$\boldsymbol{\psi}_m = \boldsymbol{C}_m\, \boldsymbol{\beta}_m \tag{3.42}$$

where

$$\boldsymbol{\beta}_m = \begin{Bmatrix} \beta_1 & \beta_2 & \beta_0 & 0 & 0 & 0 \end{Bmatrix}^\top \tag{3.43}$$

Piezoelectric properties

Piezoelectric effects are the results of the interaction between the mechanical deformation and the electrical field. The direct effect refers to the process that the electrical field causes mechanical straining, and the reverse effect features the generation of electric charge due to deformation. As summarized by Nye [172] and Ikeda [112], different crystal classes possess different symmetric features in the piezoelectric coefficients matrix.

PZT (lead zirconate titanate) is a type of widely adopted piezoelectric ceramic materials. When a PZT component is poled in the third axis direction, its dielectric permittivity matrix χ_m is:

$$\chi_m = \begin{bmatrix} \chi_{11} & 0 & 0 \\ 0 & \chi_{22} & 0 \\ 0 & 0 & \chi_{33} \end{bmatrix} \tag{3.44}$$

and the piezoelectric coefficients matrix $\boldsymbol{e}_m$ takes the following form:

$$\boldsymbol{e}_m = \begin{bmatrix} 0 & 0 & 0 & 0 & e_{15} & 0 \\ 0 & 0 & 0 & e_{24} & 0 & 0 \\ e_{31} & e_{32} & e_{33} & 0 & 0 & 0 \end{bmatrix} \tag{3.45}$$

Depending on the poling direction, piezoelectric components work in various deformation modes. Figs. 3.2a and 3.2a demonstrate the extension and shear actuation mechanisms of piezoelectric patches.

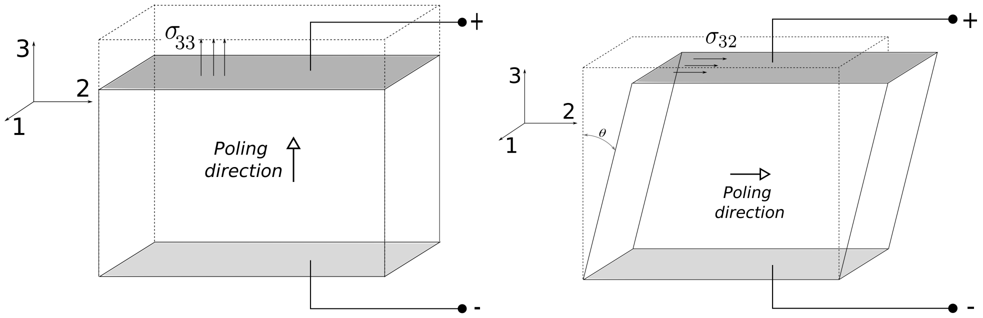

(a) Extension actuation mechanism (b) Shear actuation mechanism

Figure 3.2: Actuation mechanisms of piezoelectric components.

Thermo-electric and hygro-electric properties

Pyroelectricity refers to the effect that some material can generate voltage with the change of temperature. The pyroelectric coefficient vector $\boldsymbol{r}_m$ reads:

$$\boldsymbol{r}_m = \begin{bmatrix} 0 & 0 & r_3 \end{bmatrix} \tag{3.46}$$

The hygro-electric coupling effect is not often considered. When necessary, in analogy to the pyroelectric coefficients, the hygro-electric coefficient vector $\boldsymbol{\iota}_m$ can be set as:

$$\boldsymbol{\iota}_m = \begin{bmatrix} 0 & 0 & \iota_3 \end{bmatrix} \tag{3.47}$$

Transformation of material coefficient matrices

The above introduced material coefficients are defined in the material coordinate system (1,2,3). For structural analyses conducted in either Cartesian or curvilinear coordinate systems, the material matrices need to be transformed according to the orientation of the structure.

A global Cartesian reference system (x, y, z) is taken as an example. The coordinates in the global system and those in the material system have the following relations:

$$\begin{Bmatrix} 1 \\ 2 \\ 3 \end{Bmatrix} = \begin{bmatrix} l_1 & m_1 & n_1 \\ l_2 & m_2 & n_2 \\ l_3 & m_3 & n_3 \end{bmatrix} \begin{Bmatrix} x \\ y \\ z \end{Bmatrix} = \boldsymbol{L} \begin{Bmatrix} x \\ y \\ z \end{Bmatrix} \tag{3.48}$$

$$\begin{Bmatrix} x \\ y \\ z \end{Bmatrix} = \begin{bmatrix} a_1 & b_1 & c_1 \\ a_2 & b_2 & c_2 \\ a_3 & b_3 & c_3 \end{bmatrix} \begin{Bmatrix} 1 \\ 2 \\ 3 \end{Bmatrix} = \boldsymbol{R} \begin{Bmatrix} 1 \\ 2 \\ 3 \end{Bmatrix} \tag{3.49}$$

where l_1, m_1, n_1 are the direction cosines of x axis in the material coordinate system, l_2, m_2, n_2 the direction cosines of y axis, and l_3, m_3, n_3 the direction cosines of z axis. $\boldsymbol{R}$ is the rotation matrix from coordinates (1,2,3) to (x, y, z) that can be obtained by considering the Euler rotation angles (also see [264]), and:

$$\boldsymbol{R} = \boldsymbol{L}^{-1} = \boldsymbol{L}^{\top} \tag{3.50}$$

The relation between stresses $\boldsymbol{\sigma}$ in the global coordinate system and those in the material coordinate system $\boldsymbol{\sigma}_m$ reads:

$$[\boldsymbol{\sigma}] = \boldsymbol{R}\,[\boldsymbol{\sigma}_m]\,\boldsymbol{R}^{\top} \tag{3.51}$$

in which:

$$[\boldsymbol{\sigma}_m] = \begin{bmatrix} \sigma_{11} & \sigma_{12} & \sigma_{13} \\ \sigma_{12} & \sigma_{22} & \sigma_{23} \\ \sigma_{13} & \sigma_{23} & \sigma_{33} \end{bmatrix}; \qquad [\boldsymbol{\sigma}] = \begin{bmatrix} \sigma_{xx} & \sigma_{xy} & \sigma_{xz} \\ \sigma_{xy} & \sigma_{yy} & \sigma_{yz} \\ \sigma_{xz} & \sigma_{yz} & \sigma_{zz} \end{bmatrix} \tag{3.52}$$

By considering Eqn. (3.50) and rearranging the stress components in a vector form, the following expression can be obtained:

$$\begin{Bmatrix} \sigma_{xx} \\ \sigma_{yy} \\ \sigma_{zz} \\ \sigma_{yz} \\ \sigma_{xz} \\ \sigma_{xy} \end{Bmatrix} = \begin{bmatrix} a_1^2 & b_1^2 & c_1^2 & 2b_1c_1 & 2a_1c_1 & 2a_1b_1 \\ a_2^2 & b_2^2 & c_2^2 & 2b_2c_2 & 2a_2c_2 & 2a_2b_2 \\ a_3^2 & b_3^2 & c_3^2 & 2b_3c_3 & 2a_3c_3 & 2a_3b_3 \\ a_2a_3 & b_2b_3 & c_2c_3 & b_2c_3 + b_3c_2 & a_2c_3 + a_3c_2 & a_2b_3 + a_3b_2 \\ a_1a_3 & b_1b_3 & c_1c_3 & b_1c_3 + b_3c_1 & a_1c_3 + a_3c_1 & a_1b_3 + a_3b_1 \\ a_1a_2 & b_1b_2 & c_1c_2 & b_1c_2 + b_2c_1 & a_1c_2 + a_2c_1 & a_1b_2 + a_2b_1 \end{bmatrix} \begin{Bmatrix} \sigma_{11} \\ \sigma_{22} \\ \sigma_{33} \\ \sigma_{23} \\ \sigma_{13} \\ \sigma_{12} \end{Bmatrix} \tag{3.53}$$

which in an alternative compact form reads:

$$\boldsymbol{\sigma} = \boldsymbol{T}\,\boldsymbol{\sigma}_m \tag{3.54}$$

Similarly, one has:

$$\boldsymbol{\varepsilon}_m = \boldsymbol{T}^\top \, \boldsymbol{\varepsilon} \tag{3.55}$$

By considering:

$$\boldsymbol{\sigma} = \boldsymbol{T}\,\boldsymbol{\sigma}_m = \boldsymbol{T}\,\boldsymbol{C}_m\,\boldsymbol{\varepsilon}_m = \boldsymbol{T}\,\boldsymbol{C}_m\,\boldsymbol{T}^\top\,\boldsymbol{\varepsilon} = \boldsymbol{C}\,\boldsymbol{\varepsilon} \tag{3.56}$$

the transformation of elastic constants can be obtained as:

$$\boldsymbol{C} = \boldsymbol{T}\,\boldsymbol{C}_m\,\boldsymbol{T}^\top \tag{3.57}$$

and a tensor form of which can be found in the work of Reddy [194].

The transformation of the other material coefficient matrices can be conducted through:

$$\boldsymbol{H} = \boldsymbol{\Lambda}\,\boldsymbol{H}_m\,\boldsymbol{\Lambda}^\top \tag{3.58}$$

in which:

$$\boldsymbol{\Lambda} = \begin{bmatrix} \boldsymbol{T} & & & & & \\ & \boldsymbol{R} & & 0 & & \\ & & 1 & & & \\ & & & 1 & & \\ & 0 & & & \boldsymbol{R} & \\ & & & & & \boldsymbol{R} \end{bmatrix} \tag{3.59}$$

$$\boldsymbol{H} = \begin{bmatrix} \boldsymbol{C} & -\boldsymbol{e}^\top & -\boldsymbol{\lambda}^\top & -\boldsymbol{\psi}^\top & 0 & 0 \\ -\boldsymbol{e} & -\boldsymbol{\chi} & -\boldsymbol{r}^\top & -\boldsymbol{\iota}^\top & 0 & 0 \\ 0 & 0 & 0 & 0 & 0 & 0 \\ 0 & 0 & 0 & 0 & 0 & 0 \\ 0 & 0 & 0 & 0 & -\boldsymbol{\kappa} & -\boldsymbol{\varphi} \\ 0 & 0 & 0 & 0 & -\boldsymbol{\gamma} & -\boldsymbol{\xi} \end{bmatrix} \tag{3.60}$$

and one obtains:

$$\boldsymbol{\chi} = \boldsymbol{R}\,\boldsymbol{\chi}_m\,\boldsymbol{R}^\top \tag{3.61}$$

$$\boldsymbol{e} = \boldsymbol{R}\,\boldsymbol{e}_m\,\boldsymbol{T}^\top \tag{3.62}$$

$$\boldsymbol{\lambda} = \boldsymbol{\lambda}_m\,\boldsymbol{T}^\top \tag{3.63}$$

$$\boldsymbol{\psi} = \boldsymbol{\psi}_m\,\boldsymbol{T}^\top \tag{3.64}$$

$$\boldsymbol{r} = \boldsymbol{r}_m\,\boldsymbol{R}^\top \tag{3.65}$$

$$\boldsymbol{\iota} = \boldsymbol{\iota}_m\,\boldsymbol{R}^\top \tag{3.66}$$

$$\boldsymbol{\kappa} = \boldsymbol{R}\,\boldsymbol{\kappa}_m\,\boldsymbol{R}^\top \tag{3.67}$$

$$\boldsymbol{\xi} = \boldsymbol{R}\,\boldsymbol{\xi}_m\,\boldsymbol{R}^\top \tag{3.68}$$

$$\boldsymbol{\alpha} = \boldsymbol{R}\,\boldsymbol{\alpha}_m\,\boldsymbol{R}^\top \tag{3.69}$$

$$\boldsymbol{\beta} = \boldsymbol{R}\,\boldsymbol{\beta}_m\,\boldsymbol{R}^\top \tag{3.70}$$

Another application of Eqns. (3.61) and (3.62) is to obtain piezoelectric properties in different poling direction cases. When the poling direction is 1, χ_m and $\boldsymbol{e}_m$ can be obtained by transforming their forms in the third-direction poling case (see Enqs. 3.44 and 3.45) considering a 90° rotation around th second axis, and consequently:

$$\chi_m = \begin{bmatrix} \chi_{33} & 0 & 0 \\ 0 & \chi_{22} & 0 \\ 0 & 0 & \chi_{11} \end{bmatrix} \tag{3.71}$$

$$\boldsymbol{e}_m = \begin{bmatrix} e_{33} & e_{32} & e_{31} & 0 & 0 & 0 \\ 0 & 0 & 0 & 0 & 0 & e_{24} \\ 0 & 0 & 0 & 0 & e_{15} & 0 \end{bmatrix} \tag{3.72}$$

If the polarization direction is along the second material coordinate, χ_m and $\boldsymbol{e}_m$ read, respectively:

$$\chi_m = \begin{bmatrix} \chi_{11} & 0 & 0 \\ 0 & \chi_{33} & 0 \\ 0 & 0 & \chi_{22} \end{bmatrix} \tag{3.73}$$

$$\boldsymbol{e}_m = \begin{bmatrix} 0 & 0 & 0 & 0 & 0 & e_{15} \\ e_{31} & e_{33} & e_{32} & 0 & 0 & 0 \\ 0 & 0 & 0 & e_{24} & 0 & 0 \end{bmatrix} \tag{3.74}$$

Discussion on the transformation of the piezoelectric coefficients was also reported by Benjeddou, Trindade, and Ohayon [23], Vel and Batra [245], and Kapuria and Hagedorn [126]. The tensor form of the transformation matrices is stated by Kpeky et al. [138].

The above-introduced transformation methods can be directly applied to shell cases.

3.2.4 Equilibrium and conservation equations

The equilibrium and conservation equations discussed in Section 3.1.3 can be written into a matrix form as follows:

$$\mathbf{b}^{\top}\boldsymbol{\sigma} = 0 \tag{3.75}$$

$$\nabla^{\top}\boldsymbol{D} = 0 \tag{3.76}$$

$$\nabla^{\top}\boldsymbol{q} = 0 \tag{3.77}$$

$$\nabla^{\top}\boldsymbol{h} = 0 \tag{3.78}$$

3.2.5 Boundary conditions

The displacement boundary conditions read:

$$\boldsymbol{u} = \bar{\boldsymbol{u}}_i \quad \text{on } \Gamma_u \tag{3.79}$$

The expressions of the electric potential, temperature, and moisture concentration boundary conditions remain the same as in Eqn. (3.15).

The traction boundary conditions $\boldsymbol{\sigma}$ can be expressed as:

$$[\boldsymbol{\sigma}]\,\boldsymbol{n} = \overline{\boldsymbol{p}} \quad \text{on } \Gamma_p \tag{3.80}$$

where $\boldsymbol{n} = \{l, m, n\}^\top$ is the direction cosine vector of the external normal of boundary Γ_p, and $[\boldsymbol{\sigma}]$ takes the form as shown in Eqn. (3.52). Alternatively, Eqn. (3.80) can be written into:

$$\mathbf{G}^\top\boldsymbol{\sigma} = \overline{\boldsymbol{p}} \quad \text{on } \Gamma_p \tag{3.81}$$

in which

$$\mathbf{G} = \begin{bmatrix} l & 0 & 0 \\ 0 & m & 0 \\ 0 & 0 & n \\ 0 & n & m \\ n & 0 & l \\ m & l & 0 \end{bmatrix} \tag{3.82}$$

The boundary conditions of electric displacements, heat flux, and moisture flux are:

$$\begin{aligned} -\boldsymbol{n}^\top\,\boldsymbol{D} &= \overline{\boldsymbol{D}}_n && \text{on } \Gamma_D, \\ -\boldsymbol{n}^\top\,\boldsymbol{q} &= \overline{q}_n && \text{on } \Gamma_q, \\ -\boldsymbol{n}^\top\,\boldsymbol{h} &= \overline{h}_n && \text{on } \Gamma_h. \end{aligned} \tag{3.83}$$

3.2.6 Free energy density

In the matrix form, the free energy density G for steady-state cases reads:

$$G = \frac{1}{2}(\boldsymbol{\sigma}^\top\boldsymbol{\varepsilon} - \boldsymbol{D}^\top\boldsymbol{E} - \boldsymbol{q}^\top\boldsymbol{\vartheta} - \boldsymbol{h}^\top\boldsymbol{\Upsilon}) \tag{3.84}$$

Chapter 4

Variable kinematic finite element formulations

The displacements for multi-layered structures are expressed as in Eqn. (2.51). When finite element (FE) discretization is introduced, shape functions N_i are used to approximate $\boldsymbol{u}_\tau$, and one obtains the following displacements of an elastic body in layer k:

$$\boldsymbol{u}^k = N_i \; F_\tau^k \; \boldsymbol{u}_{i\tau} \qquad \tau = 1, \cdots, m; \quad i = 1, \cdots, n_N \tag{4.1}$$

where $\boldsymbol{u}_{i\tau}$ are the unknowns to be calculated. Note that the superscript k indicates the kth layer in the laminated structure rather than a power of F_τ.

By looking into Eqn. (4.1), it can be summarized that the mathematical refinement of FE models includes the following aspects:

1. The basis functions on the cross-section (F_τ and m);
2. The basis functions on the beam axis or the plate/shell in-plane domain (N_i and n_N);
3. The coupling of N_i and F_τ.

In the CUF framework, both the refinement of cross-section functions F_τ and the enhancement of shape functions N_i can be carried out conveniently by considering the compact expression of the weak-form governing equations as in Section 4.4. The coupling of N_i and F_τ result in Node-Dependent Kinematics (NDK), which can be exploited to construct FE models with variable nodal capabilities. These features lead to a broad spectrum of FE models on the given FE meshes.

4.1 Variable kinematic assumptions

Various kinematic models have been introduced in Chapter 2 for straight beams, plates, and doubly curved shells. In the CUF framework, these three types of models can be implemented in a unified manner. Moreover, the mathematical refinement degree can be increased till the requirements for solution accuracy are satisfied. A practical approach is illustrated as follows:

$$| \frac{u_M - u_{M-1}}{u_M} | \times 100\% \leq \delta \tag{4.2}$$

where u is the concerned displacement component, M the order of F_τ, and δ a prescribed error threshold of convergence. When required, u can also be replaced by a component of stress σ or strain ε in the above equation. For multi-layered structures, regarding the numerical convergence, in general:

- Stresses are more critical than displacements since they are calculated from the derivatives of displacements;
- Transverse stresses are more critical than the axial/in-plane stresses, and they need to satisfy the stress-free natural boundary conditions on the top and bottom surfaces and the interfacial connectivity conditions.

Section 2.4.3 illustrates the improvement of solutions with the gradual refinement of the kinematic assumptions. In numerical analyses, to obtain results with the desired accuracy often requires a convergence study. Besides the h-version and p-version refinement, CUF provides a practical framework to carry out another dimension of model enrichment, which is the kinematic refinement through variable kinematics.

4.2 Various finite element shape functions

The Lagrange interpolation polynomials (see Sections. 2.2.6 and 2.3.6) and orthogonal polynomials (see Sections. 2.2.7 and 2.3.7) can be used to build FE shape functions.

4.2.1 1D shape functions for beam elements

For 1D elements, the most widely adopted shape functions are based on the Lagrange polynomials (see Section 2.2.6). In Eqn. (2.46), by simply replacing F_τ with N_i and ζ with η, and considering the following mapping relation of coordinates:

$$y = y_i \; N_i(\eta) \tag{4.3}$$

1D shape functions for beam elements can be formulated. Linear Lagrangian beam element (B2) is commonly used, yet displacement-based B2 element does not satisfy the C^1 continuity requirement of EBBT models (see Eqn. 2.13).

Orthogonal polynomials introduced in Section 2.3.7 can also be employed in the construction of 1D beam elements when the first two basis functions are replaced by linear interpolation functions (see Eqn. 2.50).

For the correction of shear locking phenomenon in beam elements, the Mixed Interpolation of Tensorial Components (MITC) technique [87, 16, 34, 17] can be extended to beam elements. The effectiveness is reported by Carrera, Miguel, and Pagani [37].

4.2.2 2D shape functions for plate and shell elements

The construction of plate and shell shape functions is analogous to that of beam cross-section functions, as discussed in Sections. 2.2.6 and 2.2.7. The isoparametric mapping for plate elements reads:

$$\begin{aligned} x &= x_i \; N_i(\xi, \eta) \\ y &= y_i \; N_i(\xi, \eta) \end{aligned} \tag{4.4}$$

in which (x_i, y_i) represent the local coordinates of FE node i. Similarly, for shell elements:

$$\begin{aligned} \alpha &= \alpha_i \; N_i(\xi, \eta) \\ \beta &= \beta_i \; N_i(\xi, \eta) \end{aligned} \tag{4.5}$$

wherein (x_i, y_i) are the coordinates of node i in the curvilinear reference system. For hierarchical 2D elements, only the functions corresponding to $p \leq 1$ will participate in the isoparametric mapping, as explained in Section 2.2.7.

The most broadly used elements are the quadrilateral Lagrangian elements Q4 (four-node) and Q9 (nine-node). The even higher-order Lagrangian elements such as Q25, Q49, and Q81, are also used by researchers [186, 7]. Other 2D shape functions include the Hermitian [243], serendipity [8], and hierarchical elements [224, 226].

The MITC technique can help to effectively overcome the shear and membrane locking in plate elements and both the membrane and shear locking phenomena in shell elements [87, 16, 34, 17, 14]. In MITC approach, a specific set of tying points together with interpolation functions over them are designed for each kind of Lagrangian shape functions, leading to elements such as MITC4, MITC6, MITC9, and MITC16 [17]. In the CUF framework, the locking-free MITC9 element (nine-node Lagrangian quadrilateral element with MITC) with refined ESL and LW kinematics was successfully applied in the modeling of multi-layered plate [44, 94] and shell [68, 70, 69, 60] models.

The p-version shape functions have drawn considerable attention due to their hierarchical characteristics and high efficiency in numerical analyses. 1D, 2D, and 3D hierarchical functions were explained systematically by Szabó and Babuška [224] and Szabó, Düster, and Rank [226]. Due to the hierarchical characteristics, when the polynomial degree is increased from p to $p+1$, only the newly introduced shape functions and their resultant matrix blocks need to be added to the FE formulation, and the stiffness matrix of lower-order elements can be reused. p-version refinement facilitates mathematical enhancement on the same set of mesh grid. Hierarchical elements also provide the convenience for geometric mapping through the blending functions [226]. Moreover, the shear and membrane locking phenomena can be eased through the p-version refinement [221, 226]. An evaluation of hierarchical shell elements in the analysis of multi-layered structures was reported in Chapter 12.

4.3 Node-Dependent Kinematics (NDK)

Carrera et al. [58] introduced the dependency of thickness functions F_τ on the shape functions N_i through:

$$\boldsymbol{u}^k = N_i \; F_\tau^{ik} \; \boldsymbol{u}_{i\tau}^{(k)} \qquad \tau = 1, \cdots, m_i; \quad i = 1, \cdots, n_N \tag{4.6}$$

The difference of Eqn. (4.6) from Eqn. (4.1) is the additional superscript i, which is the index of the "anchoring" node. The coupling between cross-section function F_τ and shape functions N_i introduced by Eqn. (4.6) leads to FE models with Node-Dependent Kinematics (NDK). Through NDK, FE models can be refined locally regarding specific shape functions, in other words, on the chosen FE nodes. Different nodal kinematics are blended by the shape functions within the element domain. NDK approach makes it convenient to perform a local adaptable kinematic refinement. The two-level mathematical refinements and the adjustable assignment of local kinematics can lead to an adaptable refinement FE approach, with which optimal numerical efficiency can be achieved in FE numerical simulations.

4.3.1 Beam elements with NDK

Displacement field of beam elements with NDK reads:

$$\boldsymbol{u}^k(x, y, z) = N_i(y) \; F_\tau^{ik}(x, z) \; \boldsymbol{u}_{i\tau}^{(k)} \qquad \tau = 1, \cdots, m_i; \quad i = 1, \cdots, n_N \tag{4.7}$$

As an example, Fig 4.1 presents a B4 element with individual kinematic assumptions on each node. A kinematic transition is formed along the axial direction of the beam. Such a transition zone can connect two regions with different levels of kinematic refinement and facilitates rigorous local modeling.

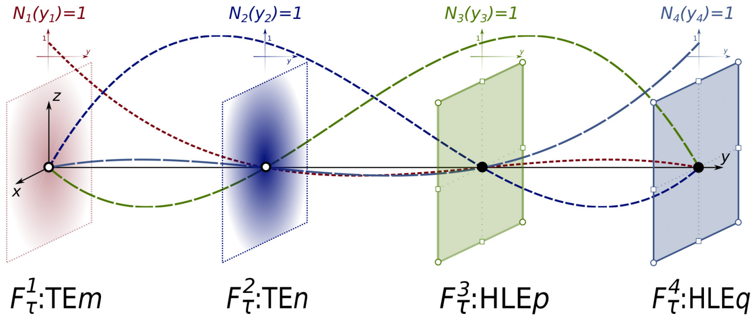

Figure 4.1: A B4 element with node-dependent kinematics.

4.3.2 Plate and shell elements with NDK

NDK plate FE models read:

$$\boldsymbol{u}^k(x, y, z) = N_i(x, y)\ F_\tau^{ik}(z)\ \boldsymbol{u}_{i\tau}^{(k)} \qquad \tau = 1, \cdots, m_i; \quad i = 1, \cdots, n_N \tag{4.8}$$

Correspondingly, displacements of NDK shell elements take the following form:

$$\boldsymbol{u}^k(\alpha, \beta, z) = N_i(\alpha, \beta)\ F_\tau^{ik}(z)\ \boldsymbol{u}_{i\tau}^{(k)} \qquad \tau = 1, \cdots, m_i; \quad i = 1, \cdots, n_N \tag{4.9}$$

A typical application of NDK is the construction of global-local models. In the example shown in Fig. 4.2, the four-node element possesses four different theories on its four nodes. A set of such elements form a kinematic transition zone Ω_r, which bridges the locally refined region Ω_β to the less refined outlying domain Ω_α. Global-local models can be constructed conveniently without changing the meshes, and the same set of mesh grid can be re-used to build a family of models for concurrent global-local analyses, as discussed by Zappino et al. [263].

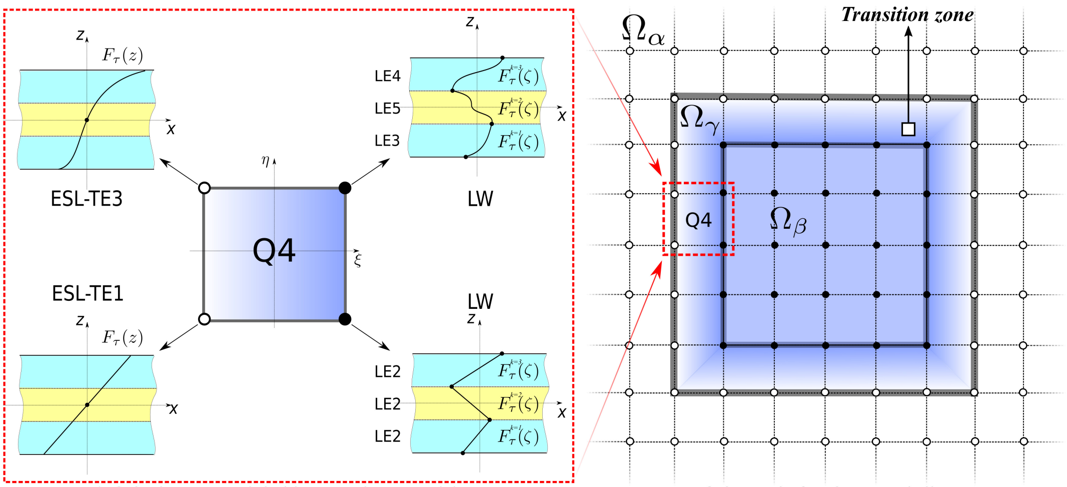

A Q4 element with kinematic transition *Q4 mesh for 2D modeling*

Figure 4.2: A FE model consists of four-node Lagrangian elements (Q4) with Node-Dependent Kinematics (NDK).

In Lagrangian elements, each shape function has a node with specific coordinates. Differently, in hierarchical 2D elements, only the $p = 1$ basis functions (vertex modes, see Eqn. 2.29) possess a real node. Still, each N_i of the hierarchical class can have an individually defined F_τ^i. For hierarchical elements with NDK, the term “node” represents the index of a shape function. In the current work, for simplicity purposes, all internal-mode basis functions and side mode functions lying on the same edge are seperately assigned to the same set of cross-section functions. Such a kinematic assignment scheme is shown in Fig. 4.3.

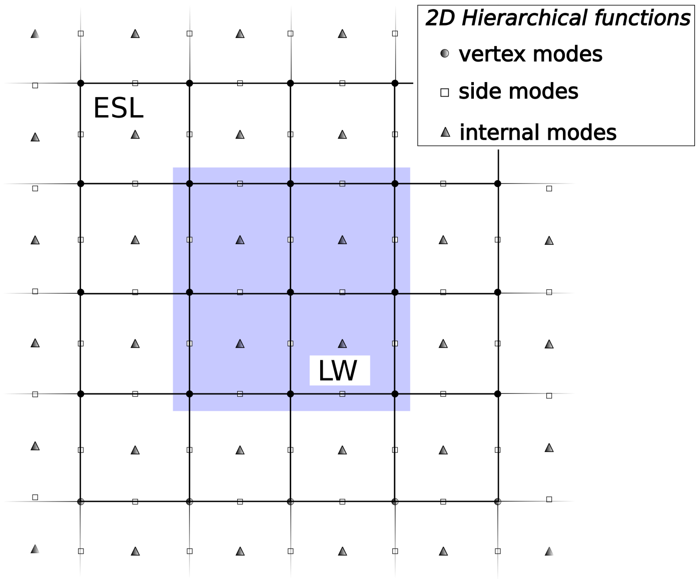

Figure 4.3: Assignment of nodal kinematics in 2D hierarchical elements.

4.4 Weak form of governing equations

In this section, the weak-form governing equations are derived in the CUF framework in a compact form. The FNs of generalized stiffness matrix and load vector are introduced, and their assembly procedure in FE models with NDK is presented.

4.4.1 Linear system of equations

For a unit volume in the kth layer, by applying the principle of virtual displacements (PVD), one has:

$$\delta E_p = \delta W \tag{4.10}$$

wherein

$$\delta E_p = \int_V (\boldsymbol{\sigma}^{k\top} \delta \boldsymbol{\varepsilon}^k - \boldsymbol{D}^{k\top} \delta \boldsymbol{E}^k - \boldsymbol{q}^{k\top} \delta \boldsymbol{\vartheta}^k - \boldsymbol{h}^{k\top} \delta \boldsymbol{\Upsilon}^k) dV \tag{4.11}$$

$$\delta W = \int_\Gamma (\delta \boldsymbol{u}^{k\top} \bar{\boldsymbol{p}} + \delta \phi^k \, \bar{D}_n + \delta \theta^k \, \bar{q}_n + \delta c^k \, \bar{h}_n) \, d\Gamma \tag{4.12}$$

In the above equations, E_p represents the potential energy, W the external work, $\boldsymbol{p}$ the surface traction vector, D_n the surface charge per unit area, q_n the normal heat flux, and h_n the normal moisture flux. In static cases, the inertial work is discarded.

The approximations of the primary variables are:

$$\boldsymbol{u}^k = N_i \, F_\tau^{ik} \boldsymbol{u}_{i\tau}^{(k)}, \qquad \delta \boldsymbol{u}^k = N_j \, F_s^{jk} \delta \boldsymbol{u}_{js}^{(k)}. \tag{4.13}$$

$$\phi^k = N_i \, F_\tau^{ik} \phi_{i\tau}^{(k)}, \qquad \delta \phi^k = N_j \, F_s^{jk} \delta \phi_{js}^{(k)}. \tag{4.14}$$

$$\theta^k = N_i\, F_\tau^{ik} \theta_{i\tau}^{(k)}, \qquad \delta\theta^k = N_j\, F_s^{jk} \delta\theta_{js}^{(k)}. \tag{4.15}$$

$$c^k = N_i\, F_\tau^{ik} c_{i\tau}^{(k)}, \qquad \delta c^k = N_j\, F_s^{jk} \delta c_{js}^{(k)}. \tag{4.16}$$

in which for ESL models $\boldsymbol{u}_{i\tau}^{(k)} = \boldsymbol{u}_{i\tau}$, and for LW models $\boldsymbol{u}_{i\tau}^{(k)} = \boldsymbol{u}_{i\tau}^k$. The same rule applies to other variables. The essential boundary conditions are considered through:

$$\begin{aligned} N_i\, F_\tau^{ik}\, \bar{\boldsymbol{u}}_{i\tau}^{(k)} &= \bar{\boldsymbol{u}} \quad \text{on } \Gamma_{\boldsymbol{u}}, & N_i\, F_\tau^{ik}\, \bar{\phi}_{i\tau}^{(k)} &= \bar{\phi} \quad \text{on } \Gamma_\phi, \\ N_i\, F_\tau^{ik}\, \bar{\theta}_{i\tau}^{(k)} &= \bar{\theta} \quad \text{on } \Gamma_\theta, & N_i\, F_\tau^{ik}\, \bar{c}_{i\tau}^{(k)} &= \bar{c} \quad \text{on } \Gamma_c. \end{aligned} \tag{4.17}$$

By considering the above approximations, the strain-displacement relations in Section 3.2.1, the gradient equations in Section 3.2.2, and the constitutive relations in Section 3.2.3, Eqn. (4.10) can be written into:

$$\begin{aligned} \delta\boldsymbol{u}_{js}^{(k)\top} &: & \boldsymbol{K}_{ij\tau s}^{\boldsymbol{uu}\ k}\boldsymbol{u}_{i\tau}^{(k)} + \boldsymbol{K}_{ij\tau s}^{\boldsymbol{u}\phi\ k}\phi_{i\tau}^{(k)} + \boldsymbol{K}_{ij\tau s}^{\boldsymbol{u}\theta\ k}\theta_{i\tau}^{(k)} + \boldsymbol{K}_{ij\tau s}^{\boldsymbol{u}c\ k}c_{i\tau}^{(k)} &= \boldsymbol{P}_{js}^{\boldsymbol{u}\ k} \\ \delta\phi_{js}^{(k)} &: & \boldsymbol{K}_{ij\tau s}^{\phi\boldsymbol{u}\ k}\boldsymbol{u}_{i\tau}^{(k)} + K_{ij\tau s}^{\phi\phi\ k}\phi_{i\tau}^{(k)} + K_{ij\tau s}^{\phi\theta\ k}\theta_{i\tau}^{(k)} + K_{ij\tau s}^{\phi c\ k}c_{i\tau}^{(k)} &= P_{js}^{\phi k} \\ \delta\theta_{js}^{(k)} &: & K_{ij\tau s}^{\theta\theta\ k}\theta_{i\tau}^{(k)} + K_{ij\tau s}^{\theta c\ k}c_{i\tau}^{(k)} &= P_{js}^{\theta\, k} \\ \delta c_{js}^{(k)} &: & K_{ij\tau s}^{c\theta\ k}\theta_{i\tau}^{(k)} + K_{ij\tau s}^{cc\ k}c_{i\tau}^{(k)} &= P_{js}^{c\ k} \end{aligned} \tag{4.18}$$

where the *fundamental nuclei* (FNs) of the generalized stiffness matrices are:

$$\boldsymbol{K}_{ij\tau s}^{\boldsymbol{uu}\ k} = \int_{V^k} (\mathbf{b}\, N_j F_s^{jk})^\top \boldsymbol{C}^k (\mathbf{b}\, N_i F_\tau^{ik}) dV \tag{4.19}$$

$$\boldsymbol{K}_{ij\tau s}^{\boldsymbol{u}\phi\ k} = \int_{V^k} (\mathbf{b}\, N_j F_s^{jk})^\top \boldsymbol{e}^{k\top} (\nabla\, N_i F_\tau^{ik}) dV \tag{4.20}$$

$$\boldsymbol{K}_{ij\tau s}^{\phi\boldsymbol{u}\ k} = \int_{V^k} (\nabla\, N_j F_s^{jk})^\top \boldsymbol{e}^k (\mathbf{b}\, N_i F_\tau^{ik}) dV \tag{4.21}$$

$$K_{ij\tau s}^{\phi\phi\ k} = -\int_{V^k} (\nabla\, N_j F_s^{jk})^\top \boldsymbol{\chi}^k (\nabla\, N_i F_\tau^{ik}) dV \tag{4.22}$$

$$\boldsymbol{K}_{ij\tau s}^{\boldsymbol{u}\theta\ k} = -\int_{V^k} (\mathbf{b}\, N_j F_s^{jk})^\top \boldsymbol{\lambda}^{k\top} (N_i F_\tau^{ik}) dV \tag{4.23}$$

$$\boldsymbol{K}_{ij\tau s}^{\boldsymbol{u}c\ k} = -\int_{V^k} (\mathbf{b}\, N_j F_s^{jk})^\top \boldsymbol{\Psi}^{k\top} (N_i F_\tau^{ik}) dV \tag{4.24}$$

$$K_{ij\tau s}^{\phi\theta\ k} = \int_{V^k} (\nabla\, N_j F_s^{jk})^\top \boldsymbol{r}^{k\top} (N_i F_\tau^{ik}) dV \tag{4.25}$$

$$K_{ij\tau s}^{\phi c\ k} = \int_{V^k} (\nabla\, N_j F_s^{jk})^\top \boldsymbol{\iota}^{k\top} (N_i F_\tau^{ik}) dV \tag{4.26}$$

$$K_{ij\tau s}^{\theta\theta\ k} = -\int_{V^k} (\nabla N_j F_s^{jk})^\top \boldsymbol{\kappa}^k (\nabla N_i F_\tau^{ik}) dV \tag{4.27}$$

$$K_{ij\tau s}^{\theta c\ k} = -\int_{V^k} (\nabla N_j F_s^{jk})^\top \boldsymbol{\varphi}^k (\nabla N_i F_\tau^{ik}) dV \tag{4.28}$$

$$K_{ij\tau s}^{c\theta\ k} = -\int_{V^k} (\nabla N_j F_s^{jk})^\top \boldsymbol{\gamma}^k (\nabla N_i F_\tau^{ik}) dV \tag{4.29}$$

$$K_{ij\tau s}^{cc\ k} = -\int_{V^k} (\nabla N_j F_s^{jk})^\top \boldsymbol{\xi}^k (\nabla N_i F_\tau^{ik}) d\Omega \tag{4.30}$$

External loads caused by the essential boundary conditions can be considered as:

$$\boldsymbol{P}_{js}^{\bar{\boldsymbol{u}}\ k} = -\boldsymbol{K}_{ij\tau s}^{\boldsymbol{uu}\ \ k} \bar{\boldsymbol{u}}_{i\tau}^{(k)} - \boldsymbol{K}_{ij\tau s}^{\boldsymbol{u}\phi\ \ k} \bar{\phi}_{i\tau}^{(k)} - \boldsymbol{K}_{ij\tau s}^{\boldsymbol{u}\theta\ \ k} \bar{\theta}_{i\tau}^{(k)} - \boldsymbol{K}_{ij\tau s}^{\boldsymbol{u}c\ \ k} \bar{c}_{i\tau}^{(k)} \tag{4.31}$$

$$P_{js}^{\bar{\phi}\,k} = -\boldsymbol{K}_{ij\tau s}^{\phi\boldsymbol{u}\ \ k} \bar{\boldsymbol{u}}_{i\tau}^{(k)} - K_{ij\tau s}^{\phi\phi\ k} \bar{\phi}_{i\tau}^{(k)} - K_{ij\tau s}^{\phi\theta\ k} \bar{\theta}_{i\tau}^{(k)} - K_{ij\tau s}^{\phi c\ \ k} \bar{c}_{i\tau}^{(k)} \tag{4.32}$$

$$P_{js}^{\bar{\theta}\ k} = -K_{ij\tau s}^{\theta\theta\ \ k} \bar{\theta}_{i\tau}^{(k)} - K_{ij\tau s}^{\theta c\ \ k} \bar{c}_{i\tau}^{(k)} \tag{4.33}$$

$$P_{js}^{\bar{c}\ k} = -K_{ij\tau s}^{c\theta\ \ k} \bar{\theta}_{i\tau}^{(k)} - K_{ij\tau s}^{cc\ \ k} \bar{c}_{i\tau}^{(k)} \tag{4.34}$$

FNs for the loads due to natural boundary conditions read:

$$\boldsymbol{P}_{js}^{\bar{\boldsymbol{p}}\ k} = \int_{\Gamma_p} N_j F_s \bar{\boldsymbol{p}} d\Gamma \quad \text{on } \Gamma_p \tag{4.35}$$

$$P_{js}^{\bar{D}k} = \int_{\Gamma_D} N_j F_s \bar{D}_n d\Gamma \quad \text{on } \Gamma_D \tag{4.36}$$

$$P_{js}^{\bar{q}\ k} = \int_{\Gamma_q} N_j F_s \bar{q}_n d\Gamma \quad \text{on } \Gamma_q \tag{4.37}$$

$$P_{js}^{\bar{h}\ k} = \int_{\Gamma_h} N_j F_s \bar{h}_n d\Gamma \quad \text{on } \Gamma_h \tag{4.38}$$

Since the boundary conditions mentioned above are imposed on different external sub-surfaces, their load vectors can be assembled separately then summed up:

$$\boldsymbol{P}^{\boldsymbol{u}} = \boldsymbol{P}^{\bar{\boldsymbol{u}}} + \boldsymbol{P}^{\bar{\boldsymbol{p}}} \tag{4.39}$$

$$\boldsymbol{P}^{\boldsymbol{\phi}} = \boldsymbol{P}^{\bar{\boldsymbol{\phi}}} + \boldsymbol{P}^{\bar{\boldsymbol{D}}} \tag{4.40}$$

$$\boldsymbol{P}^{\boldsymbol{\theta}} = \boldsymbol{P}^{\bar{\boldsymbol{\theta}}} + \boldsymbol{P}^{\bar{\boldsymbol{q}}} \tag{4.41}$$

$$\boldsymbol{P}^{\boldsymbol{c}} = \boldsymbol{P}^{\bar{\boldsymbol{c}}} + \boldsymbol{P}^{\bar{\boldsymbol{h}}} \tag{4.42}$$

To form the global linear system of equations, the generalized stiffness matrix and load vector need to be assembled within each element, then on the whole FE model level. In the above discussed displacement-based models, by solving the linear system of equations, the generalized vector containing displacements and physical field variables can be obtained. In the post-processing step, the strains and physical field gradients can then be calculated through the strain-displacement relations and gradient equations (see Section 3.2.2). Stress components, electric displacements, heat and moisture fluxes are processed through the constitutive equations (see Section 3.2.3).

It should be noted that in displacement-based FE models, the equilibrium equations (see Eqn. 3.75), stress-free natural boundary conditions, and stress continuity at domain interfaces are not satisfied rigorously but approximately. Better satisfaction of them can be approached through refinement of FE models. The use of FNs facilitates the mathematical refinements on both shape functions and cross-section functions in FE models. In the examples presented in Section 2.4.3, through the enhancement of the cross-section approximation functions in both ESL (see Fig. 2.11) and LW (see Fig. 2.12) models, the stress-free conditions of transverse stresses at the top and bottom surfaces are better respected. Also, with the refinement of LW, the transverse stresses at layer interfaces tend to be continuous, as illustrated in Fig. 2.12.

The steady-state thermal conduction and moisture diffusion are accounted for in the presented formulations. Some particular cases include partially coupled thermo-mechanical, hygro-mechanical, and fully coupled electro-mechanical models.

4.4.2 FNs of beam models

For straight beam modes, the FNs for stiffness matrix can be written into:

$$\boldsymbol{K}_{ij\tau s}^{\boldsymbol{uu}\ k} = \int_L \int_{\Omega^k} (\mathbf{b}\, N_j F_s^{jk})^\top \boldsymbol{C}^k (\mathbf{b}\, N_i F_\tau^{ik}) d\Omega^k dy \tag{4.43}$$

$$\boldsymbol{K}_{ij\tau s}^{\boldsymbol{u}\phi\ k} = \int_L \int_{\Omega^k} (\mathbf{b}\, N_j F_s^{jk})^\top \boldsymbol{e}^{k\top} (\nabla\, N_i F_\tau^{ik}) d\Omega^k dy \tag{4.44}$$

$$\boldsymbol{K}_{ij\tau s}^{\phi\boldsymbol{u}\ k} = \int_L \int_{\Omega^k} (\nabla\, N_j F_s^{jk})^\top \boldsymbol{e}^k (\mathbf{b}\, N_i F_\tau^{ik}) d\Omega^k dy \tag{4.45}$$

$$K_{ij\tau s}^{\phi\phi\ k} = -\int_L \int_{\Omega^k} (\nabla\, N_j F_s^{jk})^\top \boldsymbol{\chi}^k (\nabla\, N_i F_\tau^{ik}) d\Omega^k dy \tag{4.46}$$

$$\boldsymbol{K}_{ij\tau s}^{\boldsymbol{u}\theta\ k} = -\int_L \int_{\Omega^k} (\mathbf{b}\, N_j F_s^{jk})^\top \boldsymbol{\lambda}^{k\top} (N_i F_\tau^{ik}) d\Omega^k dy \tag{4.47}$$

$$\boldsymbol{K}_{ij\tau s}^{\boldsymbol{u}c\ k} = -\int_L \int_{\Omega^k} (\mathbf{b}\, N_j F_s^{jk})^\top \boldsymbol{\Psi}^{k\top} (N_i F_\tau^{ik}) d\Omega^k dy \tag{4.48}$$

$$K_{ij\tau s}^{\phi\theta\ k} = \int_L \int_{\Omega^k} (\nabla\, N_j F_s^{jk})^\top \boldsymbol{r}^{k\top} (N_i F_\tau^{ik}) d\Omega^k dy \tag{4.49}$$

$$K_{ij\tau s}^{\phi c\ k} = \int_L \int_{\Omega^k} (\nabla\, N_j F_s^{jk})^\top \boldsymbol{\iota}^{k\top} (N_i F_\tau^{ik}) d\Omega^k dy \tag{4.50}$$

$$K_{ij\tau s}^{\theta\theta\ k} = -\int_L \int_{\Omega^k} (\nabla\, N_j F_s^{jk})^\top \boldsymbol{\kappa}^k (\nabla\, N_i F_\tau^{ik}) d\Omega^k dy \tag{4.51}$$

$$K_{ij\tau s}^{\theta c\ k} = -\int_L \int_{\Omega^k} (\nabla\, N_j F_s^{jk})^\top \boldsymbol{\varphi}^k (\nabla\, N_i F_\tau^{ik}) d\Omega^k dy \tag{4.52}$$

$$K_{ij\tau s}^{c\theta\ k} = -\int_L \int_{\Omega^k} (\nabla\, N_j F_s^{jk})^\top \boldsymbol{\gamma}^k (\nabla\, N_i F_\tau^{ik}) d\Omega^k dy \tag{4.53}$$

$$K_{ij\tau s}^{cc\ k} = -\int_L \int_{\Omega^k} (\nabla\, N_j F_s^{jk})^\top \boldsymbol{\xi}^k (\nabla\, N_i F_\tau^{ik}) d\Omega^k dy \tag{4.54}$$

where L indicates the beam axial domain, and Ω_k the cross-sectional domain of layer k. Examples of FNs for refined beam models can be found in the works of Carrera, Zappino, and Li [58], Miglioretti, Carrera, and Petrolo [160], and Miglioretti and Carrera [159].

4.4.3 FNs of plate and shell models

Plates can be treated as particular cases of doubly curved shells, as explained in Section 3.2.1. The transformation of shell coordinates into the Cartesian system of a plate is given by Eqn. (2.8).

Stiffness matrix FNs of plate and shell models can be expressed as:

$$\boldsymbol{K}_{ij\tau s}^{\boldsymbol{uu}\ k} = \int_\Omega \int_{A^k} (\mathbf{b}\, N_j F_s^{jk})^\top \boldsymbol{C}^k (\mathbf{b}\, N_i F_\tau^{ik}) H_\alpha H_\beta dz^k d\Omega \tag{4.55}$$

$$\boldsymbol{K}_{ij\tau s}^{\boldsymbol{u}\phi\ k} = \int_\Omega \int_{A^k} (\mathbf{b}\, N_j F_s^{jk})^\top \boldsymbol{e}^{k\top} (\nabla\, N_i F_\tau^{ik}) H_\alpha H_\beta dz^k d\Omega \tag{4.56}$$

$$\boldsymbol{K}_{ij\tau s}^{\phi\boldsymbol{u}\ k} = \int_\Omega \int_{A^k} (\nabla\, N_j F_s^{jk})^\top \boldsymbol{e}^k (\mathbf{b}\, N_i F_\tau^{ik}) H_\alpha H_\beta dz^k d\Omega \tag{4.57}$$

$$K_{ij\tau s}^{\phi\phi\ k} = -\int_\Omega \int_{A^k} (\nabla\, N_j F_s^{jk})^\top \boldsymbol{\chi}^k (\nabla\, N_i F_\tau^{ik}) H_\alpha H_\beta dz^k d\Omega \tag{4.58}$$

$$\boldsymbol{K}_{ij\tau s}^{\boldsymbol{u}\theta\ k} = -\int_\Omega \int_{A^k} (\mathbf{b}\, N_j F_s^{jk})^\top \boldsymbol{\lambda}^{k\top} (N_i F_\tau^{ik}) H_\alpha H_\beta dz^k d\Omega \tag{4.59}$$

$$\boldsymbol{K}_{ij\tau s}^{\boldsymbol{u}c\ k} = -\int_\Omega \int_{A^k} (\mathbf{b}\, N_j F_s^{jk})^\top \boldsymbol{\Psi}^{k\top} (N_i F_\tau^{ik}) H_\alpha H_\beta dz^k d\Omega \tag{4.60}$$

$$K_{ij\tau s}^{\phi\theta\ k} = \int_\Omega \int_{A^k} (\nabla\, N_j F_s^{jk})^\top \boldsymbol{r}^{k\top} (N_i F_\tau^{ik}) H_\alpha H_\beta dz^k d\Omega \tag{4.61}$$

$$K_{ij\tau s}^{\phi c\ k} = \int_\Omega \int_{A^k} (\nabla\, N_j F_s^{jk})^\top \boldsymbol{\iota}^{k\top} (N_i F_\tau^{ik}) H_\alpha H_\beta dz^k d\Omega \tag{4.62}$$

$$K_{ij\tau s}^{\theta\theta\ k} = -\int_\Omega \int_{A^k} (\nabla\, N_j F_s^{jk})^\top \boldsymbol{\kappa}^k (\nabla\, N_i F_\tau^{ik}) H_\alpha H_\beta dz^k d\Omega \tag{4.63}$$

$$K^{\theta c\ \ k}_{ij\tau s} = -\int_{\Omega}\int_{A^k} (\nabla\ N_j F_s^{jk})^{\top} \boldsymbol{\varphi}^k (\nabla\ N_i F_\tau^{ik}) H_\alpha H_\beta dz^k d\Omega \tag{4.64}$$

$$K^{c\theta\ \ k}_{ij\tau s} = -\int_{\Omega}\int_{A^k} (\nabla\ N_j F_s^{jk})^{\top} \boldsymbol{\gamma}^k (\nabla\ N_i F_\tau^{ik}) H_\alpha H_\beta dz^k d\Omega \tag{4.65}$$

$$K^{cc\ \ k}_{ij\tau s} = -\int_{\Omega}\int_{A^k} (\nabla\ N_j F_s^{jk})^{\top} \boldsymbol{\xi}^k (\nabla\ N_i F_\tau^{ik}) H_\alpha H_\beta dz^k d\Omega \tag{4.66}$$

in which A^k is the thickness domain of the kth layer and Ω the element domain on the middle surface. For examples of FNs of refined plate and shell models, one is referred to the works of Carrera, Boscolo, and Robaldo [35], Cinefra et al. [73, 74], and Li et al. [147].

4.5 Assembly of stiffness matrix and load vector

FNs are core units of stiffness matrix and load vector. Through proper loops, the full stiffness matrix and load vector can be assembled step by step. The component-wise assembly procedure for 1D and 2D FEs with uniform kinematics has been well explained by Carrera et al. [59].

4.5.1 Characteristics of assembly procedure for NDK FE models

For NDK FEs with various nodal kinematic models, a sub-matrix of the stiffness matrix might become rectangular instead of being square. This can be demonstrated by considering a unit of the mechanical stiffness matrix $\boldsymbol{K}^{\boldsymbol{uu}}_{ij}$. Assume that the number of expansions on node i is $m_i = 3$ and that on node j is $m_j = 4$, the resultant $\boldsymbol{K}^{\boldsymbol{uu}}_{ii}$ has the dimension of 9×9, $\boldsymbol{K}^{\boldsymbol{uu}}_{jj}$ 12×12, $\boldsymbol{K}^{\boldsymbol{uu}}_{ij}$ 9×12, and $\boldsymbol{K}^{\boldsymbol{uu}}_{ji}$ 12×9 (see Fig. 4.4). The dimension of the corresponding load vector needs to be compatible, as shown on the right-hand side of Fig. 4.4.

4.5.2 Mixing ESL and LW nodal kinematics

Fig. 4.5 shows the assembly of mechanical stiffness matrix and load vector of a Q4 (four-node Lagrangian 2D element) *el*, in which ESL and LW models coexist. As shown on the left-hand side of Fig. 4.5, LW kinematics are assigned to nodes a and d, ESL assumptions to nodes b and c.

$\boldsymbol{K}^{\boldsymbol{uu}}_{aa}$ and $\boldsymbol{K}^{\boldsymbol{uu}}_{bb}$ are the diagonal sub-matrices with typical LW and ESL assembly, respectively. $\boldsymbol{K}^{\boldsymbol{uu}}_{aa}$ is formed by joining the sub-matrices of each layer at the interfacial cross-sectional nodes. When the number of cross-section functions differs from layer to layer, the dimensions of sub-matrices of layers are also different. $\boldsymbol{K}^{\boldsymbol{uu}}_{bb}$ is obtained by superimposing the stiffness contributions from all layers. $\boldsymbol{K}^{\boldsymbol{uu}}_{ab}$ and $\boldsymbol{K}^{\boldsymbol{uu}}_{ba}$ are the coupling

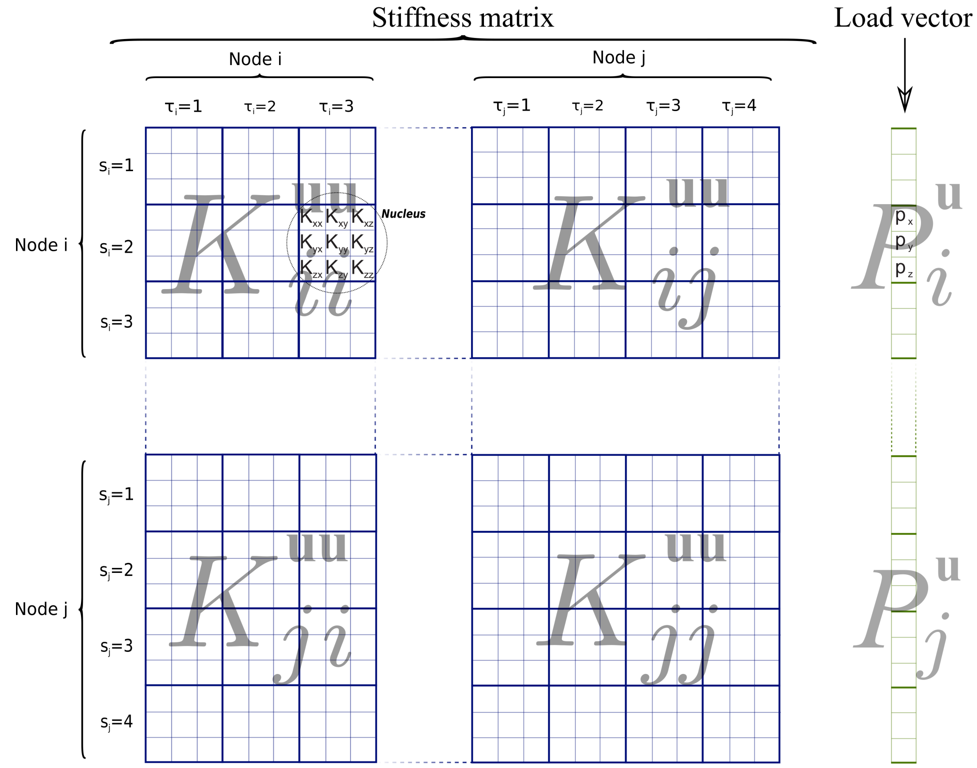
Stiffness matrix
Load vector
Node i
Node j
τ_i=1
τ_i=2
τ_i=3
τ_j=1
τ_j=2
τ_j=3
τ_j=4
s_i=1
s_i=2
s_i=3
s_j=1
s_j=2
s_j=3
s_j=4
Node i
Node j
K_ii^uu
K_ij^uu
K_ji^uu
K_jj^uu
K_xx K_xy K_xz
K_yx K_yy K_yz
K_zx K_zy K_zz
Nucleus
P_i^u
P_j^u
p_x
p_y
p_z

Figure 4.4: Assembly of stiffness matrix and load vector of FE models with node-dependent kinematics.

matrices between nodes a and b, and their sub-matrices turn out to be in a striped distribution. The compatible load vector is assembled accordingly, as shown on the right-hand side of Fig. 4.5.

The above-introduced assembly procedure can be easily extended to 1D beam FE models. In the beam model shown in Fig. 4.6, ESL model (TE) and LW model (LE4) both exist in the two-node beam (B2) elements el_A and el_C. The coupling matrices between the ESL-nodes and the LW-nodes are $\boldsymbol{K}^s_{ab}$, $\boldsymbol{K}^s_{ba}$, $\boldsymbol{K}^s_{cd}$, and $\boldsymbol{K}^s_{dc}$, which are in a striped manner.

4.5.3 Consideration of patches

Patches, such as surface-mounted or embedded piezo patches, are important local structural features. Fig. 4.6 shows a beam model with a surface-mounted piezo patch. The LW approach provides the physical boundary between the piezo domain and the substrate mechanical domain. Therefore, LW kinematics are used on the two nodes of the beam element el_B. Note that for the piezo domain, the fully coupled electro-mechanical FNs matrix has dimension 4×4, while the pure mechanical FNs matrix is 3×3. These two domains with dissimilar materials can be connected by superimposing

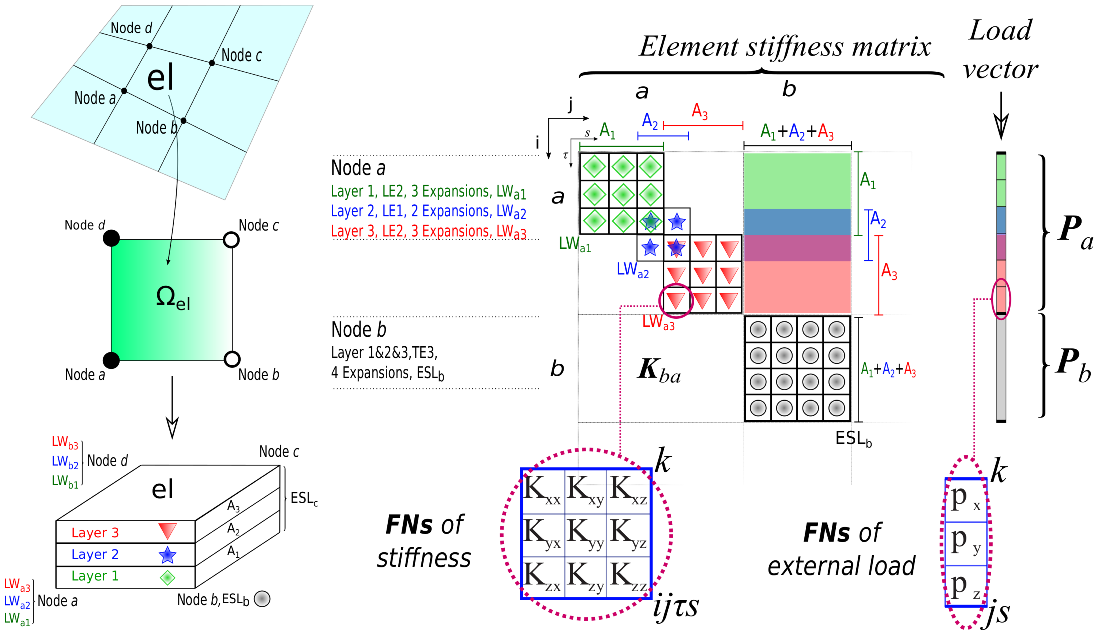
Node d
Node c
el
Node a
Node b
Node d
Node c
Ω_el
Node a
Node b
LW_b3
LW_b2
LW_b1
Node d
Node c
el
A_3
A_2
A_1
ESL_c
Layer 3
Layer 2
Layer 1
LW_a3
LW_a2
LW_a1
Node a
Node b,ESL_b
Element stiffness matrix
Load vector
a
b
j
i
s
τ
A_1
A_2
A_3
A_1+A_2+A_3
Node a
Layer 1, LE2, 3 Expansions, LW_a1
Layer 2, LE1, 2 Expansions, LW_a2
Layer 3, LE2, 3 Expansions, LW_a3
LW_a1
LW_a2
LW_a3
Node b
Layer 1&2&3,TE3,
4 Expansions, ESL_b
K_ba
ESL_b
P_a
P_b
FNs of stiffness
K_xx K_xy K_xz
K_yx K_yy K_yz
K_zx K_zy K_zz
k
ijτs
FNs of external load
p_x
p_y
p_z
k
js

Figure 4.5: Assembly of the stiffness matrix and load vector of elements with various nodal kinematics.

the mechanical stiffness components at the patch-substrate interface, as illustrated in Fig. 4.6.

4.6 Decomposition of strain energy

Decomposition of strain energy can help with the understanding of structural behavior through the energy components stored in different deformation modes, for example, in the evaluation of locking phenomena in FE models.

In a pure mechanical model, the constitutive relations read:

$$\boldsymbol{\sigma} = \boldsymbol{C}\,\boldsymbol{\varepsilon} \tag{4.67}$$

and the density of strain energy is:

$$U = \frac{1}{2}\boldsymbol{\sigma}^{\top}\boldsymbol{\varepsilon} = \sigma_{11}\,\varepsilon_{11} + \sigma_{22}\,\varepsilon_{22} + \sigma_{33}\,\varepsilon_{33} + \sigma_{23}\,\varepsilon_{23} + \sigma_{13}\,\varepsilon_{13} + \sigma_{12}\,\varepsilon_{12} \tag{4.68}$$

which consists of six components. For different types of models (beam, plate, or shell), these components and their combinations can be interpreted differently.

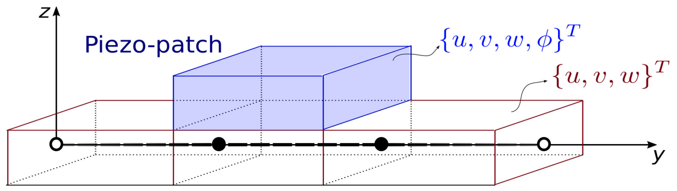
z
Piezo-patch
$\{u, v, w, \phi\}^T$
$\{u, v, w\}^T$
y

(a) Geometric features and coordinate system.

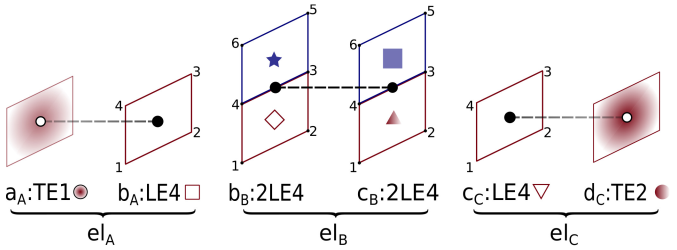
a_A:TE1
b_A:LE4
b_B:2LE4
c_B:2LE4
c_C:LE4
d_C:TE2
el_A
el_B
el_C
1
2
3
4
5
6

(b) Assignment of nodal kinematics.

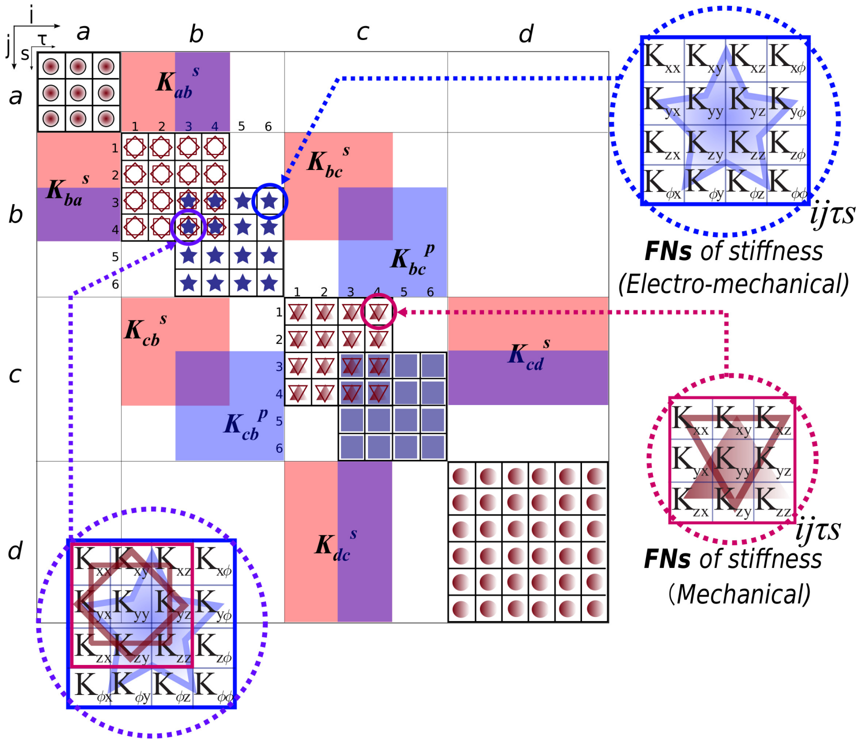
i
j
τ
s
a
b
c
d
K_{ab}^s
K_{ba}^s
K_{bc}^s
K_{bc}^p
K_{cb}^s
K_{cb}^p
K_{cd}^s
K_{dc}^s
K_{xx} K_{xy} K_{xz} $K_{x\phi}$
K_{yx} K_{yy} K_{yz} $K_{y\phi}$
K_{zx} K_{zy} K_{zz} $K_{z\phi}$
$K_{\phi x}$ $K_{\phi y}$ $K_{\phi z}$ $K_{\phi\phi}$
$ij\tau s$
FNs of stiffness
(Electro-mechanical)
K_{xx} K_{xy} K_{xz}
K_{yx} K_{yy} K_{yz}
K_{zx} K_{zy} K_{zz}
$ij\tau s$
FNs of stiffness
(Mechanical)

(c) Stiffness matrix and load vector.

Figure 4.6: Assembly of the stiffness matrix and load vector of a beam model with a piezo patch.

4.6.1 Strain energy decomposition in beam models

For a beam element with multiple layers, the strain energy can be decomposed into three parts:

$$U_c = \sum_{k=1}^{N_l} {U_c}^k; \qquad U_s = \sum_{k=1}^{N_l} {U_s}^k; \qquad U_a = \sum_{k=1}^{N_l} {U_a}^k. \tag{4.69}$$

where N_l is the number of layers, k the layer index, U_c the cross-sectional in-plane deformation energy, U_s the transverse shear energy, and U_a the axial deformation energy. For a basic volume V^k in the kth layer of the beam element:

$${U_c}^k = \int_{V^k} \frac{1}{2}({\varepsilon_{xx}}^k \, {\sigma_{xx}}^k + {\varepsilon_{zz}}^k \, {\sigma_{zz}}^k + {\varepsilon_{xz}}^k \, {\sigma_{\alpha\beta}}^k) \, dV \tag{4.70}$$

$${U_s}^k = \int_{V^k} \frac{1}{2}({\varepsilon_{xy}}^k \, \sigma_{xy}^k + {\varepsilon_{yz}}^k \, {\sigma_{yz}}^k) \tag{4.71}$$

$${U_a}^k = \int_{V^k} \frac{1}{2} {\varepsilon_{yy}}^k \, {\sigma_{yy}}^k \, dV \tag{4.72}$$

By considering the strain-displacement equations (see Section 3.2.1), the displacement approximations in Eqn. (4.13), and the constitutive equations in Eqn. (4.67), the above strain energy components can be written into:

$$\delta {U_c}^k = \delta \boldsymbol{u}_{js}^{(k)\top} \, {\boldsymbol{K}^c_{ij\tau s}}^k \, \boldsymbol{u}_{i\tau}^{(k)} \tag{4.73}$$

$$\delta {U_s}^k = \delta \boldsymbol{u}_{js}^{(k)\top} \, {\boldsymbol{K}^s_{ij\tau s}}^k \, \boldsymbol{u}_{i\tau}^{(k)} \tag{4.74}$$

$$\delta {U_a}^k = \delta \boldsymbol{u}_{js}^{(k)\top} \, {\boldsymbol{K}^a_{ij\tau s}}^k \, \boldsymbol{u}_{i\tau}^{(k)} \tag{4.75}$$

where the ${\boldsymbol{K}^c_{ij\tau s}}^k$, ${\boldsymbol{K}^s_{ij\tau s}}^k$, and ${\boldsymbol{K}^a_{ij\tau s}}^k$ are the corresponding stiffness FNs. Their explicit expressions read:

$${\boldsymbol{K}^c_{ij\tau s}}^k = \int_{V^k} (\mathbf{b}_c^\top \, N_j F_s^{jk}) \, {\boldsymbol{C}_c}^k \, (\mathbf{b} \, N_i F_\tau^{ik}) \, dV \tag{4.76}$$

$${\boldsymbol{K}^s_{ij\tau s}}^k = \int_{V^k} (\mathbf{b}_s^\top \, N_j F_s^{jk}) \, {\boldsymbol{C}_s}^k \, (\mathbf{b} \, N_i F_\tau^{ik}) \, dV \tag{4.77}$$

$${\boldsymbol{K}^a_{ij\tau s}}^k = \int_{V^k} (\mathbf{b}_a^\top \, N_j F_s^{jk}) \, {\boldsymbol{C}_a}^k \, (\mathbf{b} \, N_i F_\tau^{ik}) \, dV \tag{4.78}$$

in which

$$\mathbf{b}_c = \begin{bmatrix} \partial_x & 0 & 0 \\ 0 & 0 & \partial_z \\ \partial_z & 0 & \partial_x \end{bmatrix} \tag{4.79}$$

$$\mathbf{b}_s = \begin{bmatrix} 0 & \partial_z & \partial_y \\ \partial_y & \partial_x & 0 \end{bmatrix} \tag{4.80}$$

$$\mathbf{b}_a = \begin{bmatrix} 0 & \partial_y & 0 \end{bmatrix} \tag{4.81}$$

$$\boldsymbol{C_c}^k = \begin{bmatrix} C_{11} & C_{12} & C_{13} & C_{14} & C_{15} & C_{16} \\ C_{31} & C_{32} & C_{33} & C_{34} & C_{35} & C_{36} \\ C_{51} & C_{52} & C_{53} & C_{54} & C_{55} & C_{56} \end{bmatrix}_k \tag{4.82}$$

$$\boldsymbol{C_s}^k = \begin{bmatrix} C_{41} & C_{42} & C_{43} & C_{44} & C_{45} & C_{46} \\ C_{61} & C_{62} & C_{63} & C_{64} & C_{65} & C_{66} \end{bmatrix}_k \tag{4.83}$$

$$\boldsymbol{C_a}^k = \begin{bmatrix} C_{21} & C_{22} & C_{23} & C_{24} & C_{25} & C_{26} \end{bmatrix}_k \tag{4.84}$$

Thus, the strain energy components in a beam element can be obtained as:

$$U_c = \sum_{k=1}^{N_l} \frac{1}{2} \boldsymbol{u}_{js}^{(k)\top} \ \boldsymbol{K}^{c}_{ij\tau s}{}^{k} \ \boldsymbol{u}_{i\tau}^{(k)}; \tag{4.85}$$

$$U_s = \sum_{k=1}^{N_l} \frac{1}{2} \boldsymbol{u}_{js}^{(k)\top} \ \boldsymbol{K}^{s}_{ij\tau s}{}^{k} \ \boldsymbol{u}_{i\tau}^{(k)}; \tag{4.86}$$

$$U_a = \sum_{k=1}^{N_l} \frac{1}{2} \boldsymbol{u}_{js}^{(k)\top} \ \boldsymbol{K}^{a}_{ij\tau s}{}^{k} \ \boldsymbol{u}_{i\tau}^{(k)}. \tag{4.87}$$

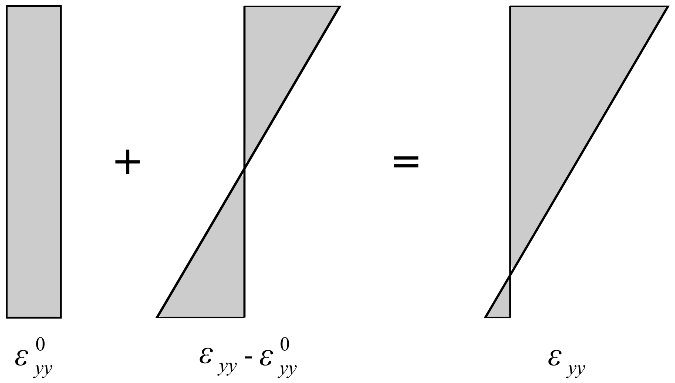

Figure 4.7: Axial strains on the cross-section of a beam model.

The normal axial strain contains the contribution of bending and rod-mode strain (analogous to membrane strains in plates and shells), as shown in Fig. 4.7. When the neutral line of bending coincides with the beam axis, the axial deformation energy U_a can be conveniently divided into two parts as:

$$\delta {U_{rod}}^k = \int_{V^k} \frac{1}{2} \delta\varepsilon^0_{yy} \ {\sigma_{yy}}^k \ dV \tag{4.88}$$

$$\delta {U_{bend}}^k = \int_{V^k} \frac{1}{2} (\delta{\varepsilon_{yy}}^k - \delta\varepsilon^0_{yy}) \ {\sigma_{yy}}^k \ dV \tag{4.89}$$

in which ε^0_{yy} is calculated at the beam axis. Note that the coordinates of the axis are $(0, y, 0)$. Thus, ε^0_{yy} can be obtained through:

$$\delta\varepsilon^0_{yy} = \mathbf{b}_a \, \delta\boldsymbol{u}(0, y, 0) = \begin{bmatrix} 0 & \partial_y & 0 \end{bmatrix} \cdot N_j \ F^j_s(0,0) \ \delta\boldsymbol{u}^{(k)}_{js} \tag{4.90}$$

The virtual variation of ${U_{rod}}^k$ can be written into:

$$\delta {U_a}^k = \delta \boldsymbol{u}_{js}^{(k)\top} \; \boldsymbol{K}_{ij\tau s}^{rod\ k} \; \boldsymbol{u}_{i\tau}^{(k)} \tag{4.91}$$

and accordingly the FNs for rod-mode strain energy are:

$$\boldsymbol{K}_{ij\tau s}^{rod\ k} = \int_{V^k} [\mathbf{b}_a^\top \, N_j F_s^j(0{,}0)] \; {\boldsymbol{C}_a}^k \; (\mathbf{b} \, N_i F_\tau^{ik}) \; dV \tag{4.92}$$

The rod-mode strain energy in the beam element can be calculated utilizing:

$$U_{rod} = \sum_{k=1}^{N_l} \frac{1}{2} \boldsymbol{u}_{js}^{(k)\top} \; \boldsymbol{K}_{ij\tau s}^{rod\ k} \; \boldsymbol{u}_{i\tau}^{(k)} \tag{4.93}$$

and the bending energy can then be obtained through:

$$U_{bend} = U_a - U_{rod} \tag{4.94}$$

4.6.2 Strain energy decomposition in plate and shell models

In plate and shell elements, strain energy can be decomposed in the same way, and a plate is treated as a particular case of a curved shell (see Section 3.2.1). In this section, the decomposition of strain energy is demonstrated through shell models and can be extended to plate cases by considering the coordinate transformation given by Eqn. (2.8).

For a multi-layered shell structure, the strain energy can be decomposed into four parts as follows:

$$U_{pn} = \sum_{k=1}^{N_l} {U_{pn}}^k; \quad U_{ps} = \sum_{k=1}^{N_l} {U_{ps}}^k; \quad U_{zs} = \sum_{k=1}^{N_l} {U_{zs}}^k; \quad U_{zz} = \sum_{k=1}^{N_l} {U_{zz}}^k. \tag{4.95}$$

where U_{pn} represents the in-plane normal energy, U_{ps} the in-plane shear energy, U_{zs} the transverse shear energy, and U_{zz} the thickness stretch energy. The transverse shear energy allows us to evaluate the shear locking effects in shell elements. The introduction of the thickness stretch energy also makes it convenient to assess the performance of the adopted kinematic assumptions. Note that the above decomposition applies to arbitrarily laminated shells.

For a unit volume V^k corresponding to a layer k in the shell element:

$$\begin{aligned}
{U_{pn}}^k &= \int_{V^k} \frac{1}{2} ({\varepsilon_{\alpha\alpha}}^k \, {\sigma_{\alpha\alpha}}^k + {\varepsilon_{\beta\beta}}^k \, {\sigma_{\beta\beta}}^k) \; dV && (4.96)\\
{U_{ps}}^k &= \int_{V^k} \frac{1}{2} {\varepsilon_{\alpha\beta}}^k \, {\sigma_{\alpha\beta}}^k \; dV && (4.97)\\
{U_{zs}}^k &= \int_{V^k} \frac{1}{2} ({\varepsilon_{\alpha z}}^k \, {\sigma_{\alpha z}}^k + {\varepsilon_{\beta z}}^k \, {\sigma_{\beta z}}^k) dV && (4.98)\\
{U_{zz}}^k &= \int_{V^k} \frac{1}{2} {\varepsilon_{zz}}^k \, {\sigma_{zz}}^k \; dV && (4.99)
\end{aligned}$$

The calculation of the strain energy components requires their corresponding stiffness matrices. These matrices can be obtained through standard FE procedure in the framework of CUF. The transverse shear energy ${U_{zs}}^k$ can be taken as an example. The virtual variation of ${U_{zs}}^k$ reads:

$$\delta {U_{zs}}^k = \int_{V^k} (\delta {\varepsilon_{\alpha z}}^k {\sigma_{\alpha z}}^k + \delta {\varepsilon_{\beta z}}^k {\sigma_{\beta z}}^k) dV \tag{4.100}$$

The related virtual strains are:

$$\begin{Bmatrix} \delta {\varepsilon_{\beta z}}^k \\ \delta {\varepsilon_{\alpha z}}^k \end{Bmatrix} = \mathbf{b}_{zs} \cdot \delta \boldsymbol{u} = \begin{bmatrix} 0 & \partial_z - \frac{1}{H_\beta R_\beta} & \frac{\partial_\beta}{H_\beta} \\ \partial_z - \frac{1}{H_\alpha R_\alpha} & 0 & \frac{\partial_\alpha}{H_\alpha} \end{bmatrix} \cdot N_j F_s^{jk} \; \delta \boldsymbol{u}_{js}^{(k)} \tag{4.101}$$

and the used stresses are obtained as:

$$\begin{Bmatrix} {\sigma_{\beta z}}^k \\ {\sigma_{\alpha z}}^k \end{Bmatrix} = {\boldsymbol{C}_{zs}}^k \cdot \boldsymbol{\varepsilon} = \begin{bmatrix} C_{41} & C_{42} & C_{43} & C_{44} & C_{45} & C_{46} \\ C_{51} & C_{52} & C_{53} & C_{54} & C_{55} & C_{56} \end{bmatrix}_k \cdot (\mathbf{b} \, N_i F_\tau^{ik} \; \boldsymbol{u}_{i\tau}^{(k)}) \tag{4.102}$$

By substituting Eqns. (4.101) and (4.102) into Eqn. (4.100), one obtains:

$$\delta {U_{zs}}^k = \delta \boldsymbol{u}_{js}^{(k)\top} \; [\int_{V^k} (\mathbf{b}_{zs}^\top \, N_j F_s^{jk}) \; {\boldsymbol{C}_{zs}}^k \; (\mathbf{b} \;\; N_i F_\tau^{ik}) dV] \; \boldsymbol{u}_{i\tau}^{(k)} = \delta \boldsymbol{u}_{js}^{(k)\top} \;\; {\boldsymbol{K}_{ij\tau s}^{zs}}^{\,k} \; \boldsymbol{u}_{i\tau}^{(k)} \tag{4.103}$$

Thus, the FNs for the transverse shear stiffness matrix can be obtained as:

$$ {\boldsymbol{K}_{ij\tau s}^{zs}}^{\,k} = \int_{V^k} (\mathbf{b}_{zs}^\top \, N_j F_s^{jk}) \; {\boldsymbol{C}_{zs}}^k \; (\mathbf{b} \;\; N_i F_\tau^{ik}) dV \tag{4.104}$$

Finally, the transverse shear strain energy component can be calculated through:

$$U_{zs} = \sum_{k=1}^{N_l} {U_{zs}}^k = \sum_{k=1}^{N_l} \frac{1}{2} \; \boldsymbol{u}_{js}^{(k)\top} \, {\boldsymbol{K}_{ij\tau s}^{zs}}^{\,k} \boldsymbol{u}_{i\tau}^{(k)} \tag{4.105}$$

By following the same procedure, one can obtain:

$$U_{pn} = \sum_{k=1}^{N_l} {U_{pn}}^k = \sum_{k=1}^{N_l} \frac{1}{2} \; \boldsymbol{u}_{js}^{(k)\top} \, {\boldsymbol{K}_{ij\tau s}^{pn}}^{\,k} \boldsymbol{u}_{i\tau}^{(k)} \tag{4.106}$$

$$U_{ps} = \sum_{k=1}^{N_l} {U_{ps}}^k = \sum_{k=1}^{N_l} \frac{1}{2} \; \boldsymbol{u}_{js}^{(k)\top} \, {\boldsymbol{K}_{ij\tau s}^{ps}}^{\,k} \boldsymbol{u}_{i\tau}^{(k)} \tag{4.107}$$

$$U_{zz} = \sum_{k=1}^{N_l} {U_{zz}}^k = \sum_{k=1}^{N_l} \frac{1}{2} \; \boldsymbol{u}_{js}^{(k)\top} \, {\boldsymbol{K}_{ij\tau s}^{zz}}^{\,k} \boldsymbol{u}_{i\tau}^{(k)} \tag{4.108}$$

in which the FNs for each strain energy component separately are:

$$\boldsymbol{K}^{pn\ \ k}_{ij\tau s} = \int_{V^k} (\mathbf{b}^{\top}_{pn}\, N_j F^{jk}_s)\ \boldsymbol{C}_{pn}{}^{k}\ (\mathbf{b}\, N_i F^{ik}_{\tau}) dV \tag{4.109}$$

$$\boldsymbol{K}^{ps\ \ k}_{ij\tau s} = \int_{V^k} (\mathbf{b}^{\top}_{ps}\, N_j F^{jk}_s)\ \boldsymbol{C}_{ps}{}^{k}\ (\mathbf{b}\, N_i F^{ik}_{\tau}) dV \tag{4.110}$$

$$\boldsymbol{K}^{zz\ \ k}_{ij\tau s} = \int_{V^k} (\mathbf{b}^{\top}_{zz}\, N_j F^{jk}_s)\ \boldsymbol{C}_{zz}{}^{k}\ (\mathbf{b}\, N_i F^{ik}_{\tau}) dV \tag{4.111}$$

wherein $\mathbf{b}_{pn}$, $\mathbf{b}_{ps}$, and $\mathbf{b}_{zz}$ are the sub-matrices of the differential operator matrix $\mathbf{b}$ (see Eqn. 3.25), and thier explicit expressions are:

$$\mathbf{b}_{pn} = \begin{bmatrix} \frac{\partial_\alpha}{H_\alpha} & 0 & \frac{1}{H_\alpha R_\alpha} \\ 0 & \frac{\partial_\beta}{H_\beta} & \frac{1}{H_\beta R_\beta} \end{bmatrix} \tag{4.112}$$

$$\mathbf{b}_{ps} = \begin{bmatrix} \frac{\partial_\beta}{H_\beta} & \frac{\partial_\alpha}{H_\alpha} & 0 \end{bmatrix} \tag{4.113}$$

$$\mathbf{b}_{zz} = \begin{bmatrix} 0 & 0 & \partial_z \end{bmatrix} \tag{4.114}$$

The corresponding material coefficient matrices (sub-matrices of the material coefficients matrix $\boldsymbol{C}^k$) are as follows:

$$\boldsymbol{C}_{pn}{}^{k} = \begin{bmatrix} C_{11} & C_{12} & C_{13} & C_{14} & C_{15} & C_{16} \\ C_{21} & C_{22} & C_{23} & C_{24} & C_{25} & C_{26} \end{bmatrix} \tag{4.115}$$

$$\boldsymbol{C}_{ps}{}^{k} = \begin{bmatrix} C_{61} & C_{62} & C_{63} & C_{64} & C_{65} & C_{66} \end{bmatrix} \tag{4.116}$$

$$\boldsymbol{C}_{zz}{}^{k} = \begin{bmatrix} C_{31} & C_{32} & C_{33} & C_{34} & C_{35} & C_{36} \end{bmatrix} \tag{4.117}$$

Note that the complete stiffness FNs are a sum of above FNs:

$$\boldsymbol{K}_{ij\tau s}{}^{k} = \boldsymbol{K}^{pn\ \ k}_{ij\tau s} + \boldsymbol{K}^{ps\ \ k}_{ij\tau s} + \boldsymbol{K}^{zs\ \ k}_{ij\tau s} + \boldsymbol{K}^{zz\ \ k}_{ij\tau s} \tag{4.118}$$

If the multi-layered shell has symmetric lamination properties, the neutral surface of bending will coincide with the geometric middle surface. The in-plane normal strain energy, as in Eqn. (4.106), can be conveniently further decomposed into membrane energy $U_{memb}{}^{k}$ and bending energy $U_{bend}{}^{k}$ through:

$$\delta U_{memb}{}^{k} = \int_V \frac{1}{2} (\delta\varepsilon^0_{\alpha\alpha}\ \sigma_{\alpha\alpha}{}^{k} + \varepsilon^0_{\beta\beta}\ \sigma_{\beta\beta}{}^{k})\ dV \tag{4.119}$$

$$\delta U_{bend}{}^{k} = \int_V \frac{1}{2} [(\delta\varepsilon_{\alpha\alpha}{}^{k} - \delta\varepsilon^0_{\alpha\alpha})\ \sigma_{\alpha\alpha}{}^{k} + (\delta\varepsilon_{\beta\beta}{}^{k} - \delta\varepsilon^0_{\beta\beta})\ \sigma_{\beta\beta}{}^{k}]\ dV \tag{4.120}$$

wherein $\delta\varepsilon^0_{\alpha\alpha}$ and $\delta\varepsilon^0_{\beta\beta}$ are the virtual normal strains due to the mid-surface straining, and they can be calculated through:

$$\begin{Bmatrix} \delta\varepsilon^0_{\alpha\alpha} \\ \delta\varepsilon^0_{\beta\beta} \end{Bmatrix} = \mathbf{b}_{pn} \cdot \delta\boldsymbol{u} = \begin{bmatrix} \frac{\partial_\alpha}{H_\alpha} & 0 & \frac{1}{H_\alpha R_\alpha} \\ 0 & \frac{\partial_\beta}{H_\beta} & \frac{1}{H_\beta R_\beta} \end{bmatrix} \cdot N_j F_s{}^{j}(0)\ \delta\boldsymbol{u}^{(k)}_{js} \tag{4.121}$$

therefore, Eqn. (4.121) can be written into:

$$\delta U_{memb}{}^{k} = \delta \boldsymbol{u}_{js}^{(k)\top} \boldsymbol{K}_{ij\tau s}^{membk} \ \boldsymbol{u}_{i\tau}^{(k)} \tag{4.122}$$

in which the FNs for the membrane stiffness matrix are:

$$\boldsymbol{K}_{ij\tau s}^{membk} = \int_{V^k} [\mathbf{b}_{pn}^{\top} \, N_j F_s^j(0)] \ \boldsymbol{C}_{pn}{}^{k} \ (\mathbf{b} \, N_i F_\tau^{ik}) dV \tag{4.123}$$

The membrane energy can be calculated through:

$$U_{memb} = \sum_{k=1}^{N_l} \frac{1}{2} \, \boldsymbol{u}_{js}^{(k)\top} \boldsymbol{K}_{ij\tau s}^{membk} \boldsymbol{u}_{i\tau}^{(k)} \tag{4.124}$$

The bending energy can be then obtained:

$$U_{bend} = U_{pn} - U_{memb} \tag{4.125}$$

This separation of membrane and bending energy components provides the convenience for evaluating the membrane locking and better understanding the structural responses. It should be noted that E_{pn} and E_{ps} are both in-plane strain energy components. However, since the calculation of E_{ps} in laminated plates and shells does not depend on a specific neutral surface as the membrane and bending energy components do, it is considered separately.

For an FE model under bending, shear locking phenomenon will appear when bending energy is erroneously absorbed by the shear modes. For curved shell models that undergo bending deformation, membrane locking happens when the parasitic stretching of the middle surface causes the membrane energy to overshadows the bending energy. These effects on shell elements will be further discussed in Chapter 12.

Part II

Adaptable Refinement Approach

Chapter 5

Refined beam FE models with Node-Dependent Kinematics

This chapter present refined beam FE models with Node-Dependent Kinematics (NDK) and their application in the analysis of multi-layered beam structures. In particular, 2D hierarchical functions (see Section 2.2.7) are used as cross-section functions of refined beam models and are referred to as Hierarchical Legendre Expansions (HLE). High efficiency is expected to be obtained through the use of HLE on refined beam models. Meanwhile, by utilizing NDK, kinematic refinement can be carried out on the targeted nodes, which can be decided in an adaptable way. The combination of HLE and NDK in refined beam FE models will result in appreciable improvement of efficiency.

The effectiveness of the adaptable refinement approach on beam FE models is demonstrated through two numerical examples. Besides the accuracy, the influences of the transition zone and the kinematics in the non-critical region on the accuracy are discussed.

5.1 Case 1: A simply supported sandwich beam under local pressure

A sandwich beam consisting of two composite faces and a soft core is studied, as illustrated in Fig. 5.1. This numerical case was also used by Wenzel et al. [253] and Zappino et al. [263] in their works. The width of the sandwich structure is $a = 2$mm, length $b = 10$mm, and height $h = 2$mm. The thickness of the faces is $0.1h$, and the core $0.8h$. The elastic properties are listed in Table 5.1. The constant pressure load $p_0 = -1$MPa covers the central 10% of the length.

Half of the structure is modeled with FEs with symmetric boundary conditions. Twenty B4 (four-node Lagrangian 1D) elements, which can give satisfactory numerical accuracy, are used along the axis of the beam. The cross-section is approximated through a set of basis functions HLEp (p indicates the polynomial degree) in each sub-domain

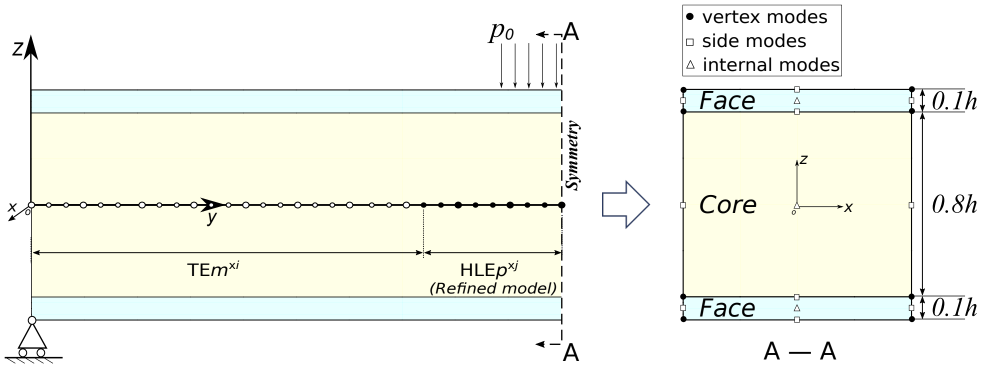

Figure 5.1: Geometry, boundary conditions and FE model for the sandwich beam.

Table 5.1: Elastic constants of materials used on the sandwich beam.

	E_{11}(GPa)	E_{22}(GPa)	E_{33}(GPa)	ν_{12}	ν_{13}	ν_{23}	G_{12}(GPa)	G_{13}(GPa)	G_{23}(GPa)
Face	131.1	6.9	6.9	0.32	0.32	0.49	3.588	3.088	2.3322
Core	0.2208×10^{-3}	0.2001×10^{-3}	2.76	0.99	0.00003	0.00003	16.56×10^{-3}	0.5451	0.4554

in the LW way, as demonstrated in Fig. 5.1.

The refinement of the kinematics is first conducted through uniformly used HLEp on all the nodes, then TEm (m represents the order of basis functions TE) cross-section functions are used in the region outside the loaded zone through NDK. The NDK models are denoted as TE$m^{\times i}$-HLE$p^{\times j}$, where i and j indicate the corresponding number of nodes with TEm and HLEp kinematic assumptions, respectively. The deflection and stress evaluations obtained are reported in Table 5.2. Results obtained through uniformly used TEm kinematics are also listed for comparison purposes.

From the results in Table 5.2, it can be observed that the numerical convergence can be reached by gradually increasing the polynomial degree of HLE used on the cross-section. The theoretical solution of σ_{zz} on the loaded surface is -1 MPa, which can be achieved through the use of HLEp kinematic in LW approach.

The variations of σ_{yz} through the thickness obtained through different HLEp kinematics are compared in Fig. 5.2a. It can be observed that the stress σ_{yz} in the core is much lower in comparison with the faces due to the difference in stiffness. Among all the HLEp kinematic assumptions, HLE2 fails in capturing the variation of σ_{yz} in the two composite faces. From HLE2 to HLE7, the distribution of σ_{yz} gradually converges, and the theoretical zero value on the stress-free top surface is progressively approached, though not reached. The relative errors of σ_{yz} obtained through different cross-section functions (concerning the solutions given by HLE7) are plotted versus the DOFs in the FE models in Fig. 5.2b. The global trend of the relative errors shows a converging trend.

NDK is adopted to construct FE models with variable TE/HLE nodal kinematics. In the zone within and nearby the loaded area, HLE7 is used as nodal assumptions, and the rest of the beam is simulated with TE models. The transition zone covers the range

Table 5.2: Displacement and stress evaluation on the sandwich beam under local pressure.

Mesh	Kinematics	$-w(10^{-3}\text{mm})$ $(0, \frac{b}{2}, -\frac{h}{2})$	$-\sigma_{yy}(\text{MPa})$ $(0, \frac{b}{2}, \frac{h}{2})$	$-\sigma_{yz}(\text{MPa})$ $(\frac{a}{2}, \frac{9b}{20}, \frac{9h}{20})$	$-\sigma_{zz}(\text{MPa})$ $(0, \frac{b}{2}, \frac{h}{2})$	DOFs
B4×10	HLE2	2.467	17.72	0.8339	1.097	1674
B4×20	HLE2	2.467	17.77	0.8164	1.015	3294
B4×20	HLE3	2.469	18.33	1.062	1.048	5124
B4×20	HLE4	2.469	18.14	1.083	0.9965	7503
B4×20	HLE5	2.469	18.11	1.060	0.9884	10431
B4×20	HLE6	2.469	18.24	1.079	0.9789	13908
B4×20	HLE7	2.469	18.24	1.094	0.9771	17934
B4×20	TE1	1.515	7.300	1.163	0.9547	549
B4×20	TE3	2.309	17.52	0.8777	1.502	1830
B4×20	TE5	2.338	17.25	0.8815	0.7839	3843
B4×20	TE1$^{\times 49}$-HLE7$^{\times 12}$(α)	1.547	15.63	1.437	0.9791	3969
B4×20	TE1$^{\times 31}$-HLE7$^{\times 30}$(β)	1.820	18.07	1.112	0.9772	9099
B4×20	TE3$^{\times 31}$-HLE7$^{\times 30}$(β)	2.376	18.23	1.096	0.9771	9750
B4×20	TE5$^{\times 31}$-HLE7$^{\times 30}$(β)	2.388	18.23	1.096	0.9771	10773
B4×20	TE7$^{\times 31}$-HLE7$^{\times 30}$(β)	2.419	18.24	1.095	0.9771	12168
	Zappino et al. [263] (2D)	2.471	18.11	1.180	0.9989	37479

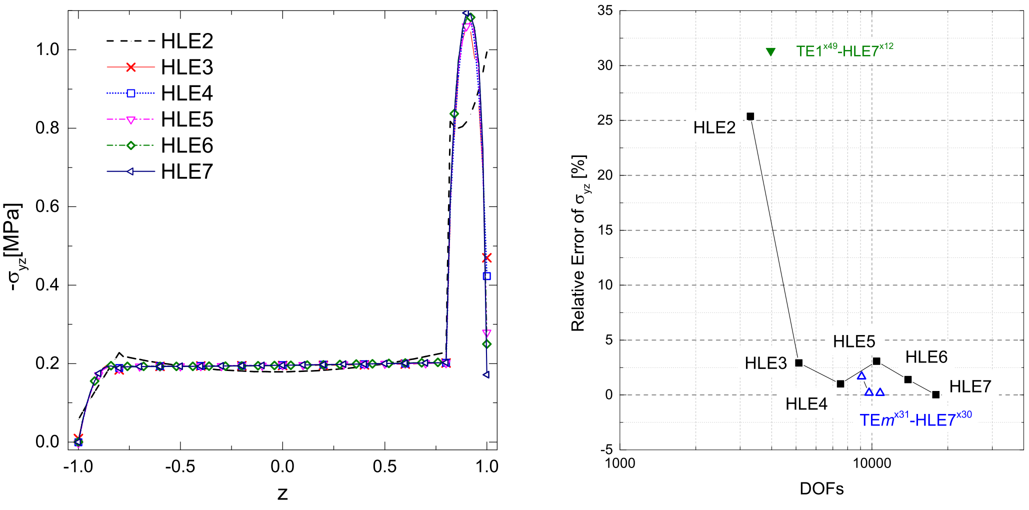

(a) σ_{yz} through $(\frac{a}{2}, \frac{9b}{20}, \bar{z})$ (b) Relative error of $\sigma_{yz}(\frac{a}{2}, \frac{9b}{20}, \frac{9h}{20})$.

Figure 5.2: Evaluation of σ_{yz} on the sandwich beam under local pressure.

of one element, and two locations of the transition zone are considered. Transition zone α is placed at around 75% beam length which leads to NDK model TE$m^{\times 49}$-HLE7$^{\times 12}$, and the transition zone β is located near 50% of the length range and corresponds to models denoted by TE$m^{\times 31}$-HLE7$^{\times 30}$.

As illustrated in Fig.5.2b, with reduced DOFs, the NDK models with the transition zone β result in comparable accuracy with uniformly refined models with HLE7 regarding σ_{yz}. However, the evaluations given by the transition zone α are far from being satisfactory. Also, from Table 5.2 and Fig. 5.3, it can be found that TE1$^{\times 31}$-HLE7$^{\times 30}$ (transition zone β) gives better accuracy than TE1$^{\times 49}$-HLE7$^{\times 12}$ (transition zone α) concerning the accuracy in the composite faces. These facts prove that transition zone β is more appropriate than transition zone α. Moreover, in models with transition β, namely models TE$m^{\times 31}$-HLE7$^{\times 30}$, the refinement of TEm also improves the accuracy. Concerning σ_{yz}, TE5 fails in giving accurate evaluation, while TE1$^{\times 31}$-HLE7$^{\times 30}$ leads to good accuracy, and the DOFs are reduced by 49% compared to uniform HLE7 model.

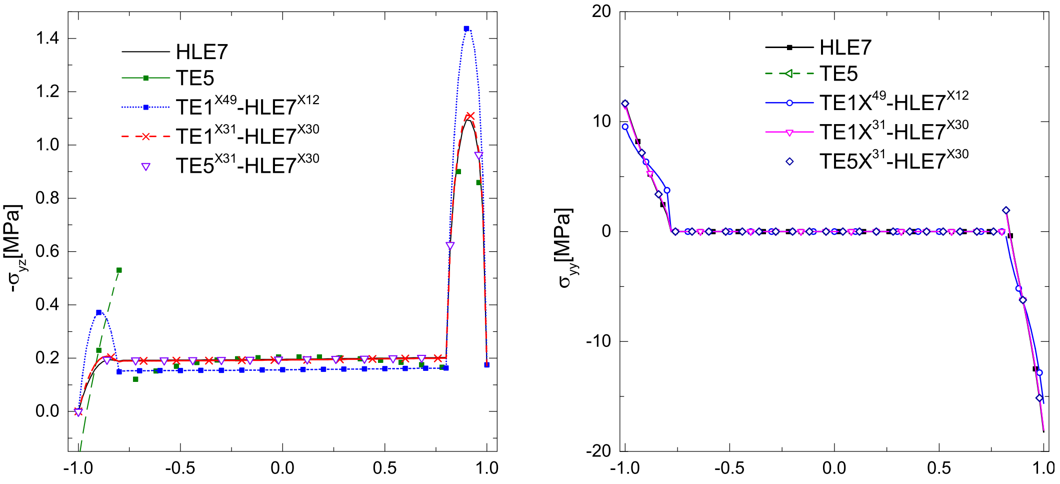

(a) $\bar{\sigma}_{yz}$ through $(\frac{a}{2}, \frac{9b}{20}, \bar{z})$ (b) $\bar{\sigma}_{yy}$ through $(0, \frac{b}{2}, \bar{z})$

Figure 5.3: Through-the-thickness variation of $\bar{\sigma}_{yz}$ and $\bar{\sigma}_{yy}$ on the sandwich beam under local pressure.

The distributions of w, σ_{yy}, and σ_{yz} along the beam axial direction are shown in Fig. 5.4. A stress oscillation can be observed in the vicinity of the transition zone. The results show that transition zone β is more appropriate than transition zone α. The refinement of kinematics used in the non-critical region helps improve the solution accuracy of stresses.

In Figs. 5.5 and 5.6, the contours of σ_{yz} and σ_{zz} given by HLE7 model and TE5$^{\times 31}$-HLE7$^{\times 30}$ are compared. Stress concentration exists on the right-hand side of Figs. 5.5 and 5.6 within the upper composite face. The oscillation of stress σ_{yz} exists nearby the transition zone. Similar effects due to the use of a global-local coupling technique, eXtended Variational Formulation, were reported by Wenzel et al. [253]. In the critical

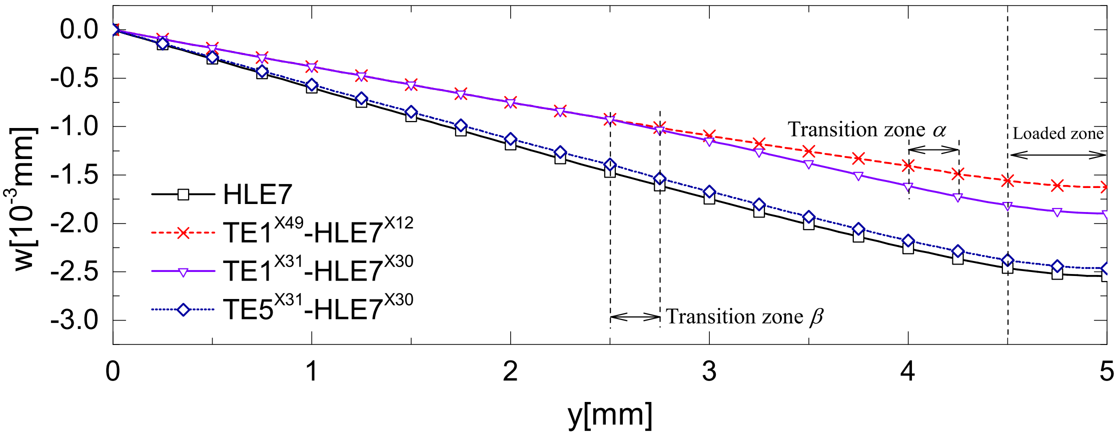

(a) $\bar{w}$ along $(0, y, 0)$

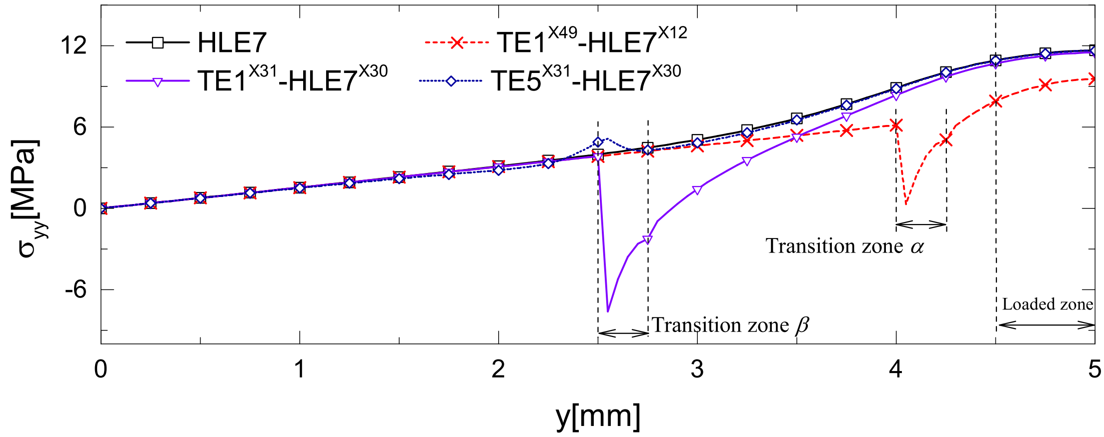

(b) $\bar{\sigma}_{yy}$ along $(0, y, -\frac{h}{2})$

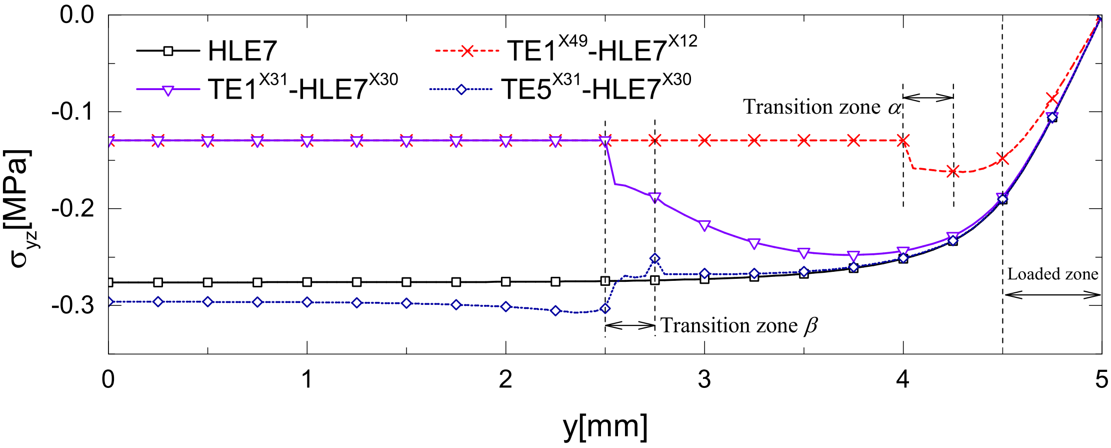

(c) $\bar{\sigma}_{yz}$ along $(0, y, 0)$

Figure 5.4: Variation of w, σ_{yy}, and σ_{yz} along the axial direction of the sandwich beam.

region within and nearby the loaded area, the stress fields obtained with these two models are in excellent agreement.

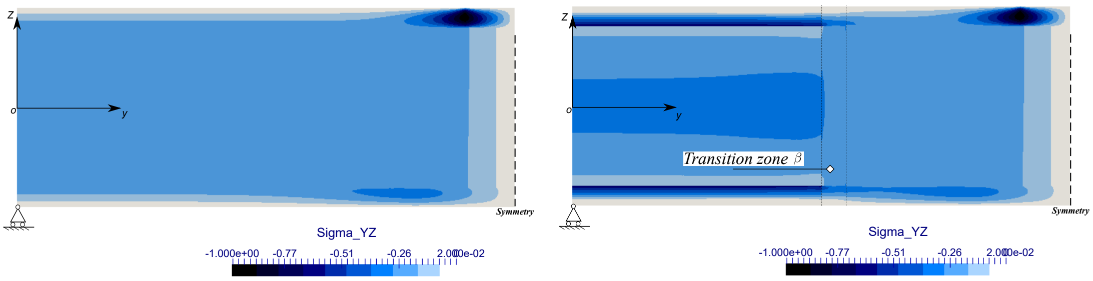

(a) HLE7 (b) TE5$^{\times 31}$-HLE7$^{\times 30}$

Figure 5.5: Contour plot of σ_{yz} on surface $(\frac{a}{2}, y, z)$ of the sandwich beam under local pressure.

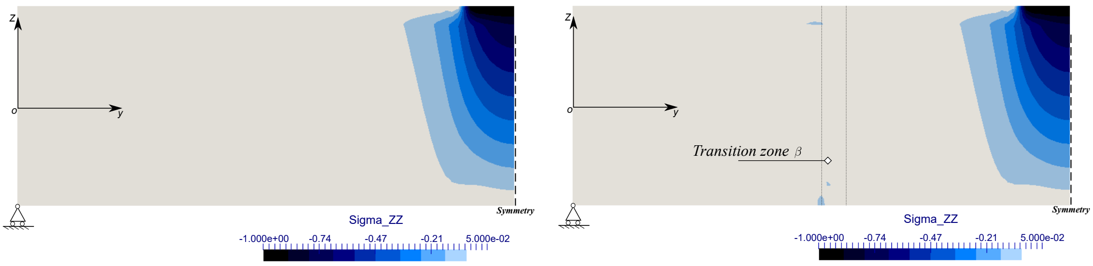

(a) HLE7 (b) TE5$^{\times 31}$-HLE7$^{\times 30}$

Figure 5.6: Contour plot of σ_{zz} on surface $(\frac{a}{2}, y, z)$ of the sandwich beam under local pressure.

5.2 Case 2: A two-layered cantilever beam under four points loads

In this example, a cantilever beam with two orthotropic layers is modeled. The two-layered beam is clamped on one end and imposed to concentrate loads at the four vertexes on the other end, as illustrated in Fig. 5.7. The beam has length $b = 0.09$m, width $a = 0.001$m, and height $h = 0.01$m. Each layer has thickness $t = h/2$. The upper and lower layers respectively adopt Material 1 and 2, which are aligned along the beam axial. The elastic constants of the used materials are listed in Table 5.3, in which L and T signify the fiber longitudinal and transverse directions, respectively.

The beam structure is modeled with B4 elements. HLEp and TEm kinematic assumptions are both tested, where p and m stand for the corresponding polynomial

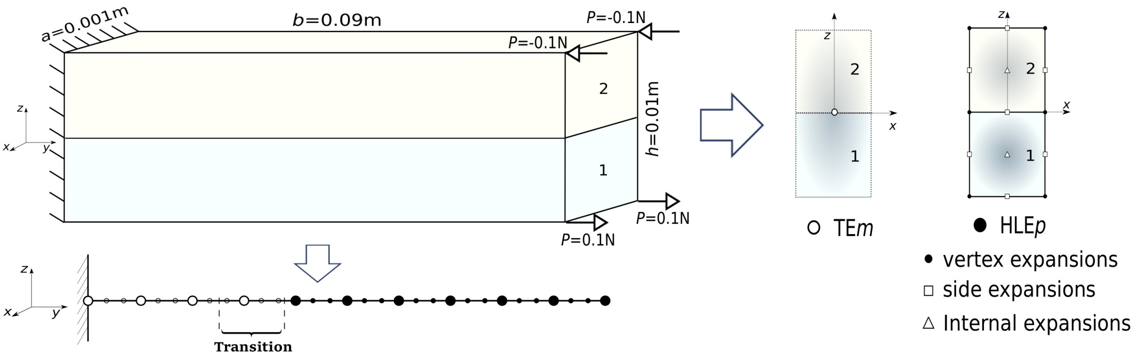

Figure 5.7: The two-layered cantilever beam under four points loads.

Table 5.3: Elastic properties of the materials used in the two-layered cantilever beam.

	E_L(GPa)	E_T(GPa)	ν_{LT}	G_{LT}(GPa)
Material 1	30	1	0.25	0.5
Material 2	5	1	0.25	0.5

orders. NDK is used to implement local refinement on the loaded end and assign less-refined kinematics to the outlying region, resulting in NDK models TE1$^{\times 49}$-HLE7$^{\times 12}$ and TE1$^{\times 31}$-HLE7$^{\times 30}$. Similar to the case studied in Section 5.1, the superscripts indicate the number of nodes with the corresponding kinematic assumptions.

The obtained results are reported in Table 5.4, from which it can be observed that 20 B4 elements with HLE kinematics can give comparable accuracy with ABAQUS 3D model using 4×180×32 ($x \times y \times z$) C3D20R brick elements. The numerical convergence can be observed from the variation of σ_{yz} through the thickness at $(0, \frac{8b}{9})$, as shown in Fig. 5.8.

In the NDK models with TE1 assumption made on nodes in the non-critical region, a significant reduction of DOFs is obtained. To be specific, a reduction of 65% is achieved through TE1$^{\times 31}$-HLE7$^{\times 30}$ and 49% with TE1$^{\times 49}$-HLE7$^{\times 12}$. By looking into the Table 5.4 and the stress variation in Fig. 5.9, it can be found that TE1$^{\times 31}$-HLE7$^{\times 30}$ has better accuracy compared to model TE1$^{\times 49}$-HLE7$^{\times 12}$ concerning σ_{yz}. These results show that the model with a transition zone β is a more decent choice.

5.3 Conclusions

Hierarchical Legendre Expansions (HLE) are used as cross-section function of refined beam elements, and NDK is used to build FE models with variable TE/HLE nodal kinematics. When used in global-local simulations, since the local model can be implemented by switching the nodal kinematic properties without using any additional

Table 5.4: Deflection and stress evaluations on the two-layered cantilever beam.

Mesh	Kinematics	$w(10^{-3}\text{mm})$ $(0, b, 0)$	$\sigma_{yy}(\text{KPa})$ $(0, \frac{8b}{9}, -\frac{h}{2})$	$\sigma_{yz}(\text{KPa})$ $(0, \frac{8b}{9}, -\frac{h}{4})$	DOFs
B4×10	HLE2	9.041	236.6	2.563	1209
B4×20	HLE2	9.036	234.0	2.610	2379
B4×20	HLE3	9.082	245.1	4.518	3660
B4×20	HLE4	9.065	236.4	4.432	5307
B4×20	HLE5	9.075	233.4	4.972	7320
B4×20	HLE6	9.063	233.8	4.986	9699
B4×20	HLE7	9.074	234.8	4.972	12444
B4×20	TE1	9.053	215.1	0.000	549
B4×20	$\text{TE1}^{\times 49}\text{-HLE7}^{\times 12}(\alpha)$	9.120	234.0	4.294	2889
B4×20	$\text{TE1}^{\times 31}\text{-HLE7}^{\times 30}(\beta)$	9.117	234.8	4.970	6399
	ABAQUS (3D)	9.071	235.3	4.963	337251

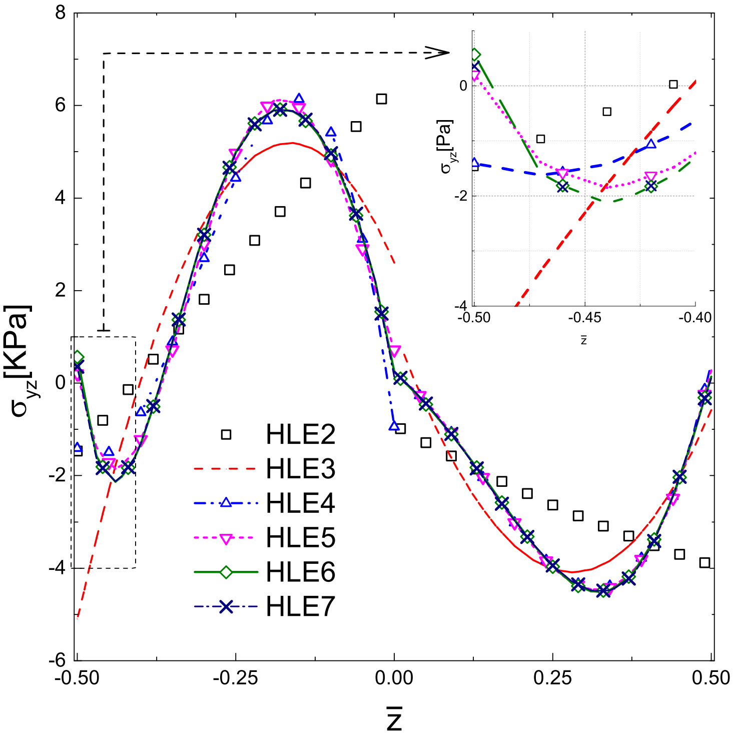

Figure 5.8: Distribution of σ_{yz} along $(0, \frac{8b}{9}, \bar{z})$ on the two-layered cantilever beam, obtained with HLEp kinematics.

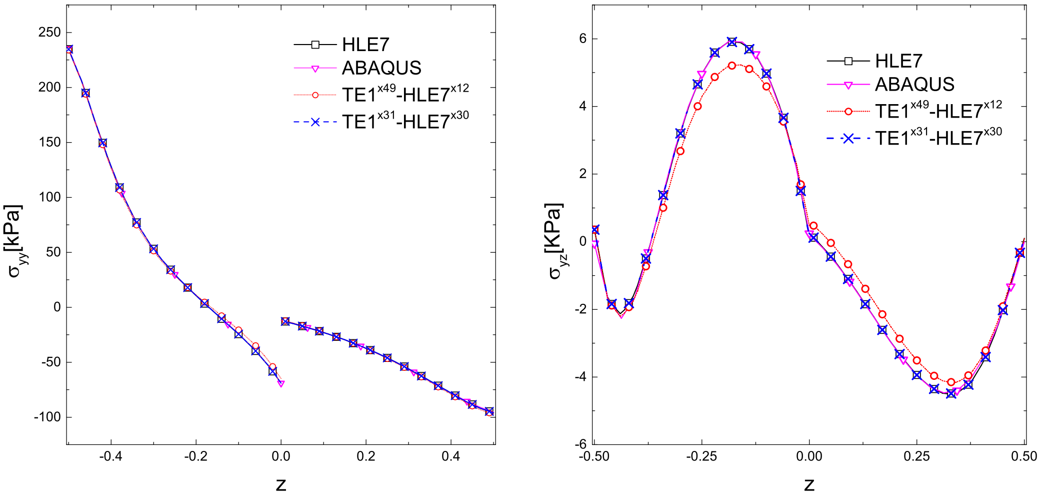

(a) σ_{yy}

(b) σ_{yz}

Figure 5.9: Variation of σ_{yy} and σ_{yz} through $(0, \frac{8b}{9}, \bar{z})$ on the two-layered cantilever beam.

coupling technique, model preparation will be greatly simplified. Due to high adaptability and the convenience of re-using FE meshes, this variable ESL/LW nodal kinematic refinement approach can shorten the time consumption of engineering simulations.

The numerical investigation has demonstrated that:

- NDK approach is a practical and efficient tool to integrate the low costs of ESL kinematics and the high accuracy of LW models for the analysis of multi-layered beams;
- Through using HLE and NDK together, both solution and pre-processing efficiency can be improved;
- When using NDK, the location of the transition zone and the kinematic refinement in the non-critical region should be appropriately set to guarantee the accuracy;
- In the results obtained with NDK models, stress oscillation was detected, which can be alleviated by refining the kinematics in the non-critical area and placing the transition in a proper region outside the area with strong local effects.

In the next two chapters, hierarchical 2D functions will be used as shape functions of refined plate and shells models, and the NDK technique will be further extended to the adaptable refinement approach.

Chapter 6

Refined plate FE models with Node-Dependent Kinematics

In the current chapter, hierarchical 2D functions are used in combination with NDK in the FE simulation of laminated plates. Firstly, a benchmark case consisting of composite laminated plates under bi-sinusoidal distributed pressure is studied with p-refinement and LW kinematic models. Secondly, a plate subjected to a point load and a plate under constant local pressure are simulated through NDK FE models with adaptable ESL/LW local kinematic refinement. Various FE models are compared regarding accuracy and computational costs.

In the following sections, TEm indicates TE-type kinematics of the mth order, and LEn represents LE-type assumptions with Lagrange polynomials of order n. For FE models with multiple assumed kinematics, TEm/LEn is used as an acronym.

6.1 Case 1: Simply-supported cross-ply plates under bi-sinusoidal pressure

The benchmark case presented by Pagano [177] is used in this section. The considered simply supported three-layered composite plates have lamination sequence (0°/90°/0°) and are subjected to bi-sinusoidal transverse pressure on the top surface. Distribution of the pressure load follows:

$$p(x,y) = p_0 \cdot \sin(\frac{\pi x}{a}) \sin(\frac{\pi y}{b}) \tag{6.1}$$

The plates have width a, length b, and height h. It is assumed that $b = 3a$ and each layer has a thickness of $h/3$. The considered cases include both thick ($a/h = 2$) and thin ($a/h = 100$) plates. The dimensionless material constants of each lamina are: $E_L = 25$, $E_T = 1$, $G_{LT} = 0.5$, $G_{TT} = 0.2$, $\nu_{LT} = \nu_{TT} = 0.25$, where L and T indicate the fiber longitudinal and transverse directions, respectively. The following parameters are used when reporting the results:

$$\bar{w} = \frac{100E_T h^3}{p_0 a^4} w, \qquad \bar{\sigma}_{xx} = \frac{h^2}{p_0 a^2}\sigma_{xx}, \qquad \bar{\sigma}_{yy} = \frac{10h^2}{p_0 a^2}\sigma_{yy}, \qquad \bar{\sigma}_{xy} = \frac{10h^2}{p_0 a^2}\sigma_{xy},$$
$$\bar{\sigma}_{xz} = \frac{10h}{p_0 a}\sigma_{xz}, \qquad \bar{\sigma}_{yz} = \frac{10h}{p_0 a}\sigma_{yz}, \qquad \bar{\sigma}_{zz} = \frac{1}{p_0}\sigma_{zz}. \tag{6.2}$$

The following boundary conditions (simple supports) are applied to the edges:

$$\begin{aligned} x = 0, a: &\quad v = w = 0; \\ y = 0, b: &\quad u = w = 0. \end{aligned} \tag{6.3}$$

By considering the symmetric boundary conditions, 1/4 of the plate is simulated through FE models, as shown in Fig. 6.1.

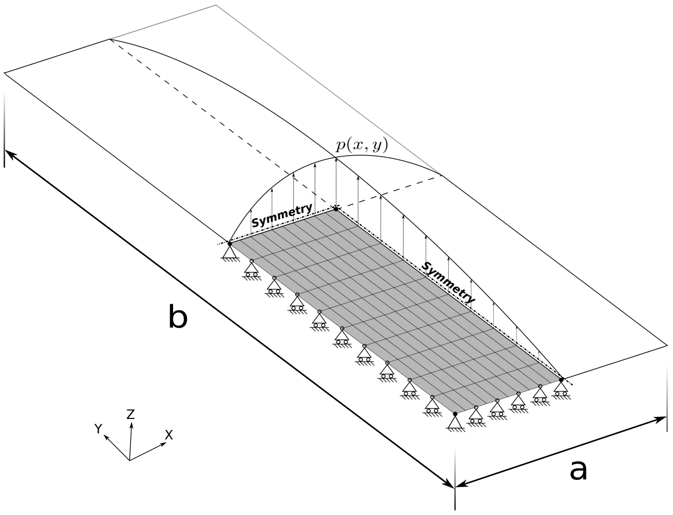

Figure 6.1: FE model for the composite laminated plate under bi-sinusoidal pressure.

In the numerical modeling, LE4 thickness functions are uniformly used on the three layers, and hierarchical functions are adopted for the *p*-refinement. For comparison purposes, Q9 (nine-node Lagrangian) elements with full integration and MITC9 (Q9 with MITC) elements are used on the thick ($a/h = 2$) and thin ($a/h = 100$) plates in the *h*-refinement approach, respectively. The obtained results are summarized in Tables 6.1 and 6.2. The results presented by Kulikov and Plotnikova [140] and Carrera et al. [60] are also listed for comparison.

From Table 6.1, one can observe that the single-element models with $p \geq 6$ give results as accurate as the Q9 model with 5×5 elements, and the *p*-version refinement leads to much fewer DOFs. When used on the thin plate ($a/h = 100$), Q9 element with full integration suffers from a low convergence rate regarding $\bar{\sigma}_{yz}$, as shown in Table 6.2 and Fig. 6.2b. In contrast, the hierarchical functions result in a much higher convergence rate, which can be observed from Fig. 6.2. In the $h-p$ approach (p-refinement with mesh 2×2), the numerical accuracy can be further improved. Indeed, for the studied cases, high accuracy can be achieved through p-refinement even with only one hierarchical plate element.

Table 6.1: Deflection and stresses on the three-layered cross-ply plate with $a/h = 2$ under bi-sinusoidal pressure, obtained with LE4 as thickness functions.

Element	Mesh	$\bar{w}$ $(\frac{a}{2},\frac{b}{2},0)$	$\bar{\sigma}_{yy}$ $(\frac{a}{2},\frac{b}{2},\frac{h}{6})$	$10\bar{\sigma}_{yz}$ $(\frac{a}{2},0,0)$	$\bar{\sigma}_{zz}$ $(\frac{a}{2},\frac{b}{2},\frac{h}{2})$	DOFs
Q9	2×2	8.167	2.356	7.525	1.010	975
Q9	4×4	7.882	2.315	6.904	0.9693	3159
Q9	5×5	8.165	2.308	6.825	1.004	4719
$p2$	1×1	8.137	2.671	9.853	1.038	312
$p3$	1×1	8.005	2.866	6.961	0.9598	468
$p4$	1×1	8.120	2.333	6.600	0.9918	663
$p5$	1×1	8.167	2.279	6.622	1.004	897
$p6$	1×1	8.166	2.293	6.688	1.004	1170
$p7$	1×1	8.165	2.295	6.686	1.004	1482
Pagano [177]		8.17	2.30	6.68	–	
Kulikov and Plotnikova [140]		8.1659	2.6772	6.6778	1.0001	
Carrera et al. [60]		8.166	2.296	6.690	1.000	

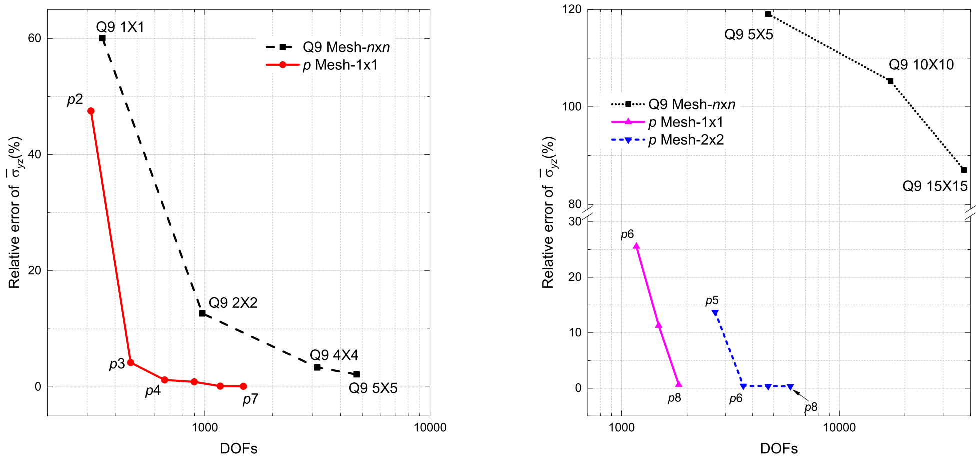

(a) Thick plate, $a/h = 2$

(b) Thin plate, $a/h = 100$

Figure 6.2: Relative error of $\bar{\sigma}_{yz}$ on the three-layered cross-ply plates under pressure load, obtained with LE4 as thickness functions.

Table 6.2: Deflection and stresses on the three-layered cross-ply plate with $a/h = 100$ under bi-sinusoidal pressure, obtained with LE4 as thickness functions.

Element	Mesh	$\bar{w}$ $(\frac{a}{2},\frac{b}{2},0)$	$\bar{\sigma}_{yy}$ $(\frac{a}{2},\frac{b}{2},\frac{h}{6})$	$10\bar{\sigma}_{yz}$ $(\frac{a}{2},0,0)$	$\bar{\sigma}_{zz}$ $(\frac{a}{2},\frac{b}{2},\frac{h}{2})$	DOFs
Q9	5×5	0.5069	0.2511	2.365	1.813	4719
Q9	10×10	0.5076	0.2528	2.217	1.128	17199
Q9	15×15	0.5076	0.2530	2.020	1.041	37479
*p*3	1×1	0.4487	0.5085	105.1	5.404	468
*p*4	1×1	0.5054	0.3479	42.23	-1.431	663
*p*5	1×1	0.5087	0.2830	-7.019	0.4908	897
*p*6	1×1	0.5077	0.2486	0.8042	1.164	1170
*p*7	1×1	0.5077	0.2531	1.202	1.011	1482
*p*8	1×1	0.5077	0.2532	1.087	0.9971	1833
*p*3	2×2	0.5075	0.3472	8.386	2.541	1287
*p*4	2×2	0.5075	0.2629	3.799	0.8828	1911
*p*5	2×2	0.5077	0.2540	0.9318	0.9758	2691
*p*6	2×2	0.5077	0.2530	1.075	1.003	3627
*p*7	2×2	0.5077	0.2531	1.084	1.000	4719
*p*8	2×2	0.5077	0.2531	1.084	1.000	5967
Pagano [177]		0.508	0.253	1.08	–	
Kulikov and Plotnikova [140]		0.50766	0.25236	1.0836	1.000	
Carrera et al. [60]		0.5077	0.2533	1.085	1.000	

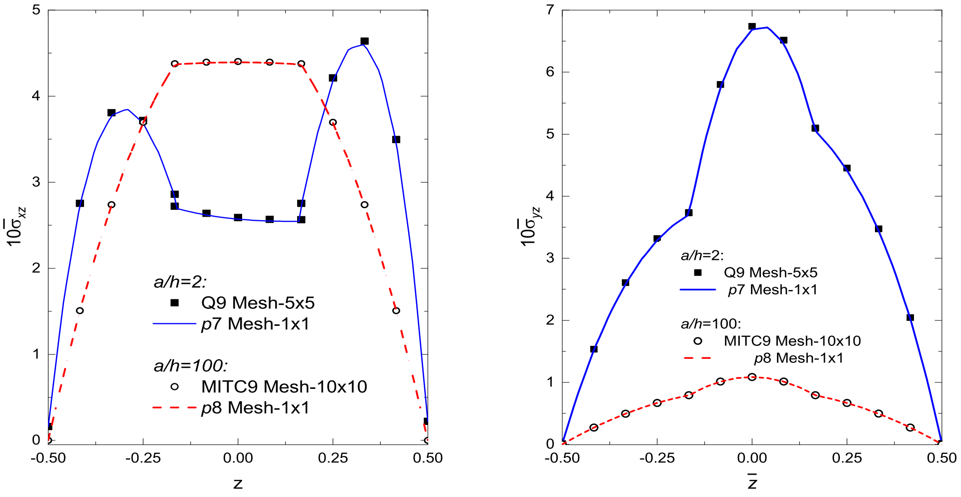

(a) $\bar{\sigma}_{xz}$ at $(0,\frac{b}{2},\bar{z})$

(b) $\bar{\sigma}_{yz}$ at $(\frac{a}{2},0,\bar{z})$

Figure 6.3: Distribution of the transverse shear stresses through the thickness of the plates under bi-sinusoidal pressure.

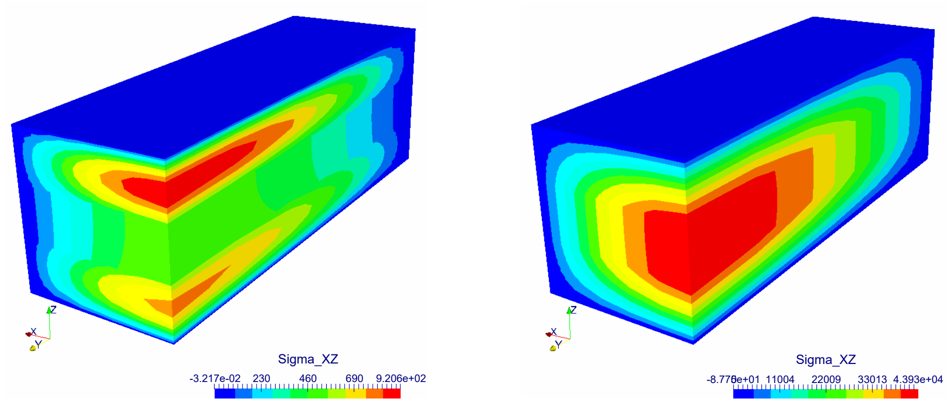
Z
X
Y
Sigma_XZ
-3.217e-02 230 460 690 9.206e+02
Z
X
Y
Sigma_XZ
-8.776e+01 11004 22009 33013 4.393e+04

(a) $a/h = 2$, $p7$, mesh 1×1 (b) $a/h = 100$, $p8$, mesh 1×1 ($z \times 50$)

Figure 6.4: Distribution of σ_{xz} obtained with hierarchical plate elements employing LE4 as thickness functions.

The variation of transverse shear stresses through the plate thickness obtained with different FE models are compared in Fig. 6.3. For the thick plate, the $p7$ single-element model gives results in great agreement with Q9 5×5 model. In the thin laminated plate with $a/h = 100$, it can be observed that $p8$ produces results as satisfactory as that of 10×10 MITC9 elements. The field of σ_{xz} shown in Fig. 6.4 demonstrates that the used two-level refinement approach leads to 3D accuracy even with only one element.

6.2 Case 2: Simply supported three-layered plates subjected to a point load

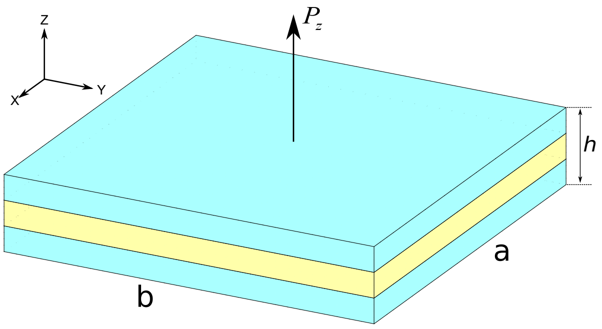

Figure 6.5: Simply-supported cross-ply composite plates subjected to a point load.

This section considers simply supported square cross-ply plates with three composite layers, as shown in Fig. 6.5. The closed-form solutions for this numerical example were presented by Carrera and Ciuffreda [45]. A thick ($a/h = 4$) and a thin ($a/h = 100$)

plates are analyzed. The three plies have equal thickness $h/3$, and the lamination sequence is (0°/90°/0°). The plates are subjected to a concentrated load at the central point on the top surface. The elastic properties of the lamina are assumed to be: $E_L = 25$, $E_T = 1$, $G_{LT} = 0.5$, $G_{TT} = 0.2$, $\nu_{LT} = \nu_{TT} = 0.25$, where L denotes the fiber longitudinal direction and T the transverse direction. The simply supported boundary conditions are set by the following Eqn. 6.3. The deflection results are reported by considering the following dimensionless factors:

$$\bar{w} = \frac{100E_T h^3}{pa^2} w \tag{6.4}$$

where p is the magnitude of the point load.

Point loads cause strong local effects and become a challenge for FE simulations. Through this numerical case, the capabilities of hierarchical plate elements with refined kinematics are examined. The layered plates are mesh into 4 × 4 rectangular elements, as illustrated in Fig. 6.6. Uniform kinematic refinement with LE4 on all layers is first adopted, then local nodal kinematic refined is conducted through NDK. In the NDK models, the LE4 assumptions are made on shape functions surrounding the loading point, while the rest shape functions possess TEm models, as shown in Fig. 6.6. As discussed in Section 4.3.2, shape functions of the same mode at the same feature position (a vertex, an edge, or the surface) will be assigned the same kinematics for brevity.

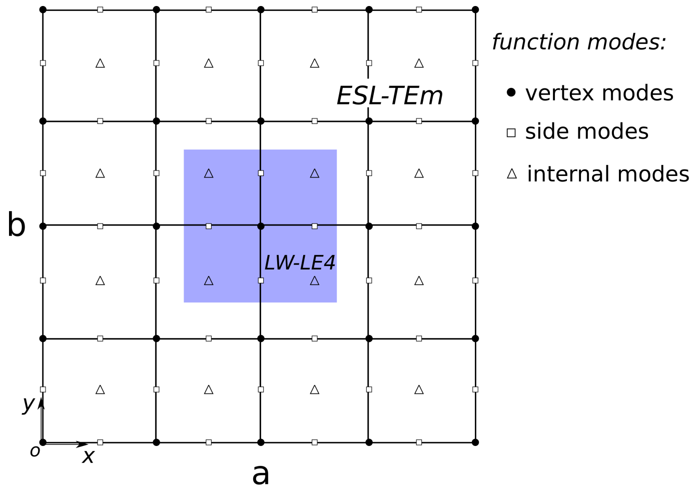

Figure 6.6: Assignment of nodal kinematics on the NDK FE models for the laminated plates under a point load.

The obtained distributions of the deflections $\bar{w}$ through the plate thickness at the central point are reported in Fig. 6.7. It can be found that, with the increase of the polynomial degree of the hierarchical plate elements, the solution accuracy can be improved greatly. It should be pointed out that, when the structure is subjected to a concentrated load at a point, the displacement at the loaded point theoretically goes to infinite. In the weak-form techniques, this infinite displacement will not be captured but can be approximated represented. Fig. 6.7 demonstrates that the competence of the refined FE model can be significantly improved through the *p*-refinement.

The results obtained with the NDK models are compared to the uniformly refined model in Fig. 6.7 and Table 6.3. It can be observed that the NDK technique leads to a significantly reduced number of DOFs while keeping the numerical accuracy.

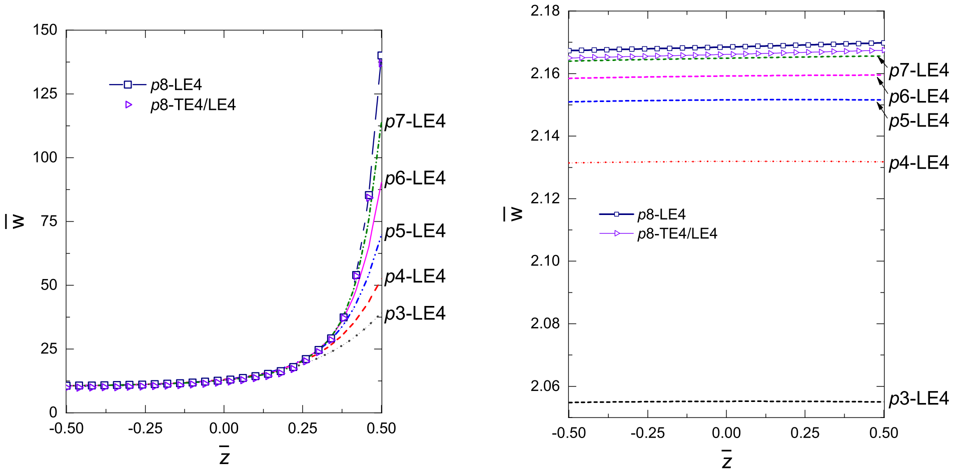

(a) $a/h = 4$ (b) $a/h = 100$

Figure 6.7: Variation of $\bar{w}$ through $(a/2, b/2, \bar{z})$ on the three-layered plates under a point load.

Table 6.3: $\bar{w}$ at $(\frac{a}{2}, \frac{b}{2}, 0)$ on the simply-supported cross-ply plates under a point load.

Element	Kinematics	$\bar{w}(a/h = 4)$	$\bar{w}(a/h = 100)$	DOFs
*p*8	LE4	12.80	2.169	21255
*p*8	FSDT/LE4	10.96	2.167	5751
*p*8	TE2/LE4	11.04	2.165	7575
*p*8	TE3/LE4	11.88	2.166	8943
*p*8	TE4/LE4	11.95	2.166	10311
Carrera and Ciuffreda [45]		13.188	2.172	–

6.3 Case 3: Three-layered cross-ply composite plate under local pressure

A simply supported square laminated plate subjected to local pressure in the central area on the top surface is considered, as shown in Fig. 6.8. The laying up sequence is (0°/90°/0°), and each layer have equal thickness $h/3$. The plate has length and width $a = b = 0.1m$, and span-to-thickness ratio $a/h = 10$. The area covered by the uniform pressure is $a/5 \times b/5$. The simple support constraints on the four edges are set according to Eqn.6.3. The elastic constants of the composite material used in each layer are: E_L =132.5GPa, E_T =10.8GPa, ν_{LT} =0.24, ν_{TT} =0.49, G_{LT} =5.7GPa, and G_{TT} =3.4GPa.

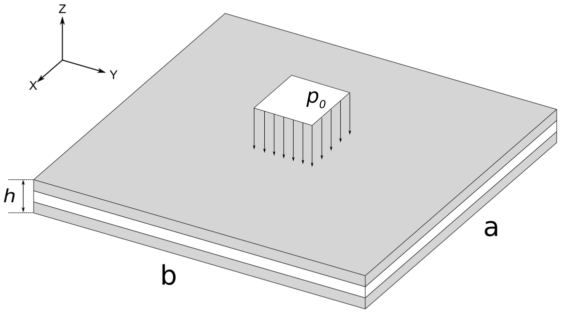

Figure 6.8: The three-layered cross-ply composite plate under uniform local pressure.

With symmetric boundary conditions, FE models consisting of 5×5 hierarchical plate elements are built for 1/4 of the plates, as demonstrated in Fig. 6.9. p-refinement is carried out on FE models with only LE4 kinematics. Second, NDK approach is used to assign FSDT to the shape functions of elements in the non-critical region. The assignment of the nodal kinematics is shown in Fig. 6.9.

The obtained results are reported in Table 6.4, in which the solutions given by Biscani et al. [29] and Zappino et al. [263] are also listed for comparison. It can be observed that the numerical convergence is reached when $p = 6$, and the corresponding results agree well with the reference solutions. Within the loaded zone, the stresses at the monitoring points (A, B, C, and D) are well captured with the NDK FE models. The variations of transverse shear stresses through the thickness obtained with different FE models are compared in Fig. 6.10. It can be found that the NDK LE4/FSDT model leads to results in excellent agreement with the pure LE4 model at much lower computational consumption.

6.4 Conclusions

In this chapter, the NDK technique is used in combination with hierarchical plate elements in the analysis of multi-layered plate structures. The effectiveness and the

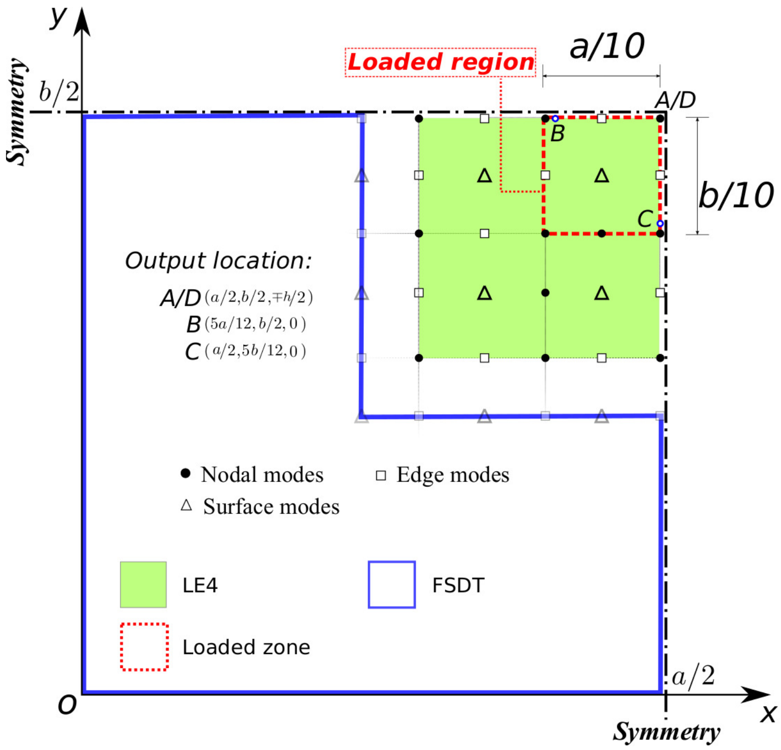
y
Symmetry
b/2
Loaded region
a/10
A/D
B
b/10
C
Output location:
A/D (a/2,b/2,∓h/2)
B (5a/12,b/2,0)
C (a/2,5b/12,0)
● Nodal modes
□ Edge modes
△ Surface modes
LE4
FSDT
Loaded zone
O
a/2
x
Symmetry

Figure 6.9: Assignment of nodal kinematics on the FE model for the three-layered cross-ply composite plate under local pressure.

Table 6.4: Deflection and stresses on the layered plate under uniform local pressure.

Element	Mesh	Kinematics	$w(10^{-5}\text{m})$ $\text{A}(\frac{a}{2},\frac{b}{2},\frac{-h}{2})$	$\sigma_{xx}(\text{MPa})$ $\text{A}(\frac{a}{2},\frac{b}{2},\frac{-h}{2})$	$\sigma_{yy}(\text{MPa})$ $\text{A}(\frac{a}{2},\frac{b}{2},\frac{-h}{2})$	$-10\sigma_{xz}(\text{MPa})$ $\text{B}(\frac{5a}{12},\frac{b}{2},0)$	$-10\sigma_{yz}(\text{MPa})$ $\text{C}(\frac{a}{2},\frac{5b}{12},0)$	$-\sigma_{zz}(\text{MPa})$ $\text{D}(\frac{a}{2},\frac{b}{2},\frac{h}{2})$	DOFs
*p*3	5×5	LE4	1.681	12.08	2.061	6.596	7.094	1.241	6084
*p*4	5×5	LE4	1.682	11.92	2.023	6.501	6.965	0.881	9399
*p*5	5×5	LE4	1.682	11.97	2.039	6.497	6.972	1.045	13689
*p*6	5×5	LE4	1.682	11.98	2.037	6.499	6.974	1.003	18954
*p*6	5×5	FSDT	1.610	10.44	1.850	3.829	4.647	0.938	2430
*p*6	5×5	FSDT/LE4	1.702	12.50	2.036	6.516	6.941	1.008	5592
Biscani et al. [29]			1.674	11.94	2.019	6.524	–	–	–
Zappino et al. [263]			1.675	11.99	2.033	6.463	6.902	0.993	37479

efficiency of this adaptable kinematic refinement approach are demonstrated through three numerical examples with reference solutions available from the literature. Based on the numerical investigations, some conclusions can be drawn:

- With NDK, plate FE models with variable LW/ESL nodal kinematics can be conveniently built by simply switching the nodal kinematic properties, and no mesh modification is necessary;

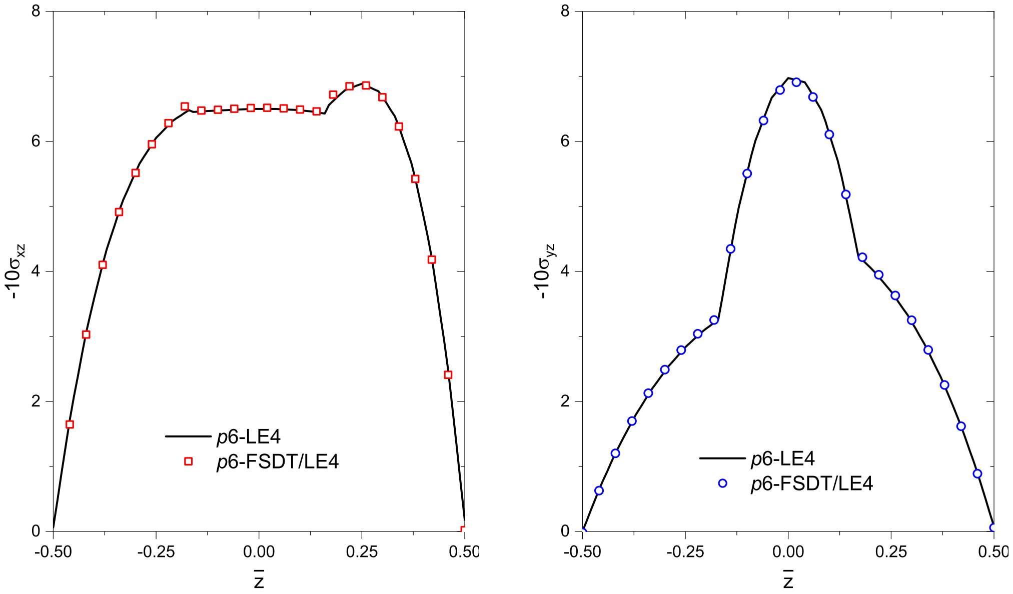

(a) $-10\sigma_{xz}$, $(\frac{5a}{12}, \frac{b}{2}, \bar{z})$ (b) $-10\sigma_{yz}$, $(\frac{a}{2}, \frac{5b}{12}, \bar{z})$

Figure 6.10: Distribution of transverse shear stresses through the thickness of the layered plate under local uniform pressure.

- The combination of NDK and *p*-refinement leads to FE models with high efficiency, which means 3D accuracy in the critical region at a controlled number of DOFs.
- This adaptable refinement approach is ideal for global-local modeling considering both numerical efficiency and the convenience of FE model preparation.

This adaptable kinematic refinement approach based on CUF will be applied to FE modeling of multi-layered shell structures in the next chapter.

Chapter 7

Refined shell FE models with Node-Dependent Kinematics

In this chapter, the adaptable refinement approach is applied to the FE simulation of laminated shells with double curvatures. By using 2D hierarchical shape functions as shape functions (see Section 2.2.7) and NDK variable nodal ESL/LW kinematics, FE models with optimal efficiency is explored.

To verify FE models with the two-level refinements (p-refinement and kinematic refinement), two benchmark cases with exact solutions, including two-layered cylindrical shells [244] and layered spherical shells [193] under pressure loads, were first studied. Then, laminated shell panels loaded to locally distributed bi-sinusoidal pressure are analyzed and compared against results obtained through ABAQUS 3D modeling regarding both accuracy and computational consumption.

Refined TE and LE kinematics are both tested and compared. In the FE models adopted, the same LE-type thickness functions will be uniformly applied to all the layers. For comparison purposes, h-refinement is tested by utilizing Q9 (nine-node quadrilateral Lagrangian) elements on thick shells and MITC9 (Q9 with MITC) elements on thin shells.

7.1 Case 1: Two-layered cylindrical shells under distributed pressure

This benchmark case was proposed by Varadan and Bhaskar [244]. The cylindrical shells are simply supported on the two ends and subjected to transverse distributed pressure on the inner surface. The load distribution reads:

$$p(\alpha, \beta) = -p_0 \, \sin \frac{\pi \alpha}{L} \, \cos \frac{4\beta}{R_\beta} \tag{7.1}$$

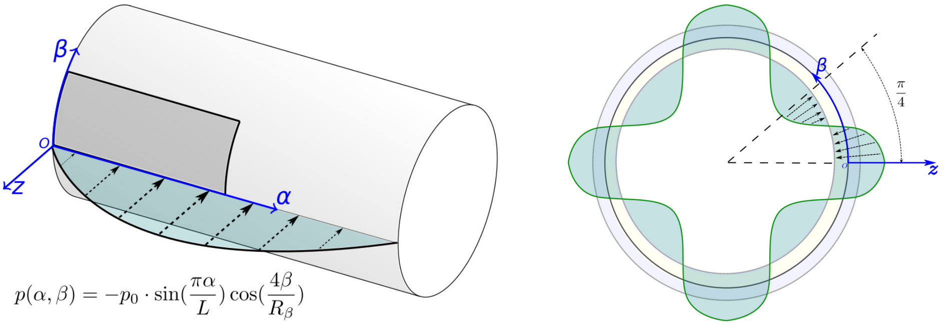
β
o
z
α
$p(\alpha,\beta) = -p_0 \cdot \sin(\frac{\pi\alpha}{L})\cos(\frac{4\beta}{R_\beta})$
β
$\frac{\pi}{4}$
o
z

(a) Axial variation of the inner pressure (b) Pressure sectional profile

Figure 7.1: Simply-supported cylindrical shells under inner distributed pressure.

where L is the cylinder length, R_β the middle surface radius, and $L = 4R_\beta$. Fig. 7.1a and Fig. 7.1b illustrate the axial variation and the sectional profile of the pressure load, respectively. The total shell thickness is h, and the circumference of the cylinder is $b = 2\pi R_\beta$. The material coefficients of the lamina are: $E_L = 25E_T$, $G_{LT} = 0.5E_T$, $G_{TT} = 0.2E_T$, and $\nu_{LT} = \nu_{TT} = 0.25$, where the subscripts L and T represent the longitudinal and transverse directions of the fibers, respectively. The displacement and stress results are non-dimensionalized through:

$$\begin{aligned}
\bar{w} &= -\frac{10E_L h^3}{p_0 R_\beta^4}\; w(\frac{L}{2},0,0), \quad \bar{\sigma}_{\alpha\alpha} = -\frac{10h^2}{p_0 R_\beta^2}\; \sigma_{\alpha\alpha}(\frac{L}{2},0,\frac{h}{2})\,,\\
\bar{\sigma}_{\beta\beta} &= -\frac{10h^2}{p_0 R_\beta^2}\; \sigma_{\beta\beta}(\frac{L}{2},0,\frac{h}{2})\,, \quad \bar{\sigma}_{\alpha\beta} = -\frac{10h^2}{p_0 R_\beta^2}\; \sigma_{\alpha\beta}(0,\frac{b}{16},\frac{-h}{2})\,,\\
\bar{\sigma}_{\alpha z} &= -\frac{10h}{p_0 R_\beta}\; \sigma_{\alpha z}(0,0,\frac{-h}{4})\,, \quad \bar{\sigma}_{\beta z} = -\frac{10h}{p_0 R_\beta}\; \sigma_{\beta z}(\frac{L}{2},\frac{b}{16},\frac{h}{4}),\\
\bar{\sigma}_{zz} &= -\frac{1}{p_0}\; \sigma_{zz}(\frac{L}{2},0,\frac{h}{4})\,.
\end{aligned} \tag{7.2}$$

The considered case in this section consists of two-layered shells with laying-up sequence (0°/90°) (from bottom to top). The thickness of each ply is $h/2$. Three different radius-to-thickness ratios, $R_\beta/h = 2,100$, and 500, are considered. By making use of the cyclic/symmetric features, a 1/16 FE model which covers 1/2 of the length and 1/8 of the circumference is built, as signified by the shaded area in Fig. 7.1a.

The FE models are first refined by enhancing the kinematic assumptions (F_t and F_s), then by increasing the polynomial order of the hierarchical shape functions (N_i, N_j). When a single-element model is used in the simulation, obviously p =1 and p =2 are not competent, thus the p-refinement starts from p =3 to p =8. In the final step, the mesh density is increased to further improve the numerical accuracy.

The results obtained are summarized in Tables 7.1, 7.2, and 7.3. Note that *pn* indicates the use of p refinement with polynomial degree n. It can be observed that the refined kinematics and p-version 2D elements give results in excellent agreement with the exact solutions. As shown in Fig. 7.2, when the LE kinematics is sufficiently refined, through-the-thickness distributions of $\bar{\sigma}_{\alpha z}$ and $\bar{\sigma}_{\beta z}$ become continuous at the layer interfaces. Also, the LE kinematics adopted can account for the stretch in the thickness direction. ESL kinematic models based on TE result in good accuracy regarding the displacements and in-plane stresses but fail in the capturing of transverse stresses. Additionally, the thin shells ($R_\beta/h = 100$ and 500) require a fewer number of expansions compared to the thick shell case ($R_\beta/h = 2$).

From Tables 7.2 and 7.3, it can be observed that the transverse shear stresses $\bar{\sigma}_{\alpha z}$ and $\bar{\sigma}_{\beta z}$ given by Q9 elements are far from being converged to the analytical solutions given that the mesh density is already high. This is mainly due to the shear locking on the thin shells. When MITC9 elements are used, the accuracy is significantly improved. For the hierarchical elements, the locking is alleviated through the gradual refinement of the shape functions. In Table 7.3 (for the very thin shell $R_\beta/h = 500$), $p3$ case suffers from locking, yet $p8$ is much less affected. The locking phenomena in hierarchical shell elements will be further discussed in Chapter 12.

Table 7.1: Deflection and stresses on the two-layered cylindrical shell with $R_\beta/h = 2$.

Theory(F_τ, F_s)	FE(N_i, N_j)	Mesh	$\bar{w}$ $(\frac{L}{2},0,0)$	$\bar{\sigma}_{\alpha\alpha}$ $(\frac{L}{2},0,\frac{h}{2})$	$\bar{\sigma}_{\beta\beta}$ $(\frac{L}{2},0,\frac{h}{2})$	$\bar{\sigma}_{\alpha\beta}$ $(0,\frac{b}{16},\frac{-h}{2})$	$\bar{\sigma}_{\alpha z}$ $(0,0,\frac{-h}{4})$	$\bar{\sigma}_{\beta z}$ $(\frac{L}{2},\frac{b}{16},\frac{h}{4})$	$\bar{\sigma}_{zz}$ $(\frac{L}{2},0,\frac{h}{4})$	DOFs
LE7	Q9	3×6	14.034	0.2517	9.564	-0.5139	0.5016	-3.006	-0.3156	4095
		10×20	14.035	0.2515	9.756	-0.5026	0.4807	-2.938	-0.3132	38745
TE1	$p8$	1×2	13.232	-0.02005	6.653	-0.3233	0.4321	-2.227	-0.4408	510
TE3			13.590	0.2600	9.248	-0.4745	0.4294	-2.689	-0.3261	1020
TE5			13.822	0.2637	9.615	-0.4961	0.4488	-2.832	-0.3129	1530
LE3	$p3$	1×1	15.317	0.4371	8.563	-0.3941	0.3579	-3.131	-0.3359	252
LE4			15.328	0.4085	8.597	-0.3950	0.3586	-3.133	-0.3372	324
LE5			15.343	0.4293	8.685	-0.3954	0.3533	-3.028	-0.3293	396
LE6			15.344	0.4236	8.678	-0.3954	0.3533	-3.028	-0.3291	468
LE7			15.344	0.4257	8.681	-0.3954	0.3543	-3.037	-0.3300	540
LE7	$p4$	1×1	14.002	0.3546	9.981	-0.5257	0.6039	-3.091	-0.2975	765
	$p5$		13.951	0.2609	10.09	-0.5077	0.4706	-2.989	-0.3056	1035
	$p6$		14.034	0.2494	9.762	-0.5029	0.4737	-2.945	-0.3127	1350
	$p7$		14.036	0.2509	9.747	-0.5020	0.4788	-2.934	-0.3133	1710
	$p8$		14.034	0.2514	9.775	-0.5016	0.4787	-2.931	-0.3130	2115
LE7	$p8$	1×2	14.035	0.2514	9.776	-0.5016	0.4786	-2.931	-0.3130	3825
		2×4	14.035	0.2514	9.775	-0.5016	0.4786	-2.931	-0.3130	13005
Varadan and Bhaskar [244]			14.034	0.2511	9.775	-0.5016	0.4786	-2.931	-0.31	

Table 7.2: Deflection and stresses on the two-layered cylindrical shell with $R_\beta/h = 100$.

Theory(F_τ, F_s)	FE(N_i, N_j)	Mesh	$\bar{w}$ $(\frac{L}{2},0,0)$	$\bar{\sigma}_{\alpha\alpha}$ $(\frac{L}{2},0,\frac{h}{2})$	$\bar{\sigma}_{\beta\beta}$ $(\frac{L}{2},0,\frac{h}{2})$	$\bar{\sigma}_{\alpha\beta}$ $(0,\frac{b}{16},\frac{-h}{2})$	$\bar{\sigma}_{\alpha z}$ $(0,0,\frac{-h}{4})$	$\bar{\sigma}_{\beta z}$ $(\frac{L}{2},\frac{b}{16},\frac{h}{4})$	$\bar{\sigma}_{zz}$ $(\frac{L}{2},0,\frac{h}{4})$	DOFs
LE3	Q9	6×12	1.359	0.1789	4.764	-0.3455	-0.04168	-7.897	-7.674	6825
		10×20	1.366	0.1844	5.282	-0.3457	-0.05320	-5.168	-7.956	18081
		15×30	1.367	0.1860	5.438	-0.3455	-0.07126	-4.003	-8.004	39711
LE3	MITC9	6×12	1.367	0.1882	5.592	-0.3491	-0.1516	-2.989	-7.749	6825
		10×20	1.367	0.1875	5.571	-0.3466	-0.1514	-2.979	-7.726	18081
		15×30	1.367	0.1873	5.565	-0.3459	-0.1513	-2.975	-7.717	39711
TE1	*p*8	2×4	1.356	0.2162	5.555	-0.3423	-0.2406	-1.889	50.53	1734
TE3			1.367	0.1868	5.559	-0.3452	-0.2448	-2.284	-6.769	3468
TE5			1.367	0.1867	5.560	-0.3452	-0.1387	-2.820	-5.887	5202
LE1	*p*3	1×1	0.1793	3.61E-03	-2.766	-0.02262	-2.635	5.587	1.990	108
LE2			0.1794	-1.31E-04	-2.772	-0.02262	-2.636	5.589	2.010	180
LE3			0.1794	5.43E-05	-2.772	-0.02262	-2.628	5.481	1.648	252
LE4			0.1794	5.15E-05	-2.772	-0.02262	-2.628	5.481	1.648	324
LE3	*p*4	1×1	1.062	0.2123	-8.10E-07	-1.27E-12	23.26	1.127	0.1536	357
	*p*5		1.301	0.2514	9.156	-0.2814	-8.026	-6.152	-8.960	483
	*p*6		1.361	0.1895	5.889	-0.3670	0.1842	-3.479	-7.704	630
	*p*7		1.366	0.1815	5.217	-0.3467	-0.05745	-2.988	-7.516	798
	*p*8		1.367	0.1867	5.537	-0.3453	-0.1610	-2.989	-7.708	987
LE3	*p*8	1×2	1.367	0.1872	5.561	-0.3452	-0.1527	-2.975	-7.709	1785
		2×4	1.367	0.1872	5.560	-0.3452	-0.1512	-2.972	-7.707	6069
		3×6	1.367	0.1872	5.560	-0.3452	-0.1512	-2.972	-7.707	12873
Varadan and Bhaskar [244]			1.367	0.1871	5.560	-0.3452	-0.1512	-2.972	-7.71	

Table 7.3: Deflection and stresses on the two-layered cylindrical shell with $R_\beta/h = 500$.

Theory(F_τ, F_s)	FE(N_i, N_j)	Mesh	$\bar{w}$ $(\frac{L}{2},0,0)$	$\bar{\sigma}_{\alpha\alpha}$ $(\frac{L}{2},0,\frac{h}{2})$	$\bar{\sigma}_{\beta\beta}$ $(\frac{L}{2},0,\frac{h}{2})$	$\bar{\sigma}_{\alpha\beta}$ $(0,\frac{b}{16},\frac{-h}{2})$	$\bar{\sigma}_{\alpha z}$ $(0,0,\frac{-h}{4})$	$\bar{\sigma}_{\beta z}$ $(\frac{L}{2},\frac{b}{16},\frac{h}{4})$	$\bar{\sigma}_{zz}$ $(\frac{L}{2},0,\frac{h}{4})$	DOFs
LE3	Q9	10×20	0.1004	0.04390	0.3302	-0.1046	-0.07552	-1.184	-2.990	18081
		15×30	0.1005	0.04447	0.3883	-0.1046	-0.07552	-0.9957	-3.089	39711
LE3	MITC9	10×20	0.1005	0.04500	0.4354	-0.1049	-0.08424	-0.2279	-3.088	18081
		15×30	0.1005	0.04495	0.4349	-0.1047	-0.08417	-0.2276	-3.088	39711
TE1	*p*8	2×4	0.1005	0.04697	0.4367	-0.1044	-0.1216	-0.1482	74.80	1734
TE3			0.1005	0.04508	0.4347	-0.1045	-0.1206	-0.1792	-10.96	3468
TE5			0.1005	0.04477	0.4343	-0.1045	-0.07686	-0.2155	3.165	5202
LE1	*p*3	1×1	7.57E-03	-3.13E-03	-0.7363	-3.73E-03	-2.788	6.174	3.550	108
LE2			7.57E-03	-3.29E-03	-0.7365	-3.73E-03	-2.788	6.174	3.554	180
LE3			7.57E-03	-3.29E-03	-0.7365	-3.73E-03	-2.788	6.169	3.476	252
LE4			7.57E-03	-3.29E-03	-0.7365	-3.73E-03	-2.788	6.169	3.476	324
LE3	*p*4	1×1	0.0629	0.03145	-0.3267	-0.0478	34.49	4.057	18.07	357
	*p*5		0.0905	0.05295	1.353	-0.0789	-12.58	-6.901	-4.191	483
	*p*6		0.1005	0.04709	0.6831	-0.1121	0.32547	-0.8957	-4.138	630
	*p*7		0.1005	0.04424	0.3911	-0.1050	-0.02924	-0.0621	-3.182	798
	*p*8		0.1005	0.04490	0.4323	-0.1045	-0.08594	-0.2232	-3.091	987
LE3	*p*8	1×2	0.1005	0.04491	0.4346	-0.1045	-0.08923	-0.2261	-3.083	1785
		2×4	0.1005	0.04491	0.4345	-0.1045	-0.08410	-0.2274	-3.086	6069
		3×6	0.1005	0.04491	0.4345	-0.1045	-0.08410	-0.2274	-3.086	12873
Varadan and Bhaskar [244]			0.1005	0.0449	0.4345	-0.1045	-0.0841	-0.227	-3.09	

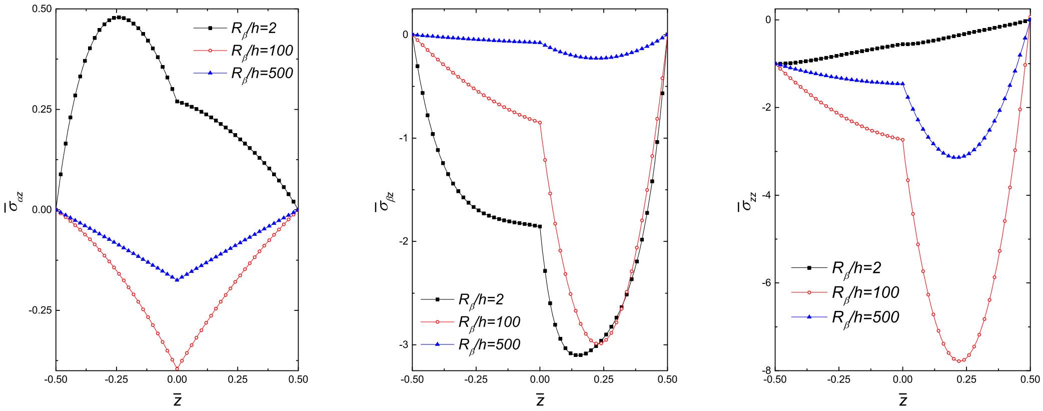

(a) $\bar{\sigma}_{\alpha z}$ through (0,0, $\bar{z}$) (b) $\bar{\sigma}_{\beta z}$ through ($\frac{L}{2}$, $\frac{b}{16}$, $\bar{z}$) (c) $\bar{\sigma}_{zz}$ through ($\frac{L}{2}$,0, $\bar{z}$)

Figure 7.2: Distribution of transverse stresses through the thickness of the two-layered cylindrical shells ($R_\beta/h = 2$: p8-LE7, mesh 1×2; $R_\beta/h = 100$: p8-LE3, mesh 2×4; $R_\beta/h = 500$: p8-LE3, mesh 2×4).

7.2 Case 2: Simply-supported cross-ply spherical shells under sinusoidal distributed pressure

In this section, the bending response of a set of cross-ply spherical shells, whose closed-form solutions were presented by Reddy [193], is studied. The elastic properties of the lamina are the same as those used in Section. 7.1. The dimensions of the shell mid-surface along the α and β axes are assumed to be $a/b = 1.0$, and the constant radii are $R_\alpha = R_\beta = R$. The laminated shells are loaded to bi-sinusoidal distributed pressure on the middle surface which reads:

$$p(\alpha, \beta) = p_0 \sin \frac{\pi \alpha}{a} \sin \frac{\pi \beta}{b} \tag{7.3}$$

The simple supports imposed on the four edges are:

$$\begin{aligned} \alpha = 0, a: \quad & v = 0, w = 0; \\ \beta = 0, b: \quad & u = 0, w = 0. \end{aligned} \tag{7.4}$$

Stacking sequences (0°/90) and (0°/90°/90°/0°) are considered. Various radius-to-thickness (R/h) and span-to-thickness ratios (a/h) are examined. The deflection solutions at the shell central point ($\frac{a}{2}$, $\frac{b}{2}$,0) are compared against those provided by Reddy [193]. The following dimensionless parameters are adopted:

$$\bar{w} = \frac{h^3 E_T}{p_0 a^4} w \tag{7.5}$$

A 1/4 FE model is built by considering the symmetric features of the boundary conditions. Table 7.4 reports the results for a thin ($a/h = 100$) and a moderate thick shell ($a/h = 10$) consisting of two layers with layering-up sequence (0°/90°). The two-level mathematical refinement approach utilized in Section 7.1 is also used here. Kinematic assumptions through the thickness are first refined gradually then the order of the hierarchical shape functions is increased step by step.

Table 7.5 summarizes results for the thin shells ($a/h = 100$) with (0°/90°/90°/0°) with different radius-to-thickness ratios varying from 1 to 10^{30}. In fact, $R = a \times 10^{30}$ leads to a plate case. From Tables 7.4 and 7.5, it can be found that the obtained results are in great agreement with the closed-form solutions given by Reddy [193]. The two-level refinement approach leads to models with significantly reduced DOFs compared to the h-refinement with MITC9 elements. If the results are evaluated concerning only displacements ($\bar{w}$), lower-order models can be competent most times.

Table 7.4: Spherical shells with (0°/90°) and $R/h = 5$ under bi-sinusoidal pressure.

$a/h = 100$					$a/h = 10$				
Theory(F_τ, F_s)	FE(N_i, N_j)	Mesh	$\bar{w}$	DOFs	Theory(F_τ, F_s)	FE(N_i, N_j)	Mesh	$\bar{w}$	DOFs
FSDT	$p7$	1×1	1.1947	190	FSDT	$p7$	1×1	11.181	190
TE1			1.1958	228	TE1			11.189	228
TE3			1.1949	456	TE7			11.406	912
TE5			1.1949	684	TE9			11.411	912
LE2	MITC9	1×1	1.2317	135	LE4	MITC9	1×1	11.528	243
		2×2	1.1981	375			2×2	11.435	675
		4×4	1.1951	1215			4×4	11.427	2187
		8×8	1.1949	4335			8×8	11.427	7803
LE1	$p2$	1×1	0.6374	72	LE1	$p2$	1×1	9.975	72
LE2			0.6377	120	LE2			10.063	120
LE2	$p3$	1×1	1.1054	180	LE3			10.141	168
LE2	$p4$		1.1788	180	LE4			10.141	216
LE2	$p5$		1.1930	345	LE4	$p3$	1×1	10.738	324
LE2	$p6$		1.1950	450	LE4	$p4$		11.334	459
LE2	$p7$		1.1949	570	LE4	$p5$		11.421	621
LE3	$p7$		1.1949	798	LE4	$p6$		11.428	810
LE2	$p7$	2×2	1.1949	1815	LE4	$p7$		11.427	1026
					LE5	$p7$		11.427	1254
					LE4	$p7$	2×2	11.427	3267
Reddy[193]			1.1948		Reddy[193]			11.429	

7.3 Case 3: Simply-supported three-layered cross-ply spherical shells under local distributed pressure

In this section, a set of simply supported cross-ply spherical shells with lamination sequence (90°/0°/90°) under local bi-sinusoidal pressure are studied. The three layers are of equal thickness $h/3$. The elastic properties of the used lamina are assumed to be

Table 7.5: spherical shells with (0°/90°/90°/0°) and $a/h = 100$ under bi-sinusoidal distributed pressure.

R/a	Theory(F_τ, F_s)	FE(N_i, N_j)	Mesh	$\bar{w}$	DOFs
1	LE2	$p7$	1×1	0.05323	1026
	LE2	MITC9	8×8	0.05323	7803
	FSDT	$p7$	1×1	0.05322	190
	TE5	$p7$	1×1	0.05323	684
	Reddy[193]			0.0532	
5	LE2	$p7$	1×1	1.0286	1026
	LE2	MITC9	8×8	1.0286	7803
	FSDT	$p7$	1×1	1.0277	190
	TE5	$p7$	1×1	1.0285	684
	Reddy[193]			1.0279	
10^{30}	LE2	$p7$	1×1	4.3463	1026
	LE2	MITC9	4×4	4.3463	7803
	FSDT	$p7$	1×1	4.3327	190
	TE5	$p7$	1×1	4.3451	684
	Reddy[193]			4.3368	

the same as Section. 7.1. The geometric features and the imposed load are as shown in Fig. 7.3. The origin point of the curvilinear reference system is located at the central point. The middle-surface radii are $R_\alpha = R_\beta = R = 1$. a and b ($a = b$) are dimensions of the middle surface in α and β directions, respectively. The local pressure is imposed on to the top surface, and its distribution follows:

$$p(\alpha, \beta) = -p_0 \cos \frac{\pi\alpha}{a/10} \cos \frac{\pi\beta}{b/5} \tag{7.6}$$

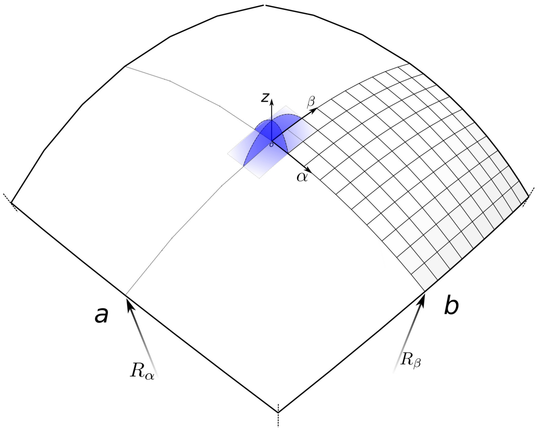

Figure 7.3: Three-layered cross-ply spherical shells under local bi-sinusoidal distributed pressure.

where $p_0 = 1$ is the magnitude of the load. The loaded region covers the central area of $\frac{a}{10} \times \frac{b}{5}$. Simple supports are applied to the four edges, which follow:

$$\begin{aligned} \alpha = \pm\frac{a}{2}: \quad & v = 0, w = 0; \\ \beta = \pm\frac{b}{2}: \quad & u = 0, w = 0. \end{aligned} \tag{7.7}$$

Radius-to-thickness ratios $R/h = 10{,}100$ and 1000 are considered. The transverse displacement and stresses are non-dimensionalized through the following parameters:

$$\begin{gathered} \bar{w} = -\frac{10^6 E_L h^3}{p_0 R^4} w\,, \quad \bar{\sigma}_{\alpha\alpha} = -\frac{10^4 h^2}{p_0 R^2} \sigma_{\alpha\alpha}\,, \quad \bar{\sigma}_{\beta\beta} = -\frac{10^4 h^2}{p_0 R^2} \sigma_{\beta\beta}\,, \quad \bar{\sigma}_{zz} = -\frac{1}{p_0} \sigma_{zz}\,, \\ \bar{\sigma}_{\alpha z} = \frac{100h}{p_0 R} \sigma_{\alpha z}\,, \quad \bar{\sigma}_{\beta z} = \frac{100h}{p_0 R} \sigma_{\beta z}\,, \quad \bar{\sigma}_{\alpha\beta} = -\frac{10^5 h^2}{p_0 R^2} \sigma_{\alpha\beta}\,. \end{gathered} \tag{7.8}$$

A quarter of the structure is modeled through the symmetric boundary conditions. This 1/4 FE model consists of 10 × 10 elements, and the local load covers the range of two elements, as shown in Fig. 7.3. The FE models are mathematically enhanced on the kinematic level and shape function level till a numerical convergence is reached by considering a relative error of 1% between two refinement steps. Then, NDK approach is employed to construct FE models with local kinematic refinement to capture the local effects caused by the pressure. The assignment of kinematics to shape functions is conducted as illustrated in Fig. 4.3.

For verification of the used FE models, C3D20R element (20-node quadratic brick element with reduced integration) in ABAQUS is utilized in 3D FE modeling. Note that the stresses at a node are extrapolated from the integration point values in solid elements. Also, high aspect ratio (span-to-thickness ratio) should be avoided when using brick elements. Generally, the aspect ratio should be controlled within 10 to avoid possible poor accuracy [89]. It should be pointed out that high aspect ratios do not always lead to inaccurate results, depending on the structural features and the boundary conditions. Meanwhile, to obtain detailed stress field, at least five layers of hexahedral elements are used in each layer in the present work. When the shell becomes thinner, more refined in-lane meshes are required to reduce the aspect ratio. For the very thin shell with $R/h = 1000$, 3D FE modeling will be very computationally expansive and thus not considered. The maximum aspect ratios of the brick elements used in 3D FE modeling are listed in Table 7.6. It can be observed that one of the 3D FE models for the shell with $R/h = 100$ contains brick elements whose aspect ratio is larger than 10.

The obtained results are reported in Tables 7.7, 7.8, and 7.9. The CPU time values $\bar{t}$ listed are relative to the least refined model (mesh 10×10, $p2$-LE1). The FSDT is treated as a particular case of TE1 and implemented through a penalty method in the in-house FE code used to collect the simulation results, and its CPU time is not reported since it

Table 7.6: Aspect-ratios of C3D20R elements in the 3D models for the three-layered spherical shells under local pressure.

R/h	Mesh($\alpha \times \beta \times z$)	Element aspect ratio
10	$50 \times 50 \times 5$	1.7
	$50 \times 50 \times 10$	3.3
100	$50 \times 50 \times 5$	15.8
	$100 \times 100 \times 5$	7.9

cannot reflect the real efficiency of FSDT. Also, the CPU time consumption of ABAQUS 3D FE models are not listed for a fair comparison.

The obtained results through ABAQUS 3D modeling and the variable kinematic simulation are compared in Tables 7.7, 7.8 and Figs. 7.5, 7.6, in which it can be observed that great agreement is achieved when numerical convergence is reached under the threshold of 1% regarding both deflection and stresses. Figs. 7.7, 7.8, 7.9 show that the refined shell FE models are capable of giving detailed 3D stress fields agreeing well with ABAQUS 3D simulation. Note that the thickness of the thin shells in 7.8 and 7.9 is respectively multiplied by 10 and 100 for the convenience of comparison. Indeed, 2D elements are free of this aspect ratio problem, and the use of CUF empowers the shell elements with adequately enriched kinematic assumptions to obtain 3D accuracy.

From Tables 7.7, 7.8, and 7.9, it can be observed that with the increase of the radius-to-thickness ratio R/h, lower-order LE kinematic assumptions become competent, and higher-order shape functions become essential in reaching satisfactory accuracy. With TE models, the deflection and in-plane stresses are well captured, yet the transverse stresses are not always reliable. When only global displacement responses are of interest, TE basis functions are preferred to LE functions due to the relatively low computational consumption. Compared to hierarchical elements, MITC9 elements lead to a lot more shape functions and longer solution time when the obtained results are almost equally accurate. Noticeably, no obvious locking can be observed in hierarchical shell elements in the model for the very thin shell with $R/h = 1000$.

The NDK technique is used to develop FE models with variable TE/LE nodal kinematics, and LE kinematics is only allocated to the shape functions within and adjacent to the critical region. In the numerical analysis, it is found that shells with different radius-to-thickness ratios (R/h) need different locally refined regions to obtain accurate results. Three models with different local regions are compared in Fig. 7.4, where TEm indicates TE kinematics of order m, LEn represents LE thickness functions of order n, and the superscripts of LE$n^{\times Ne}$ indicate the number of elements employing LEn on all of their affiliated shape functions. By observing the results in Table 7.7, it can be found that the moderate-thick shell with $R/h = 10$ requires a comparatively large locally refined zone, which leads to NDK model C (p5-TE5/LE5$^{\times 20}$) in Fig. 7.4c. In contrast, thin

Table 7.7: Deflection and stress evaluation on the three-layered spherical shells under local pressure, $R/h = 10$.

Mesh ($\alpha \times \beta$)	Theory (F_τ, F_s)	Element (N_i, N_j)	$\bar{w}$ (0,0,0)	$\bar{\sigma}_{\alpha\alpha}$ $(0,0,\frac{h}{6})$	$\bar{\sigma}_{\beta\beta}$ $(0,0,\frac{h}{2})$	$\bar{\sigma}_{\alpha\beta}$ $(\frac{a}{20},\frac{b}{10},\frac{-h}{2})$	$\bar{\sigma}_{\alpha z}$ $(\frac{a}{25},0,0)$	$\bar{\sigma}_{\beta z}$ $(0,\frac{2b}{25},0)$	$\bar{\sigma}_{zz}$ $(0,0,\frac{h}{2})$	Total shape functions	DOFs	CPU time $\bar{t}$
10×10	LE1	$p2$	5607	265.9	425.8	101.2	3.037	1.702	0.8903	341	4092	1.0
	LE2		5669	311.6	512.7	112.4	3.005	1.637	1.088	341	7161	2.0
	LE3		5718	355.6	552.3	117.9	3.506	1.717	1.050	341	10230	3.5
	LE4		5718	356.1	552.4	118.1	3.506	1.716	1.029	341	13299	5.9
	LE5		5719	357.5	550.8	118.2	3.432	1.716	1.024	341	16368	8.6
	LE6		5719	357.4	550.5	118.2	3.433	1.716	1.024	341	19437	11.9
10×10	LE5	$p3$	5722	363.8	539.3	110.8	3.428	1.769	0.9889	561	26928	20.5
		$p4$	5726	361.8	537.4	110.8	3.435	1.771	1.000	881	42288	45.0
		$p5$	5727	361.4	537.5	111.2	3.426	1.770	1.001	1301	62448	88.9
10×10	FSDT	$p5$	5320	365.5	252.7	92.18	2.940	1.104	–	1301	6505	–
	TE1		5290	352.5	264.3	87.24	2.914	1.113	0.5265	1301	7806	3.8
	TE3		5590	274.4	499.9	109.3	3.220	1.512	1.100	1301	15612	14.1
	TE5		5623	257.8	521.8	108.2	3.046	1.577	1.003	1301	23418	31.8
10×10	LE5	MITC9	5724	376.6	565.7	122.7	3.413	1.713	1.030	441	21168	66.3
20×20			5727	367.4	544.2	114.4	3.335	1.770	1.005	1681	80688	308.9
30×30			5727	364.2	540.4	112.7	3.386	1.770	1.002	3721	178608	841.5
40×40			5727	363.0	539.2	112.1	3.426	1.766	1.001	6561	314928	5742.2
50×50			5727	362.4	538.6	111.8	3.453	1.774	1.001	10201	489648	9789.1
10×10	TE1/LE5$^{\times 6}$	$p5$	5522	361.0	543.3	110.5	3.437	1.693	1.001	1301	11922	7.7
	TE1/LE5$^{\times 12}$		5603	360.9	545.7	111.7	3.418	1.739	1.001	1301	15366	11.7
	TE1/LE5$^{\times 20}$		5655	361.4	545.0	111.5	3.421	1.758	1.001	1301	19818	17.4
	TE3/LE5$^{\times 20}$		5694	360.9	538.8	111.2	3.425	1.766	1.001	1301	25908	25.7
	TE5/LE5$^{\times 20}$		5713	361.2	538.2	111.2	3.426	1.770	1.001	1301	31998	41.6
$50 \times 50 \times 5^{\ddagger}$		C3D20R*	5680	349.3	519.7	108.3	3.291	1.744	1.005	162231	486693	–
$50 \times 50 \times 10^{\ddagger}$			5680	358.6	528.2	109.1	3.403	1.757	1.001	316761	950283	–

‡ Mesh ($\alpha \times \beta \times z$); ∗ ABAQUS 20-node quadratic brick element with reduced integration.

Table 7.8: Deflection and stress evaluation on the three-layered spherical shells under local pressure, $R/h = 100$.

Mesh ($\alpha \times \beta$)	Theory (F_τ, F_s)	Element (N_i, N_j)	$\bar{w}$ (0,0,0)	$\bar{\sigma}_{\alpha\alpha}$ $(0,0,\frac{h}{6})$	$\bar{\sigma}_{\beta\beta}$ $(0,0,\frac{h}{2})$	$\bar{\sigma}_{\alpha\beta}$ $(\frac{a}{20},\frac{b}{10},\frac{-h}{2})$	$\bar{\sigma}_{\alpha z}$ $(\frac{a}{25},0,0)$	$\bar{\sigma}_{\beta z}$ $(0,\frac{2b}{25},0)$	$\bar{\sigma}_{zz}$ $(0,0,\frac{h}{2})$	Total shape functions	DOFs	CPU time $\bar{t}$
10×10	LE1	$p2$	185.6	91.53	104.1	52.05	2.145	1.941	2.088	341	4092	1.0
	LE2		186.2	91.61	104.4	52.39	2.154	1.939	1.277	341	7161	1.7
	LE3		186.2	91.52	104.5	52.49	2.712	1.948	1.295	341	10230	3.1
	LE4		186.2	91.52	104.5	52.49	2.712	1.948	1.304	341	13299	4.8
	LE5		186.2	91.52	104.5	52.49	2.706	1.948	1.304	341	16368	7.0
10×10	LE4	$p3$	189.8	111.7	111.0	49.26	2.328	2.386	0.9956	561	21879	11.0
		$p4$	190.1	106.5	109.8	49.17	2.535	2.403	0.9891	881	34359	24.2
		$p5$	190.2	106.0	109.5	49.26	2.493	2.391	0.9994	1301	50739	48.3
		$p6$	190.2	106.2	109.6	49.32	2.483	2.388	1.000	1821	71019	89.2
10×10	FSDT	$p6$	187.0	104.8	107.5	48.26	1.490	0.895	–	1821	9105	–
	TE1		187.2	104.9	107.5	48.26	1.490	0.896	4.022	1821	10926	5.6
	TE3		189.1	105.2	109.6	49.06	1.989	1.727	1.151	1821	21852	20.0
	TE5		189.6	105.5	109.5	49.16	2.062	2.169	0.9900	1821	32778	45.7
10×10	LE4	MITC9	190.0	116.2	114.4	54.20	2.502	2.284	1.123	441	17199	36.6
20×20			190.2	110.8	111.0	50.88	2.357	2.394	1.034	1681	65559	168.4
30×30			190.2	108.4	110.2	50.08	2.426	2.391	1.009	3721	145119	477.4
40×40			190.2	107.5	109.9	49.76	2.488	2.381	1.003	6561	255879	3377.8
50×50			190.2	107.0	109.8	49.61	2.533	2.399	1.001	10201	397839	5875.8
10×10	TE1/LE4$^{\times 6}$	$p6$	190.0	106.2	109.5	49.13	2.482	2.389	1.003	1821	15315	9.3
	TE1/LE4$^{\times 12}$		190.1	106.2	109.5	49.26	2.482	2.389	1.000	1821	19077	13.2
	TE3/LE4$^{\times 12}$		190.2	106.2	109.6	49.31	2.483	2.388	1.000	1821	28521	27.0
$50 \times 50 \times 5^{\ddagger}$		C3D20R*	192.4	106.7	110.5	49.48	2.463	2.394	0.9886	162231	486693	–
$100 \times 100 \times 5^{\ddagger}$			192.1	106.4	110.1	49.30	2.459	2.389	1.000	639431	1918293	–

‡ Mesh ($\alpha \times \beta \times z$); ∗ ABAQUS 20-node quadratic brick element with reduced integration.

Table 7.9: Deflection and stress evaluation on the three-layered spherical shells under local pressure, $R/h = 1000$.

Mesh $(\alpha \times \beta)$	Theory (F_τ, F_s)	Element (N_i, N_j)	$\bar{w}$ (0,0,0)	$\bar{\sigma}_{\alpha\alpha}$ $(0,0,\frac{h}{6})$	$\bar{\sigma}_{\beta\beta}$ $(0,0,\frac{h}{2})$	$\bar{\sigma}_{\alpha\beta}$ $(\frac{a}{20},\frac{b}{10},\frac{-h}{2})$	$\bar{\sigma}_{\alpha z}$ $(\frac{a}{25},0,0)$	$\bar{\sigma}_{\beta z}$ $(0,\frac{2b}{25},0)$	$\bar{\sigma}_{zz}$ $(0,0,\frac{h}{2})$	Total shape functions	DOFs	CPU time $\bar{t}$
10×10	LE1	$p2$	5.011	5.423	8.499	13.56	1.634	-0.9300	6.446	341	4092	1.0
	LE2		5.012	5.410	8.487	13.56	1.634	-0.9280	2.392	341	7161	1.6
	LE3		5.012	5.410	8.487	13.56	1.678	-0.9279	2.429	341	10230	3.1
	LE4		5.012	5.410	8.487	13.56	1.678	-0.9279	2.433	341	13299	4.7
10×10	LE3	$p3$	5.986	14.16	18.73	11.95	-0.0323	-0.1520	1.094	561	16830	7.3
		$p4$	6.160	15.68	19.01	13.31	-0.5414	0.2285	0.9472	881	26430	15.5
		$p5$	6.216	15.15	17.72	13.24	0.3871	0.5052	0.9819	1301	39030	29.9
		$p6$	6.219	15.12	17.72	13.25	0.3847	0.4946	1.036	1821	54630	72.3
		$p7$	6.219	15.10	17.77	13.25	0.3809	0.4829	1.000	2441	73230	93.1
		$p8$	6.219	15.09	17.76	13.25	0.3865	0.4852	1.000	3161	94830	142.1
10×10	FSDT	$p8$	6.217	15.09	17.77	13.25	0.2336	0.1746	–	3161	15805	–
	TE1		6.227	15.19	17.80	13.25	0.2339	0.1748	36.05	3161	18966	13.9
	TE3		6.218	15.09	17.77	13.25	0.3092	0.3449	0.7835	3161	37932	54.1
	TE5		6.218	15.09	17.77	13.25	0.3206	0.4396	1.353	3161	56898	124.5
10×10	LE3	MITC9	6.314	17.56	19.80	14.52	0.4110	0.4424	2.304	441	13230	23.7
20×20			6.227	15.86	18.16	13.65	0.3422	0.4920	1.509	1681	50430	128.2
30×30			6.220	15.43	17.92	13.46	0.3633	0.4861	1.082	3721	111630	380.5
40×40			6.219	15.28	17.85	13.38	0.3903	0.4813	1.018	6561	196830	741.1
50×50			6.219	15.21	17.82	13.34	0.4137	0.4915	1.006	10201	306030	1245.9
10×10	TE1/LE3$^{\times 6}$	$p8$	6.219	15.09	17.76	13.25	0.3865	0.4852	1.004	3161	24270	19.4
	TE1/LE3$^{\times 12}$		6.219	15.09	17.76	13.25	0.3865	0.4852	1.000	3161	28974	24.6

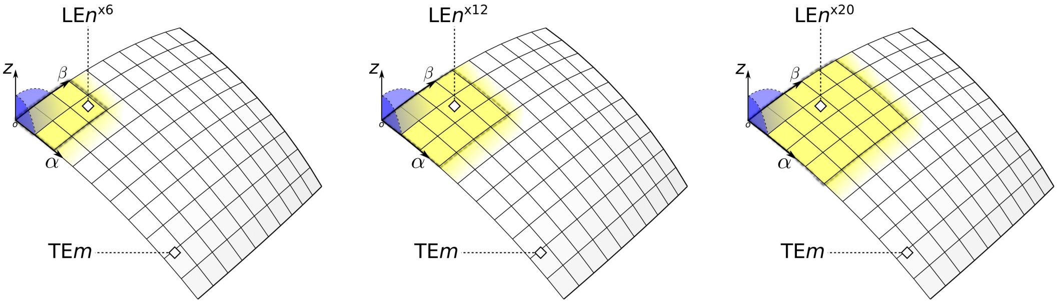

(a) A: TEm/LE$n^{\times 6}$ (b) B: TEm/LE$n^{\times 12}$ (c) C: TEm/LE$n^{\times 20}$

Figure 7.4: NDK FE models with variable TE/LE nodal capabilities for the three-layered spherical shells under local pressure.

and very thin shells need locally refined area consisting of only twelve p-version elements which correspond to NDK model B in Fig. 7.4b. It can also be concluded that the order of TE kinematics used in the non-critical region dramatically affects the solution accuracy of stresses in the local area especially in the FE model for the thick shell with $R/h = 10$.

From Tables 7.7, 7.8, and 7.9, it can be observed that the NDK approach helps to reduce the computational costs considerably without sacrificing accuracy. By comparing the through-the-thickness variation of transverse shear stresses obtained with different FE approaches shown in Figs. 7.5 and 7.6, it can be noticed that NDK models give results

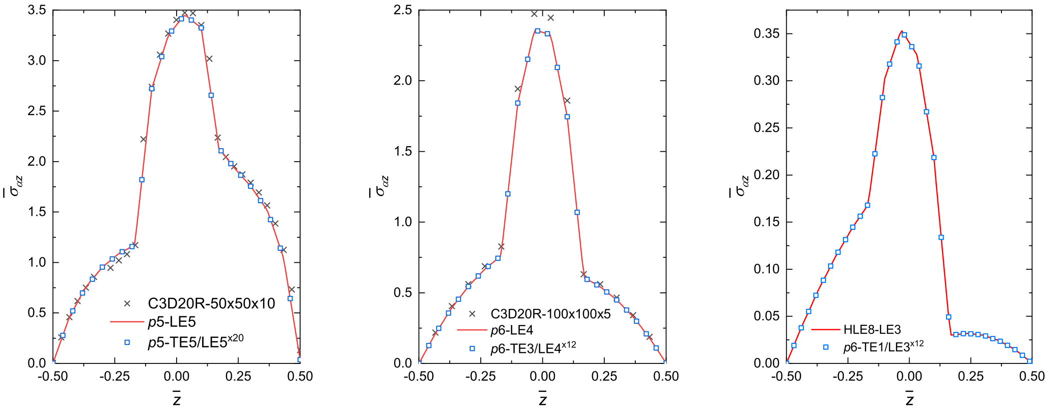

(a) $R/h = 10$ (b) $R/h = 100$ (c) $R/h = 1000$

Figure 7.5: Through-the-thickness distribution of $\bar{\sigma}_{\alpha z}$ through $(\frac{a}{25}, 0, \bar{z})$ in the three-layered spherical shells under local pressure.

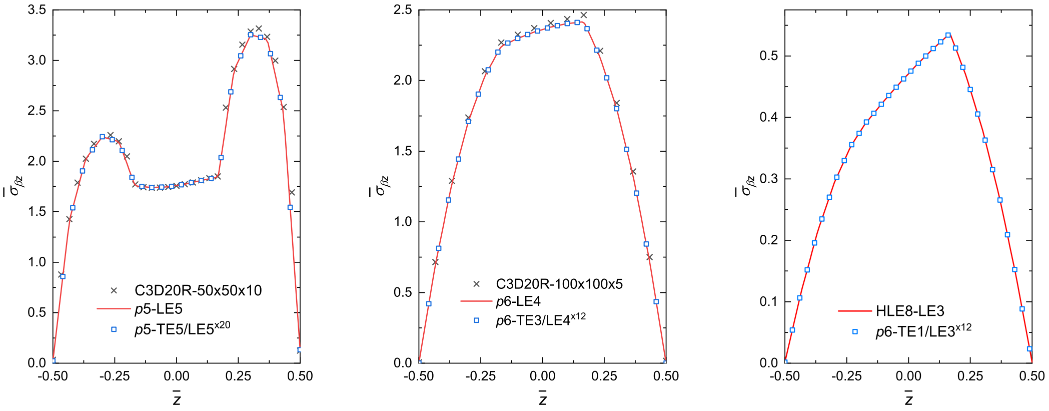

(a) $R/h = 10$ (b) $R/h = 100$ (c) $R/h = 1000$

Figure 7.6: Through-the-thickness distribution of $\bar{\sigma}_{\beta z}$ through $(0, \frac{2b}{25}, \bar{z})$ in the three-layered spherical shells under local pressure.

in excellent agreement with those obtained with uniform refinement.

Figs. **??**, **??**, and **??** demonstrate that the NDK models are able to reproduce 3D stress fields in consistency with those obtained through uniformly refined FE models. The data listed in Table 7.10 show that the NDK model is particularly efficient for the very thin shell ($R/h = 1000$) by giving a reduction of 69.4% regarding the DOFs and a decrease of 82.7% in solution time compared to the uniform kinematic refinements. For the thick shell ($R/h = 10$), the solution consumption can be saved by around 50%.

Fig.7.10 compares the computational efficiency of different FE models. The FE models considered are those who give the best solutions within their category as noted

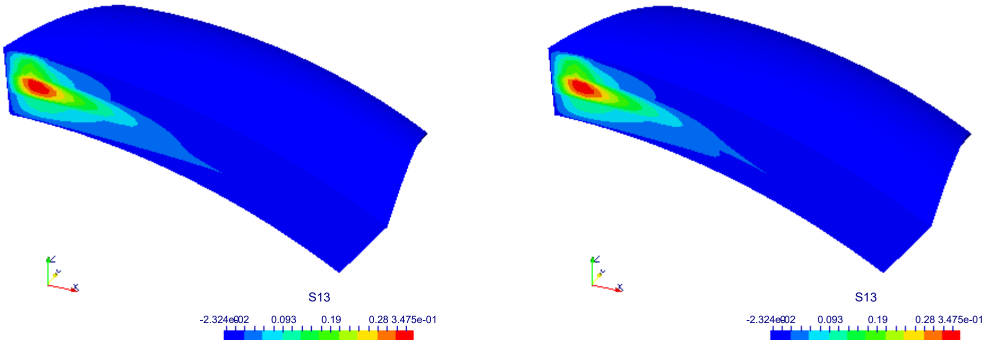
S13
-2.324e-02
0.093
0.19
0.28
3.475e-01
S13
-2.324e-02
0.093
0.19
0.28
3.475e-01

(a) $p5$-LE5, $h \times 1$ (b) $p5$-TE5/LE5$^{\times 20}$, $h \times 1$

Figure 7.7: $\sigma_{\alpha z}$ on the three-layered spherical shell ($R/h = 10$) under local pressure.

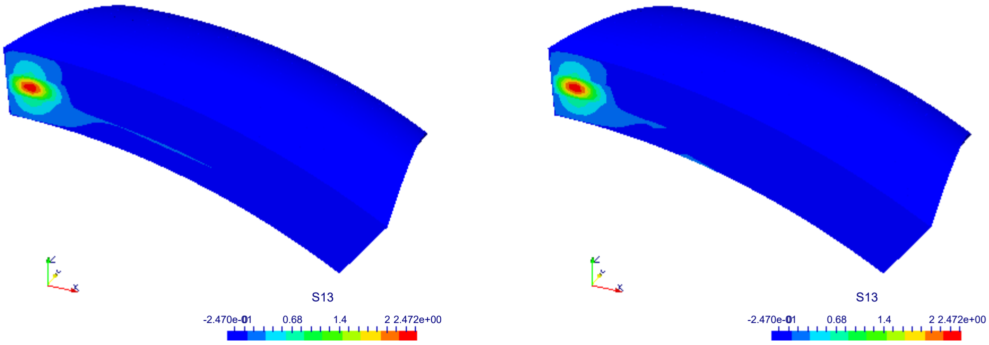
S13
-2.470e-01
0.68
1.4
2
2.472e+00
S13
-2.470e-01
0.68
1.4
2
2.472e+00

(a) $p6$-LE4, $h \times 10$ (b) $p6$-TE3/LE4$^{\times 12}$, $h \times 10$

Figure 7.8: $\sigma_{\alpha z}$ on the three-layered spherical shell ($R/h = 100$) under local pressure.

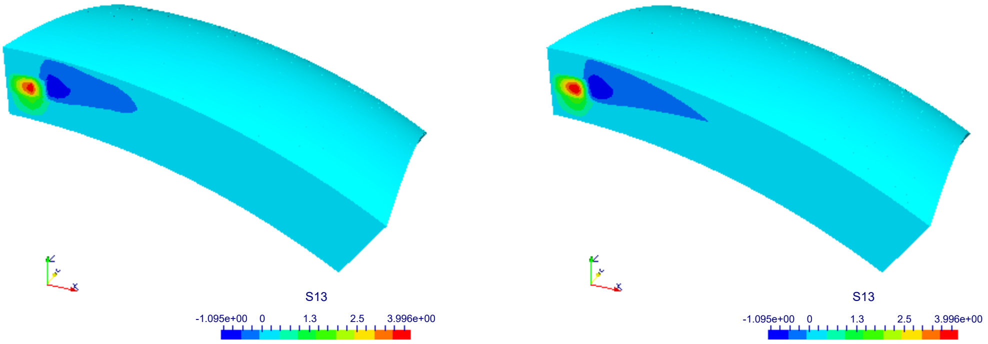
S13
-1.095e+00
0
1.3
2.5
3.996e+00
S13
-1.095e+00
0
1.3
2.5
3.996e+00

(a) $p8$-LE3, $h \times 100$ (b) $p8$-TE1/LE3$^{\times 12}$, $h \times 100$

Figure 7.9: $\sigma_{\alpha z}$ on the three-layered spherical shell ($R/h = 1000$) under local pressure.

Table 7.10: A comparison between uniformly refined models and NDK models for the three-layered spherical shells under local pressure regarding computational costs.

R/h	Element	Theory	DOFs	Reduction of DOFs	Relative CPU time $\bar{t}$	Reduction of CPU time
10	$p5$	LE5	62448	–	88.9	–
		TE5/LE5$^{\times 20}$	31998	48.8%	41.6	53.2%
100	$p6$	LE4	71019	–	89.2	–
		TE3/LE4$^{\times 12}$	28521	59.8%	27.0	69.7%
1000	$p8$	LE3	94830	–	142.1	–
		TE1/LE3$^{\times 12}$	28974	69.4%	24.6	82.7%

in Fig.7.10a. It is shown that the DOFs of the C3D20R models increase significantly when the shell gets thinner from $R/h = 10$ to $R/h = 100$. The refined shell elements used can give comparable accuracy with a much lower number of DOFs. These required DOFs in the refined shell FE models are not quite sensitive to the radius-to-thickness ratio. In comparison with MITC9 elements, the hierarchical elements can also overcome the locking phenomena, and the computational costs are much lower. The use of NDK leads to significantly improved numerical efficiency with reference to the uniformly refined shell FE models. The CPU time consumptions of different FE models are compared in Fig.7.10b. For the MITC-LE models, a descending trend in solution time with the increase of the radius-to-thickness ratio can be observed. Time consumption of p-LE models shows a slightly increasing trend. The efficiency of p-NDK FE models is evident

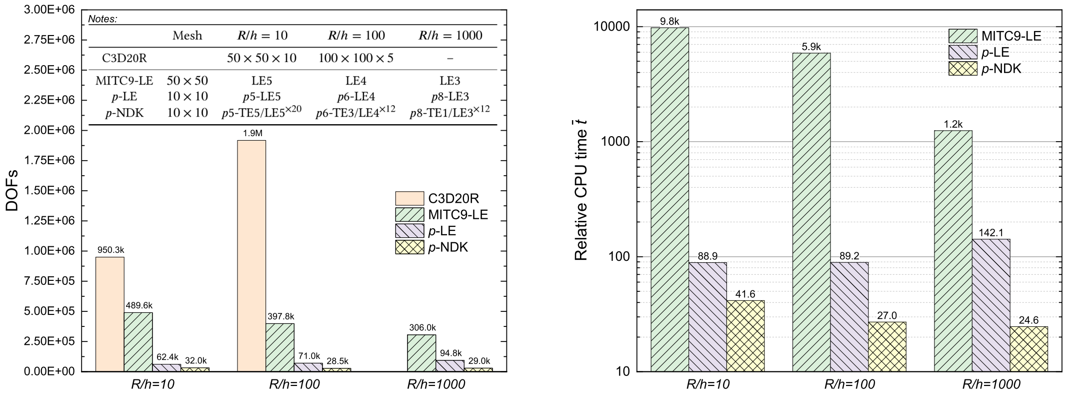

Notes:

	Mesh	$R/h = 10$	$R/h = 100$	$R/h = 1000$
C3D20R		$50 \times 50 \times 10$	$100 \times 100 \times 5$	–
MITC9-LE p-LE p-NDK	50×50 10×10 10×10	LE5 $p5$-LE5 $p5$-TE5/LE5$^{\times 20}$	LE4 $p6$-LE4 $p6$-TE3/LE4$^{\times 12}$	LE3 $p8$-LE3 $p8$-TE1/LE3$^{\times 12}$

(a) Total number of degrees of freedom (DOFs)   (b) Relative CPU time consumption $\bar{t}$

Figure 7.10: Numerical efficiency of various FE models in the analysis of the three-layered spherical shells under local pressure.

regarding the time reduction.

7.4 Conclusions

In the CUF framework, the proposed shll FE models can accommodate two-level mathematical refinements, namely the kinematic refinement and the shape function enhancement. The NDK method allows the definition of variable ESL/LE nodal kinematic assumptions in the critical region. The adaptable refinement approach, based on the *p*-refinement and NDK, can help to build FE models for the analysis of laminated shells with optimal efficiency. The following conclusions can be drawn:

- The two-level mathematical refinements based on CUF empower one to fully utilize the capabilities of given 2D mesh grid to obtain accurate structural response with 3D accuracy;
- Through Node-Dependent Kinematics (NDK) technique, a local refinement on the chosen FE shape functions can be implemented in an adaptable way, and the computational costs can be further reduced while keeping the accuracy;
- The locally refined region and the kinematics in the non-critical zone are both crucial to the success of the NDK FE modeling.

It should be pointed out that, in engineering analyses, meshing takes up the majority of the total time consumption (e.g., 80%). The adaptable refinement approach presented can help engineers to reduce the simulation time in both pre-processing and solution phases. Besides, this approach enables engineers to re-use the mesh files which can further reduce the time consumption in subsequent analysis iterations. In future work, adaptive routines can be developed for engineering applications.

Part III

Multi-field Modeling

Chapter 8

Thermo-mechanical plate and shell FE models with various kinematics

In this chapter, in steady-state thermo-mechanical analyses with the variable kinematic plate and shell FE models, various thickness functions are tested, including Taylor series, sine and cosine functions, exponential functions, and miscellaneous expansions. These kinematic models are implemented in ESL approach, and the obtained results are compared against LW models with Lagrange expansions (LE). The used thermo-elastic model in the present chapter is a particular case of the multi-filed models presented in Chapter 4, and the obtained temperature field by solving the thermal conduction equation is substituted into the calculation of mechanical response in a subsequent step. The numerical examples include cross-ply plates and cylindrical shells under bi-sinusoidal distributed temperature on external surfaces. Thermal stresses under assumed and calculated temperature fields are compared. In the current work, it is assumed that the thermal conductivity coefficients do not change with temperature. The FE results are also compared against Navier-type analytical solutions obtained through LW models with LE4 (fourth-order Lagrange polynomials). In the current chapter, MITC9 element is used to contrast the possible locking phenomena.

8.1 Various kinematic assumptions

As introduced in Chapter 2, various basis functions can be used in the kinematic assumptions and implemented in the CUF framework. A series of acronyms are introduced to indicate various kinematics used, as listed in Table 8.1. The initial letter "E" indicates the ESL approach. For example, "ES2C2" and "ET1Exp2Z", respectively, refer to the following expansions:

$$\begin{aligned}\boldsymbol{u}(x,y,z) =& \boldsymbol{u}_0(x,y) + \sin(\frac{\pi z}{h})\boldsymbol{u}_1(x,y) + \cos(\frac{\pi z}{h})\boldsymbol{u}_2(x,y) + \sin(\frac{2\pi z}{h})\boldsymbol{u}_3(x,y) \\ &+ \cos(\frac{2\pi z}{h})\boldsymbol{u}_4(x,y)\end{aligned} \tag{8.1}$$

$$\boldsymbol{u}(x,y,z) = \boldsymbol{u}_0(x,y) + z\boldsymbol{u}_1(x,y) + e^{\frac{z}{h}}\boldsymbol{u}_2(x,y) + e^{\frac{2z}{h}}\boldsymbol{u}_3(x,y) + (-1)^k\zeta_k\boldsymbol{u}_Z \tag{8.2}$$

Table 8.1: Acronyms of various ESL kinematic models.

	z^0	$z^1 \rightarrow z^N$	$\sin\left(\frac{z\pi}{h}\right) \rightarrow \sin\left(\frac{nz\pi}{h}\right)$	$\cos\left(\frac{z\pi}{h}\right) \rightarrow \cos\left(\frac{nz\pi}{h}\right)$	$e^{(z/h)} \rightarrow e^{(nz/h)}$	$(-1)^k\zeta_k$
ET*n*	√	√	×	×	×	×
ET*n*Z	√	√	×	×	×	√
ES*n*	√	×	√	×	×	×
ES*n*Z	√	×	√	×	×	√
EC*n*	√	×	×	√	×	×
EC*n*Z	√	×	×	√	×	√
ES*n*C*n*	√	×	√	√	×	×
ES*n*C*n*Z	√	×	√	√	×	√
ET*n*S*n*C*n*	√	√	√	√	×	×
ET*n*S*n*C*n*Z	√	√	√	√	×	√
EEXP*n*	√	×	×	×	√	×
EEXP*n*Z	√	×	×	×	√	√
ET*n*Exp*n*	√	√	×	×	√	×
ET*n*Exp*n*Z	√	√	×	×	√	√

LE*n* indicates an LW model adopting *n*th order Lagrange polynomials. A subscript *a* denotes the adoption of assumed linear temperature profiles through the thickness, and *c* indicates that the through-the-thickness distribution is calculated by solving Fourier's equation.

8.2 Three-layered square plates under thermal load

Bhaskar, Varadan, and Ali [26] proposed analytical solutions for a set of simply supported cross-ply square composite plates under distributed temperature on the top and bottom surfaces, and the temperature profile through the thickness is assumed to be linear. In this section, this benchmark case is studied through refined plate elements, and an exact temperature field is considered. The composite square plates consist of three layers with lamination sequence (0°/90°/0°), which have equal thickness $h/3$. Length-to-thickness ratios $a/h = 2$, 10, and 100 are studied. The elastic constants and heat conduction coefficients of the lamina are listed in 8.2, wherein L and T indicate the direction parallel and perpendicular to the fiber axis, respectively. The three-dimensional temperature field follows:

$$\theta(x,y,z) = \theta_A(z) \cdot \sin(\frac{\pi x}{a})\sin(\frac{\pi y}{b}) \tag{8.3}$$

The temperature boundary conditions are $\hat{\theta}_A(\frac{h}{2}) = 1\text{K}$ and $\hat{\theta}_A(-\frac{h}{2}) = -1\text{K}$. In the work of Bhaskar, Varadan, and Ali [26], it is assumed that the temperature varies linearly through the thickness. The obtained deflections and stresses are non-dimensionalized through:

$$\bar{u}_z = \frac{w}{h\alpha_L\theta_A S^2}, \quad \bar{\sigma}_{ii} = \frac{\sigma_{ii}}{E_T\alpha_L\theta_A}, \quad \bar{\sigma}_{ij} = \frac{\sigma_{ij}}{E_T\alpha_L\theta_A}, \quad S = a/h \tag{8.4}$$

where $i, j = x, y, z$.

Table 8.2: Material properties of the lamina used on the three-layered square plates.

E_L/E_T	G_{LT}/E_T	G_{LT}/E_T	ν_{LT}, ν_{TT}	α_T/α_L	K_L/K_T
25	0.5	0.2	0.25	1125	36.42/0.96

A mesh convergence study is first conducted on the thin plate with $a/h = 100$ by using LE4 kinematics, and the assumed linear temperature profile is used. A quarter of the plate is modeled with the help of symmetric boundary conditions. The results shown in Fig. 8.3 show that 10×10 MITC9 elements can give satisfactory numerical accuracy.

Table 8.3: Mesh convergence study with LE4 on the three-layered plate with $a/h = 100$ subjected to assumed linear temperature profiles.

a/h	Mesh	$\bar{w}(\frac{a}{2}, \frac{b}{2}, \frac{h}{2})$	$\bar{\sigma}_{xx}(\frac{a}{2}, \frac{b}{2}, \frac{h}{2})$	$\bar{\sigma}_{xz}(0, \frac{b}{2}, \frac{h}{6})$
100	4×4	10.26	981.7	7.166
	6×6	10.26	972.6	7.115
	8×8	10.26	969.5	7.097
	10×10	10.26	968.0	7.088
	Bhaskar et al. [26]	10.26	965.4	7.073

With the refinement of kinematics, the numerical convergence is achieved gradually, as demonstrated in Fig. 8.1, in which the stresses are multiplied by ten times when necessary (denoted by "*10") for the convenience of illustration. The results show that LE4 is capable of capturing satisfactory distribution of transverse shear stresses through the thickness.

The assumed linear and calculated temperature profiles through LE4 kinematics are compared in Fig. 8.2, from which it can be observed that in the thick plates the variation of calculated temperature is quite different from the assumed liner profile.

The displacement and stresses obtained with LW kinematics are presented in Table 8.4, where N_{exp} indicates the number of total expansion terms. Through-the-thickness variations of stresses are shown in Fig.8.3. One can notice that the adopted refined plate FE models achieved great agreement with the analytical solutions. Meanwhile, on the thick plate, thermal-mechanical response caused by the calculated exact temperature

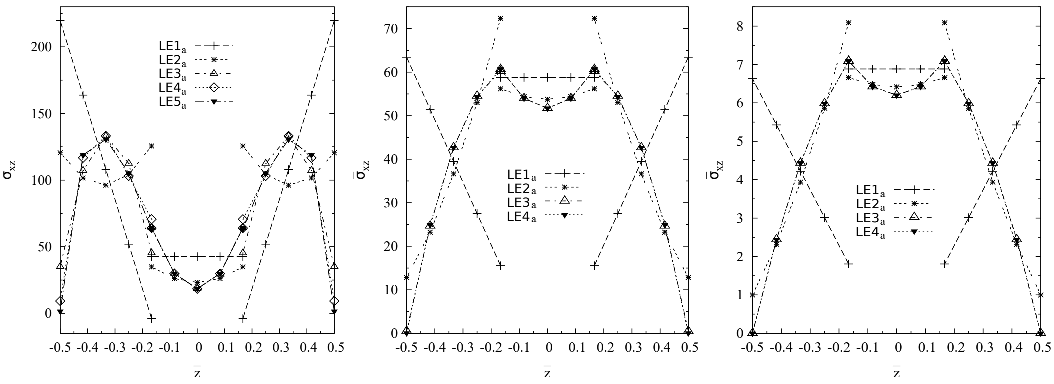

(a) $a/h = 2$ (b) $a/h = 10$ (c) $a/h = 100$

Figure 8.1: $\bar{\sigma}_{xz}$ through the thickness of the composite plates under assumed linear temperature profile, obtained with LW models.

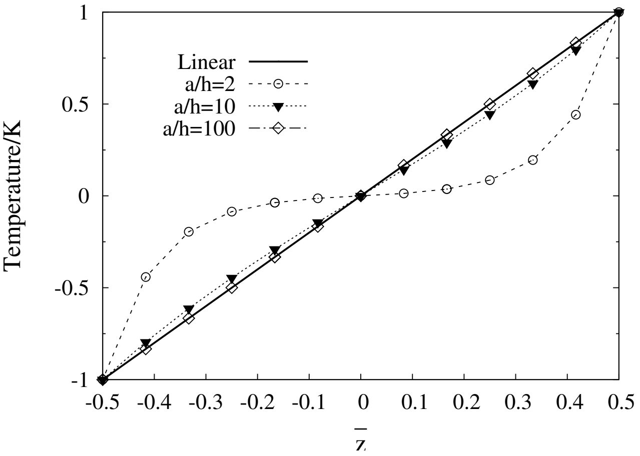

Figure 8.2: Through-the-thickness temperature profiles $\bar{\theta}_A$ for the three-layered composite plates with various thickness ratios (a/h).

field is very different from that due to the assumed linear distribution. On the thin layered plate with $a/h = 100$, the displacement and stresses under these two sets of temperature fields show almost no difference.

Various ESL models were then applied to the thermal-mechanical analyses with calculated temperature fields. The results obtained with ETn are reported in Table 8.5. Since FSDT is not a complete linear case, its number of expansions is denoted as "2*". The obtained through-the-thickness variations of $\bar{\sigma}_{xz}$ are shown in Fig. 8.4. Nine expansions are essential for the thick plate, while six terms are sufficient for the moderate thick and thin plates. More often than not, FSDT failed to provide accurate displacement and stress evaluations. The use of Murakami zig-zag function improves the distribution of transverse shear stresses through the thickness. Compared with LE4, the presented

Table 8.4: Deflections and stresses obtained with LW models for the three-layer square plates with various a/h under thermal fields.

a/h	Model	Assumed temperature			Calculated temperature			N_{exp}
		$^{\S}\bar{w}$	$^{\dagger}\bar{\sigma}_{xx}$	$^{\ddagger}\bar{\sigma}_{xz}$	$^{\S}\bar{w}$	$^{\dagger}\bar{\sigma}_{xx}$	$^{\ddagger}\bar{\sigma}_{xz}$	
2	LE1	89.25	641.8	42.56	44.17	34.58	31.70	16
	LE4	96.78	1393	63.95	48.85	487.9	30.01	13
	LE4(analytical)	96.784	1389.6	63.823	48.908	488.56	30.009	13
	Bhaskar et al. [26]	96.79	1390	63.92	–	–	–	–
10	LE1	17.63	906.7	58.78	16.67	811.9	56.35	4
	LE4	17.39	1029	60.66	16.40	950.5	57.19	13
	LE4(analytical)	17.392	1026.3	60.540	16.395	947.96	57.070	13
	Bhaskar et al. [26]	17.39	1026	60.54	–	–	–	–
100	LE1	10.91	895.7	6.883	10.91	894.6	6.880	4
	LE4	10.26	968.0	7.088	10.25	967.2	7.084	13
	LE4(analytical)	10.260	965.37	7.0732	10.253	964.55	7.0688	13
	Bhaskar et al. [26]	10.26	965.4	7.073	–	–	–	–

Variables are evaluated at: $^{\S}(\frac{a}{2}, \frac{b}{2}, \frac{h}{2})$; $^{\dagger}(\frac{a}{2}, \frac{b}{2}, \frac{h}{2})$; $^{\ddagger}(0, \frac{b}{2}, \frac{h}{6})$.

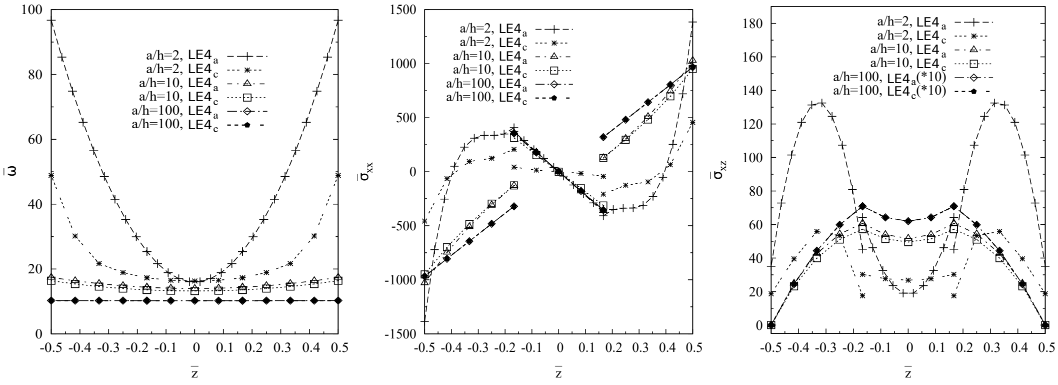

(a) $\bar{w}$ (b) $\bar{\sigma}_{xx}$ (c) $\bar{\sigma}_{xz}$

Figure 8.3: Through-the-thickness variation of deflections and stresses on the three-layered plates with various a/h ratios under thermal load, obtained with LW models.

ESL kinematics are more efficient when used on moderate thick and thin plates. The Murakami zig-zag function will be used in the following discussed ESL models.

Table 8.6 and Fig. 8.5 summarize the results obtained through exponential expansions EExp$n$Z and ET1Exp$n$Z in ESL approach. One can find that such kinematic models are less accurate compared with the ETnZ theories, even if the additional first-order

Table 8.5: Deflections and stresses on three-layer square plates with various a/h under calculated temperature profiles, obtained with ESL models ETn and ETnZ.

a/h	Model	$\bar{w}(\frac{a}{2}, \frac{b}{2}, \frac{h}{2})$	$\bar{\sigma}_{xx}(\frac{a}{2}, \frac{b}{2}, \frac{h}{2})$	$\bar{\sigma}_{xz}(0, \frac{b}{2}, \frac{h}{6})$	N_{exp}
2	FSDT$_c$	20.36	-281.6	22.10	2*
	ET4$_c$	49.30	411.4	23.97	5
	ET6$_c$	48.45	477.7	23.71	7
	ET7$_c$	48.87	493.1	22.11	8
	ET3Z$_c$	50.09	405.1	23.43	5
	ET5Z$_c$	48.75	444.0	31.34	7
	ET7Z$_c$	48.79	489.6	31.01	9
	LE4$_c$(analytical)	48.908	488.56	30.009	13
10	FSDT$_c$	17.26	962.7	26.41	2*
	ET3$_c$	15.95	919.4	34.62	4
	ET4$_c$	15.93	944.0	34.55	5
	ET3Z$_c$	16.41	924.8	50.44	5
	ET4Z$_c$	16.38	948.5	50.02	6
	LE4$_c$(analytical)	16.395	947.96	57.070	13
100	FSDT$_c$	15.05	1193	3.071	2*
	ET3$_c$	10.25	966.8	4.149	4
	ET4$_c$	10.25	967.1	4.149	5
	ET2Z$_c$	10.25	966.3	6.656	4
	ET3Z$_c$	10.25	966.9	6.260	5
	ET4Z$_c$	10.25	967.2	6.260	6
	LE4$_c$(analytical)	10.253	964.55	7.0688	13

term improves the accuracy to some extent.

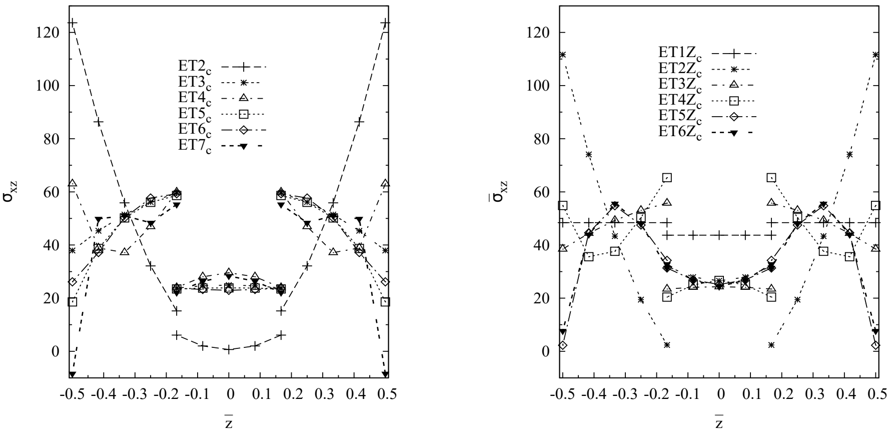

(a) ETn, $a/h = 2$ (b) ETnZ, $a/h = 2$

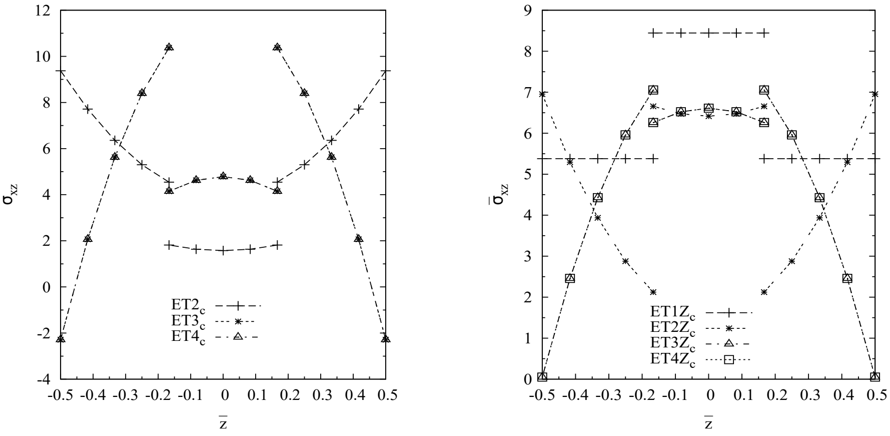

(c) ETn, $a/h = 100$ (d) ETnZ, $a/h = 100$

Figure 8.4: Variation of $\bar{\sigma}_{xz}$ through the thickness of the three-layered plates under calculated temperature profiles, obtained with ESL models ETn and ETnZ.

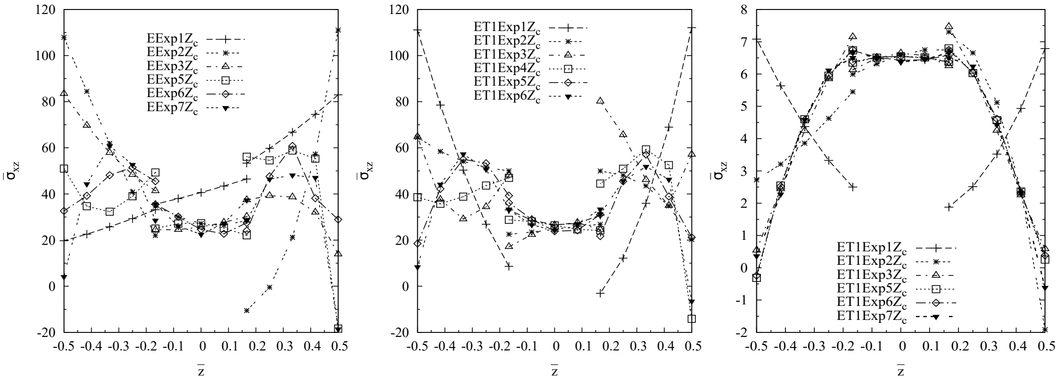

(a) EExp$n$Z,$a/h = 2$ (b) ET1Exp$n$Z,$a/h = 2$ (c) ET1Exp$n$Z,$a/h = 100$

Figure 8.5: $\bar{\sigma}_{xz}$ through the thickness of the three-layered plates under calculated temperature profiles, obtained with EExp$n$Z and ET1Exp$n$Z.

Table 8.6: Deflections and stresses on the three-layered plates under calculated temperature profiles, obtained with ESL models EExp$n$Z and ET1Exp$n$Z.

a/h	Model	$\bar{w}(\frac{a}{2},\frac{b}{2},\frac{h}{2})$	$\bar{\sigma}_{xx}(\frac{a}{2},\frac{b}{2},\frac{h}{2})$	$\bar{\sigma}_{xz}(0,\frac{b}{2},\frac{h}{6})$	N_{exp}
2	EExp3Z$_c$	48.66	429.7	30.22	5
	EExp5Z$_c$	48.50	459.0	22.06	7
	EExp7Z$_c$	48.77	472.6	37.32	9
	ET1Exp3Z$_c$	47.95	454.4	24.52	6
	ET1Exp5Z$_c$	48.74	521.3	31.09	8
	ET1Exp6Z$_c$	48.74	482.1	33.37	9
	LE4$_c$(analytical)	48.908	488.56	30.009	13
10	EExp3Z$_c$	16.38	905.7	58.85	5
	EExp5Z$_c$	16.38	941.2	48.90	7
	EExp7Z$_c$	16.39	948.6	52.27	9
	ET1Exp3Z$_c$	16.38	960.8	50.21	6
	ET1Exp5Z$_c$	16.39	951.5	51.76	8
	LE4$_c$(analytical)	16.395	947.96	57.070	13
100	EExp3Z$_c$	9.705	855.8	17.54	5
	EExp5Z$_c$	10.25	962.4	5.074	7
	EExp7Z$_c$	10.25	966.6	6.515	9
	ET1Exp3Z$_c$	10.25	970.3	6.254	6
	ET1Exp5Z$_c$	10.25	967.3	6.380	8
	LE4$_c$(analytical)	10.253	964.55	7.0688	13

Table 8.7 and Figs. 8.6 present the results given by ESL models with trigonometric functions. For the thick plate with $a/h = 2$, both ES5C5Z and ET1S3C3Z are capable of giving satisfactory estimations, while the latter is preferable due to a fewer number of expansion terms are used. For the moderate thick ($a/h = 10$) and thin ($a/h = 100$) plates, it is challenging for ESnCnZ kinematics to give satisfactory approximation of stress distribution through the thickness, and the additional first-order Taylor term helps to improve the convergence rate and numerical stability significantly, as shown in Fig. 8.6.

The discussed kinematics above are compared in Fig. 8.7. It can be observed that ETnZ and ET1SnCnZ perform well. Thus, they are used in the thermo-mechanical modeling of a set of laminated cylindrical shells.

Table 8.7: Deflections and stresses on the three-layer plates calculated temperature profiles, obtained with ESL models ES*n*C*n*Z and ET1S*n*C*n*Z.

a/h	Model	$\bar{w}(\frac{a}{2},\frac{b}{2},\frac{h}{2})$	$\bar{\sigma}_{xx}(\frac{a}{2},\frac{b}{2},\frac{h}{2})$	$\bar{\sigma}_{xz}(0,\frac{b}{2},\frac{h}{6})$	N_{exp}
2	ES1C1Z$_c$	44.69	-11.88	31.46	4
	ES3C3Z$_c$	48.62	445.5	40.80	8
	ES5C5Z$_c$	48.83	494.2	30.70	12
	ET1S1C1Z$_c$	48.66	375.1	24.44	5
	ET1S3C3Z$_c$	48.84	467.8	30.67	9
	ET1S4C4Z$_c$	48.83	488.6	30.90	11
	LE4$_c$(analytical)	48.908	488.56	30.009	13
10	ES1C1Z$_c$	12.94	430.5	58.02	4
	ES3C3Z$_c$	16.36	943.0	57.05	8
	ES5C5Z$_c$	16.39	950.3	55.54	12
	ET1S1C1Z$_c$	16.57	860.5	51.26	5
	ET1S3C3Z$_c$	16.39	946.6	53.62	9
	ET1S5C5Z$_c$	16.39	950.3	55.57	13
	LE4$_c$(analytical)	16.395	947.96	57.070	13
100	ES1C1Z$_c$	0.4448	-349.0	8.452	4
	ES3C3Z$_c$	9.241	838.0	35.87	8
	ES5C5Z$_c$	10.25	966.9	6.981	12
	ET1S1C1Z$_c$	10.34	890.0	6.354	5
	ET1S3C3Z$_c$	10.25	964.5	6.611	9
	ET1S5C5Z$_c$	10.25	967.1	6.872	13
	LE4$_c$(analytical)	10.253	964.55	7.0688	13

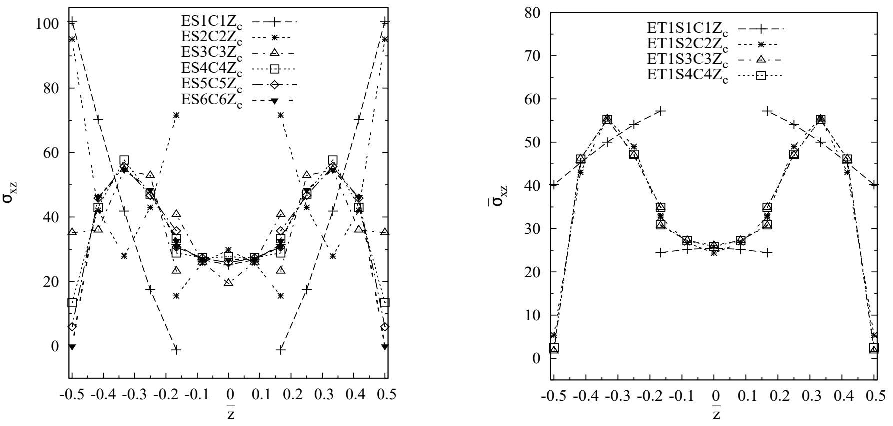

(a) ESnCnZ, $a/h = 2$ (b) ET1SnCnZ, $a/h = 2$

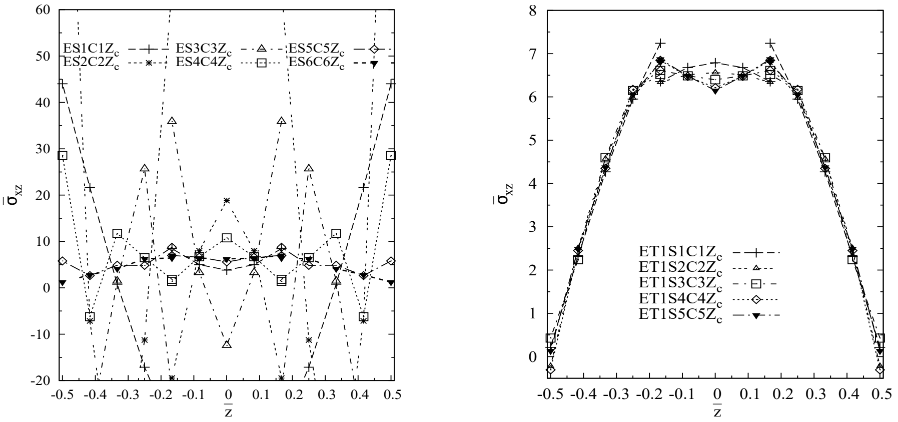

(c) ESnCnZ, $a/h = 100$ (d) ET1SnCnZ, $a/h = 100$

Figure 8.6: $\bar{\sigma}_{xz}$ through the thickness of the three-layered plates under calculated temperature profiles, obtained with ESnCnZ and ET1SnCnZ.

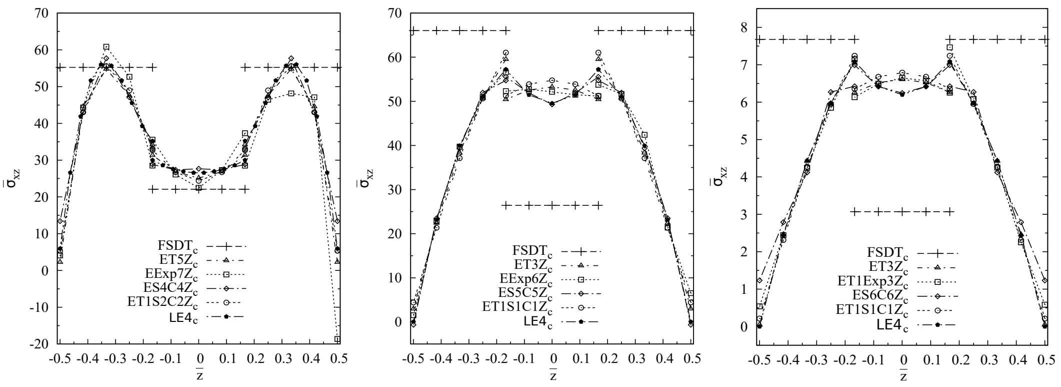

(a) $a/h = 2$ (b) $a/h = 10$ (c) $a/h = 100$

Figure 8.7: $\bar{\sigma}_{xz}$ through the thickness of the three-layered plates under calculated temperature profiles, obtained by ESL models with various thickness functions.

8.3 Two-layered cylindrical shells under thermal load

The thermal response of two-layered cylindrical shells with lamination (0°/90°) (from bottom to top) is investigated. The dimensions are: $a = b = 0.1$m, $R_\alpha = 0.1$m, $R_\beta = \infty$. Radius-to-thickness ratios $R_\alpha/h = 2,10$ and 500 are considered. Tables 8.8 presents the mechanical and thermal properties of the lamina, which are assumed with reference to the work of Jacquemin and Vautrin [113]. The thermal conduction coefficients (κ_{11}, κ_{22}, and κ_{33}) are taken from the work of Hicks [102].

Table 8.8: Mechanical properties of T300/5208 composite lamina.

E_1 (GPa)	E_2, E_3 (GPa)	G_{12}, G_{13} (GPa)	G_{23} (GPa)	ν_{12}, ν_{13}	ν_{23}	α_{11} (10^{-6}/K)	α_{22}, α_{33} (10^{-6}/K)	κ_{11} (W/mK)	κ_{22}, κ_{33} (W/mK)
181	10.3	7.17	2.39	0.28	0.43	0.02	22.5	4.6	0.7

The distribution of the temperature field follows:

$$\theta(\alpha, \beta, z) = \theta_A(z) \cdot \sin(\frac{\pi\alpha}{a}) \sin(\frac{\pi\beta}{b}) \tag{8.5}$$

The temperature boundary conditions are $\theta_A(-\frac{h}{2}) = 0$K and $\theta_A(\frac{h}{2}) = 50$K.

The mesh convergence study is conducted through LE4 models on the thin shell with $R_\alpha/h = 500$ under assumed linear temperature distribution through the thickness. By taking advantage of the symmetric characteristics, a quarter of the structure is modeled. The results summarized in Table 8.9 show that 10×10 MITC9 shell elements can ensure the convergence of the FE solutions.

Table 8.9: Mesh convergence study with LE4 on the cylindrical shells with $R_\alpha/h = 500$ under assumed temperature filed.

R_α/h	Mesh	$^\S w(10^{-3}\text{mm})$ $(\frac{a}{2}, \frac{b}{2}, \frac{h}{2})$	$^\dagger\sigma_{\alpha\alpha}$(KPa) $(\frac{a}{2}, \frac{b}{2}, \frac{h}{2})$	$^\ddagger\sigma_{\alpha z}$(KPa) $(a, \frac{b}{2}, \frac{h}{4})$
500	4×4	8.228	-11014	15.10
	6×6	8.226	-11021	15.12
	8×8	8.225	-11023	15.11
	10×10	8.225	-11024	15.10
	LE4$_a$(analytical)	8.2246	-11025	15.070

The calculated thorough-the-thickness profiles of temperature on the cylindrical shells are reported in 8.8. It can be observed that on the shell with $a/h = 500$, the exact temperature almost coincides with the assumed linear one. However, on the thick shell with $a/h = 2$, the calculated profile is far from being linear.

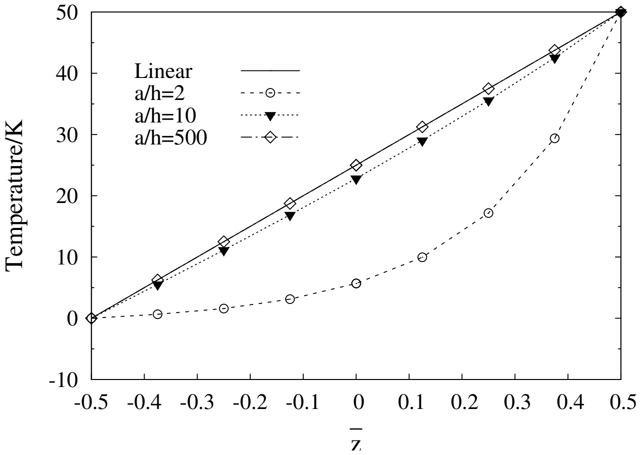

Figure 8.8: Temperature profiles $\theta_A(z)$ for composite cylindrical shells with various thickness ratios (R_α/h).

Table 8.10: Deflection and stresses obtained with LW models for the two-layer cylindrical shells under thermal fields.

R_α/h	Model	Assumed profiles			Calculated profiles			N_{exp}
		$^\S w$ (10^{-3}mm)	$^\dagger\sigma_{\alpha\alpha}$ (KPa)	$^\ddagger\sigma_{\alpha z}$ (KPa)	$^\S w$ (10^{-3}mm)	$^\dagger\sigma_{\alpha\alpha}$ (KPa)	$^\ddagger\sigma_{\alpha z}$ (KPa)	
2	LE1	25.28	-6097	595.8	14.78	-11474	579.4	3
	LE4	27.39	-4271	261.1	16.39	-7074	538.3	9
	LE4(analytical)	27.393	-4287.8	260.56	16.403	-7073.4	541.76	9
10	LE1	20.51	-10607	587.2	19.98	-11003	577.5	3
	LE4	19.11	-8849	554.4	18.57	-8952	544.6	9
	LE4(analytical)	19.110	-8854.6	553.23	18.570	-8957.6	543.49	9
500	LE1	8.325	-13271	15.53	8.325	-13271	15.53	3
	LE4	8.225	-11024	15.10	8.225	-11024	15.10	9
	LE4(analytical)	8.2246	-11025	15.070	8.2244	-11025	15.069	9

Variables are evaluated at: $^\S(\frac{a}{2}, \frac{b}{2}, \frac{h}{2})$; $^\dagger(\frac{a}{2}, \frac{b}{2}, \frac{h}{2})$; $^\ddagger(a, \frac{b}{2}, \frac{h}{4})$.

The thermal-mechanical response of the cylindrical shells obtained with variable kinematic LW models is summarized in Table 8.10. The through-the-thickness variation of deflection and stresses are reported in Fig. 8.9, in which the stresses are multiplied by 50 times in the plots when necessary and denoted by "∗50" for the convenience of comparison. It can be observed that the displacements and stresses obtained are in great agreement with the Naiver analytical solutions. By comparing the results given by the assumed and calculated temperature fields, it can be noticed that the thicker the shell

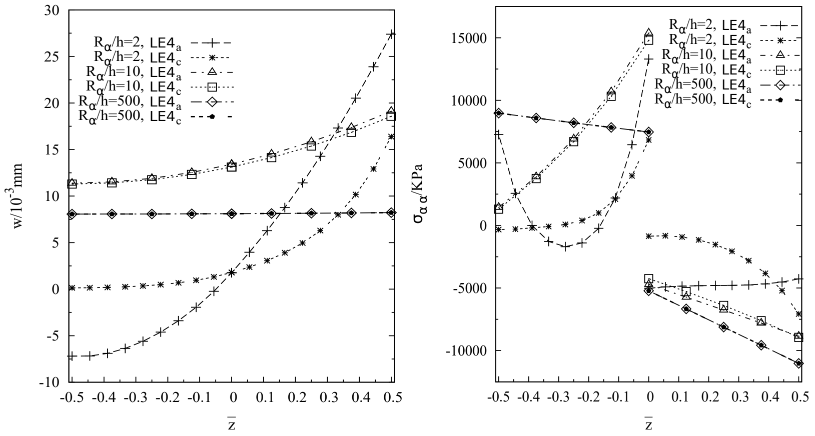

(a) w (b) $\sigma_{\alpha\alpha}$

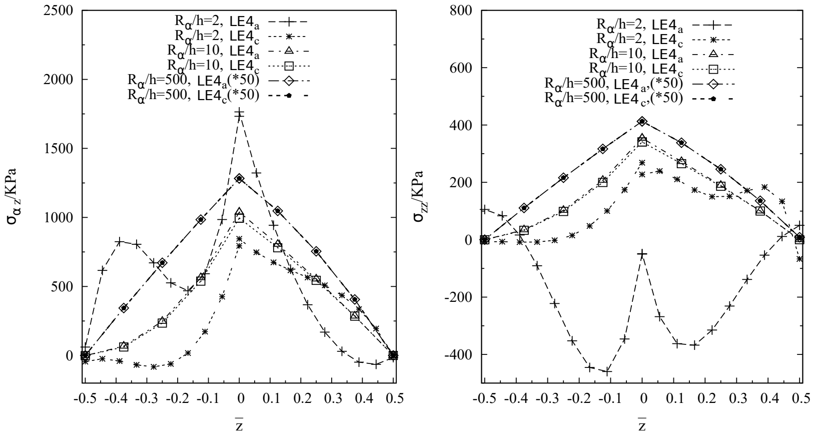

(c) $\sigma_{\alpha z}$ (d) σ_{zz}

Figure 8.9: Distribution of deflections and stresses through the thickness of the two-layered cylindrical shells under assumed and calculated temperature fields obtained with LW kinematics.

is, the more evident the difference will be. Besides, LE4 kinematics is sufficient to give satisfactory accuracy.

Various ESL models were then used in the thermal analysis of cylindrical shells under calculated temperature fields. From the results summarized in Tables 8.11 and 8.12, one can notice that compared to LW kinematics, when a sufficient number of expansions are used, the ESL models result in estimations quit accurate on the moderate thick ($R_\alpha/h = 10$) and thin ($R_\alpha/h = 500$) shells, yet less accurate on the thick shell. The variations of $\sigma_{\alpha z}$ through the thickness obtained with different ESL kinematics are shown in Figs. 8.10, 8.11, 8.12, and 8.13. From which, the convergence of the solution with the increase of the expansion number can be observed. Notably, the convergence rate of ES*n*C*n*Z is much improved with the help of an additional first-order term.

Table 8.11: Deflections and stresses on the two-layer cylindrical shells under calculated temperature fields, obtained with ESL models EExp$n$Z and ESnCnZ.

R_α/h	Model	$w(\frac{a}{2},\frac{b}{2},\frac{h}{2})$ (10^{-3}mm)	$\sigma_{\alpha\alpha}(\frac{a}{2},\frac{b}{2},\frac{h}{2})$ (KPa)	$\sigma_{\alpha z}(a,\frac{b}{2},\frac{h}{4})$ (KPa)	N_{exp}
2	FSDT$_c$	5.239	-14985	162.8	2*
	EExp5Z$_c$	16.38	-6999	586.4	7
	EExp7Z$_c$	16.39	-7064	531.8	9
	EExp9Z$_c$	16.39	-7043	506.6	11
	ES3C3Z$_c$	16.37	-7485	525.1	8
	ES4C4Z$_c$	16.39	-7167	503.3	10
	ES5C5Z$_c$	16.40	-7059	507.6	12
	LE4$_c$(analytical)	16.403	-7073.4	541.76	9
10	FSDT$_c$	22.79	-14890	350.9	2*
	EExp5Z$_c$	18.55	-8967	604.0	7
	EExp7Z$_c$	18.56	-8963	545.4	9
	EExp9Z$_c$	18.57	-8906	460.2	11
	ES3C3Z$_c$	18.53	-9324	523.7	8
	ES4C4Z$_c$	18.56	-9044	524.5	10
	ES5C5Z$_c$	18.57	-8964	531.9	12
	LE4$_c$(analytical)	18.570	-8957.6	543.49	9
500	FSDT$_c$	14.47	-16891	10.67	2*
	EExp5Z$_c$	8.224	-11080	17.02	7
	EExp7Z$_c$	8.225	-11028	15.13	9
	EExp9Z$_c$	8.224	-10878	17.77	11
	ES3C3Z$_c$	8.184	-11415	1.951	8
	ES4C4Z$_c$	8.223	-11110	13.18	10
	ES5C5Z$_c$	8.224	-11042	15.68	12
	LE4$_c$(analytical)	8.2244	-11025	15.069	9

8.4 Conclusions

Various and miscellaneous thickness functions implemented in the ESL approach have been tested in the thermal-mechanical modeling of laminated plates and shells. The numerical results show that:

1. For thin laminates, linear variation of temperature through the thickness is an effective assumption, whereas for thick layered plates, this assumption can lead

Table 8.12: Deflections and stresses on the two-layer cylindrical shells under calculated temperature fields, obtained with ESL models ET*n*Z and ET1S*n*C*n*Z.

R_α/h	Model	$^\S w(\frac{a}{2},\frac{b}{2},\frac{h}{2})$ (10^{-3}mm)	$^\dagger\sigma_{\alpha\alpha}(\frac{a}{2},\frac{b}{2},\frac{h}{2})$ (KPa)	$^\ddagger\sigma_{\alpha z}(a,\frac{b}{2},\frac{h}{4})$ (KPa)	N_{exp}
2	FSDT$_c$	5.239	-14985	162.8	2*
	ET7Z$_c$	16.39	-7072	527.5	9
	ET9Z$_c$	16.39	-7026	511.4	11
	ET11Z$_c$	16.40	-7081	513.1	13
	ET1S3C3Z$_c$	16.39	-7124	522.9	9
	ET1S4C4Z$_c$	16.39	-7040	509.1	11
	ET1S5C5Z$_c$	16.40	-7057	516.2	13
	LE4$_c$(analytical)	16.403	-7073.4	541.76	9
10	FSDT$_c$	22.79	-14890	350.9	2*
	ET5Z$_c$	18.56	-8936	567.2	7
	ET7Z$_c$	18.56	-8963	543.2	9
	ET9Z$_c$	18.57	-8944	532.3	11
	ET1S2C2Z$_c$	18.57	-9064	561.4	7
	ET1S3C3Z$_c$	18.57	-8983	538.9	9
	ET1S4C4Z$_c$	18.57	-8949	531.5	11
	LE4$_c$(analytical)	18.570	-8957.6	543.49	9
500	FSDT$_c$	14.47	-16891	10.67	2*
	ET3Z$_c$	8.225	-11024	15.66	5
	ET5Z$_c$	8.225	-11024	15.66	7
	ET7Z$_c$	8.225	-11024	15.13	9
	ET1S1C1Z$_c$	8.229	-11772	15.51	5
	ET1S2C2Z$_c$	8.225	-11154	15.43	7
	ET1S3C3Z$_c$	8.225	-11047	15.06	9
	LE4$_c$(analytical)	8.2244	-11025	15.069	9

to overestimated stresses compared to results obtained by using calculated temperature fields.

2. It is clear that ESL models work better on thin laminates than on thick structures;
3. When a sufficient number of expansion terms are used, most of the ESL kinematics theories studied can achieve a good approximation of displacements and stresses;

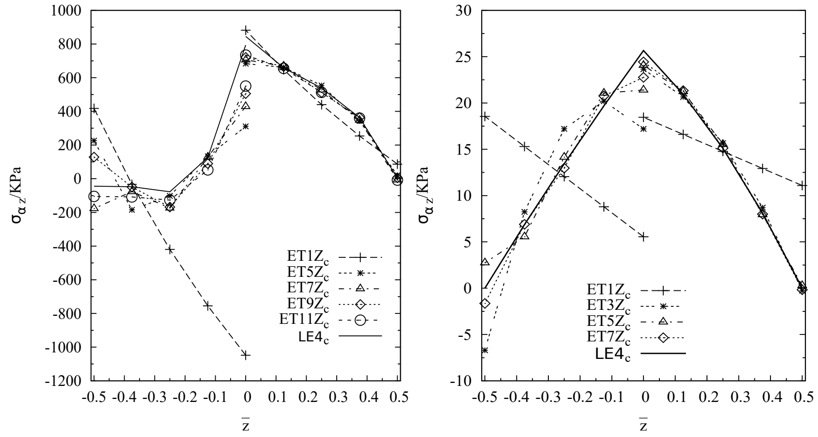

(a) $R_\alpha/h = 2$ (b) $R_\alpha/h = 500$

Figure 8.10: $\sigma_{\alpha z}$ through the thickness of the two-layered cylindrical shells under calculated temperature field, obtained with ET*n*Z kinematics.

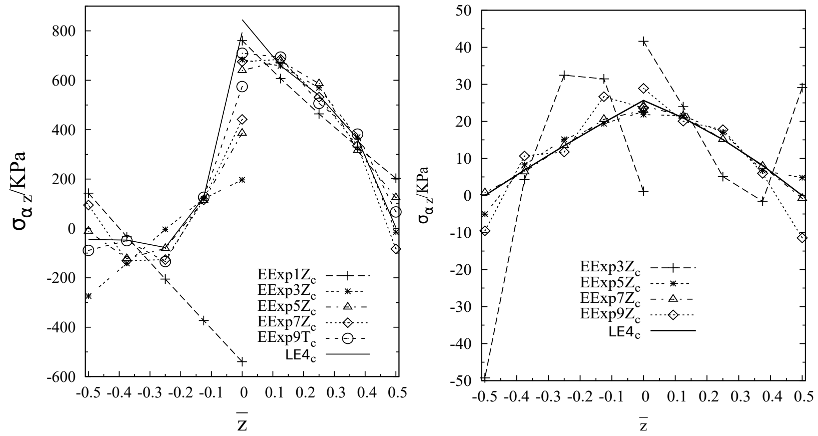

(a) $R_\alpha/h = 2$ (b) $R_\alpha/h = 500$

Figure 8.11: Transverse shear stress $\sigma_{\alpha z}$ through the thickness of the composite shells with various R_α/h ratios, obtained with EExp*n*Z kinematics.

4. The studied various kinematics theories exhibit different numerical convergence rates, and in general Taylor series have higher convergence rate than exponential and trigonometric functions;

5. With Murakami's zig-zag function, the through-the-thickness distribution of the transverse shear stress obtained with ESL models can be improved significantly;

6. In all the cases tested, LW models employing fourth-order Lagrange polynomials (LE4) can achieved reliable accuracy and guarantee continuous transverse shear stress through the thickness of both thick and thin laminates.

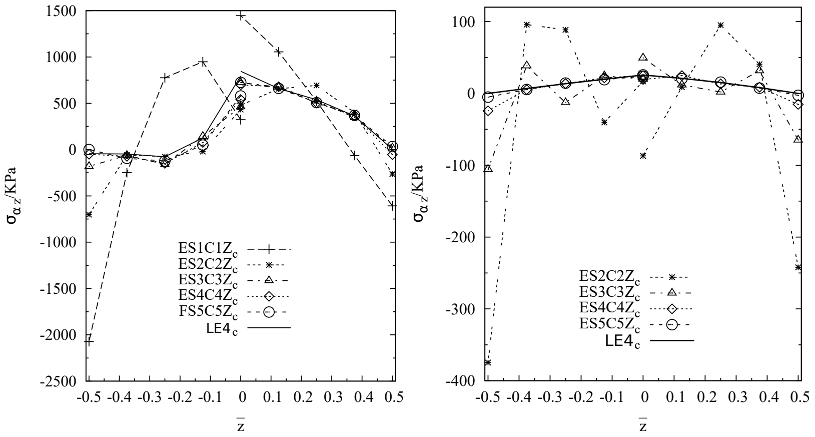

(a) $R_\alpha/h = 2$ (b) $R_\alpha/h = 500$

Figure 8.12: $\sigma_{\alpha z}$ through the thickness of the two-layered cylindrical shells under calculated temperature fields, obtained with ESnCnZ kinematics.

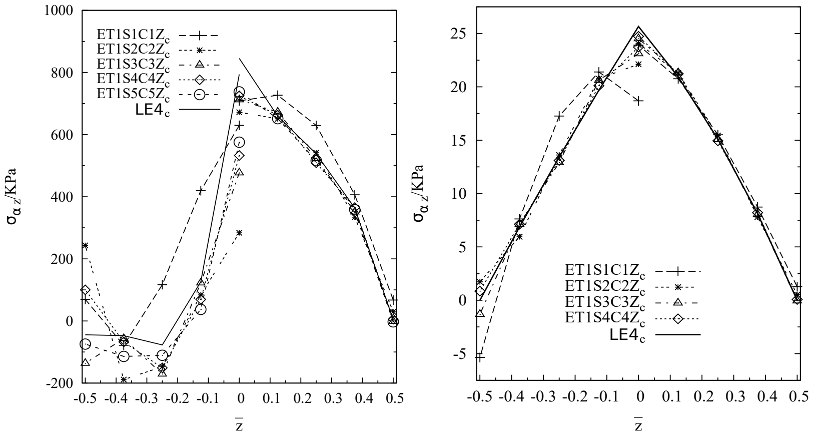

(a) $R_\alpha/h = 2$ (b) $R_\alpha/h = 500$

Figure 8.13: $\sigma_{\alpha z}$ through the thickness of the two-layered cylindrical shells under calculated temperature fields, obtained with ET1SnCnZ kinematics.

Chapter 9

Hygro-mechanical plate and shell models with variable kinematics

In this chapter, hygro-mechanical modeling with variable kinematic plate and shell models are demonstrated through two numerical examples. Similar to the partially coupled thermo-mechanical modeling in Chapter 8, the partially coupled hygro-mechanical simulation is considered in a two-step procedure, in which the calculated moisture fields will be used as input in the calculation of hygroscopic stresses. It is assumed that water diffusivity and hygroscopic expansion coefficients do not change with the variation of moisture concentration. Variable kinematic ESL and LW models are used in the refined plate and shell models.

9.1 Three-layered square plates with (0°/90°/0°) under hygroscopic fields

The square cross-ply laminated plates considered have width and length $a = b = 0.1$m and stacking sequence (0°/90°/0°). Length-to-thickness ratios $a/h = 2, 10$, and 100 are investigated. The elastic and hygroscopic properties of the lamina are listed in Tables 9.1. The moisture expansion coefficients (β_{11}, β_{22}, and β_{33}) and diffusivity (ξ_{11}, ξ_{22}, and ξ_{33}, under temperature 300K) are assumed by referring to the works of Jacquemin and Vautrin [113] and Tsai [238], respectively. The imposed distribution of moisture concentration follows:

$$c(x, y, z) = c_A(z) \cdot \sin(\frac{\pi x}{a}) \sin(\frac{\pi y}{b}) \tag{9.1}$$

where $c_A(z)$ is the moisture concentration profile through the thickness, and the boundary conditions are $c_A(-\frac{h}{2}) = 0$ and $c_A(\frac{h}{2}) = 1\%$.

10×10 MITC9 elements are used to model a quarter of the plates with symmetric boundary conditions. LW models with fourth-order Lagrange polynomials (LE4) are

Table 9.1: Mechanical and hygroscopic properties of T300/5208 lamina.

E_1 (GPa)	E_2, E_3 (GPa)	G_{12}, G_{13} (GPa)	G_{23} (GPa)	ν_{12}, ν_{13}	ν_{23}	β_{11} (wt.%H$_2$O)$^{-1}$	β_{22}, β_{33} (wt.%H$_2$O)$^{-1}$	ξ_{11} (mm^2/s)	ξ_{22}, ξ_{33} (mm^2/s)
181	10.3	7.17	2.39	0.28	0.43	0	0.006	2.87×10^{-8}	1.63×10^{-8}

first adopted in the simulations. The calculated distributions of moisture concentration through the thickness are shown in 9.1. It is evident that on the thick plate ($a/h = 2$), a linear assumption is far from being accurate. On the moderate thick ($a/h = 10$) and thin ($a/h = 100$) plates, the calculate profiles are quite close to the linear one.

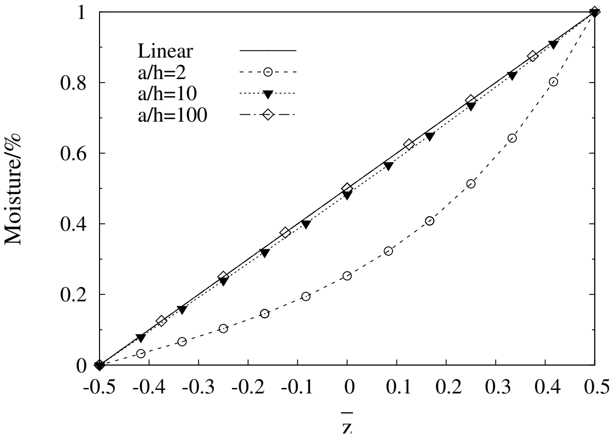

Figure 9.1: Moisture concentration profiles on the three-layered plates with various a/h.

Table 9.2: Deflection and stresses on the three-layered plates under hygroscopic fields, obtained with LW models.

a/h	Model	Assumed profiles $^{\S}w$ (10^{-3}mm)	Assumed profiles $^{\dagger}\sigma_{xx}$ (MPa)	Assumed profiles $^{\ddagger}\sigma_{xz}$ (MPa)	Calculated profiles $^{\S}w$ (10^{-3}mm)	Calculated profiles $^{\dagger}\sigma_{xx}$ (MPa)	Calculated profiles $^{\ddagger}\sigma_{xz}$ (MPa)	N_{exp}
2	LE1	144.0	66.79	3.996	108.3	38.04	2.821	4
	LE4	148.2	106.5	9.461	112.1	71.42	5.609	13
	LE4(analytical)	148.68	105.56	9.4418	112.11	71.238	5.5973	13
10	LE1	76.59	34.22	2.167	75.91	33.02	2.146	4
	LE4	73.08	38.75	3.021	72.39	37.97	2.967	13
	LE4(analytical)	73.078	38.636	3.0147	72.388	37.859	2.9619	13
100	LE1	403.1	31.00	0.2370	403.1	30.99	0.2370	4
	LE4	359.1	34.09	0.3208	359.1	34.08	0.3208	13
	LE4(analytical)	359.12	33.983	0.32018	359.10	33.976	0.32013	13

Variables are evaluated at: $^{\S}(\frac{a}{2}, \frac{b}{2}, \frac{h}{2})$; $^{\dagger}(\frac{a}{2}, \frac{b}{2}, \frac{h}{2})$; $^{\ddagger}(0, \frac{b}{2}, \frac{h}{6})$.

The displacements and stresses obtained with LW models are summarized in Table 9.2. It can be observed that the results match the analytical solutions well. On the thick plate ($a/h = 2$), the assumed linear and calculated temperature profiles through the thickness cause significant difference regarding both displacements and stresses. On the moderate thick ($a/h = 10$) and thin ($a/h = 100$) plates, structural responses under these two set of moisture fields are quite close.

Table 9.3: Deflections and stresses on the three-layered plates under calculated moisture field obtained with ESL models ETnZ and ET1SnCnZ.

a/h	Model	$w(\frac{a}{2},\frac{b}{2},\frac{h}{2})$ (10^{-3}mm)	$\sigma_{xx}(\frac{a}{2},\frac{b}{2},\frac{h}{2})$ (MPa)	$\sigma_{xz}(0,\frac{b}{2},\frac{h}{6})$ (MPa)	N_{exp}
2	FSDT$_c$	23.36	1.623	1.381	2*
	ET3Z$_c$	112.9	62.44	1.611	5
	ET7Z$_c$	112.4	72.04	3.135	9
	ET11Z$_c$	112.3	71.67	3.767	13
	ET13Z$_c$	112.2	71.67	3.708	15
	ET1S3C3Z$_c$	112.4	71.64	3.257	9
	ET1S5C5Z$_c$	112.2	71.61	3.737	13
	LE4$_c$(analytical)	112.10734	71.238	5.5973	13
10	FSDT$_c$	70.44	44.93	0.7585	2*
	ET5Z$_c$	72.38	37.93	1.790	7
	ET9Z$_c$	72.39	38.01	2.198	11
	ET11Z$_c$	72.39	38.00	2.272	13
	ET1S3C3Z$_c$	72.39	37.89	2.085	9
	ET1S5C5Z$_c$	72.39	37.99	2.263	13
	LE4$_c$(analytical)	72.388142	37.859	2.9619	13
500	FSDT$_c$	643.4	49.08	0.08121	2*
	ET5Z$_c$	359.1	34.08	0.1976	7
	ET9Z$_c$	359.1	34.08	0.2409	11
	ET11Z$_c$	359.1	34.08	0.2487	13
	ET1S3C3Z$_c$	359.1	33.96	0.2290	9
	ET1S5C5Z$_c$	359.1	34.08	0.2478	13
	LE4$_c$(analytical)	359.099	33.976	0.32013	13

Table 9.3 reports the displacements and stresses obtained with ESL kinematics ETnZ and ET1SnCnZ for the plates under calculated moisture fields. One can notice that excellent agreement is achieved between the results given by ESL kinematics and the

analytical solutions for different a/h values.

The distributions of deflections and stresses through the thickness of the three-layered plates under calculated moisture fields are given in Fig. 9.2, in which the stresses are amplified by 50 or 500 times and denoted by "$*50$" or "$*500$" in the plots when necessary for the convenience of illustration. A significant difference can be observed between results for the thick plate with $a/h = 2$ under the assumed and calculated moisture fields. For the moderate thick ($a/h = 10$) and thin ($a/h = 500$) plates, the calculated moisture profiles through the thickness exhibit almost a linear variation, and the resultant structural response is also close to that caused by an assumed moisture profile.

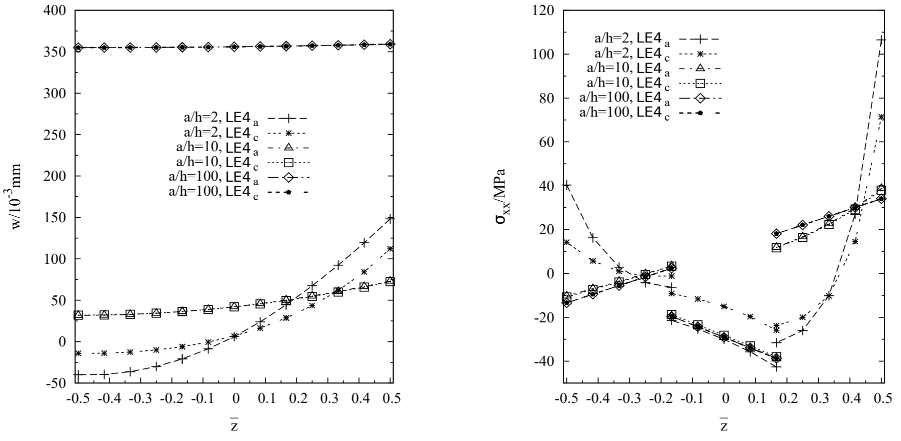

(a) w (b) σ_{xx}

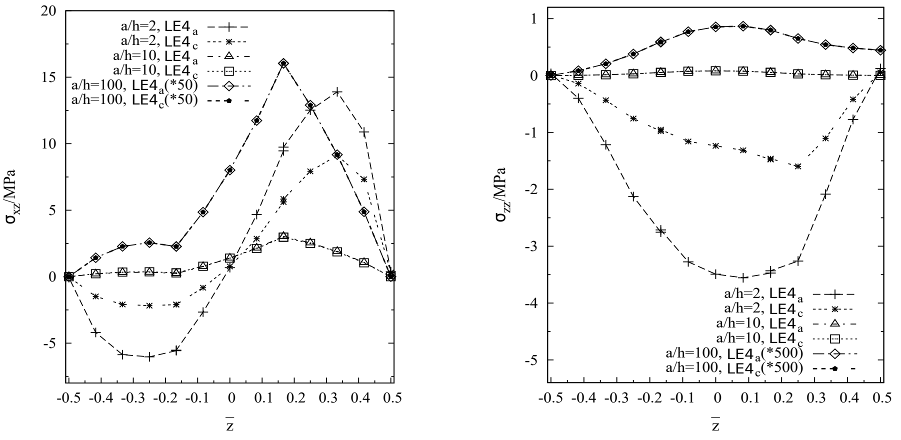

(c) σ_{xz} (d) σ_{zz}

Figure 9.2: Through-the-thickness variation of deflection and stresses on the three-layered plates under calculated moisture fields.

The variations of σ_{xz} through the plate thickness obtained with ETnZ and ET1SnCnZ kinematics under calculated moisture fields are shown in Fig. 9.3. It can be noticed that in the tested cases, these ESL models do not show as satisfactory performance as the

LW models do regarding the interfacial continuity.

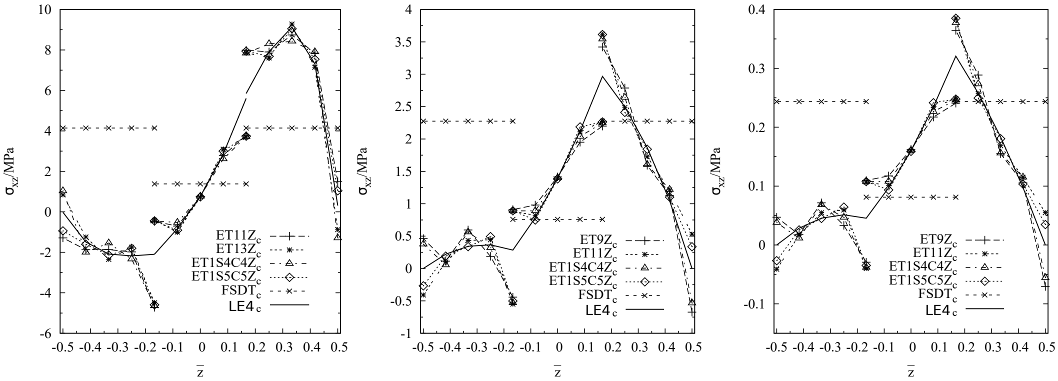

(a) $a/h = 2$ (b) $a/h = 10$ (c) $a/h = 500$

Figure 9.3: σ_{xz} through the thickness of the three-layered plates under calculated moisture fields, obtained with ESL models with ETnZ and ET1SnCnZ.

9.2 Two-layered cylindrical shells with (0°/90°) under hygroscopic fields

Two-layered cylindrical shells with stacking sequence (0°/90°) (from bottom to top) are considered. The in-lane dimensions are $a = b = 0.1$m, and radii $R_\alpha = 0.1$m, $R_\beta = \infty$. Radius-to-thickness ratios $R_\alpha/h = 2$,10 and 500 are investigated. The material properties can be found in 9.1. The moisture field is described by:

$$c(\alpha, \beta, z) = c_A(z) \cdot \sin(\frac{\pi\alpha}{a})\sin(\frac{\pi\beta}{b}) \tag{9.2}$$

and the boundary conditions are $c_A(-\frac{h}{2}) = 0$ and $c_A(\frac{h}{2}) = 1\%$.

LW models are first employed in the simulations. 10×10 MITC9 shell elements are used to model a quarter of the whole shells together with symmetric boundary conditions. The calculated moisture distributions through-the-thickness of the cylindrical shells are given in Fig. 9.4. Similar to the above-discussed case, on the thin shell $R_\alpha/h = 500$, the calculated moisture profiles coincide with the assumed linear ones, and an minor difference can be observed between these two sets of fields on the moderate thick shell ($R_\alpha/h = 10$). On the thick shell with $R_\alpha/h = 2$, the calculated moisture profile shows an obvious nonlinear distribution through the shell thickness.

The results obtained with LW kinematics are summarized in Table 9.4 and Fig. 9.5. It can be observed that the LE4 models can give results agreeing well with the analytical solutions. For moderately thick ($R_\alpha/h = 10$) and thin ($R_\alpha/h = 500$) shells, the linear moisture concentration variation through the thickness is a reasonable assumption. For

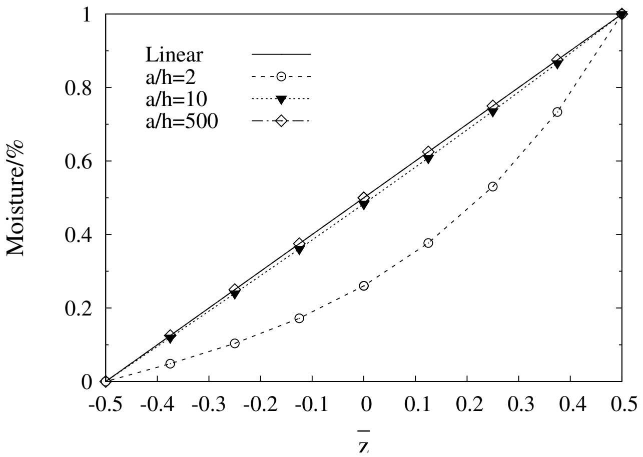

Figure 9.4: Moisture profiles on the two-layered cylindrical shells.

Table 9.4: Deflections and stresses on the two-layered cylindrical shells under hygroscopic fields, obtained with LW models.

R_α/h	Model	Assumed profiles			Calculated profiles			N_{exp}
		$^{\S}w$ (10^{-3}mm)	$^{\dagger}\sigma_{\alpha\alpha}$ (MPa)	$^{\ddagger}\sigma_{\alpha z}$ (MPa)	$^{\S}w$ (10^{-3}mm)	$^{\dagger}\sigma_{\alpha\alpha}$ (MPa)	$^{\ddagger}\sigma_{\alpha z}$ (MPa)	
2	LE1	134.8	-32.51	3.189	104.1	-47.83	3.254	3
	LE4	146.0	-22.78	1.402	113.9	-30.76	2.411	9
	LE4(analytical)	146.01	-22.869	1.3991	113.21	-31.009	2.4303	9
10	LE1	109.0	-56.60	3.136	108.0	-57.39	3.117	3
	LE4	101.5	-47.23	2.961	100.5	-47.43	2.942	9
	LE4(analytical)	101.53	-47.258	2.9547	100.46	-47.461	2.9355	9
500	LE1	43.90	-70.79	0.08282	43.90	-70.79	0.08282	3
	LE4	43.36	-58.80	0.08053	43.36	-58.80	0.08053	9
	LE4(analytical)	43.359	-58.808	0.080387	43.359	-58.808	0.080387	9

Variables are evaluated at: $^{\S}(\frac{a}{2}, \frac{b}{2}, \frac{h}{2})$; $^{\dagger}(\frac{a}{2}, \frac{b}{2}, \frac{h}{2})$; $^{\ddagger}(a, \frac{b}{2}, \frac{h}{4})$.

the thick shell with $R_\alpha/h = 2$, assumed linear moisture profile results in erroneous displacements and stresses.

Various ESL models are then tested, and the obtained results are represented in Table 9.5 and Fig. 9.6. It can be concluded that for shells with aspect ratios $R_\alpha = 2, 10$ and 500, the necessary expansion terms are 13, 11, and 9, separately. Meanwhile, these numbers are 9, 7, and 5 for LW models. In this case, the ESL models are not as efficient as the LW ones.

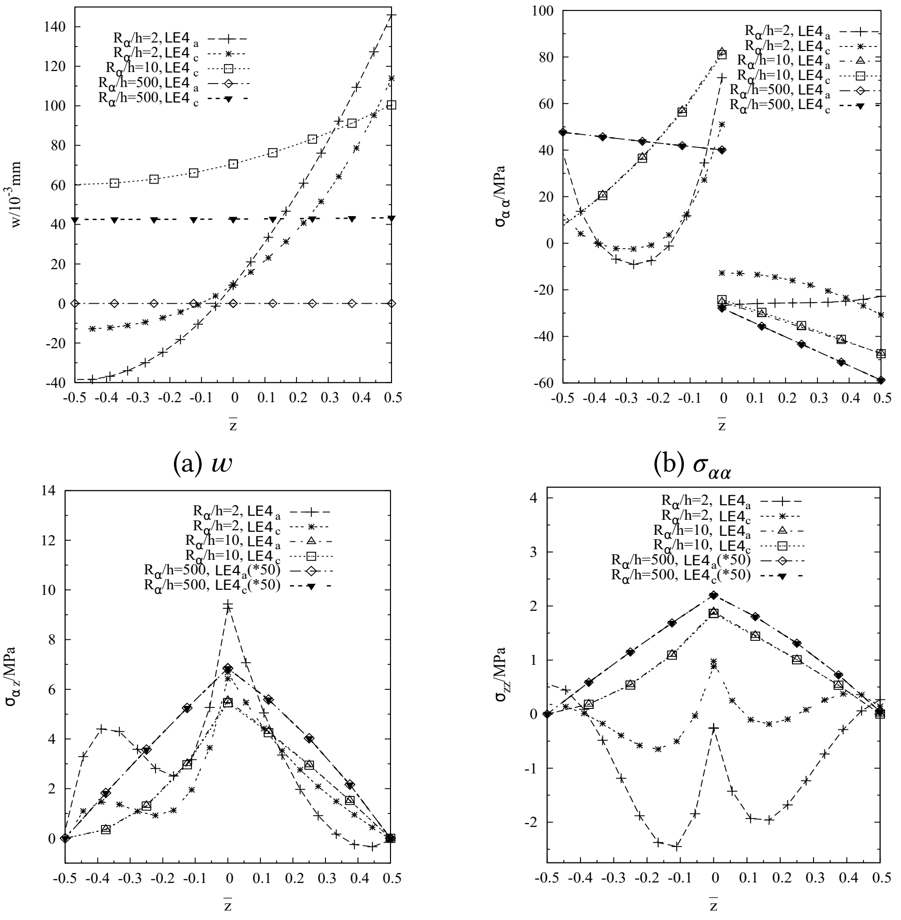

(a) w

(b) $\sigma_{\alpha\alpha}$

(c) $\sigma_{\alpha z}$

(d) σ_{zz}

Figure 9.5: Transverse displacement w and stresses through the thickness of the composite cylindrical shells with various R_α/h ratios under hygroscopic fields, LE4 solutions with both linear and calculated moisture profiles.

9.3 Conclusions

Various and miscellaneous thickness functions are implemented in the ESL approach through the CUF framework and applied in the hygro-mechanical modeling of laminated plates and shells. A MITC9 shell element is employed to guarantee the locking free FE analysis. Both assumed linear moisture concentration profiles through the thickness and calculated variations (by solving the diffusion law) are considered.

Based on the numerical investigations, some conclusions can be drawn as:

1. For laminates with various aspect ratios, the numbers of essential expansion terms to achieve numerical convergence are usually different, and variable kinematics can be adapted to determine the appropriate approximation models;

Table 9.5: Deflections and stresses on the two-layered cylindrical shells under calculated moisture fields, obtained with ESL models ETnZ and ET1SnCnZ.

R_α/h	Model	$^\S w(\frac{a}{2},\frac{b}{2},\frac{h}{2})$ (10^{-3}mm)	$^\dagger\sigma_{\alpha\alpha}(\frac{a}{2},\frac{b}{2},\frac{h}{2})$ (MPa)	$^\ddagger\sigma_{\alpha z}(a,\frac{b}{2},\frac{h}{4})$ (MPa)	N_{exp}
2	FSDT$_c$	34.14	-75.38	1.215	2*
	ET7Z$_c$	113.9	-31.03	2.347	9
	ET9Z$_c$	113.9	-30.67	2.198	11
	ET11Z$_c$	113.9	-30.96	2.214	13
	ET1S3C3Z$_c$	113.9	-31.12	2.273	9
	ET1S4C4Z$_c$	113.9	-30.72	2.183	11
	ET1S5C5Z$_c$	113.9	-30.94	2.251	13
	LE4$_c$(analytical)	113.21	-31.009	2.4303	9
10	FSDT$_c$	123.1	-79.09	1.921	2*
	ET5Z$_c$	100.4	-47.34	3.068	7
	ET7Z$_c$	100.4	-47.49	2.934	9
	ET9Z$_c$	100.5	-47.39	2.874	11
	ET1S2C2Z$_c$	100.4	-47.99	3.036	7
	ET1S3C3Z$_c$	100.4	-47.59	2.910	9
	ET1S4C4Z$_c$	100.5	-47.42	2.869	11
	LE4$_c$(analytical)	100.46	-47.461	2.9355	9
500	FSDT$_c$	76.64	-90.10	0.05690	2*
	ET3Z$_c$	43.36	-58.80	0.08356	5
	ET5Z$_c$	43.36	-58.80	0.08286	7
	ET7Z$_c$	43.36	-58.80	0.08071	9
	ET1S1C1Z$_c$	43.38	-62.79	0.08274	5
	ET1S2C2Z$_c$	43.36	-59.50	0.08233	7
	ET1S3C3Z$_c$	43.36	-58.93	0.08036	9
	LE4$_c$(analytical)	43.359	-58.808	0.080387	9

2. When applied to hygro-mechanical analysis, classical theories (e.g. FSDT) gives incorrect results even for thin laminates;
3. For thin structures, linear variation of moisture through the thickness is an effective assumption, whereas for thick laminates it can lead to overestimated stress evaluation compared with results using profiles obtained by solving Fick's Law;
4. In some cases, even if the Murakami zig-zag function is used, ETnZ and ET1SnCnZ

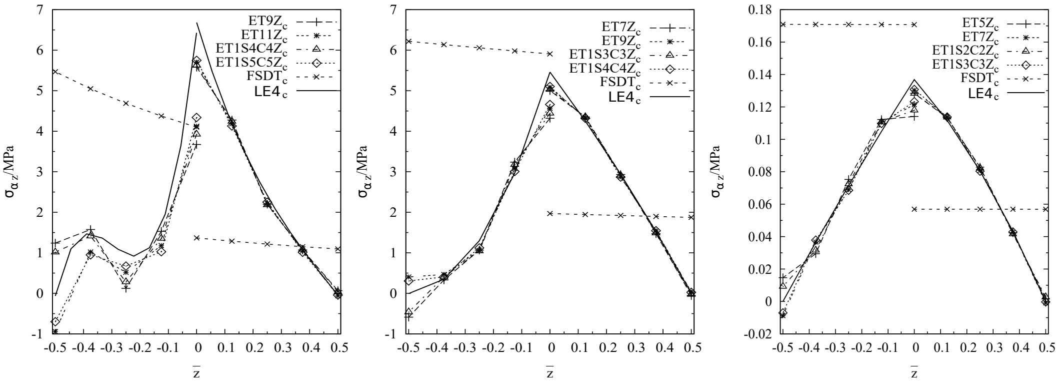

(a) $R_\alpha/h = 2$ (b) $R_\alpha/h = 10$ (c) $R_\alpha/h = 500$

Figure 9.6: $\sigma_{\alpha z}$ through the thickness of the two-layered cylindrical shells under calculated moisture fields.

cannot lead to a satisfactory approximation of continuous through-the-thickness variation of transverse shear stresses;

5. Compared with ESL models, LW models can provide results with better accuracy, and LW models employing fourth-order Lagrange polynomials (LE4) can give continuous transverse shear stress distribution through the thickness for composite laminates with a broad range of length-to-thickness ratios.

Chapter 10

Piezoelectric modeling with beam models

This chapter presents examples of NDK beam FE models for the modeling of slender structures with piezoelectric components, particularly piezo-patches. The interaction of the piezoelectric components and the substrate structures is well captured through the LW approach. ESL approach is used on nodes in the non-critical region without piezo-patches. Both extension and shear mechanisms are considered.

10.1 Cantilever beams containing piezo-patches with variable locations

In this example, cantilever beams with piezo-patches exploiting both extension actuation mechanism (EAM) and shear actuation mechanism (SAM) are investigated, as shown in Figs. 10.1a and 10.1b, respectively. This example has been reported to be used by Sun and Zhang [218], Zhang and Sun [265], Benjeddou, Trindade, and Ohayon [23], and Kpeky et al. [138]. The considered beams have width $a = 0.02$m and length $b = 0.1$m. The piezoelectric components take the whole width range (in x direction). In the EAM configuration, the two patches have equal thickness $h_p = 0.001$m, and the total beam thickness is $h_e = 0.018$m; while the single piezo-patch used in the SAM configuration has thickness 0.002m, and the total thickness of the beam is $h_s = 0.018$m. In both configurations, the aluminum substrates are as thick as $h = 0.016$m.

Two types of structures are considered in the current work:

- *Case A*: the piezo-patches take up the whole length range;
- *Case B*: the piezo-patches have length $c = 0.01$m with variable positions along the axial direction from $d = 0.01$m to $d = 0.09$m (see Fig. 10.1).

For the EAM, the piezoelectric components are polled in the third direction z. The difference of electric potential (voltage) applied on the top and bottom surfaces $\Delta\phi =$

$\phi_{bottom} - \phi_{top} = 10$V for the upper patch and $\Delta\phi = -10$V for the lower one. For the SAM, the poling direction is along the axis y and $\Delta\phi = 20$V is used. The substrate structure is made of aluminum with Young's modulus $E = 70.3$GPa and Poisson's ratio $\nu = 0.345$. PZT-5H is used for the piezo-patches, and the properties are listed in Table 10.1. For the SAM configuration in *Case B*, the rest part of the core besides the piezo-patch is made of foam with $E = 35.3$MPa and $\nu = 0.38$.

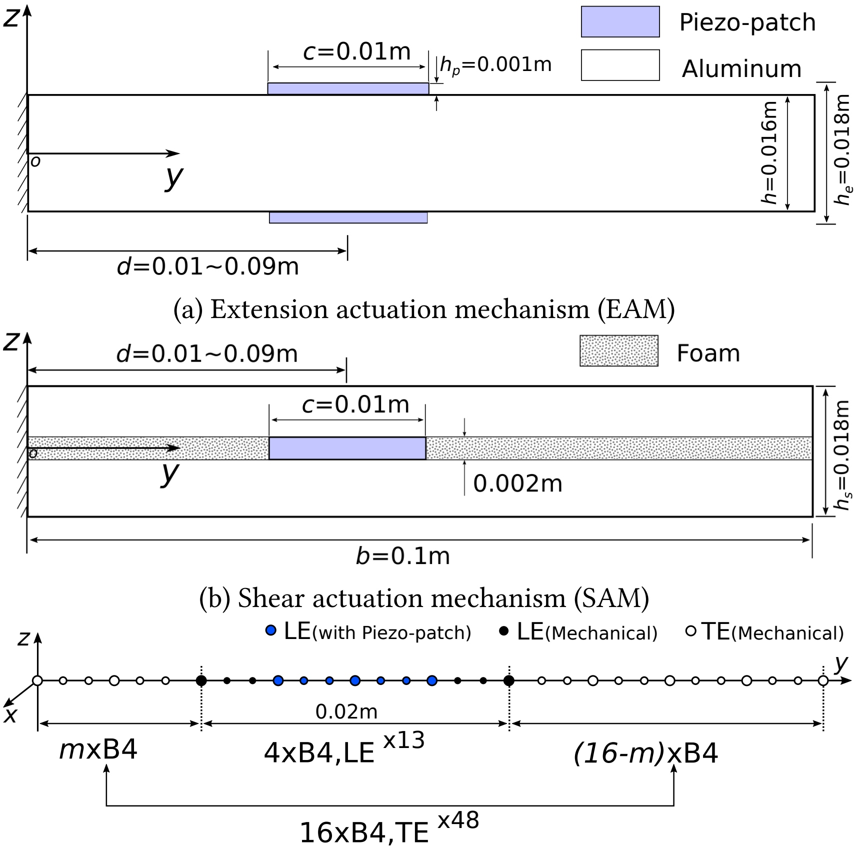
z
c=0.01m
h_p=0.001m
Piezo-patch
Aluminum
o
y
h=0.016m
h_e=0.018m
d=0.01~0.09m
z
d=0.01~0.09m
Foam
c=0.01m
o
y
0.002m
h_s=0.018m
b=0.1m
z
LE(with Piezo-patch)
LE(Mechanical)
TE(Mechanical)
y
x
0.02m
mxB4
4xB4,LE x13
(16-m)xB4
16xB4,TE x48

(a) Extension actuation mechanism (EAM)

(b) Shear actuation mechanism (SAM)

(c) FE models

Figure 10.1: Cantilever beams with surface-mounted and embedded piezo-patches.

Table 10.1: Material properties of PZT-5H

C_{11},C_{22},C_{33} (GPa)	C_{12} (GPa)	C_{13},C_{23} (GPa)	C_{44},C_{55},C_{66} (GPa)	e_{15},e_{24} (C/m^2)	e_{31},e_{32} (C/m^2)	e_{33} (C/m^2)	χ_{11},χ_{22} (F/m)	χ_{33} (F/m)
126	79.5	84.1	23.0	17.0	-6.5	23.3	1.503×10^{-8}	1.30×10^{-8}

For *Case A*, uniform LE nodal kinematics 12LE9, which approximates the cross-section as twelve sub-domains as illustrated in Fig. 10.2, is used. Along the beam axis, twenty B4 elements are used. An ABAQUS 3D model consisting of eight layers of C3D20R (elastic) brick elements and another eight layers of C3D20RE (piezoelectric) brick elements is also constructed for comparison purposes, and the mesh in the (x, y) plane is 8×40. The obtained results are compared against solutions given by Benjeddou, Trindade, and Ohayon [23] and Kpeky et al. [138]. It is worthy of noting that in the work of Benjeddou, Trindade, and Ohayon [23] the solutions were obtained by using plane-stress reduced constitutive equations, and Kpeky et al. [138] adopted FE models with solid-shell piezoelectric elements SHB8PSE and SHB20E.

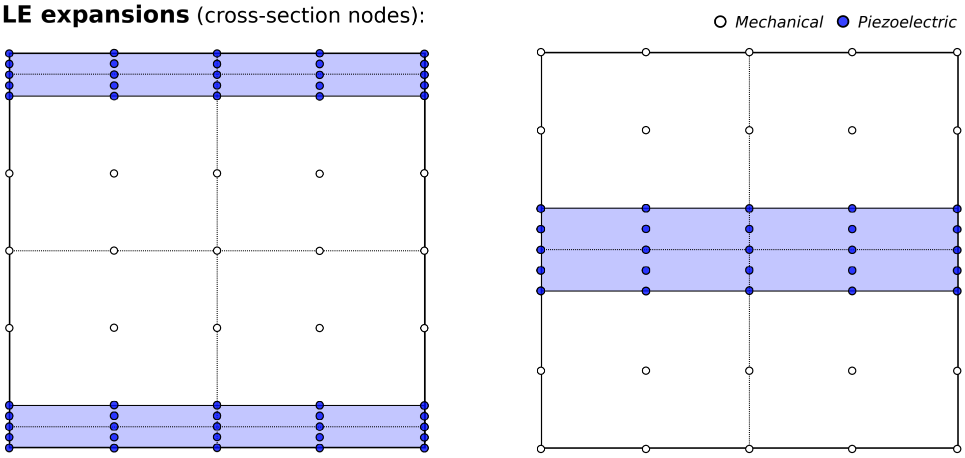
LE expansions (cross-section nodes):
○ *Mechanical* ● *Piezoelectric*

(a) EAM (b) SAM

Figure 10.2: Cross-section discretization with 12LE9 for the beam structures in *Case A*.

For the structures in *Case A*, the distributions of deflections along the beam axis are shown in Fig. 10.3 and the deflections on the free ends are reported in Table 10.2. It can be noticed that results obtained with refined beam models agree well with those through ABAQUS 3D modeling. Regarding the displacements of EAM beams in Fig. 10.3a, the employed refined beam elements give results lower than those in the work of Benjeddou, Trindade, and Ohayon [23], yet agreeing well with those given by Kpeky et al. [138]. For the SAM beams, the presented results are in agreement with the reference solutions.

For the beam structures in *Case B*, 12LE9 is used on the cross-section with piezo-patches, and correspondingly 4LE9 is employed on the substrate cross-section. The local piezo-patches are modeled through the component-wise assembly technique as introduced in Section 4.5.3. The numerical results are summarized in Fig. 10.4, wherein 12LE9 refers to FE models adopting the aforementioned LW cross-section functions. It can be observed that the obtained results agree well with the solutions given by Kpeky et al. [138]. For the EAM configuration in *Case B*, the actuation efficiency of the piezo-patches drops with the increase of the distance of them from the clamped end, which means the

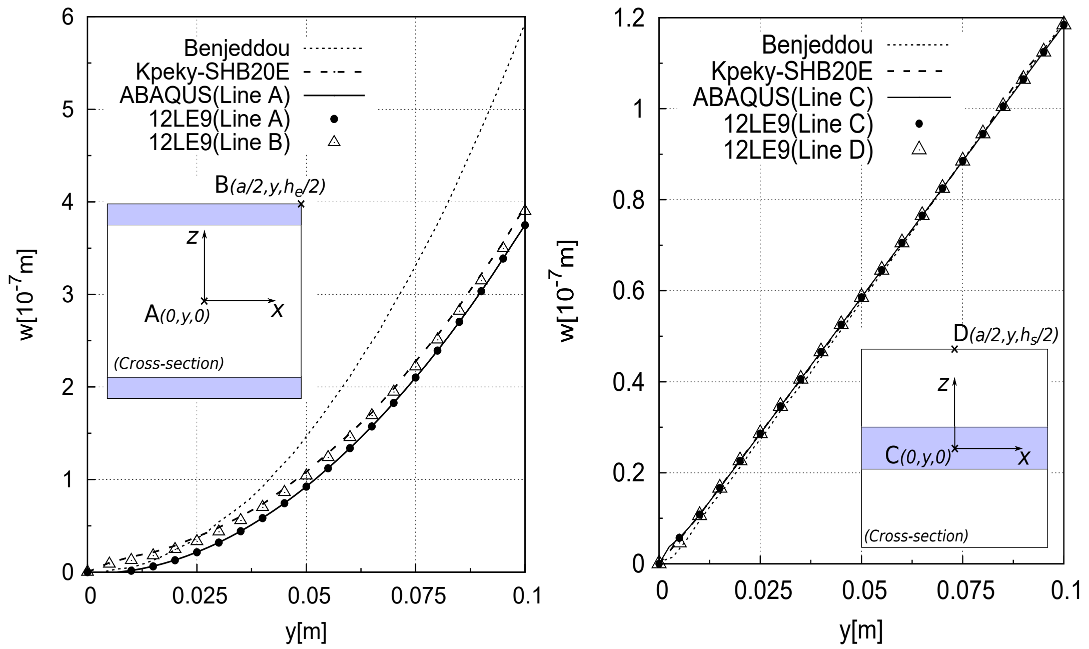

(a) EAM (b) SAM

Figure 10.3: Variation of w along the beam axis of the beams in *Case A*.

Table 10.2: Deflections on the free end of the beams in *Case A*.

	$w(10^{-7}\text{m})$			
	EAM		SAM	
	$(0, b, 0)$	$(\frac{a}{2}, b, \frac{h_e}{2})$	$(0, b, 0)$	$(\frac{a}{2}, b, \frac{h_s}{2})$
12LE9	3.748	3.897	1.184	1.184
ABAQUS	3.749	3.913	1.184	1.184

deflection at the free end will decrease monotonically, as described by the curve for point "a" in Fig. 10.4a. Meanwhile, when the piezo-patches approach the free end, the maximum deflection will be observed on the patches (point "b" in Fig. 10.4a) rather than on the substrate. Thus the maximum deflection will show a slightly up-going trend in the end, as shown in Fig. 10.4a. For the EAM configuration in *Case B*, the actuation efficiency of the patches increases marginally as the distance d increases, then drops quickly after peaking at around $d = 0.02$m. It can be noticed that the curves corresponding to point "d" at the vertex of the piezo-patches match the results presented by Kpeky et al. [138] in both EAM and SAM cases.

NDK approach is utilized to build FE models with variable nodal ESL/LW kinematics for structures in *Case B*. To be specific, ESL models using TEm theories are applied to the region without piezo-patches, and LW kinematic theories with 12LE9 are used

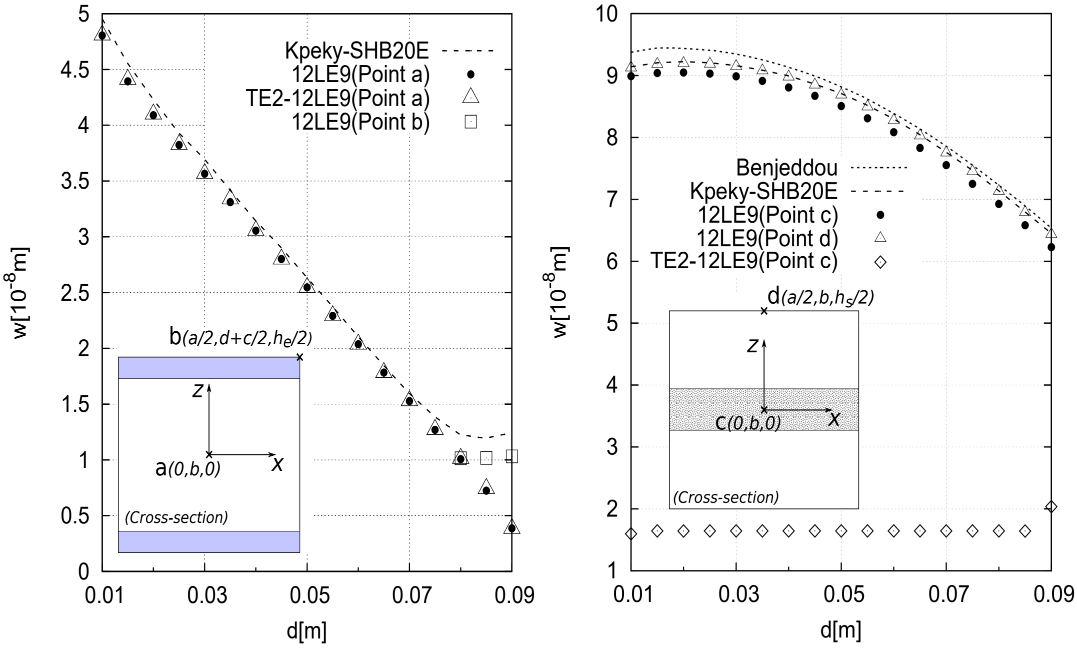

(a) EAM

(b) SAM

Figure 10.4: Deflections on the free end of the cantilever beams with piezo-patches with variable locations in *Case B*.

Table 10.3: Deflections at the center of the free-end cross-section of EAM beams with variable locations in *Case B*.

d(m)	$w^*(10^{-8}$m)	
	12LE9	TE2-12LE9
0.01	4.805	4.805
0.03	3.565	3.563
0.05	2.546	2.543
0.07	1.527	1.527
0.09	0.3863	0.3826
DOFs	5765	3317

$*$At Point a(0, b,0)

approximate the cross-section with piezo-patches. The assignment of nodal kinematics has been illustrated in Fig. 10.1c. In Fig. 10.4, the results obtained through an NDK model TE2-12LE9 are compared against those achieved through only LW kinematics 12LE9. For the EAM configuration in *Case B*, TE2-12LE9 models result in solutions in

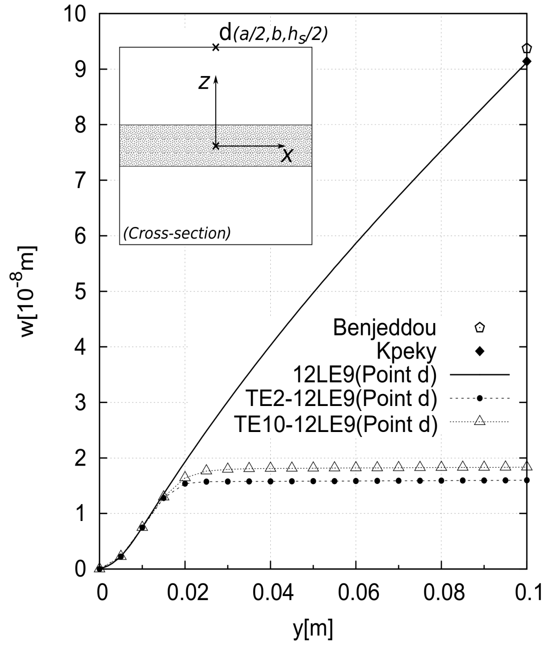

Figure 10.5: Deflection on the free-end of the SAM beam with $d = 0.01$m in *Case B*.

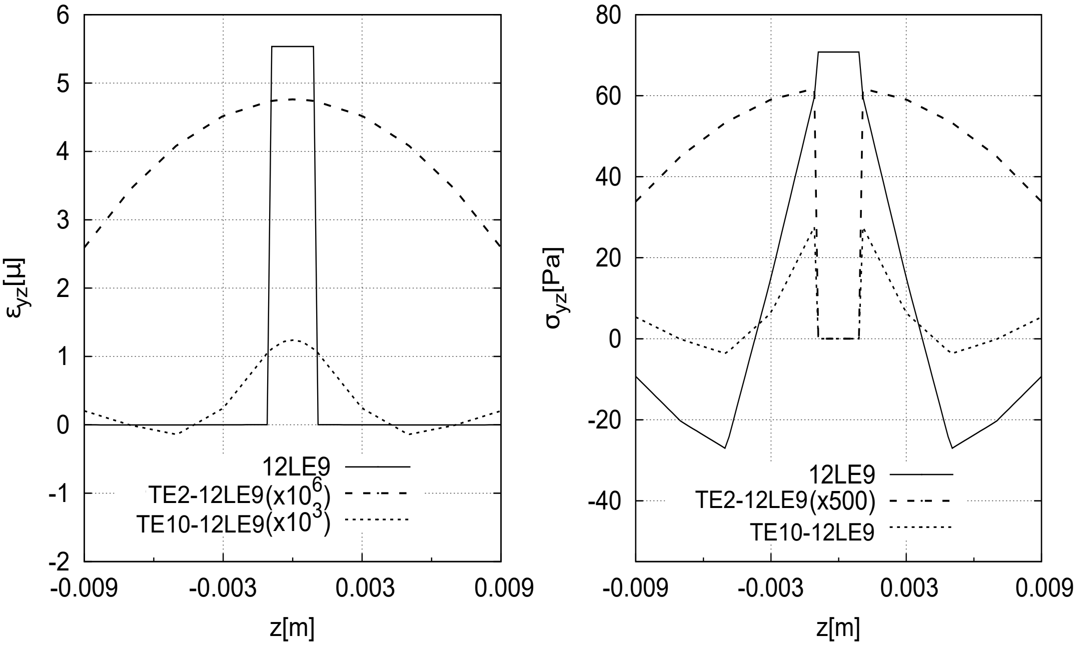

(a) ε_{yz}, $(0, b/2, z)$

(b) σ_{yz}, $(0, b/2, z)$

Figure 10.6: Deflection and stress evaluation on the SAM configuration with $d = 0.01$m in *Case B*.

good agreement with mono-kinematic LW model with 12LE9 and a reduction of 42.5% in the number of DOFs, as shown in Table 10.3. However, in Figs. 10.4b it can be noticed that TE2-12LE9 model fails in giving reasonable results for the SAM configuration in *Case B*. This is due to the inherent drawback of ESL models based on Taylor series in capturing the transverse shear effects at layer interfaces. When the transverse shear is not well approximated, the SAM cannot be accurately simulated. This can be demonstrated through a beam structure with $d = 0.01$m in *Case B*. By looking into the variation of deflection along the axis as shown in Fig. 10.5, it can be observed that the deflection remains constant at locations beyond the piezo-patch. The distributions of transverse shear strain ε_{yz} and stress σ_{yz} through the thickness on the mid-span cross-section obtained with different kinematic models are reported in Fig. 10.6. It is obvious that the ESL kinematics lead to continuous transverse strain and discontinuous transverse shear stresses through the thickness. In contrast, LW models utilizing 12LE9 have good performance when applied to the SAM configuration.

10.2 A cantilever beam with a top-mounted piezo-patch on the clamped end

By referring to the work of Biscani et al. [27], an aluminum beam containing a top-mounted PZT patch on the clamped end is considered in this section. As shown in Fig. 10.7, the beam structure has width $a = 0.01$m, length $b = 0.1$m, and height $h = 0.002$m. The piezo-patch, bonded to the top surface of the beam on the clamped end, has thickness $h_p = 0.001$m and an equal width with the substrate. The material of the piezo-patch is PZT-4, whose material coefficients have been given in Table 10.4. In this example, the piezo-patch is only used as an EAM actuator. An electrical potential 1V is imposed on the actuator top surface and 0V on the bottom.

Table 10.4: Material coefficients of PZT-4.

E_1,E_2 (GPa)	E_3 (GPa)	G_{12} (GPa)	G_{13},G_{23} (GPa)	ν_{12}	ν_{13}, ν_{23}	e_{31},e_{32} (C/m^2)	e_{33} (C/m^2)	e_{15},e_{24} (C/m^2)	χ_{11},χ_{22}	χ_{33}
81.3	64.5	30.6	25.6	0.329	0.432	-5.2	15.8	12.72	$1475\chi_0$	$1300\chi_0$

Vacuum permittivity: $\chi_0 = 8.85 \times 10^{-12}$ F/m

As illustrated in Fig. 10.7, the beam FE models contain three regions along the beam axis: the patched region with LW kinematics (LE), the un-patched region with ESL models (TE), and a transition zone in the un-patched region with variable ESL/LW kinematics. The FE models are denoted by the approximation functions for the cross-section containing the piezo-patch, and the same basis functions are used for the substrate and

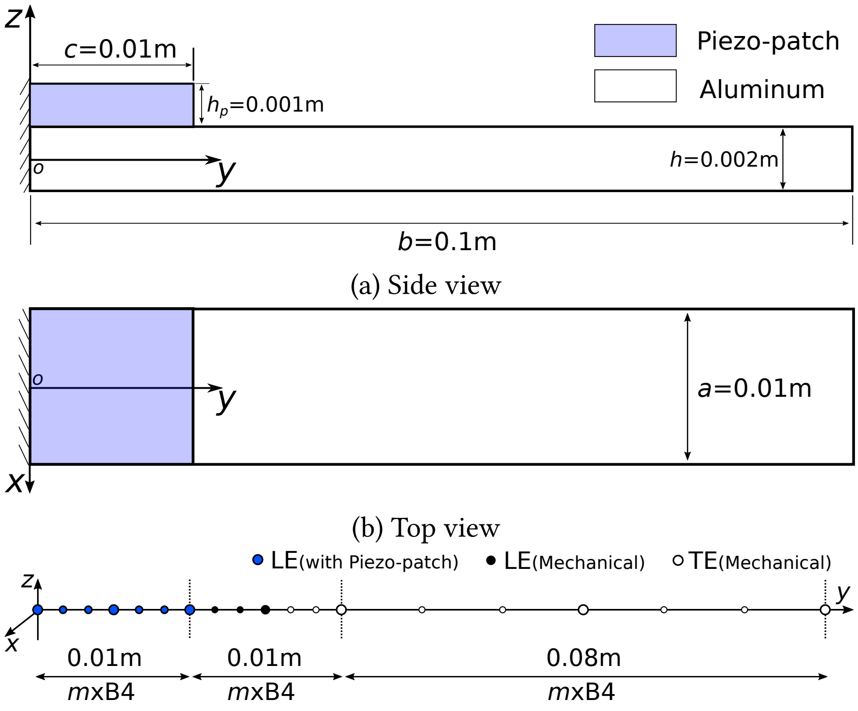

(a) Side view

(b) Top view

(c) FE models

Figure 10.7: The cantilever beam with a top-mounted piezo-patch on the clamped end.

piezoelectric cross-section domains. 4LE9 indicates that 2LE9 is used on the mechanical and piezoelectric cross-sections, and 16LE9 represents that 4×2 ($x \times z$) sub-domains are used in the discretization of the substrate and actuator. The ABAQUS 3D model contains $20 \times 20 \times 10$ ($x \times y \times z$) C3D20RE piezoelectric brick elements for the actuator and $20 \times 200 \times 10$ C3D20R brick elements for the substrate.

The results obtained through the refined beam models are summarized in Table 10.5. The solutions given by Biscani et al. [27] through refined plate models are also listed for comparison purposes. It can be observed that the best solutions are given by FE model with twenty-four B4 elements (73 nodes) adopting 16LE9 kinematics, and CUF-based refined beam models result in solutions in great agreement with the ABAQUS 3D solutions. NDK FE models TE2$^{\times 48}$-16LE9$^{\times 25}$ and TE2$^{\times 24}$-16LE9$^{\times 49}$ are also tested, where the superscripts represent the number of nodes with the corresponding assumptions. It can be noticed that the NDK models can reduce the total DOFs, and TE2$^{\times 24}$-16LE9$^{\times 49}$ give comparable accuracy with the mono-kinematic model 16LE9 with fewer DOFs. In fact, TE2$^{\times 48}$-16LE9$^{\times 25}$ is less accurate.

Fig. 10.8 shows the variation of w and σ_{yy} along the beam axis. One can find that the results given by TE2$^{\times 24}$-16LE9$^{\times 49}$ match the solutions obtained with ABAQUS 3D model

Table 10.5: Deflections and stresses on the cantilever beam with a top-mounted piezoelectric actuator.

Mesh	Kinematics	$-u_z(10^{-8}\text{m})$ $(0,\frac{b}{2},0)$	$-u_z(10^{-8}\text{m})$ $(0,b,0)$	$-\sigma_{yy}(\text{KPa})$ $(0,\frac{c}{2},-\frac{h}{2})$	$-\sigma_{yz}(\text{KPa})$ $(\frac{a}{2},\frac{c}{2},0)$	DOFs
12×B4	4LE9	2.482	5.192	5.878	0.5149	2250
12×B4	16LE9	2.444	5.109	5.131	0.6692	12852
24×B4	16LE9	2.452	5.125	5.009	0.6612	25164
24×B4	$\text{TE}2^{\times 48}$-$16\text{LE}9^{\times 25}$	2.656	5.592	5.028	0.2979	14346
24×B4	$\text{TE}2^{\times 24}$-$16\text{LE}9^{\times 49}$	2.452	5.125	5.009	0.6612	19908
ABAQUS		2.451	5.125	5.087	0.6381	196281
Biscani-2D		2.309	4.871	–	–	–

and uniform kinematic FE model 16LE9, while $\text{TE}2^{\times 48}$-$16\text{LE}9^{\times 25}$ gives less-accurate results. The distribution of σ_{yz} on the cross-section $y = c/2$ obtained with uniformly refined kinematics 16LE9 is shown in Fig. 10.9. The variations of σ_{yz} along paths $(a/2, c/2, z)$ and $(x, c/2, 0)$ are plotted in Fig. 10.10. The comparison shows that the NDK FE model $\text{TE}2^{\times 24}$-$16\text{LE}9^{\times 49}$ gives satisfactory accuracy over the cross-section, yet the $\text{TE}2^{\times 48}$-$16\text{LE}9^{\times 25}$ model fails in obtaining the desired accuracy. This also demonstrates that the transition zone in $\text{TE}2^{\times 24}$-$16\text{LE}9^{\times 49}$ is more appropriate than that in $\text{TE}2^{\times 48}$-$16\text{LE}9^{\times 25}$.

10.3 Conclusions

In this chapter, refined beam FE models with variable LW/ESL nodal kinematics through NDK are tested on slender structures with piezo-patches. Both surface-mounted and embedded piezoelectric components are considered. The coupled electro-mechanical constitutive relations are only applied to the piezo-patches, and pure mechanical constitutive relations are considered in the substrate structure. The interaction between the patch and the substrate structure is well captured with LW models, and ESL kinematic assumptions are assigned to the region without piezo-patches for efficient simulation. Some conclusions can be drawn:

- NDK facilitates the modeling of local patches by treating cross-sectional characteristics as nodal properties of refined beam FE models;
- Through the NDK approach, both surface-mounted and embedded piezo-patches can be conveniently considered in a unified manner;
- For the accurate modeling of the shear actuation mechanism, the used kinematic models should be able to well capture the transverse shear effects;

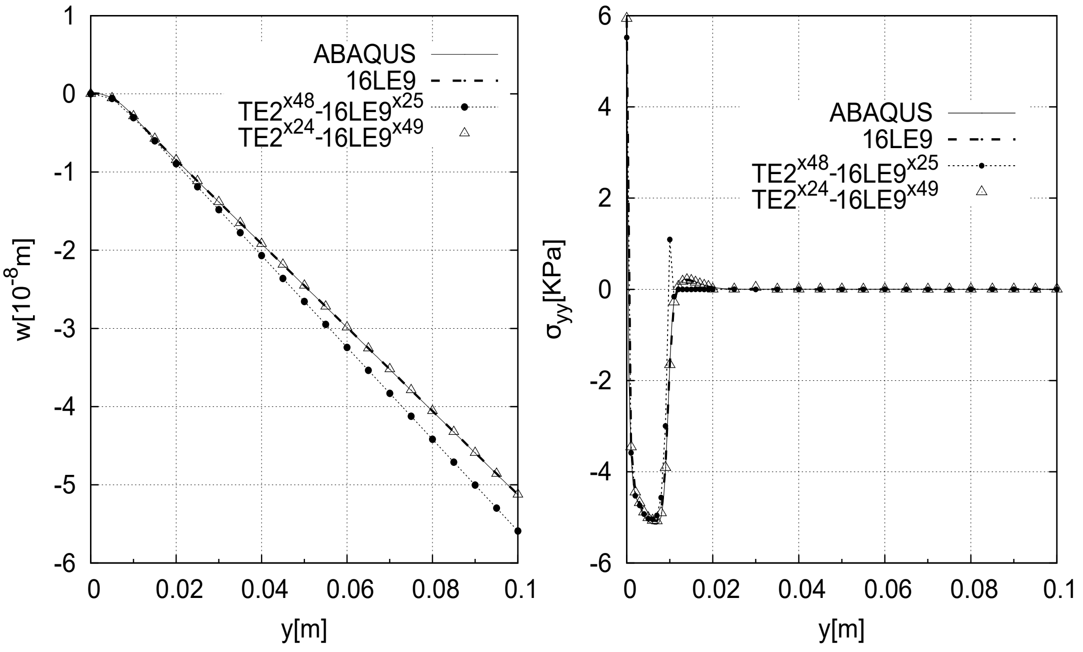

(a) w, $(0, y, 0)$ (b) σ_{yy}, $(0, y, -\frac{h}{2})$

Figure 10.8: Variation of w and σ_{yy} along the axis of the beam with a surface-mounted piezo-patch.

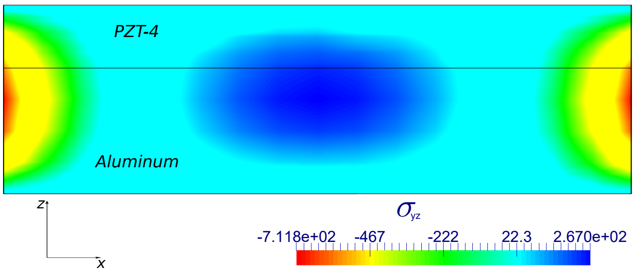

Figure 10.9: σ_{yz} on cross-section $y = c/2$ of the beam with a top-mounted piezo-patch obtained with model 16LE9.

- With NDK, the accurate response can be achieved at reduced computational costs compared to uniformly refined beam FE models;
- The properly chosen kinematic transition zone is essential to guarantee the simulation accuracy of NDK FE models.

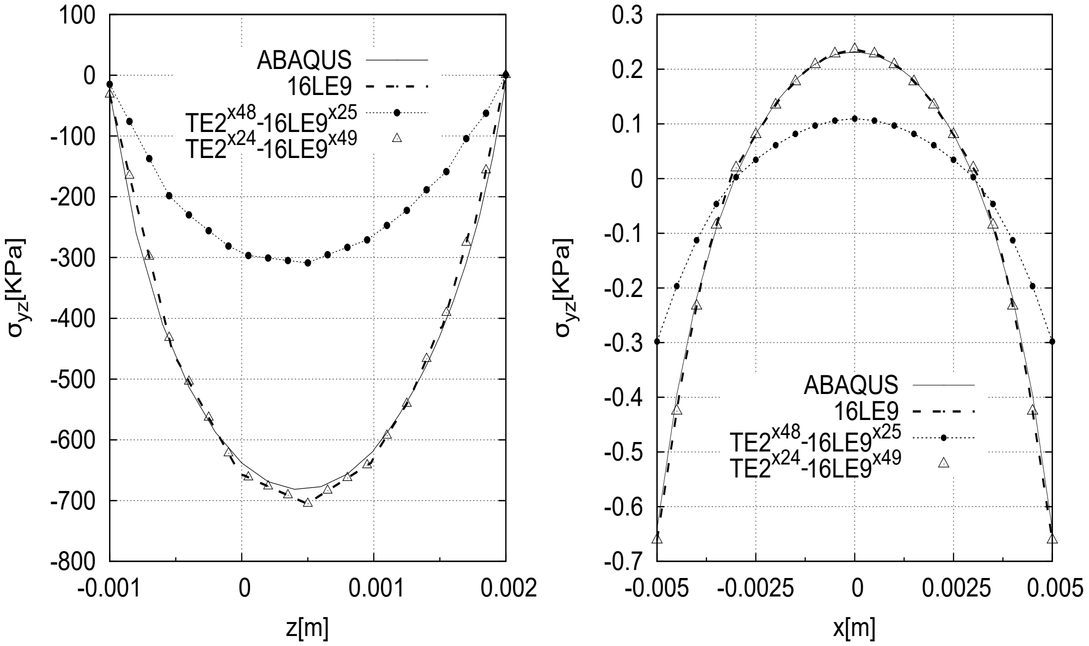

(a) σ_{yz}, $(\frac{a}{2}, \frac{c}{2}, z)$ (b) σ_{yz}, $(x, \frac{c}{2}, 0)$

Figure 10.10: Variation of σ_{yz} on cross-section $y = c/2$ of the beam with a top-mounted piezo-patch.

Part IV

Special Topics

Chapter 11

Refined finite element solutions for anisotropic laminated plates

This chapter presents several new benchmark cases for angle-ply laminated plates whose solutions are obtained with refined plate FE models based on CUF. Various laying-up sequences, boundary conditions, and span-to-thickness ratios are considered. The locking-free MITC9 element (nine-node Lagrangian 2D element with Mixed Interpolated of Tensorial Components) is adopted. LW kinematics with Chebyshev polynomials and ESL assumptions based on Trigonometric series are adopted in the construction of CUF-type refined plate models. The effectiveness of the FE approach is verified by comparing the results against analytical solutions available in the literature and those obtained through ABAQUS 3D modeling with brick element C3D20R (20-node quadratic brick element with reduced integration).

11.1 Definitions of simply supported boundary conditions

Navier's and Levy's methods are frequently used to obtain analytical solutions to cross-ply laminated plates under *simply supported* boundary conditions at four or two opposite edges, respectively. Note that different definitions of *simply supported* boundary conditions are used on cross-ply and angle-ply laminated plates. A classification was given by Hoff and Rehfield [104]. Jones [114] explained and compared these *simple supports* on plate edges as in Fig. 11.1. In Navier's and Levy's methods, S3 (or SS1) applies to cross-ply laminated plates and S2 (also known as SS2) edge conditions are used on angle-ply laminates, such as in [177, 258, 257, 199, 183, 188, 194, 273, 169]. In particular, Noor and Burton [171] and Savoia and Reddy [206] decomposed the displacement variables into symmetric and anti-symmetric parts through the thickness and further written them into double Fourier series in the in-plane Cartesian coordinate system for antisymmetric angle-ply plates, and boundary values for each set of unknown functions need to be set respectively. The same method was reported to be used by Carvelli and Savoia [61] and Kulikov and Plotnikova [140, 141]. Notably, in the novel approach suggested by Loredo [151] to define simple supports on the four edges of both cross-ply and angle-ply cases, the displacements on each pair of parallel edges were coupled. However, analytical solutions for anisotropic plates with arbitrary stacking sequences are difficult to be obtained with Navier's or Levy's method.

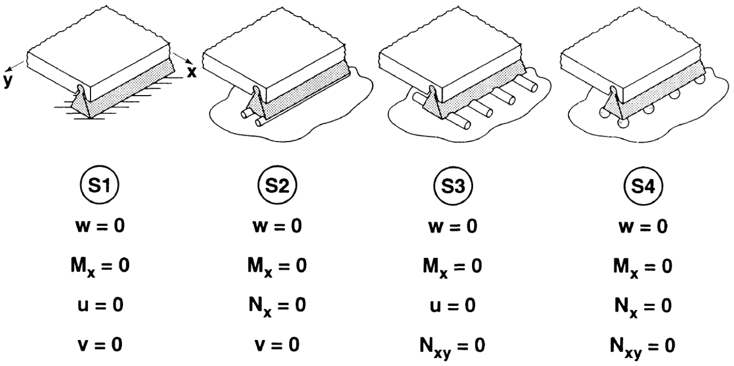

Figure 11.1: Simply supported edge boundary conditions for a plate, Figure 5-7 in [114].

It should be pointed out that, the constraints on displacement components are essential boundary conditions, while the forces and bending/twisting moments on edges are natural boundary conditions. In displacement-based FE formulations, the displacement constraints should be specified explicitly, and the natural boundary conditions will be satisfied in the weak-form formulations, as discussed by Section 4.4. Özakça, Hinton, and Rao [174] used so-called "hard simple support" and "soft simple support" defined on displacements in the analysis of isotropic plates with displacement-based solid elements. In fact, the "soft simple support" discussed in Özakça, Hinton, and Rao [174] was equivalent to the S4 in Fig. 11.1. Bogdanovich and Birger [32] applied such "soft simple support" in the modeling of three-layered orthotropic plates under constant pressure. Through a Levy-type solution, Kumari and Kapuria investigated boundary layer effects in laminated plates by using a third order zig-zag theory [143] and a layer-wise theory [127], and specific "hard" and "soft" simple supports were examined. In the work of Tornabene and Viola [235], a set of similar "soft" simply supported boundary conditions were used.

As shown in Fig. 11.1, the "soft" simple support used by Özakça, Hinton, and Rao [174], which is also referred to as S4 simply supported boundary conditions in [114], permits translation in any direction in the x-y plane. When applied to displacement-based elements, only $w = 0$ needs to be considered. Such a definition can easily be applied to displacement-based refined plate elements in the analysis of arbitrarily laminated anisotropic plates.

In the current chapter, in CUF-based refined plate FE models, the adopted simply supported and clamped boundary conditions are defined as in Table. 11.1, where the superscript k signifies the layer and τ is the index of a thickness function. It should be noted that when the S4-type simple supports are imposed on the four edges of a plate, in displacement-based FE models there exist three rigid body modes, which include two in-plane translational modes and one rotational mode. A simple remedy is to introduce small penalty stiffness on two FE nodes. The penalty should be large enough to eliminate the rigid body modes and small enough to avoid influencing the stress field. In commercial software ABAQUS, this penalty stiffness can be implemented by using string elements to connect two nodes to the "ground".

Table 11.1: Edge displacement boundary conditions on laminated plates.

Boundary type	CUF-based plate models		3D brick element
	ESL	LW	
Simply supported	$w_\tau = 0$	${w_\tau}^k = 0$	$w = 0$
Clamped	$u_\tau = v_\tau = w_\tau = 0$	${u_\tau}^k = {v_\tau}^k = {w_\tau}^k = 0$	$u = v = w = 0$

11.2 Numerical cases

In the following sections, LW-CBTn denotes a model adopting Chebyshev polynomials of order n that contains $n+1$ expansion terms in total (see Eqn. 2.49), and ESL-TRGmZ signifies an ESL model with one constant term, m sine expansions, m cosine functions, and Murakami zig-zag term. For instance, ESL-TRG3Z refers to the following kinematic model:

$$\begin{aligned} \boldsymbol{u}(x,y,z) =& \boldsymbol{u}_0(x,y) + \sin(\frac{\pi z}{h})\boldsymbol{u}_1(x,y) + \cos(\frac{\pi z}{h})\boldsymbol{u}_2(x,y) + \sin(\frac{2\pi z}{h})\boldsymbol{u}_3(x,y) \\ & + (-1)^k \zeta_k \boldsymbol{u}_{4_Z}(x,y) \end{aligned} \tag{11.1}$$

Square angle-ply plates under distributed loads under simple supports and mixed clamped-free boundary conditions are studied. The length and width of the considered square plates are $a = b = 1$. The plates consist of plies with equal thickness, and the lamination sequences are described from bottom to top.

By referring to Savoia and Reddy [206], in all the numerical examples, the following elastic properties are used for the orthotropic layers: $E_L = 25 \times 10^6$psi(174.6GPa, $E_T = 10^6$psi(7GPa), $G_{LT} = 0.5 \times 10^6$psi(3.5GPa), $G_{TT} = 0.2 \times 10^6$psi(1.4GPa), $\nu_{LT} = \nu_{TT} = 0.25$, where L and T respectively indicate fiber longitudinal and transverse directions.

The following non-dimensionalization parameters are adopted:

$$\begin{gathered}\bar{w} = 100w\frac{E_T h^3}{p_0 a^4}, \quad (\bar{\sigma}_{xx},\bar{\sigma}_{yy},\bar{\sigma}_{xy}) = (\sigma_{xy},\sigma_{yy},\sigma_{xy})\frac{h^2}{p_0 a^2}, \\ (\bar{\sigma}_{xz},\bar{\sigma}_{yz}) = (\sigma_{xz},\sigma_{yz})\frac{h}{p_0 a}, \quad \bar{\sigma}_{zz} = \sigma_{zz}/p_0, \quad \bar{z} = z/h.\end{gathered} \tag{11.2}$$

11.2.1 Case 1: Simply supported thick square plates with $(-15^\circ/15^\circ)$ and $(-30^\circ/30^\circ/-30^\circ/-30^\circ)$

This numerical example includes two angle-ply laminate plates with anti-symmetric stacking sequences under simple supports and are subjected to bi-sinusoidal distributed pressure on both top and bottom surfaces. The considered cases include: a plate with $(-15^\circ/15^\circ)$ and length-to-thickness ratio $a/h = 4$, and a plate with $(-30^\circ/30^\circ/-30^\circ/30^\circ)$ and length-to-thickness ratio $a/h = 10$. The imposed pressure follows:

$$p_t(x,y) = -\frac{p_0}{2}\sin\frac{\pi x}{a}\sin\frac{\pi y}{b}, \quad p_b(x,y) = -\frac{p_0}{2}\sin\frac{\pi x}{a}\sin\frac{\pi y}{b} \tag{11.3}$$

where the subscripts t and b represent the top and bottom surfaces, respectively.

The analytical solutions to the studied problems were proposed by Savoia and Reddy [206]. Note that the boundary conditions used here are different from those used by Savoia and Reddy [206]. For these angle-ply laminated plates, the whole structures need to be modeled. By increasing the mesh density and the number of expansions used in the thickness functions, the numerical convergence can be gradually achieved under the relative error threshold of 2%. The ABAQUS 3D models employ eight layers of brick elements through the thickness of each composite ply, and the elements have an aspect ratio (in-plane dimension over thickness) of 6.4 for the two-layered plate and 20 for the four-layered laminates, respectively.

The variation of stresses through the thickness is reported in Figs. 11.2 and 11.3, which shows that the used refined plate elements give results agreeing well with ABAQUS 3D modeling. Due to the difference in the boundary conditions, the obtained results are slightly different from those provided by Savoia and Reddy [206]. Also, it should be noted that the ESL models with trigonometric functions and zig-zag terms lead to accurate results when sufficiently refined, and the continuity of transverse shear stresses at layer interfaces is well approximated except for $\bar{\sigma}_{yz}$ on the four-layered plate. LW models with Chebyshev polynomials give good accuracy in all the cases. In the work of Savoia and Reddy [206], the signs of $\bar{\sigma}_{xy}$ and $\bar{\sigma}_{yz}$ are possibly inverted.

11.2.2 Case 2: Simply supported square plates with $(0^\circ/30^\circ)$

Two-layered square plates with lamination sequence $(0^\circ/30^\circ)$ under simply supported boundary conditions and bi-sinusoidal distributed pressure on both top and bottom surfaces are studied. The load distribution follows Eqn. (11.3). Span-to-thickness

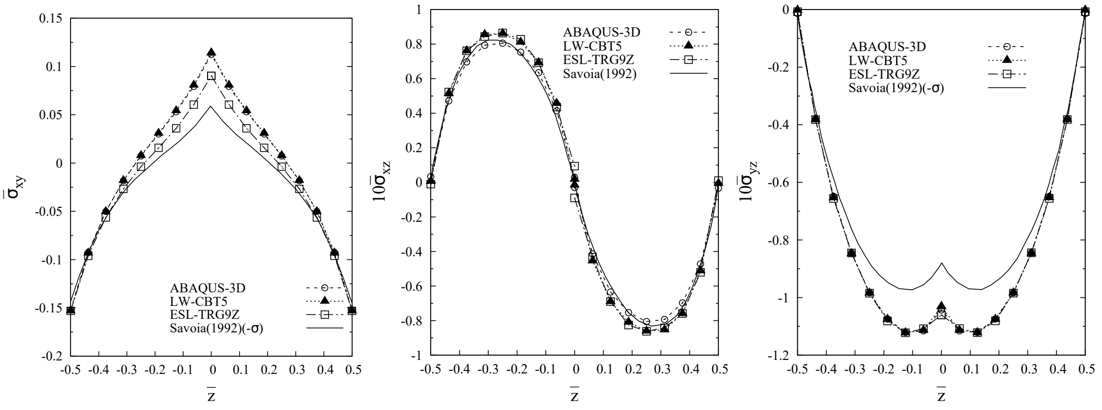

(a) $\bar{\sigma}_{xy}(\frac{a}{2}, \frac{b}{2}, \bar{z})$ (b) $\bar{\sigma}_{xz}(\frac{a}{2}, 0, \bar{z})$ (c) $\bar{\sigma}_{yz}(\frac{a}{2}, 0, \bar{z})$

Figure 11.2: Through-the-thickness variation of stresses on the simply supported square plate with (−15°/15°) under distributed pressure on top and bottom surfaces.

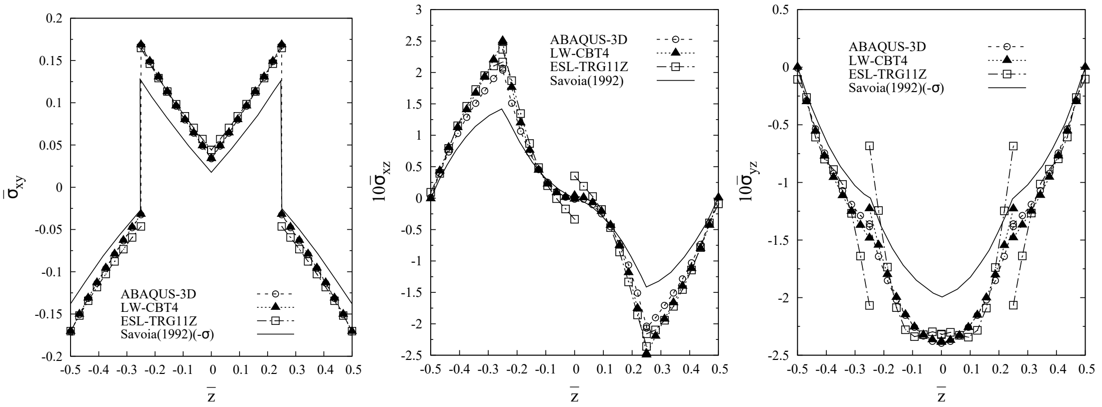

(a) $\bar{\sigma}_{xy}(\frac{a}{2}, \frac{b}{2}, \bar{z})$ (b) $\bar{\sigma}_{xz}(\frac{a}{2}, 0, \bar{z})$ (c) $\bar{\sigma}_{yz}(\frac{a}{2}, 0, \bar{z})$

Figure 11.3: Through-the-thickness variation of stresses on the simply supported square plate with (−30°/30°/ − 30°/30°) under distributed pressure on top and bottom surfaces.

ratios $a/h = 4$ and 50 are considered.

The numerical results obtained with variable kinematic models LW-CBT*n* and ESL-TRG*m*Z as well as ABAQUS 3D models are reported in Table. 11.2. The variations of stresses through the plate thickness at several positions are reported in Fig. 11.4. The obtained fields of σ_{yz} on the thick ($a/h = 4$) and thin ($a/h = 50$) plates are plotted in Fig. 11.5 and Fig. 11.6, respectively, where the thickness dimension is scaled by certain times for the convenience of observation.

From Table. 11.2, it can be observed that when the FE models are sufficiently refined, the results with different types of kinematics agree well with each other. Note that in the thin plate with $a/h = 50$, the in-plane mesh grid is 80×80 which leads to an aspect ratio

Table 11.2: Deflection and stresses on the simply supported square plates with (0°/30°) under bi-sinusoidal distributed pressure on top and bottom surfaces.

a/h	Kinematics	Mesh	$\bar{w}$ $(\frac{a}{2},\frac{b}{2},0)$	$\bar{\sigma}_{xx}$ $(\frac{a}{2},\frac{b}{2},\frac{-h}{2})$	$\bar{\sigma}_{yy}$ $(\frac{a}{2},\frac{b}{2},\frac{h}{2})$	$\bar{\sigma}_{xy}$ $(\frac{a}{2},\frac{b}{2},\frac{h}{2})$	$10\bar{\sigma}_{xz}$ $(\frac{a}{2},0,\frac{h}{4})$	$10\bar{\sigma}_{yz}$ $(\frac{a}{2},0,\frac{h}{4})$	$\bar{\sigma}_{zz}$ $(\frac{a}{2},\frac{b}{2},\frac{-h}{2})$	DOFs
4	LW-CBT4	8×8	-1.956	0.8171	-0.2299	-0.2561	-1.543	-1.483	0.5036	6069
	LW-CBT4	10×10	-1.957	0.8138	-0.2301	-0.2568	-1.534	-1.475	0.5032	9261
	LW-CBT5	10×10	-1.957	0.8139	-0.2301	-0.2569	-1.487	-1.453	0.5012	11907
	LW-CBT6	10×10	-1.957	0.8139	-0.2301	-0.2569	-1.487	-1.453	0.5004	14553
	ESL-TRG7Z	10×10	-1.957	0.8131	-0.2299	-0.2566	-1.546	-1.486	0.5036	11907
	ESL-TRG9Z	10×10	-1.958	0.8139	-0.2301	-0.2569	-1.498	-1.458	0.5052	14553
	ESL-TRG11Z	10×10	-1.958	0.8138	-0.2300	-0.2569	-1.482	-1.450	0.4984	17199
	ABAQUS-3D	10×10	-1.941	0.8067	-0.2298	-0.2571	-1.451	-1.449	0.5017	23199
50	LW-CBT3	18×18	-0.7833	0.6175	-0.1578	-0.1937	-8.897	-3.256	0.5410	20535
	LW-CBT3	20×20	-0.7836	0.6174	-0.1579	-0.1939	-9.093	-3.287	0.5430	25215
	LW-CBT4	20×20	-0.7836	0.6174	-0.1579	-0.1939	-9.091	-3.286	0.5010	35301
	ESL-TRG11Z	20×20	-0.7836	0.6173	-0.1579	-0.1939	-9.026	-3.147	0.5635	65559
	ESL-TRG13Z	20×20	-0.7836	0.6174	-0.1579	-0.1939	-9.000	-3.240	0.5070	75645
	ABAQUS-3D	50×50	-0.7846	0.6170	-0.1581	-0.1944	-8.719	-2.981	0.5025	517599
	ABAQUS-3D	80×80	-0.7848	0.6169	-0.1581	-0.1944	-9.154	-3.036	0.5025	1310499

of 10 for the brick elements. Regarding $\bar{\sigma}_{yz}$, a slight difference can be noticed between the results obtained with refined plate elements and C3D20R elements, as shown in Fig. 11.4c. The comparisons demonstrate that the adopted variable kinematic refined plate elements with LW-CBT*n* and ESL-TRG*m*Z are effective and more efficient than brick elements in the modeling of thin layered plates. Also, such refined plates are not limited by the aspect ratio that has to be considered for brick elements.

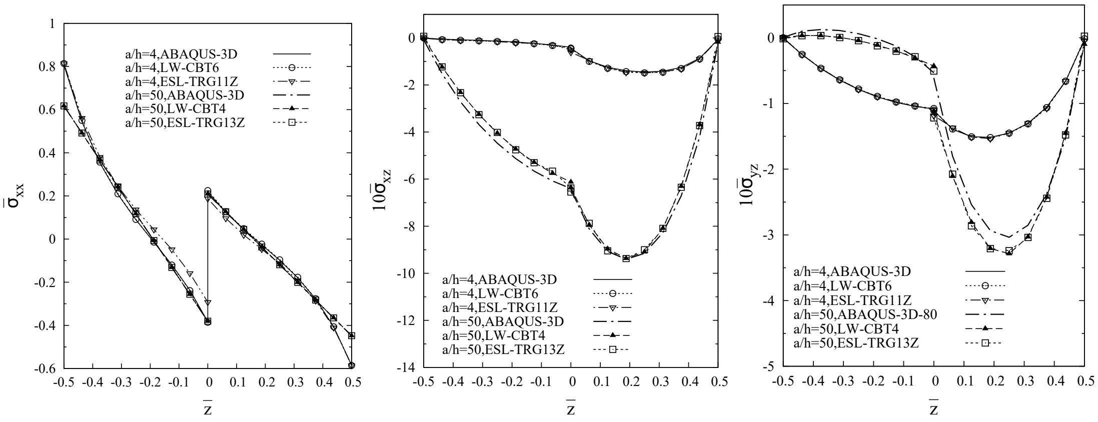

(a) $\bar{\sigma}_{xx}(\frac{a}{2},\frac{b}{2},\bar{z})$ (b) $\bar{\sigma}_{xz}(\frac{a}{2},0,\bar{z})$ (c) $\bar{\sigma}_{yz}(\frac{a}{2},0,\bar{z})$

Figure 11.4: Distribution of stresses through the thickness of the simply supported square plates with (0°/30°) under bi-sinusoidal distributed load on top and bottom surfaces.

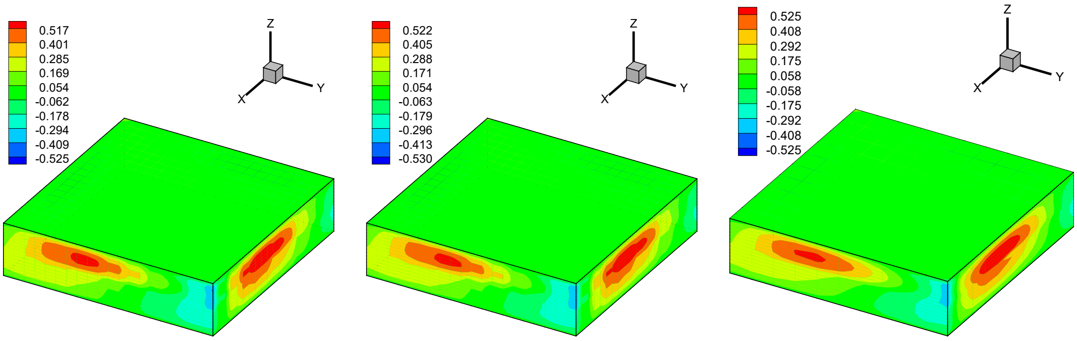

(a) LW-CHT6, Mesh 10×10 (b) ESL-TRG11Z, Mesh 10×10 (c) ABAQUS-3D, Mesh 10×10

Figure 11.5: σ_{yz} on the simply supported thick ($a/h = 4$) plate with (0°/30°), $z \times 1$.

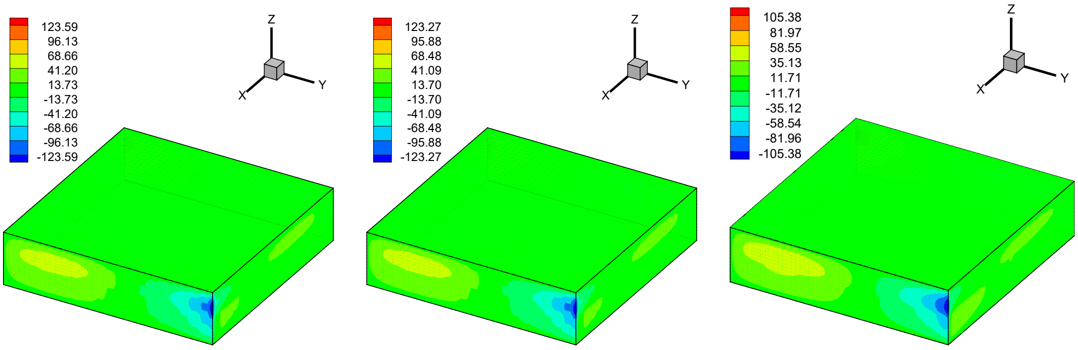

(a) LW-CHT4, Mesh 20×20 (b) ESL-TRG13Z, Mesh 20×20 (c) ABAQUS-3D, Mesh 80×80

Figure 11.6: σ_{yz} on the simply supported thin ($a/h = 50$) plate with (0°/30°), $z \times 12.5$.

It should be pointed out that, in brick elements in most commercial software, stresses on integration points are more accurate yet stresses outputted on nodes are extrapolated from results on the integration points. In the current work, in the CUF-based plate FE models, strains on an arbitrary point are calculated by considering $\boldsymbol{\varepsilon} = (\mathbf{b}\, N_i F_\tau)\boldsymbol{u}_{i\tau}$.

11.2.3 Case 3: Simply supported square plates with (−45°/45°)

In the above assessments, the refined plate FE models LW-CBTn and ESL-TRGmZ have been verified. This section reports numerical study on simply supported square plates with lamination (−45°/45°), and both thin and thick cases are considered. The two layers have equal thickness $h/2$. A constant pressure load p_0 is imposed on the top surface. Various length-to-thickness ratios $a/h = 4, 20, 100$ are considered.

The obtained results are summarized in Table. 11.3. It can be observed that thinner laminated plates tend to require better-refined mesh to achieve numerical accuracy. Also, when a sufficient number of expansions are used in the thickness functions, the refined ESL kinematics give comparable accuracy with the LW kinematics used. The through-the-thickness variations of stresses obtained with LW-CBTn models are shown in Fig. 11.7.

Table 11.3: Deflection and stresses on the simply supported square plates with (−45°/45°) under constant pressure on the top surface.

a/h	Kinematics	Mesh	$\bar{w}$ $(\frac{a}{2},\frac{b}{2},\frac{h}{2})$	$\bar{\sigma}_{xx}$ $(\frac{a}{2},\frac{b}{2},\frac{h}{2})$	$\bar{\sigma}_{yy}$ $(\frac{a}{2},\frac{b}{2},\frac{h}{2})$	$\bar{\sigma}_{xy}$ $(\frac{a}{2},\frac{b}{2},\frac{-h}{2})$	$10\bar{\sigma}_{xz}$ $(\frac{a}{2},0,\frac{h}{4})$	$10\bar{\sigma}_{yz}$ $(\frac{a}{2},0,\frac{h}{4})$	$\bar{\sigma}_{zz}$ $(\frac{a}{2},\frac{b}{2},\frac{h}{2})$	DOFs
4	LW-CBT4	8×8	3.227	0.5423	0.5423	0.4046	3.262	5.400	0.9976	6069
	LW-CBT4	10×10	3.227	0.5453	0.5453	0.4073	3.269	5.431	1.000	9261
	LW-CBT5	10×10	3.229	0.5454	0.5454	0.4074	3.167	5.316	1.001	11907
	LW-CBT6	10×10	3.229	0.5454	0.5454	0.4073	3.169	5.319	0.9988	14553
	ESL-TRG7Z	10×10	3.224	0.5443	0.5443	0.4066	3.333	5.472	0.9902	11907
	ESL-TRG9Z	10×10	3.228	0.5453	0.5453	0.4073	3.187	5.353	1.005	14553
	ESL-TRG11Z	10×10	3.228	0.5453	0.5453	0.4073	3.150	5.325	0.9951	17199
20	LW-CBT3	10×10	1.245	0.3727	0.3727	0.2907	3.723	5.531	1.057	6615
	LW-CBT3	12×12	1.246	0.3737	0.3737	0.2916	3.789	5.620	1.059	9375
	LW-CBT4	12×12	1.246	0.3737	0.3737	0.2916	3.788	5.619	0.9975	13125
	LW-CBT5	12×12	1.246	0.3737	0.3737	0.2916	3.771	5.600	0.9973	16875
	ESL-TRG7Z	12×12	1.245	0.3733	0.3733	0.2914	3.949	5.807	1.036	16875
	ESL-TRG9Z	12×12	1.246	0.3737	0.3737	0.2916	3.776	5.610	1.013	20625
	ESL-TRG11Z	12×12	1.246	0.3737	0.3737	0.2916	3.742	5.592	0.9947	24375
100	LW-CBT3	14×14	1.056	0.3493	0.3493	0.2751	3.213	4.823	1.003	12615
	LW-CBT3	16×16	1.057	0.3496	0.3496	0.2754	3.225	4.883	1.031	16335
	LW-CBT4	16×16	1.057	0.3496	0.3496	0.2754	3.221	4.880	1.000	22869
	ESL-TRG9Z	16×16	1.057	0.3495	0.3495	0.2753	2.763	3.773	1.196	35937
	ESL-TRG11Z	16×16	1.057	0.3496	0.3496	0.2754	3.195	4.982	1.034	42471

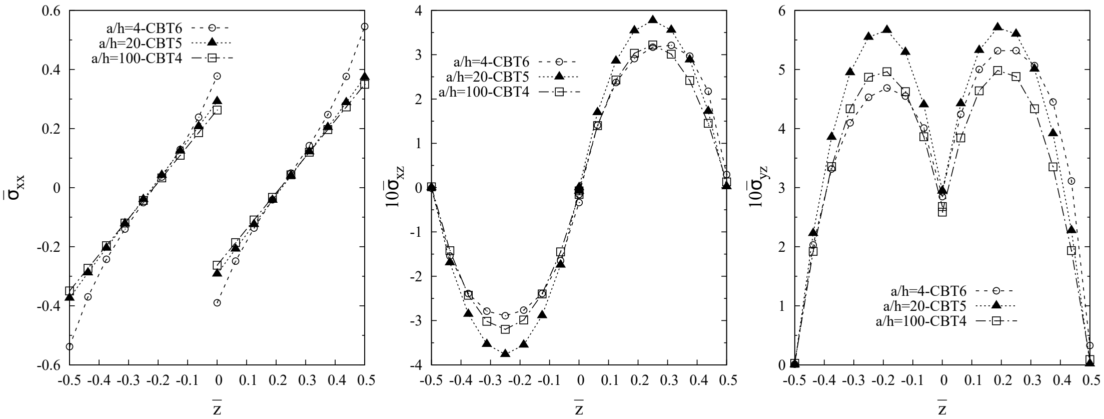

(a) $\bar{\sigma}_{xx}(\frac{a}{2},\frac{b}{2},\bar{z})$ (b) $\bar{\sigma}_{xz}(\frac{a}{2},0,\bar{z})$ (c) $\bar{\sigma}_{yz}(\frac{a}{2},0,\bar{z})$

Figure 11.7: Through-the-thickness distribution of stresses on the simply supported square plate with (−45°/45°) under constant pressure on the top surface.

11.2.4 Case 4: Simply supported square plates with (−45°/0°/90°/45°)

This section presents numerical solutions for a simply supported square laminated plate with lamination (−45°/0°/90°/45°). Length-to-thickness ratios $a/h = 4$ and 50 are considered. The imposed bi-sinusoidal pressure on the top surface follows:

$$p_t(x, y) = p_0 \sin \frac{\pi x}{a} \sin \frac{\pi y}{b} \tag{11.4}$$

The numerical results at several monitoring points are reported in Table. 11.4, from which it can be observed that the ESL-TRG*m*Z models suffer from a slow convergence rate in the thin plate case $a/h = 50$.

Table 11.4: Deflection and stresses on the simply supported square plates with (−45°/0°/90°/45°) under bi-sinusoidal distributed pressure on the top surface.

a/h	Kinematics	Mesh	$\bar{w}$ $(\frac{a}{2},\frac{b}{2},\frac{h}{2})$	$\bar{\sigma}_{xx}$ $(\frac{a}{2},\frac{b}{2},\frac{h}{2})$	$\bar{\sigma}_{yy}$ $(\frac{a}{2},\frac{b}{2},\frac{h}{2})$	$\bar{\sigma}_{xy}$ $(\frac{a}{2},\frac{b}{2},\frac{-h}{2})$	$10\bar{\sigma}_{xz}$ $(\frac{a}{2},0,\frac{3h}{8})$	$10\bar{\sigma}_{yz}$ $(\frac{a}{2},0,\frac{h}{8})$	$\bar{\sigma}_{zz}$ $(\frac{a}{2},\frac{b}{2},\frac{h}{2})$	DOFs
4	LW-CBT3	6×6	2.517	0.3913	0.3834	0.2421	1.259	3.060	1.016	4563
	LW-CBT3	8×8	2.518	0.3935	0.3856	0.2453	1.263	3.057	1.014	7803
	LW-CBT4	8×8	2.518	0.3933	0.3854	0.2453	1.266	3.058	1.001	11271
	ESL-TRG9Z	8×8	2.508	0.3925	0.3841	0.2445	1.154	3.010	1.004	9537
	ESL-TRG11Z	8×8	2.510	0.3924	0.3842	0.2445	1.148	3.060	1.003	11271
50	LW-CBT3	14×14	0.6846	0.1791	0.1650	0.1159	0.4639	3.485	1.016	22707
	LW-CBT3	16×16	0.6852	0.1793	0.1651	0.1161	0.4537	3.559	1.012	29403
	LW-CBT4	16×16	0.6852	0.1792	0.1651	0.1161	0.4552	3.558	1.000	42471
	ESL-TRG11Z	16×16	0.6847	0.1793	0.1651	0.1160	0.3534	3.572	1.651	42471
	ESL-TRG13Z	16×16	0.6848	0.1792	0.1650	0.1160	0.4473	3.595	0.5273	49005
	ESL-TRG15Z	16×16	0.6849	0.1792	0.1651	0.1160	0.5329	3.589	1.095	55539
	ESL-TRG17Z	16×16	0.6849	0.1792	0.1651	0.1160	0.4852	3.590	1.065	62073

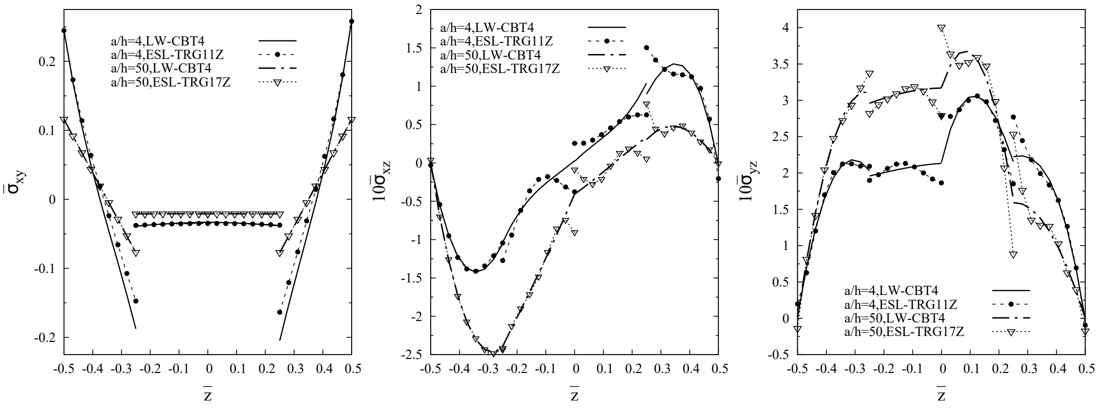

(a) $\bar{\sigma}_{xy}(\frac{a}{2},\frac{b}{2},\bar{z})$ (b) $\bar{\sigma}_{xz}(\frac{a}{2},0,\bar{z})$ (c) $\bar{\sigma}_{yz}(\frac{a}{2},0,\bar{z})$

Figure 11.8: Through-the-thickness distribution of stresses on the simply supported plates with (−45°/0°/90°/45°) under bi-sinusoidal distributed pressure on the top surface.

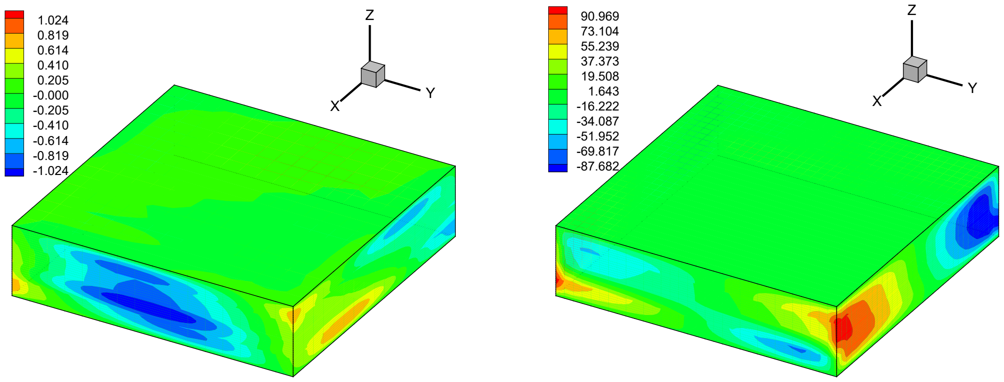

(a) σ_{xz}, $a/h = 4$, $z \times 1$, LW-CBT4 (b) σ_{xz}, $a/h = 50$, $z \times 12.5$, LW-CBT4

Figure 11.9: σ_{xz} on the simply supported plates with (−45°/0°/90°/45) under bi-sinusoidal distributed pressure on the top surface.

The variations of stresses through the thickness are given in Fig. 11.8. Regarding the interfacial continuity of the transverse shear stresses σ_{xz} and σ_{yz}, LW-CBT*n* models give more satisfactory results than ESL-TRG*m*Z models do in capturing the zig-zag effects. The σ_{xz} fields of both the thick and thin plates are shown in Figs. 11.9a and 11.9b, which shows that the variable kinematic refined plate models can give detailed 3D stress fields for laminated structures.

11.2.5 Case 5: Square plates with (0°/60°) under mixed clamped-free boundary conditions

Square plates with lamination (0°/60°) under constant pressure load $p_0/2$ on the top and bottom surfaces are investigated in this section. The two layers have equal thickness $h/2$. The considered span-to-thickness ratios include $a/h = 10$ and 50. The adopted mixed clamped-free boundary conditions (denoted as CFCC) are: clamped on edge $x = 0$, free on edge $y = 0$, clamped on edge $x = a$, and clamped on edge $y = b$.

The obtained displacement and stress evaluations are summarized in Table. 11.5. In this case, ESL-TRG*m*Z models achieved results with comparable accuracy with LW-CBT*n* models at the costs of more DOFs. The variations of stresses through the thickness displayed in Fig. 11.10 show that the ESL and LW models lead to results in great agreement with the solutions presented by Nik and Tahani [169].

Table 11.5: Deflection and stresses on the square plates with (0°/60) under constant pressure on the top and bottom surfaces respectively and mixed boundary conditions CFCC.

a/h	Kinematics	Mesh	$\bar{w}$ $(\frac{a}{2},\frac{b}{2},\frac{h}{2})$	$\bar{\sigma}_{xx}$ $(\frac{a}{2},\frac{b}{2},\frac{-h}{2})$	$\bar{\sigma}_{yy}$ $(\frac{a}{2},\frac{b}{2},\frac{h}{2})$	$\bar{\sigma}_{xy}$ $(\frac{a}{4},\frac{b}{4},\frac{h}{2})$	$\bar{\sigma}_{xz}$ $(\frac{a}{4},\frac{b}{4},\frac{-h}{4})$	$\bar{\sigma}_{yz}$ $(\frac{a}{2},\frac{b}{4},\frac{h}{4})$	$\bar{\sigma}_{zz}$ $(\frac{a}{2},\frac{b}{2},\frac{h}{2})$	DOFs
10	LW-CBT3	8×8	0.7987	-0.5601	0.2196	0.09479	0.5288	0.08173	0.5250	4335
	LW-CBT3	12×12	0.7992	-0.5521	0.2156	0.08228	0.5204	0.08187	0.5311	9375
	LW-CBT4	12×12	0.7994	-0.5518	0.2155	0.08424	0.5202	0.08219	0.5001	13125
	LW-CBT5	12×12	0.7996	-0.5517	0.2157	0.08774	0.5194	0.08067	0.5007	16875
	ESL-TRG11Z	12×12	0.7996	-0.5516	0.2157	0.09352	0.5185	0.08089	0.4975	24375
	ESL-TRG13Z	12×12	0.7997	-0.5517	0.2154	0.09528	0.5156	0.07977	0.4934	28125
50	LW-CBT3	16×16	0.4982	-0.5333	0.2021	0.05675	0.5322	0.09120	0.5345	16335
	LW-CBT3	20×20	0.4984	-0.5321	0.2017	0.05510	0.5292	0.09111	0.5285	25215
	LW-CBT4	20×20	0.4984	-0.5320	0.2018	0.05589	0.5295	0.09101	0.5022	35301
	LW-CBT5	20×20	0.4984	-0.5320	0.2018	0.05649	0.5290	0.09032	0.4970	45387
	ESL-TRG9Z	20×20	0.4984	-0.5321	0.2017	0.05510	0.5292	0.09111	0.5285	55473
	ESL-TRG11Z	20×20	0.4984	-0.5320	0.2015	0.05693	0.5297	0.08992	0.4978	65559

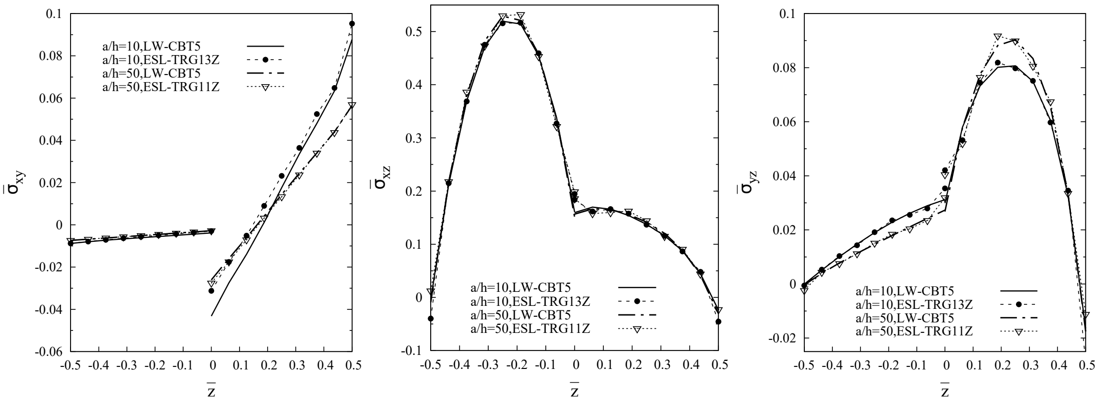

(a) $\bar{\sigma}_{xy}(\frac{a}{4},\frac{b}{4},\bar{z})$ (b) $\bar{\sigma}_{xz}(\frac{a}{4},\frac{b}{4},\bar{z})$ (c) $\bar{\sigma}_{yz}(\frac{a}{4},\frac{b}{4},\bar{z})$

Figure 11.10: Through-the-thickness variation of stresses on the plates with (0°/60°) under constant pressure on the top and bottom surfaces and mixed boundary conditions.

11.3 Conclusions

In this chapter, angle-ply laminated plates under various loads and boundary conditions are modeled through variable kinematic LW models adopting Chebyshev polynomials and ESL models using trigonometric series. “Soft” simply supported and mixed clamped-free boundary conditions are considered.

The following conclusions can be drawn based on the numerical investigation:

1. When serving as thickness functions in LW approach, Chebyshev polynomials give great accuracy and continuous transverse shear stresses at layer interfaces;

2. In ESL approach, trigonometric series can be used as kinematic assumptions, and give accurate solutions in general when used together with a Murakami zig-zag term though fail in capturing interfacial continuity of transverse shear stresses in some cases;
3. In some thin laminated plates, trigonometric thickness functions may encounter a slow convergence rate in variable kinematic models.

Numerical results for several angle-ply laminated plates are presented, which can be adopted as new benchmark cases.

Chapter 12

Evaluation of shear and membrane locking in hierarchical shell elements

The hierarchical concept of finite elements (*p*-version) can be traced back to the 1970s [179, 225, 267]. The numerical efficiency of the hierarchical elements has been reported by many researchers [86, 226, 222, 224].

The locking phenomena are caused by the greatly overestimated stiffness of thin structures and will lead to a loss of convergence rate of the numerical solution. If no treatment is introduced, the meshes of the shell FE models have to be immensely refined, which probably makes the analysis numerically prohibitive. Shear locking, caused by the so-called "parasitic shear" in the bending of a thin shell, is a typical locking phenomenon [269]. Due to the incompetence of the shell elements in capturing the bending deformation appropriately, the strain energy is absorbed by the shear mode erroneously. As the shell structures become thinner, the transverse shear energy approaches zero, mathematically. On the other hand, membrane locking can be observed on shell elements when bending deformation is incorrectly accompanied by the stretching of the mid-surface, and the membrane energy overshadows the bending part [216, 21].

Pioneering simple remedies to the locking phenomena are the reduced integration and selectively reduced integration techniques [269, 108]. Zienkiewicz, Taylor, and Too [269] pointed out that by reducing the order of numerical integration, the stiffness of displacement-based finite elements can be decreased. The main idea of selective integration is to reduce the shear stiffness, thus the reduced quadrature is selectively used on the stiffness component related to transverse shearing. This method is reported to be useful in bending problems yet was found less effective compared with uniformly reduced integration on all the stiffness components for general shell problems [269]. This reduced integration approach brings significant improvement to the convergence rate. The equivalence of the reduced integration procedure with mixed formulation was demonstrated by Hughes, Cohen, and Haroun [108] and Zienkiewicz and Nakazawa [268].

A drawback of the reduced integration technique is the introduction of "spurious modes" due to the erroneously evaluated stiffness matrix. A typical example is the "hour-glass" mode of four-node bi-linear shell elements with reduced integration. Zienkiewicz and Taylor [272] commented that for general applications mixed elements are preferred to reduced integration procedures. This numerical singularity problem can also be avoided by using alternative techniques such as the Mixed Interpolation of Tensorial Components (MITC) proposed by Bathe et al. [87, 16, 34, 17]. In the MITC formulation, the shear locking can be overcome by the additional independent interpolation functions for the transverse shear strains. This approach is also referred to as the "assumed shear strain field" method [52]. The link between MITC formulation and the Hellinger-Reissner mixed variation principle was demonstrated by Bathe, Iosilevich, and Chapelle [17]. The mathematical justification of MITC formulation was established through the Babuska-Brezzi conditions [11]. In the framework of CUF, MITC has been successfully applied to build locking-free refined elements with variable kinematics for the multi-layered plates [44, 60, 43] and shell structures [69, 60]. Very recent developments of four-node MITC elements were presented by Ko, Lee, and Bathe [137, 136].

Indeed, shear locking effects are more pronounced on low-order elements [15]. The loss of convergence can be alleviated by adopting higher order elements [221, 210], such as higher-order hierarchical elements [86, 226]. Combination of hierarchical elements and mixed interpolation method was proposed and applied to isotropic plates based on Reissner-Mindlin assumption by Scapolla and Della Croce [207, 208]. Application of hierarchical elements using Naghdi shell model on isotropic structures was reported by Chinosi, Della Croce, and Scapolla [67]. The selective and reduced integration schemes on hierarchical elements were primarily discussed by Della Croce and Scapolla [81]. Li et al. [147] reported a comparison of MITC and plain hierarchical elements with full integration regarding the mitigation of shear on refined plate elements for multi-layered structures.

In this chapter, an evaluation of hierarchical elements concerning the mitigation of shear and membrane locking phenomena in the analysis of multi-layered shells is presented. Numerically efficient full, reduced, and selective integration schemes in hierarchical 2D elements are discussed. The alleviation of shear and membrane locking phenomena in hierarchical shell elements is demonstrated through two numerical examples, respectively.

12.1 Integration schemes for hierarchical elements

This section addresses the efficient integration schemes of 2D hierarchical elements with full, reduced, and reduced integration. According to Szabó and Babuška [224] and Szabó, Düster, and Rank [226], the hierarchical shape functions for 2D elements can be expressed as in Eqn. (2.27). The *nodal (vertex) modes*, *edge (side) modes*, and *surface (internal) modes* are illustrated in Fig. 2.7. In the FNs of stiffness matrix as given by

Eqn. (4.55), the contribution of the shape functions to the stiffness matrix includes the following integrals:

$$\begin{aligned}
&\lhd N_i N_j \rhd_\Omega, && \lhd N_i N_{j,\alpha} \rhd_\Omega, && \lhd N_i N_{j,\beta} \rhd_\Omega,\\
&\lhd N_{i,\alpha} N_j \rhd_\Omega, && \lhd N_{i,\beta} N_j \rhd_\Omega, && \lhd N_{i,\alpha} N_{j,\alpha} \rhd_\Omega,\\
&\lhd N_{i,\alpha} N_{j,\beta} \rhd_\Omega, && \lhd N_{i,\beta} N_{j,\alpha} \rhd_\Omega, && \lhd N_{i,\beta} N_{j,\beta} \rhd_\Omega .
\end{aligned} \tag{12.1}$$

where $\lhd \cdots \rhd_\Omega$ represents $\int_\Omega \cdots \, d\xi d\eta$. Among these terms, for given i and j combination, the highest polynomial order that of $N_i \cdot N_j$. Assume that $N_i(\xi,\eta) = \phi_m(\xi)\phi_n(\eta)$ and $N_j(\xi,\eta) = \phi_r(\xi)\phi_s(\eta)$, the product of N_i and N_j will read:

$$N_i(\xi,\eta) \cdot N_j(\xi,\eta) = \phi_m(\xi)\phi_n(\eta) \cdot \phi_r(\xi)\phi_s(\eta) = \phi_m(\xi)\phi_r(\xi) \cdot \phi_n(\eta)\phi_s(\eta) \tag{12.2}$$

where the polynomial orders of $\phi_m(\xi)$, $\phi_r(\xi)$, $\phi_n(\eta)$, and $\phi_s(\eta)$ are M, R, N, S, separately. Thus in the ξ and η directions, the highest polynomial orders are $M + R$ and $N + S$, respectively. For simplicity, in the present work, the same set of Gauss points are used to calculate the above integrals of given N_i and N_j.

12.1.1 Full integration scheme

In Gauss-Legendre quadrature, n Gauss points can guarantee the exact integration of a polynomial of order $2n - 1$. For the exact integration of $\lhd N_i N_j \rhd_\Omega$, the least number of Gauss points used in the ξ direction, N_{GX}, should be:

$$N_{GX} = \begin{cases} (M+R)/2 + 1, & \text{if } M + R = 2n; \\ (M+R+1)/2, & \text{if } M + R = 2n + 1. \end{cases} \tag{12.3}$$

wherein n is an arbitrary positive integer. The above expression also applies to the number of Gauss points N_{GY} for exact integration in the η direction.

For classical Lagrangian elements, since all the shape functions have the same polynomial order in both ξ and η directions, the scheme of Gauss points can be uniformly decided. Differently, for hierarchical elements, the required number of Gauss points varies according to different combinations of shape functions. Also, in practice, for given N_i and N_j, the same set of Gauss integration points can be used for the nine integrals in Eqn. (12.1), and these Gauss points are determined by the highest polynomial orders given by $N_i \cdot N_j$. Fig. 12.1 presents two examples of the Gauss points distribution when full integration is used on hierarchical elements. Fig. 12.1a shows the numerical calculation of $\lhd N_{13} \cdot N_{14} \rhd_\Omega$ needs 3×3 Gauss points. $\lhd N_{13} \cdot N_{15} \rhd_\Omega$ requires 5×2 Gauss points for its full integration, as illustrated in Fig. 12.1b.

12.1.2 Reduced integration scheme

In the current chapter, the reduced integration technique on the hierarchical elements is used in the following manners: applying the reduced integration to $N_i \cdot N_j$

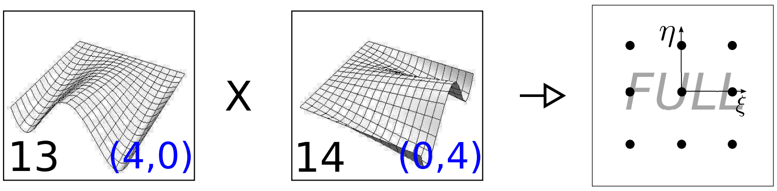

(a) $\lhd N_{13} \cdot N_{14} \rhd_{\Omega}$

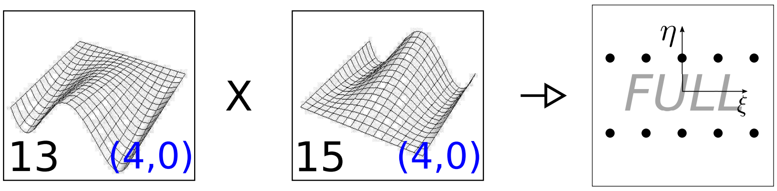

(b) $\lhd N_{13} \cdot N_{15} \rhd_{\Omega}$

Figure 12.1: Gauss points used for the full integration of hierarchical shell elements. "FULL" represents the adoption of the full integration approach.

combinations with the highest polynomial order, and using the full integration for all the lower-order combinations. In the hierarchical element with polynomial degree p, as shown in Fig. 2.7, $N_i \cdot N_j$ with the highest orders is the combination of edge modes:

$$N_i \cdot N_j = \begin{cases} \phi_p(\xi)\phi_1(\eta) \cdot \phi_p(\xi)\phi_0(\eta), & \text{in } \xi \text{ direction;} \\ \phi_1(\xi)\phi_p(\eta) \cdot \phi_0(\xi)\phi_p(\eta), & \text{in } \eta \text{ direction.} \end{cases} \tag{12.4}$$

The highest order of the polynomials to be integrated is $2p$, and p Gauss points are needed for the reduced integration. The product polynomials to be integrated in the other direction are of the second-order and will be fully integrated by using two Gauss points. Meanwhile, all of the lower-order terms should be exactly integrated.

This approach can be explained by taking hierarchical element with $p = 4$ as an example. The polynomials to be integrated with the highest order in the ξ direction are $N_{13} \cdot N_{13}$, $N_{13} \cdot N_{15}$, $N_{15} \cdot N_{13}$, and $N_{15} \cdot N_{15}$. Those with the highest order in the η direction are $N_{14} \cdot N_{14}$, $N_{14} \cdot N_{16}$, $N_{16} \cdot N_{14}$, and $N_{16} \cdot N_{16}$. When reduced integration scheme is adopted, 4×2 Gauss points should be used for the first group of polynomials (see Fig. 12.2a), and a 2×4 mesh of Gauss points for the second set (see Fig. 12.2b).

For this fourth-order hierarchical element, the interpolation schemes that should be used for different blocks of the stiffness matrix have been indicated in Fig. 12.3. Note that each block represented by a square is a sub-matrix $\boldsymbol{K}_{ij}$ of the element stiffness matrix.

12.1.3 Selectively reduced integration scheme

In the selectively reduced integration, the low-order integration is only applied to those terms related to the transverse shear stiffness. This technique is aimed to reduce

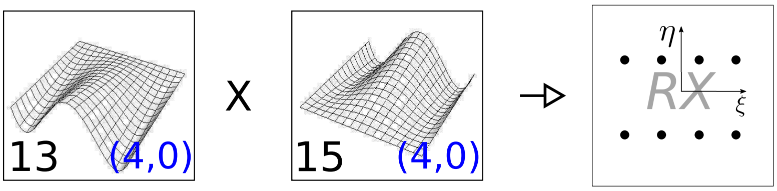
13
(4,0)
X
15
(4,0)
η
RX
ξ

(a) $\lhd N_{13} \cdot N_{15} \rhd_{\Omega}$

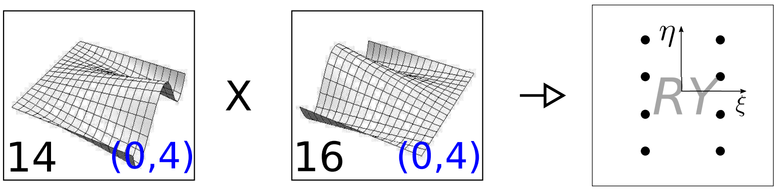
14
(0,4)
X
16
(0,4)
η
RY
ξ

(b) $\lhd N_{14} \cdot N_{16} \rhd_{\Omega}$

Figure 12.2: Gauss points used for the reduced integration of hierarchical shell elements with $p = 4$. “RX” and “RY” indicate reduced integration in the ξ and η directions, respectively.

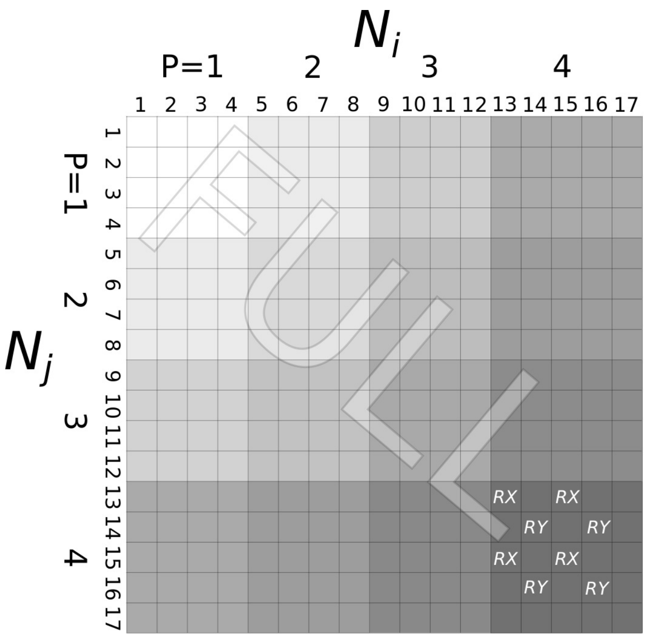
N_i
P=1
2
3
4
1 2 3 4 5 6 7 8 9 10 11 12 13 14 15 16 17
N_j
P=1
2
3
4
1 2 3 4 5 6 7 8 9 10 11 12 13 14 15 16 17
FULL
RX RX
RY RY
RX RX
RY RY

Figure 12.3: Reduced integration scheme for an hierarchical element with $p = 4$. “RX”: reduced integration in the ξ direcion; “RY”: reduced integration in the η direction; “FULL”: full integration in both directions.

the transverse shear stiffness to alleviate the shear locking phenomenon. These components can be determined by considering the FNs of the transverse shear stiffness matrix in Eqn. (4.104). Also, the sub-matrices of the stiffness matrix $\boldsymbol{K}_{ij}$ that should be selectively integrated follow the same rule of the reduced integration technique as discussed in Section 12.1.2.

12.1.4 Properties of the stiffness matrix of hierarchical elements with reduced and selective integration

When reduced and selective integration techniques are used on low-order Lagrangian elements, spurious modes may appear. In this section, the eigenvalues of hierarchical elements with reduced and selective integration are calculated to examine the properties of their stiffness matrices.

The adopted FE models consist of only one element which has the in-plane geometry of 1×1 and contains only one layer with thickness $h = 1$. The used isotropic material has $E = 10^9$ and $\nu = 0.3$. The theory of structures (TOS) chosen is LE1 (LW model with Lagrangian first-order polynomials). A plate model without curvatures is used which is adequate for the examination.

Fig.12.4 reports the eigenvalues of the stiffness matrices of hierarchical elements ($p = 1,2,3$) via reduced and selective integration approaches. Note that hierarchical elements with $p = 1$ are equivalent to standard Q4 (four-node quadrilateral Lagrangian) elements. Fig. 12.4a shows that when $p = 1$, both reduced and selective integration schemes lead to more than six numerical zero eigenvalues, which means the elements are not robust. From Fig. 12.4b, it can be observed that for polynomial degree $p = 2$, the reduced integration leads to two spurious modes (which is equivalent to the number of thickness functions used), and the element with selective integration has exactly six rigid-body modes. When the polynomial degree is further increased to $p = 3$, the spurious modes are eliminated on the elements with reduced integration (see Fig. 12.4c). The results demonstrate that, for hierarchical elements, it can be guaranteed that there is zero spurious mode when reduced integration approach is used given that $p \geq 3$, and no spurious mode exists for selective integration when $p \geq 2$.

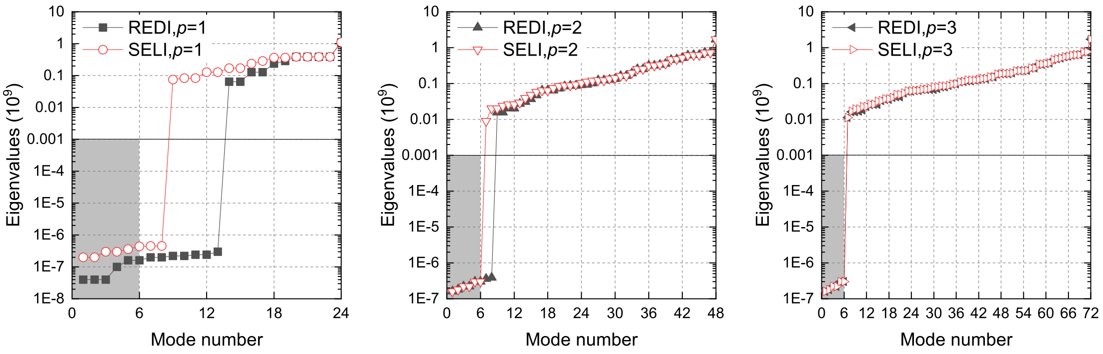

(a) $p = 1$ (b) $p = 2$ (c) $p = 3$

Figure 12.4: Eigenvalues of hierarchical elements with reduced integration (REDI) and selective integration (SELI).

12.2 Results and discussion

In this section, two numerical examples on laminated shells with a wide range of aspect ratio are presented. Single-element FE models are used with p-version refinements. It is obvious that an element with only linear shape functions is not adequate for the modeling, thus the refinement of the shape functions starts from $p = 2$. The polynomial degree is increased till the chosen convergence threshold is reached. Two kinds of TOS are used in the numerical modeling, namely the FSDT and LE4 (LW model with fourth-order Lagrange polynomials in each layer). These two theories are compared through elements with full integration. Then, with LE4 theory, different integration techniques on the hierarchical elements are compared, including full integration (FULL), reduced integration (REDI), and selective integration (SELI). Besides the displacement and stress evaluations, the strain energy components are also reported. The numerical results are compared against available analytical reference solutions.

12.2.1 Shear locking: cylindrical shells under distributed pressure

In this section, the benchmark case presented by Varadan and Bhaskar [244] is used. The geometric features, material properties, and dimensionless parameters (see Eqn. 7.2) have been described in Section 7.1. The studied cases here are three-layered cylindrical shells with symmetric lamination (0°/90°/0°). The three layers have equal thickness $h/3$. Radius-to-thickness ratios R_β/h ranging from 2 to 500 are considered.

By taking advantage of the symmetric features in the cylinder axial direction and the cyclic conditions in the circumferential direction, 1/16 of the structure is taken to build the FE model, as indicated by the shaded zone in Fig. 7.1a. The 1/16 FE models contain only one element, and the numerical accuracy is improved by increasing the polynomial degree gradually when the relative difference compared to the one-order-lower case is less than 1% regarding the deflection and stresses as well as the energy components. Considering the load distribution, this benchmark is quite challenging for a single-element model. Table 12.1 summarizes the converged solutions for each radius-to-thickness ratio value. In general, as the shell structure gets thinner, a higher polynomial degree is required to achieve the desired accuracy. The displacement and stress evaluations obtained with LE4 kinematics agree well with the reference solutions given by Varadan and Bhaskar [244]. The accuracy of the FE results of the thick shell ($R_\beta/h = 2$) can be further improved by refining the thickness functions (TOS). FSDT leads to good estimation of displacement and in-plane stresses for the thinner shells ($R_\beta/h = 50{,}100$ and 500), but fails in other stresses. Also, unlike the LE4 kinematic model, FSDT ignores the stretching effects in the thickness direction which may play an essential role on thick shells, such as the $R_\beta/h = 2$ and $R_\beta/h = 4$ cases in this numerical example.

The convergence of the normalized deflection for each aspect ratio is shown in

Table 12.1: Displacement and stress evaluation on the three-layered cylindrical shells with various R_β/h under distributed pressure.

R_β/h	TOS	Integration	p	$\bar{w}$	$\bar{\sigma}_{\alpha\alpha}$	$\bar{\sigma}_{\beta\beta}$	$\bar{\sigma}_{\alpha\beta}$	$\bar{\sigma}_{\alpha z}$	$\bar{\sigma}_{\beta z}$	$\bar{\sigma}_{zz}$	E_{memb}/E	E_{bend}/E	E_{ps}/E	E_{zs}/E	E_{zz}/E
2	FSDT	FULL	8	8.387	0.1025	2.331	-0.2258	0.2140	-0.960	–	0.1%	4.6%	0.7%	94.6%	–
	LE4	FULL	8	10.102	0.1735	7.155	-0.2916	0.3009	-1.377	-0.3368	0.0%	9.1%	0.4%	58.7%	31.7%
	LE4	REDI	8	10.102	0.1735	7.155	-0.2916	0.3009	-1.377	-0.3368	0.0%	9.1%	0.4%	58.7%	31.7%
	LE4	SELI	8	10.102	0.1735	7.155	-0.2916	0.3009	-1.377	-0.3368	0.0%	9.1%	0.4%	58.7%	31.7%
	Varadan and Bhaskar [244]			10.11	0.1761	7.168	-0.2922	0.3006	-1.379	-0.34	–	–	–	–	–
4	FSDT	FULL	8	2.867	0.0722	3.155	-0.1131	0.0467	-1.150	–	0.1%	16.3%	0.6%	83.0%	–
	LE4	FULL	8	4.009	0.1267	6.543	-0.1609	0.1739	-2.349	-0.6194	0.1%	18.5%	0.6%	68.8%	12.0%
	LE4	REDI	8	4.009	0.1267	6.543	-0.1609	0.1739	-2.349	-0.6194	0.1%	18.5%	0.6%	68.8%	12.0%
	LE4	SELI	8	4.009	0.1267	6.543	-0.1609	0.1739	-2.349	-0.6194	0.1%	18.5%	0.6%	68.8%	12.0%
	Varadan and Bhaskar [244]			4.009	0.1270	6.545	-0.1609	0.1736	-2.349	-0.62	–	–	–	–	–
10	FSDT	FULL	8	0.938	0.05690	3.718	-0.05875	0.06063	-1.258	–	0.2%	54.9%	0.5%	44.5%	–
	LE4	FULL	8	1.223	0.07392	4.682	-0.07292	0.08284	-3.264	-1.270	0.2%	43.4%	0.5%	53.3%	2.6%
	LE4	REDI	8	1.223	0.07392	4.682	-0.07292	0.08284	-3.264	-1.270	0.2%	43.4%	0.5%	53.3%	2.6%
	LE4	SELI	8	1.223	0.07392	4.682	-0.07292	0.08284	-3.264	-1.270	0.2%	43.4%	0.5%	53.3%	2.6%
	Varadan and Bhaskar [244]			1.223	0.0739	4.683	-0.0729	0.0826	-3.264	-1.27	–	–	–	–	–
50	FSDT	FULL	9	0.5372	0.06993	3.887	-0.07495	0.04622	-1.261	–	2.5%	92.4%	2.1%	3.0%	–
	LE4	FULL	9	0.5495	0.07127	3.932	-0.07600	0.08922	-3.492	-4.847	2.4%	90.4%	2.1%	5.0%	0.1%
	LE4	REDI	9	0.5495	0.07128	3.932	-0.07600	0.08910	-3.492	-4.847	2.4%	90.4%	2.1%	5.0%	0.1%
	LE4	SELI	9	0.5495	0.07127	3.932	-0.07600	0.08910	-3.492	-4.847	2.4%	90.4%	2.1%	5.0%	0.1%
	Varadan and Bhaskar [244]			0.5495	0.0712	3.930	-0.0760	0.0894	-3.491	-4.85	–	–	–	–	–
100	FSDT	FULL	9	0.4688	0.08344	3.501	-0.1035	0.0405	-1.127	–	8.8%	84.1%	6.4%	0.7%	–
	LE4	FULL	9	0.4715	0.08389	3.511	-0.1038	0.1219	-3.128	-8.300	8.2%	84.2%	6.4%	1.2%	0.1%
	LE4	REDI	11	0.4715	0.08384	3.507	-0.1038	0.1223	-3.127	-8.297	8.2%	84.2%	6.4%	1.2%	0.1%
	LE4	SELI	11	0.4715	0.08384	3.507	-0.1038	0.1223	-3.127	-8.297	8.2%	84.2%	6.4%	1.2%	0.1%
	Varadan and Bhaskar [244]			0.4715	0.0838	3.507	-0.1038	0.1223	-3.127	-8.30	–	–	–	–	–
500	FSDT	FULL	12	0.1027	0.05585	0.7898	-0.08885	0.0090	-0.2486	–	47.9%	18.6%	33.4%	0.0%	–
	LE4	FULL	12	0.1027	0.05586	0.7895	-0.08886	0.1051	-0.6907	-9.115	44.4%	22.2%	33.4%	0.0%	0.0%
	LE4	REDI	13	0.1027	0.05586	0.7897	-0.08886	0.1032	-0.6907	-9.141	44.4%	22.2%	33.4%	0.0%	0.0%
	LE4	SELI	13	0.1027	0.05586	0.7895	-0.08886	0.1078	-0.6907	-9.120	44.4%	22.2%	33.4%	0.0%	0.0%
	Varadan and Bhaskar [244]			0.1027	0.0559	0.7895	-0.0889	0.1051	-0.691	-9.12	–	–	–	–	–

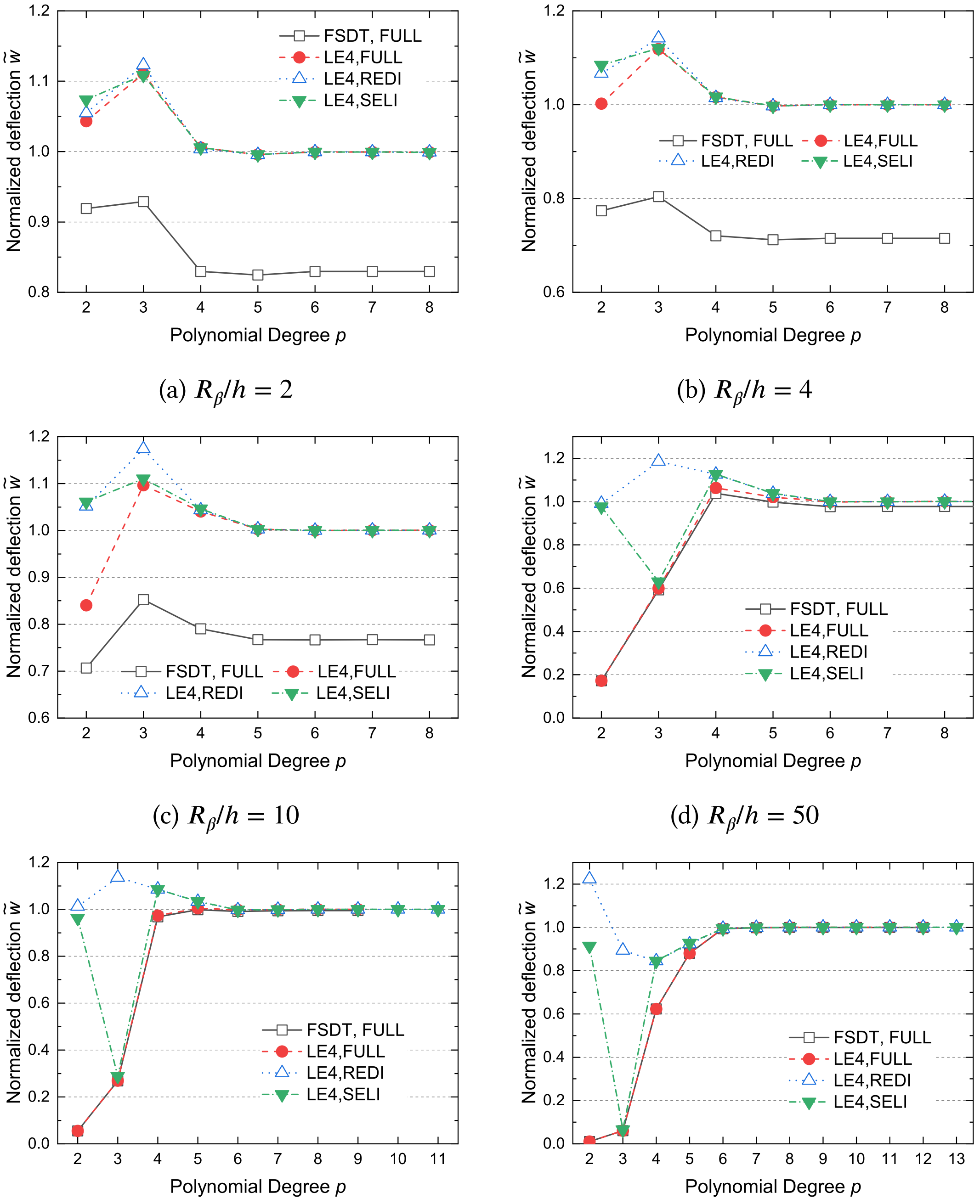

(a) $R_\beta/h = 2$

(b) $R_\beta/h = 4$

(c) $R_\beta/h = 10$

(d) $R_\beta/h = 50$

(e) $R_\beta/h = 100$

(f) $R_\beta/h = 500$

Figure 12.5: Convergence regarding the normalized deflection of FE models for the three-layered cylindrical shells under distributed pressure.

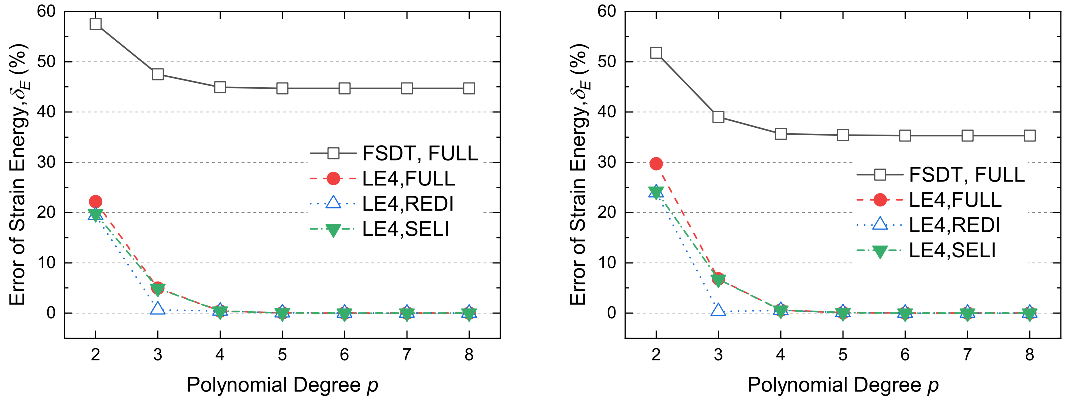

(a) $R_\beta/h = 2$ (b) $R_\beta/h = 4$

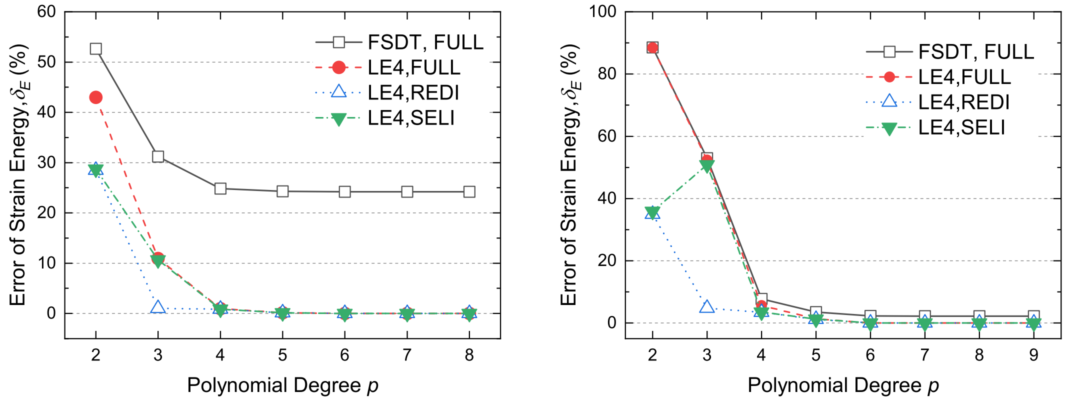

(c) $R_\beta/h = 10$ (d) $R_\beta/h = 50$

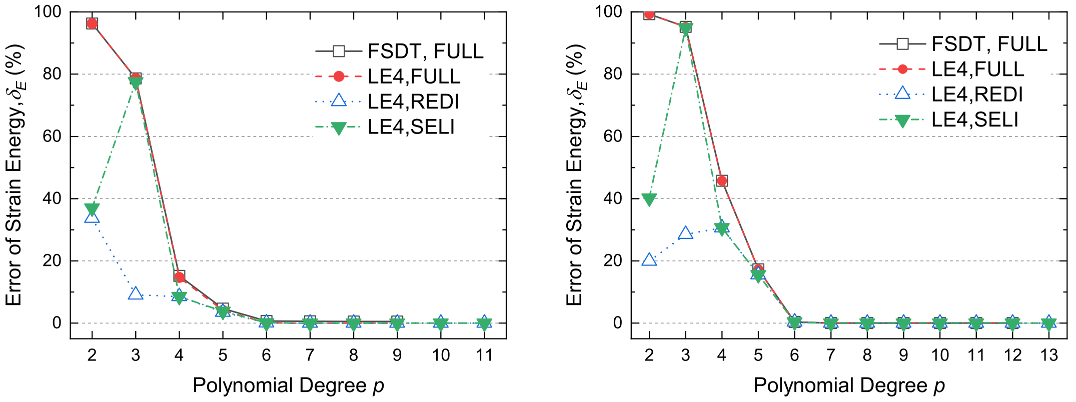

(e) $R_\beta/h = 100$ (f) $R_\beta/h = 500$

Figure 12.6: Convergence regarding the strain energy of FE models for the three-layered cylindrical shells under distributed pressure.

Fig. 12.5, in which $\tilde{w} = \bar{w}/\bar{w}_{ref}$ where $\bar{w}_{ref}$ is the reference deflection solution. Fig. 12.6 reports the convergence of the FE model regarding the strain energy error, which is calculated by taking the converged solution employing LE4 kinematics with full integration as the reference. It can be observed that for shells with different R_β/h values, convergence is achieved at different polynomial degrees. Generally, the thinner the shell structure is, the higher polynomial order will be required. Compared to the full integration scheme, the reduced integration technique can help to increase the accuracy in the low-order cases, but the eventual convergence is reached at the same time with full integration. Note that for this single-element model, the detected spurious modes in reduced integrated elements with $p = 2$ are not observed to be a significant problem. Notably, the selectively reduced integration improves the accuracy of the single-element FE model with $p = 2$ and leads to results quite close to those obtained with full integration in the higher-order cases ($p \geq 3$). When the numerical convergence is reached, all the three kinds of integration schemes lead to results that agree well with the reference solutions.

Fig. 12.7 shows the variation of the ratio of strain energy components with the increase of the polynomial degree of the hierarchical element. It can be found that for the transverse shear energy, the FSDT and LE4 models with full integration have the same trend. For $R_\beta/h = 2$,4 and 10, the in-plane shear energy is less than 1% which can be neglected (see Fig. 12.8c); as the radius-to-thickness ratio increases, the E_{ps} becomes more significant and is plotted for comparison in Fig. 12.7. The disagreement of FSDT and LE4 in Fig. 12.7 is due to that the thickness stretching effects are accounted in LE4 model but ignored by FSDT. When the thickness stretching energy is negligible (less than 1% for $R_\beta/h = 50,100,500$), the transverse shear energy values obtained with FSDT and LE4 are quite close, which demonstrates that the kinematic assumptions do not affect the shear locking in thin shells. The fully integrated lower-order hierarchical elements ($p = 2,3,4$) suffer from locking on these thinner shells ($R_\beta/h = 50,100,500$), and this locking can be overcome by increasing the polynomial degree p without using any mitigation techniques. When the reduced and selective integration schemes are employed, the shear locking phenomenon on the elements with $p = 2$ can be greatly alleviated, however, these techniques become less influential when the polynomial degree is further increased, as shown in Fig. 12.7d, 12.7e, and 12.7f. Since the newly introduced shape functions lead to improved accuracy, the higher the polynomial degree is, the less necessary the reduced integrated polynomials will become. This effect is more evident for selective integration. It should be pointed out that, models with these three integration schemes will converge to comparable solutions when the polynomial order is sufficiently high. Fig.12.7 clearly demonstrates that shear locking is the dominant locking phenomenon for this numerical example.

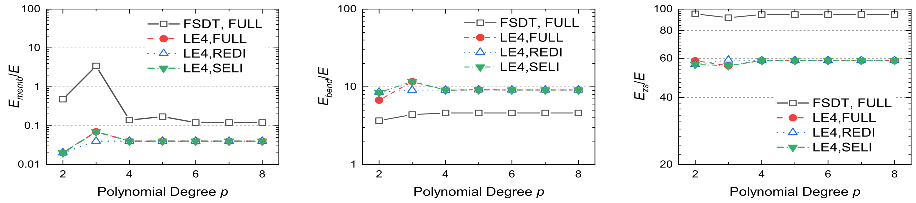

(a) $R_\beta/h = 2$

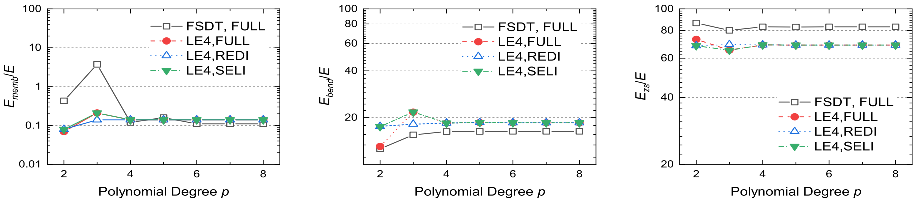

(b) $R_\beta/h = 4$

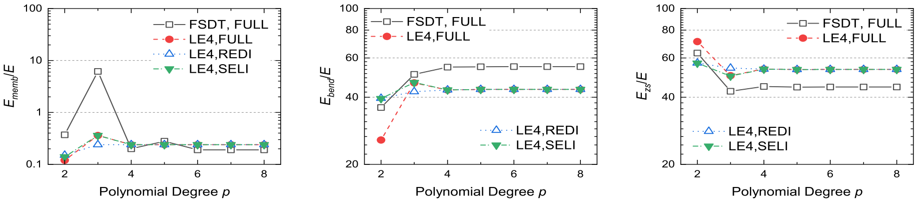

(c) $R_\beta/h = 10$

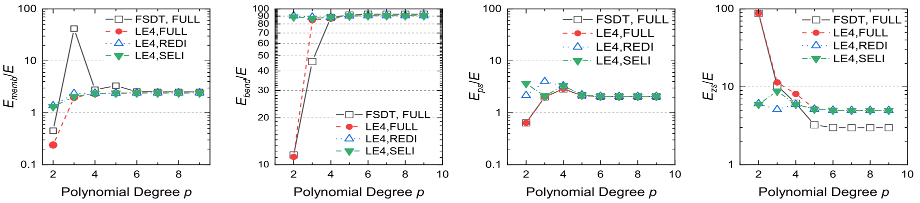

(d) $R_\beta/h = 50$

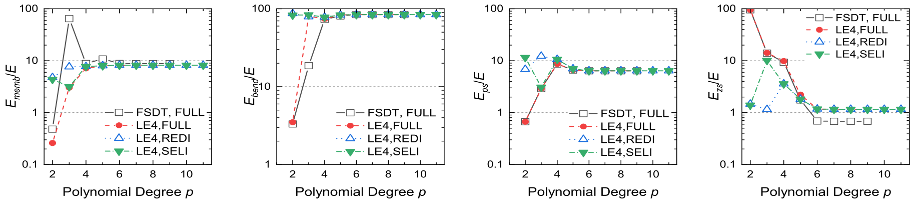

(e) $R_\beta/h = 100$

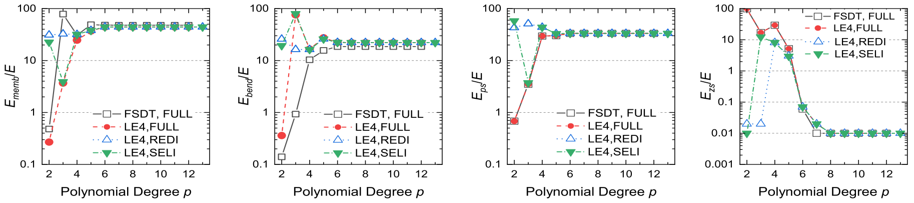

(f) $R_\beta/h = 500$

Figure 12.7: Variation of strain energy components with respect to the polynomial degree on the three-layered cylindrical shells under distributed pressure.

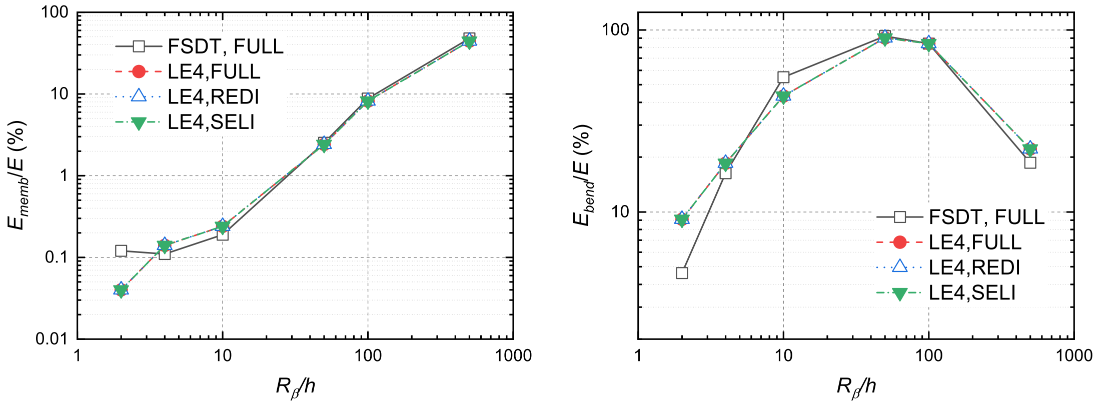

(a) Membrane energy ratio

(b) Bending energy ratio

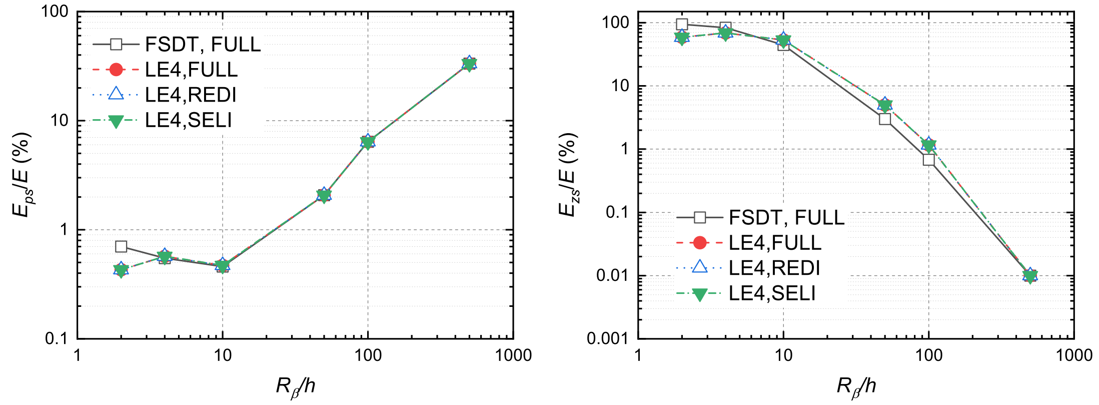

(c) In-plane shear energy ratio

(d) Transverse shear energy ratio

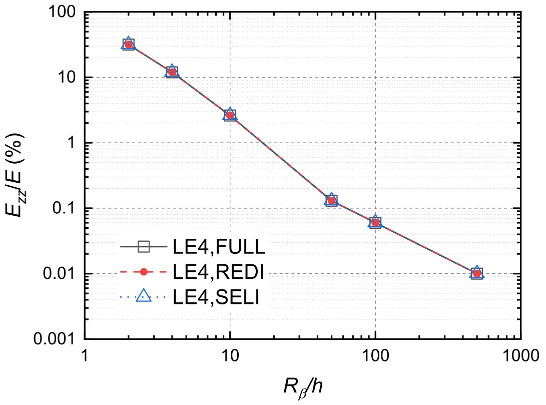

(e) Thickness stretching energy ratio

Figure 12.8: Energy components versus radius-to-thickness ratio R_β/h on the three-layered cylindrical shells under distributed pressure.

The variation of the energy components with the radius-to-thickness ratio R_β/h is summarized in Fig. 12.8. This variation provides a comprehensive understanding of the structural responses when the shell thickness decreases. It can be observed that the membrane energy ratio keeps increasing monotonically with the reduction of the shell thickness, and the ratios of transverse shear energy and thickness stretching energy decrease and approach zero when the shell is very thin ($R_\beta/h = 100{,}500$). In general, the energy ratio of the in-plane shear strains increases when the shell gets thinner. The bending energy is significant for moderate-thin shells. To sum up, the transverse strain energy components (transverse shear and thickness stretching) become less dominant with the decrease of the shell thickness.

12.2.2 Membrane locking: cylindrical panels under bending

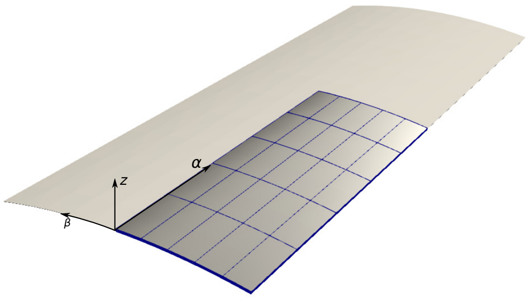

(a) Geometrical features

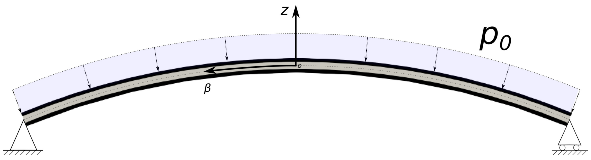

(b) Load and boundary conditions

Figure 12.9: Three-layered cylindrical panel under simple supports on two ends.

This numerical example consists of three-layered cylindrical panels that undergo bending, as shown in Fig. 12.9. The cylindrical panels have radius $R_\beta = 10$, mid-surface arch length $b = R_\beta \cdot \pi/20$ in the β direction, and length $L = 4.0$ along the cylinder axis (α direction). The radius-to-thickness ratios considered include $R_\beta/h = 10{,}100{,}1000$, and 10000. The materials used are the same as in Section 12.2.1. The lamination sequence is (0°/90°/0°), and the thicknesses of the three layers are $\frac{h}{4}$, $\frac{h}{2}$, and $\frac{h}{4}$, separately. As illustrated in Fig. 12.9b, the cylindrical panels are simply supported on the two ends along the cylinder axis, and free on the other two edges. The simple supports follow:

$$\beta = -\frac{b}{2}, \frac{b}{2} : \quad u = 0, w = 0. \tag{12.5}$$

The structure is imposed to constant pressure load p_0 on the top surface. The vertical displacement w is non-dimensionalized through the following parameters:

$$\bar{w} = -\frac{10^4 E_L h^3}{p_0 R_\beta^4} \, w(\frac{L}{2},0,0) \tag{12.6}$$

By making use of the symmetric features of the boundary conditions, a 1/4 FE model with one rectangular hierarchical element is employed, as demonstrated in Fig. 12.9a. The one-element model is refined by increasing its polynomial degree of the hierarchical shape functions when the relative difference of two neighboring orders is less than 0.5% regarding the displacement evaluation $\bar{w}$. On the whole, $p = 7$ is sufficient to guarantee the convergence. The displacement evaluation $\bar{w}$ and strain components estimation obtained through hierarchical elements with $p = 7$ are listed in Table 12.2.

Table 12.2: Displacement and energy evaluation of the three-layered cylindrical panel under bending, obtained through hierarchical elements with $p = 7$.

R_β/h	TOS	Integration	$\bar{w}$	E_{memb}/E	E_{bend}/E	E_{ps}/E	E_{zs}/E	E_{zz}/E
10	FSDT	FULL	294.5	0.0%	20.5%	0.0%	79.5%	–
	LE4	FULL	330.4	0.0%	17.0%	0.0%	59.5%	23.5%
	LE4	REDI	329.9	0.0%	17.0%	0.0%	59.4%	23.6%
	LE4	SELI	330.4	0.0%	17.0%	0.0%	59.5%	23.5%
100	FSDT	FULL	61.67	0.0%	96.3%	0.0%	3.7%	–
	LE4	FULL	62.45	0.0%	95.0%	0.0%	5.0%	0.0%
	LE4	REDI	62.33	0.0%	95.0%	0.0%	5.0%	0.0%
	LE4	SELI	62.45	0.0%	95.0%	0.0%	5.0%	0.0%
1000	FSDT	FULL	59.57	0.0%	100.0%	0.0%	0.0%	–
	LE4	FULL	59.58	0.0%	99.9%	0.0%	0.1%	0.0%
	LE4	REDI	59.48	0.0%	99.9%	0.0%	0.1%	0.0%
	LE4	SELI	59.58	0.0%	99.9%	0.0%	0.1%	0.0%
5000	FSDT	FULL	59.61	0.0%	100.0%	0.0%	0.0%	–
	LE4	FULL	59.61	0.0%	100.0%	0.0%	0.0%	0.0%
	LE4	REDI	59.52	0.0%	100.0%	0.0%	0.0%	0.0%
	LE4	SELI	59.61	0.0%	100.0%	0.0%	0.0%	0.0%

Figs. 12.10 and 12.11 summarize the convergence of the FE models with the increase of the polynomial degree concerning the normalized displacement evaluation and the error of strain energy. The reference solutions are given by FE models with full integration and $p = 8$. It can be observed that for the relative thick shells with $R_\beta/h = 10$ and 100, the reduced integration leads to less accurate displacement estimation and

lower convergence compared with full and selective integration schemes. Meanwhile, for the thinner shells with $R_\beta/h = 1000$ and 10000, reduced integration models give better accuracy than the other two integration schemes in the lower-order hierarchical shell elements ($p = 2$ for $R_\beta/h = 1000$, and $p = 2{,}3$ for $R_\beta/h = 10000$). It seems that the reduced integration "unnecessarily" leads to over-soft bending stiffness when no noticeable locking is present in this numerical example. The displacement and energy estimations obtained through selective integration show almost no difference from those of full integration when the element order $p \geq 4$.

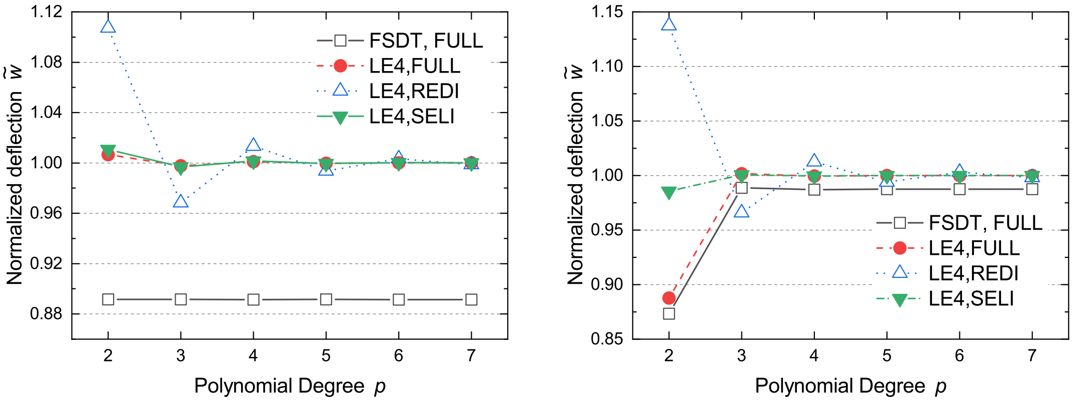

(a) $R_\beta/h = 10$ (b) $R_\beta/h = 100$

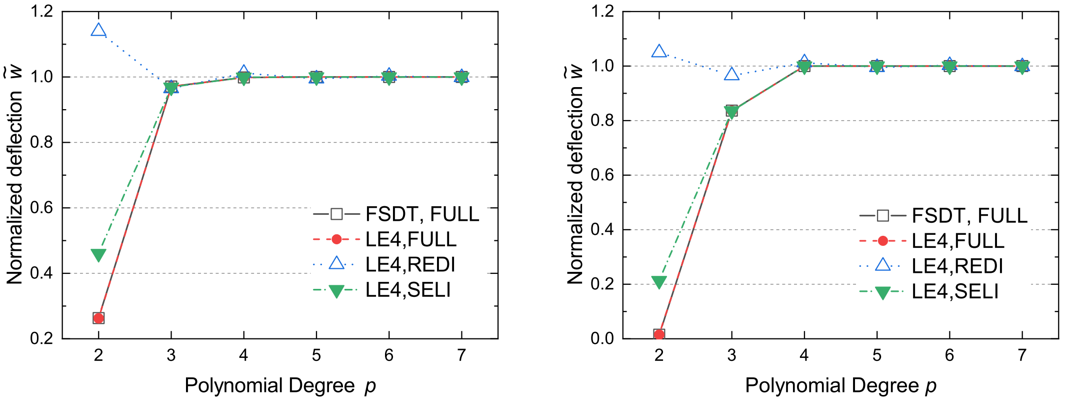

(c) $R_\beta/h = 1000$ (d) $R_\beta/h = 10000$

Figure 12.10: Convergence regarding the normalized deflection of FE models for the simply supported cylindrical panels under bending, for various radius-to-thickness ratio R_β/h.

The variation of the relevant energy terms, which is different for each aspect ratio, with respect to the element polynomial degree, is reported in Fig. 12.12. For the thick shells with $R_\beta = 10$, no apparent locking is observed on the low-order hierarchical elements. As the shell becomes thinner, locking becomes more significant on low-order elements. For the moderate-thick shell with $R_\beta/h = 100$, locking occurs on the fully

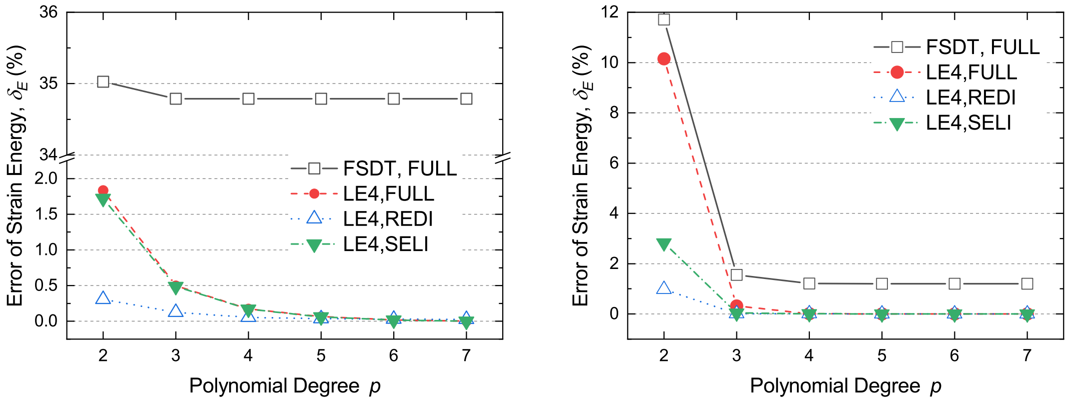

(a) $R_\beta/h = 10$ (b) $R_\beta/h = 100$

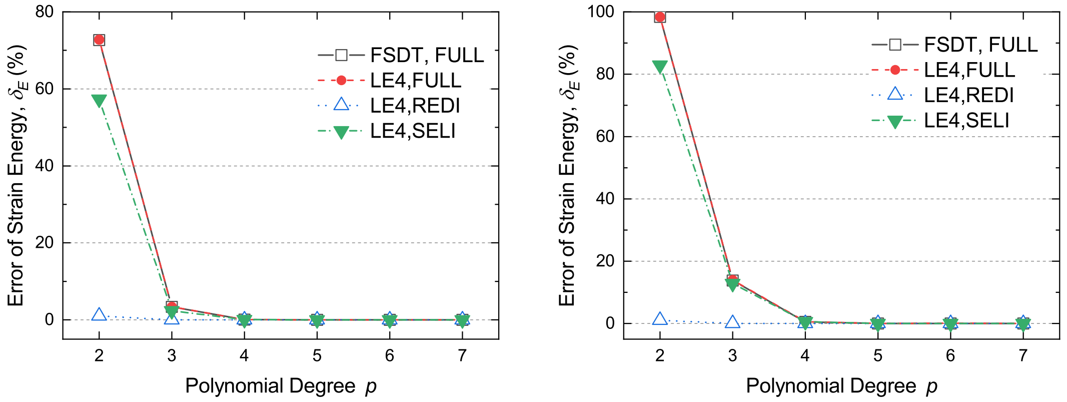

(c) $R_\beta/h = 1000$ (d) $R_\beta/h = 10000$

Figure 12.11: Convergence regarding the strain energy of FE models for the simply supported cylindrical panels under bending, for various radius-to-thickness ratio R_β/h.

integrated elements for $p = 2$ and it decreases rapidly as the polynomial degree goes higher. This locking is mainly shear locking, which can be observed through the comparison of bending energy and transverse shear energy in Fig. 12.12b. On the other hand, for the thin shells with $R_\beta/h = 1000$ and 10000, significant membrane locking emerges on the low-order element ($p = 2$,3) with full integration, which also drops rapidly with the increase of the polynomial degree. For all the relatively thin shells ($R_\beta/h = 100$, 1000, and 10000), reduced integration is able to mitigate the membrane locking effectively, which occurs on low-order hierarchical elements, as shown in Fig. 12.12b, 12.12c, and 12.12d. The selective integration technique also leads to improved energy estimation, yet less effective compared to reduced integration in this case. To sum up, when the numerical convergence is achieved via p-refinement, all the three integration schemes give equivalent locking-free solutions.

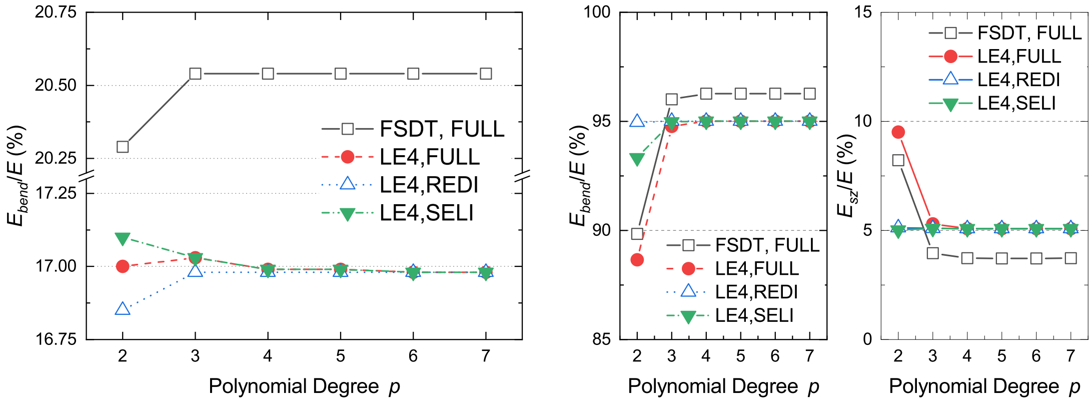

(a) $R_\beta = 10$ (b) $R_\beta = 100$

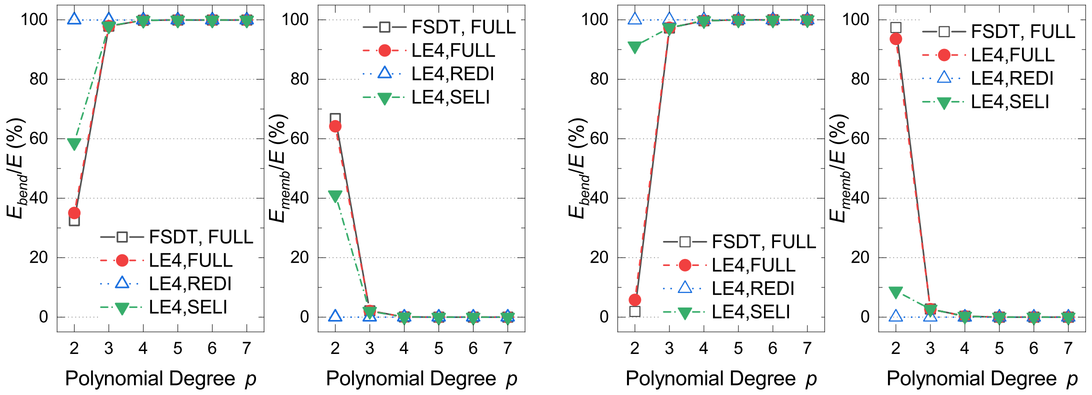

(c) $R_\beta = 1000$ (d) $R_\beta = 10000$

Figure 12.12: Variation of relevant energy components with respect to the polynomial degree of FE models for the three-layered cylindrical panel under bending.

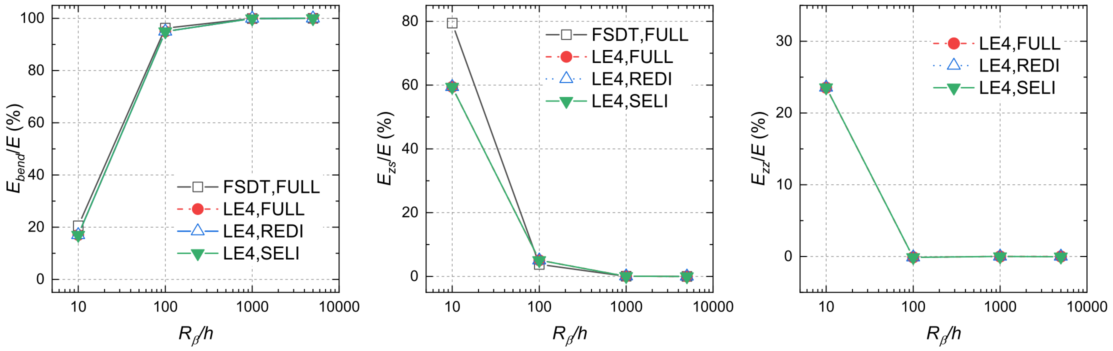

(a) E_{bend}/E (b) E_{zs}/E (c) E_{zz}/E

Figure 12.13: Ratio of different energy components versus radius-to-thickness ratio on the three-layered cylindrical panel under bending.

From Table 12.2, it can also be observed that when the hierarchical elements are sufficiently refined, all the integration schemes give results in great agreement with each other. The variation of different energy components concerning the increase of the element polynomial order is plotted in Fig. 12.13. As expected, the strain energy components due to the out-of-plane strains, including the transverse shear strain energy and thickness stretching energy, decrease rapidly with the increase of the radius-to-thickness ratio and approach zero on thin shells. Also, it can be found that the membrane energy and in-plane shear energy are absent in this numerical example. On the thin shell with $R_\beta/5000$, the strain energy contains only the bending component.

12.3 Conclusions

In this chapter, the performance of hierarchical elements in the numerical analysis of laminated shell structures is assessed regarding the shear and membrane locking phenomena. Proper energy decomposition presented in Chapter 4 is adopted in the numerical evaluation. The numerically efficient integration schemes for hierarchical shell elements are discussed. Through the numerical investigation with single-element p-version finite element models, the following conclusions can be drawn:

- Without using special locking mitigation technique, hierarchical shell elements with full integration are capable of overcoming both shear and membrane locking via plain p-refinement for structures with an aspect ratio in a wide range ;
- Hierarchical shell elements with polynomial degree $p \geq 3$ employing reduced integration scheme and $p \geq 2$ adopting selective integration technique are robust;
- Reduced and selectively reduced integration schemes are helpful with the lower-order hierarchical elements to alleviate the shear and membrane locking phenomena, yet their effects decrease rapidly with the increase of the polynomial degree;
- When numerical convergence is reached with a higher-order polynomial degree, the three integration schemes, namely the full, reduced, and selective integration, lead to the same accuracy;
- With hierarchical shell elements, the physically zero transverse shear strain energy on thin shells can be achieved numerically.

The above evaluation demonstrates the high efficiency of hierarchical shell elements in the analysis of laminated shell structures. Only rectangular elements are tested in the present article. Distorted meshes should also be considered as future work.

Concluding remarks

The construction of variable kinematic beam, plate, and shell finite element (FE) models is introduced. In the CUF framework, by applying the Principle of Virtual Displacements, starting from the compact form expression of kinematic and field assumptions, the *fundamental nuclei* (FNs) for the multi-field FE models with Node-Dependent Kinematics (NDK) are derived. The applications of the presented FE models in the analysis of multi-layered structures accounting for temperature, moisture, and electric fields have been demonstrated through various numerical examples.

The adaptable refinement approach based on the use of NDK and hierarchical shape functions is a powerful technique in building numerically efficient FE models. With this approach, besides the *p* version refinement, the local kinematic refinement can be carried out conveniently on the nodal level, and the region with refined models can also be adjustably decided. When applied to global-local modeling, the adaptable refinement approach can guarantee the solution accuracy of local stresses at globally reduced computational costs. Also, since no additional modification of FE mesh is needed, the same mesh grid can be re-used, and the pre-processing is greatly simplified.

Hierarchical 2D functions are used as cross-section functions of refined beam models and as shape functions of plate and shell elements. Due to the hierarchical characteristics and the avoidance of re-meshing during the refinement process, such functions are convenient to use and efficient in FE simulations. Through the numerical evaluation of the strain energy components, it has been demonstrated that when the polynomial degree of hierarchical shell elements is sufficiently high, the shear and membrane locking phenomena can be effectively mitigated.

Various basis functions are used as kinematic assumptions in the present work. The tested basis functions include Taylor series, trigonometric series, exponential functions, Lagrange polynomials, and Chebyshev polynomials. The numerical investigations show that different ESL kinematics vary regarding the numerical convergence rate with the increase of the number of expansions. The use of Murakami's zig-zag functions can effectively improve the approximation of transverse shear stresses, while LW models can provide even better accuracy. Besides, LW models adopting fourth-order Lagrange or Chebyshev polynomials can give satisfactory interfacial continuity of transverse shear stresses.

Partially coupled thermo-mechanical and hygro-mechanical plate and shell models are presented. Comparisons have been made between results obtained with assumed temperature/moisture fields and calculated temperature/moisture distributions by considering Fourier's/Fick's law. It is concluded that the solution of conduction/diffusion equations is essential for thick plates and shells, and the assumed linear variation of temperature is a sufficient assumption for thin structures.

In fully coupled electro-mechanical modeling, both actuators and sensors are considered. Through LW models, piezoelectric components, as either surface-mounted or embedded patches or layers, are properly considered in multi-layered structures. NDK is used to assign ESL kinematics to the region without piezoelectric components and to reduce the high computational costs caused by the LW models. The effectiveness and efficiency of the adopted FE models are demonstrated by comparing the obtained results against available reference solutions in the literature.

As future work, adaptive mathematical refinement routines, geometric mapping with blending functions, mixed formulations for multi-field modeling, effects of material non-linearity in multi-field problems, and more sophisticated dynamic and transient multi-field effects such as hygro-thermo-mechanical, thermo-electro-mechanical, and hygro-thermo-electro-mechanical couplings, can be further investigated.

List of Publications

Journal articles

- Carrera E, Cinefra M, Li G, Kulikov GM. MITC9 shell finite elements with miscellaneous through-the-thickness functions for the analysis of laminated structures. *Composite Structures.* 2016; 154:360–373.

- Zappino E, Li G, Pagani A, Carrera E. Global-local analysis of laminated plates by node-dependent kinematic finite elements with variable ESL/LW capabilities. *Composite Structures.* 2017; 172:1–14.

- Carrera E, Cinefra M, Li G. Refined finite element solutions for anisotropic laminated plates. *Composite Structures.* 2018; 183:63–76.

- Carrera E, Zappino E, Li G. Finite element models with node-dependent kinematics for the analysis of composite beam structures. *Composites Part B: Engineering.* 2018; 132(Supplement C):35 – 48.

- Cinefra M, Petrolo M, Li G, Carrera E. Variable kinematic shell elements for composite laminates accounting for hygrothermal effects. *Journal of Thermal Stresses.* 2017; 40(12):1523–1544.

- Cinefra M, Petrolo M, Li G, Carrera E. Hygrothermal analysis of multilayered composite plates by variable kinematic finite elements. *Journal of Thermal Stresses.* 2017; 40(12):1502–1522.

- Carrera E, Zappino E, Li G. Analysis of beams with piezo-patches by node-dependent kinematic finite element method models. *Journal of Intelligent Material Systems and Structures.* 2018; 29(7):1379–1393.

- Zappino E, Li G, Carrera E. Node-dependent kinematic elements for the dynamic analysis of beams with piezo-patches. *Journal of Intelligent Material Systems and Structures.* 2018; 29(16):3333–3345.

- Zappino E, Li G, Pagani A, Carrera E, de Miguel AG. Use of higher-order Legendre polynomials for multilayered plate elements with node-dependent kinematics. *Composite Structures.* 2018; 202:222 – 232. Special issue dedicated to Ian Marshall.

– Li G, de Miguel A, Pagani A, Zappino E, Carrera E. Finite beam elements based on Legendre polynomial expansions and node-dependent kinematics for the global-local analysis of composite structures. *European Journal of Mechanics-A/Solids.* 2019; 74:112 – 123.

– Li G, Carrera E, Cinefra M, de Miguel A, Pagani A, Zappino E. An Adaptable Refinement Approach for Shell Finite Element Models Based on Node-Dependent Kinematics. *Composite Structures.* 2019; 210:1–19.

– Li G, Carrera E, Cinefra M, de Miguel A, Kulikov GM, Pagani A, et al. Evaluation of locking in refined hierarchical shell finite elements for laminated structures. *Advanced Modeling and Simulation in Engineering Sciences.* 2019; Accepted manuscript.

Book chapters

– Li G, Carrera E, Cinefra M, Zappino E, Jansen E. Variable kinematic shell formulations accounting for multi-field effects for the analysis of multi-layered structures. In *Advances in Predictive Models and Methodologies for Numerically Efficient Linear and Nonlinear Analysis of Composites.* Springer.

Conference proceedings

– Cinefra M, Li G, Petrolo M, and Carrera E, Refined 2D finite elements for composite plates and shells accounting for hygrothermal effects. ECCOMAS Congress 2016.

– Carrera E, Cinefra M, Li G, and Kulikov GM, MITC9 shell finite elements with miscellaneous through-the-thickness approximating functions for the analysis of laminated structures. ICCS19, 5-9 September 2016, Porto, Portugal.

– Zappino E, Carrera E, and Li G, Free vibration analysis of beams with piezo-patches using a one-dimensional model with node-dependent kinematics. DEMEASS VIII, 22-24 May 2017, Moscow, Russia.

– Carrera E, Cinefra M, Li G, and Zappino E, Node-dependent kinematic 1D FEM models for the analysis of beams with piezo-patches. SMART 2017, 5-8 June 2017, Madrid, Spain.

– Li G, de Miguel AG, Pagani A, Zappino E, and Carrera E, Finite beam elements based on Legendre expansions and node-dependent kinematics for the global-local analysis of composite structures. ICCM21, 20-25 August, Xi'an, China.

– Li G, de Miguel AG, Zappino E, Pagani A, and Carrera E, Finite element models with node-dependent kinematics adopting Legendre polynomial expansions for the analysis of laminated plates. ICCM21, 20-25 August, Xi'an, China.

– Zappino E, Carrera E, and Li G, Thermo-piezo-elastic analysis of beam structures using node-dependent kinematics one-dimensional models. AIMETA 2017, 4-7 September, Salerno, Italy.

– Li G, Cinefra M, Kulikov GM, Carrera E, and Pagani A, Hybrid-mixed refined beam elements based on Hu-Washizu variational principle. 1st International Conference on Theoretical, Analytical and Computational Methods for Composite Materials and Composite Structures, ICOMP 2018, 23-25 May 2018, Wuhan, China.

– Li G, Haldar A, Jansen E, Zappino E, Cinefra M, Rolfes R, and Carrera E, Modeling of Composite Structures with Piezoelectric Components by Refined Shell Finite Elements. 1st International Conference on Mechanics of Advanced Materials and Structures, ICMAMS 2018, 17-20 June 2018, Turin, Italy.

– Li G, Carrera E, de Miguel AG, Pagani A, Zappino E, Use of Higher-order Legendre Polynomials in Node-dependent Kinematic Shell Elements. 10th European Solid Mechanics Conference, ESMC 2018, 2-6 July 2018, Bologna, Italy.

Bibliography

[1] Mark Ainsworth. “p-and hp-Finite Element Methods. Theory and Applications in Solid and Fluid Mechanics”. In: *Mathematics of Computation* 70.235 (2001), pp. 1335–1337.

[2] Saleh Alsubari, JS Mohamed Ali, and Yulfian Aminanda. “Hygrothermoelastic analysis of anisotropic cylindrical shells”. In: *Composite Structures* 131 (2015), pp. 151–159.

[3] G Askar Altay and M Cengiz Dökmecí. “Some variational principles for linear coupled thermoelasticity”. In: *International Journal of Solids and Structures* 33.26 (1996), pp. 3937–3948.

[4] Gülay Altay and M Cengiz Dökmeci. “Certain hygrothermopiezoelectric multifield variational principles for smart elastic laminae”. In: *Mechanics of Advanced Materials and structures* 15.1 (2008), pp. 21–32.

[5] SA Ambartsumian. “On the theory of bending plates”. In: *Izv Otd Tech Nauk AN SSSR* 5.5 (1958), pp. 69–77.

[6] Mohammad A Aminpour, Jonathan B Ransom, and Susan L McCleary. “A coupled analysis method for structures with independently modelled finite element subdomains”. In: *International Journal for Numerical Methods in Engineering* 38.21 (1995), pp. 3695–3718.

[7] RA Arciniega and JN Reddy. “Large deformation analysis of functionally graded shells”. In: *International Journal of Solids and Structures* 44.6 (2007), pp. 2036–2052.

[8] Douglas N Arnold and Gerard Awanou. “The serendipity family of finite elements”. In: *Foundations of Computational Mathematics* 11.3 (2011), pp. 337–344.

[9] Hemendra Arya, RP Shimpi, and NK Naik. “A zigzag model for laminated composite beams”. In: *Composite structures* 56.1 (2002), pp. 21–24.

[10] I Babuška and BQ Guo. “The h-p version of the finite element method for domains with curved boundaries”. In: *SIAM Journal on Numerical Analysis* 25.4 (1988), pp. 837–861.

[11] Ivo Babuška and R Narasimhan. “The Babuška-Brezzi condition and the patch test: an example”. In: *Computer Methods in Applied Mechanics and Engineering* 140.1-2 (1997), pp. 183–199.

[12] Ivo Babuška, Barna A Szabó, and I Norman Katz. “The p-version of the finite element method”. In: *SIAM Journal on Numerical Analysis* 18.3 (1981), pp. 515–545.

[13] Randolph E Bank. “The efficient implementation of local mesh refinement algorithms”. In: *Adaptive Computational Methods for Partial Differential Equations* (1983), pp. 74–81.

[14] Klaus Jürgen Bathe, Phill Seung Lee, and Jean François Hiller. “Towards improving the MITC9 shell element”. In: *Computers & Structures* 81.8 (2003), pp. 477–489.

[15] Klaus-Jürgen Bathe. *Finite element procedures.* Klaus-Jurgen Bathe, 2006.

[16] Klaus-Jürgen Bathe and Eduardo N Dvorkin. “A four-node plate bending element based on Mindlin/Reissner plate theory and a mixed interpolation”. In: *International Journal for Numerical Methods in Engineering* 21.2 (1985), pp. 367–383.

[17] Klaus-Jürgen Bathe, Alexander Iosilevich, and Dominique Chapelle. “An evaluation of the MITC shell elements”. In: *Computers & Structures* 75.1 (2000), pp. 1–30.

[18] RC Batra. “Deflection control during dynamic deformations of a rectangular plate using piezoceramic elements”. In: *AIAA Journal* 33.8 (1995), pp. 1547–1548.

[19] RC Batra and XQ Liang. “Finite dynamic deformations of smart structures”. In: *Computational mechanics* 20.5 (1997), pp. 427–438.

[20] SB Beheshti-Aval et al. “A refined sinus finite element model for the analysis of piezoelectric laminated beams”. In: *Journal of Intelligent Material Systems and Structures* (2011), p. 1045389X10396955.

[21] Ted Belytschko et al. “Stress projection for membrane and shear locking in shell finite elements”. In: *Computer Methods in Applied Mechanics and Engineering* 51.1-3 (1985), pp. 221–258.

[22] A Benjeddou. “Advances in piezoelectric finite element modeling of adaptive structural elements: a survey”. In: *Computers & Structures* 76.1 (2000), pp. 347–363.

[23] A Benjeddou, MA Trindade, and R Ohayon. “A unified beam finite element model for extension and shear piezoelectric actuation mechanisms”. In: *Journal of Intelligent Material Systems and Structures* 8.12 (1997), pp. 1012–1025.

[24] A Benkeddad, M Grediac, and A Vautrin. “Computation of transient hygroscopic stresses in laminated composite plates”. In: *Composites Science and Technology* 56.7 (1996), pp. 869–876.

[25] A Benkeddad, M Grediac, and A Vautrin. “On the transient hygroscopic stresses in laminated composite plates”. In: *Composite Structures* 30.2 (1995), pp. 201–215.

[26] K Bhaskar, TK Varadan, and JSM Ali. “Thermoelastic solutions for orthotropic and anisotropic composite laminates”. In: *Composites Part B: Engineering* 27.5 (1996), pp. 415–420.

[27] Fabio Biscani et al. “Coupling of hierarchical piezoelectric plate finite elements via Arlequin method”. In: *Journal of Intelligent Material Systems and Structures* 23.7 (2012), pp. 749–764.

[28] Fabio Biscani et al. “Variable kinematic beam elements coupled via Arlequin method”. In: *Composite Structures* 93.2 (2011), pp. 697–708.

[29] Fabio Biscani et al. “Variable kinematic plate elements coupled via Arlequin method”. In: *International Journal for Numerical Methods in Engineering* 91.12 (2012), pp. 1264–1290.

[30] Manfred Bischoff and Ekkehard Ramm. “On the physical significance of higher order kinematic and static variables in a three-dimensional shell formulation”. In: *International Journal of Solids and Structures* 37.46-47 (2000), pp. 6933–6960.

[31] PJ Blanco, RA Feijóo, and SA Urquiza. “A variational approach for coupling kinematically incompatible structural models”. In: *Computer Methods in Applied Mechanics and Engineering* 197.17 (2008), pp. 1577–1602.

[32] AE Bogdanovich and AB Birger. “Three-dimensional stress field analysis in uniformly loaded, simply supported composite plates”. In: *Computers & Structures* 52.2 (1994), pp. 237–257.

[33] Franco Brezzi and Luisa Donatella Marini. “The three-field formulation for elasticity problems”. In: *GAMM-Mitteilungen* 28.2 (2005), pp. 124–153.

[34] Miguel Luiz Bucalem and Klaus-Jüen Bathe. “Higher-order MITC general shell elements”. In: *International Journal for Numerical Methods in Engineering* 36.21 (1993), pp. 3729–3754.

[35] E Carrera, M Boscolo, and A Robaldo. “Hierarchic multilayered plate elements for coupled multifield problems of piezoelectric adaptive structures: formulation and numerical assessment”. In: *Archives of computational methods in engineering* 14.4 (2007), pp. 383–430.

[36] E Carrera, A Büttner, and P Nali. “Mixed elements for the analysis of anisotropic multilayered piezoelectric plates”. In: *Journal of Intelligent Material Systems and Structures* 21.7 (2010), pp. 701–717.

[37] E Carrera, AG de Miguel, and A Pagani. “Extension of MITC to higher-order beam models and shear locking analysis for compact, thin-walled, and composite structures”. In: *International Journal for Numerical Methods in Engineering* 112.13 (2017), pp. 1889–1908.

[38] Erasmo Carrera. “An assessment of mixed and classical theories for the thermal stress analysis of orthotropic multilayered plates”. In: *Journal of Thermal Stresses* 23.9 (2000), pp. 797–831.

[39] Erasmo Carrera. “Temperature profile influence on layered plates response considering classical and advanced theories”. In: *AIAA Journal* 40.9 (2002), pp. 1885–1896.

[40] Erasmo Carrera. “Theories and finite elements for multilayered plates and shells: a unified compact formulation with numerical assessment and benchmarking”. In: *Archives of Computational Methods in Engineering* 10.3 (2003), pp. 215–296.

[41] Erasmo Carrera. “Theories and finite elements for multilayered, anisotropic, composite plates and shells”. In: *Archives of Computational Methods in Engineering* 9.2 (2002), pp. 87–140.

[42] Erasmo Carrera, Salvatore Brischetto, and Pietro Nali. *Plates and shells for smart structures: classical and advanced theories for modeling and analysis.* Vol. 36. John Wiley & Sons, 2011.

[43] Erasmo Carrera, Maria Cinefra, and Guohong Li. “Refined finite element solutions for anisotropic laminated plates”. In: *Composite Structures* 183 (2018), pp. 63–76.

[44] Erasmo Carrera, Maria Cinefra, and Pietro Nali. “MITC technique extended to variable kinematic multilayered plate elements”. In: *Composite Structures* 92.8 (2010), pp. 1888–1895.

[45] Erasmo Carrera and Angelo Ciuffreda. “Bending of composites and sandwich plates subjected to localized lateral loadings: a comparison of various theories”. In: *Composite Structures* 68.2 (2005), pp. 185–202.

[46] Erasmo Carrera and Christian Fagiano. “Mixed piezoelectric plate elements with continuous transverse electric displacements”. In: *Journal of Mechanics of Materials and Structures* 2.3 (2007), pp. 421–438.

[47] Erasmo Carrera, Matteo Filippi, and Enrico Zappino. “Free vibration analysis of laminated beam by polynomial, trigonometric, exponential and zig-zag theories”. In: *Journal of Composite Materials* 48.19 (2014), pp. 2299–2316.

[48] Erasmo Carrera, Matteo Filippi, and Enrico Zappino. “Laminated beam analysis by polynomial, trigonometric, exponential and zig-zag theories”. In: *European Journal of Mechanics-A/Solids* 41 (2013), pp. 58–69.

[49] Erasmo Carrera, Alberto G de Miguel, and Alfonso Pagani. “Hierarchical theories of structures based on Legendre polynomial expansions with finite element applications”. In: *International Journal of Mechanical Sciences* 120 (2017), pp. 286–300.

[50] Erasmo Carrera, Alfonso Pagani, and Marco Petrolo. “Use of Lagrange multipliers to combine 1D variable kinematic finite elements”. In: *Computers & Structures* 129 (2013), pp. 194–206.

[51] Erasmo Carrera, Alfonso Pagani, and Stefano Valvano. “Shell elements with through-the-thickness variable kinematics for the analysis of laminated composite and sandwich structures”. In: *Composites Part B: Engineering* 111 (2017), pp. 294–314.

[52] Erasmo Carrera and Horst Parisch. “An evaluation of geometrical nonlinear effects of thin and moderately thick multilayered composite shells”. In: *Composite Structures* 40.1 (1997), pp. 11–24.

[53] Erasmo Carrera, Marco Petrolo, and Enrico Zappino. “Performance of CUF approach to analyze the structural behavior of slender bodies”. In: *Journal of Structural Engineering* 138.2 (2011), pp. 285–297.

[54] Erasmo Carrera and Stefano Valvano. “Analysis of laminated composite structures with embedded piezoelectric sheets by variable kinematic shell elements”. In: *Journal of Intelligent Material Systems and Structures* 28.20 (2017), pp. 2959–2987.

[55] Erasmo Carrera, Stefano Valvano, and Gennady M Kulikov. “Multilayered plate elements with node-dependent kinematics for electro-mechanical problems”. In: *International Journal of Smart and Nano Materials* (2017), pp. 1–39.

[56] Erasmo Carrera and Enrico Zappino. “Analysis of Complex Structures Coupling Variable Kinematics One-Dimensional Models”. In: *ASME 2014 International Mechanical Engineering Congress and Exposition.* American Society of Mechanical Engineers. 2014, V001T01A023–V001T01A023.

[57] Erasmo Carrera and Enrico Zappino. “One-dimensional finite element formulation with node-dependent kinematics”. In: *Computers & Structures* 192 (2017), pp. 114–125.

[58] Erasmo Carrera, Enrico Zappino, and Guohong Li. “Finite element models with node-dependent kinematics for the analysis of composite beam structures”. In: *Composites Part B: Engineering* 132.Supplement C (2018), pp. 35–48. ISSN: 1359-8368.

[59] Erasmo Carrera et al. *Finite element analysis of structures through Unified Formulation.* John Wiley & Sons, 2014.

[60] Erasmo Carrera et al. "MITC9 shell finite elements with miscellaneous through-the-thickness functions for the analysis of laminated structures". In: *Composite Structures* 154 (2016), pp. 360–373.

[61] V Carvelli and M Savoia. "Assessment of plate theories for multilayered angle-ply plates". In: *Composite Structures* 39.3 (1997), pp. 197–207.

[62] Kt Chandrashekhara and AN Agarwal. "Active vibration control of laminated composite plates using piezoelectric devices: a finite element approach". In: *Journal of Intelligent Material Systems and Structures* 4.4 (1993), pp. 496–508.

[63] Fu-Kuo Chang, Jose Luis Perez, and Kuo-Yen Chang. "Analysis of thick laminated composites". In: *Journal of Composite Materials* 24.8 (1990), pp. 801–822.

[64] Reaz A Chaudhuri and Paul Seide. "An approximate method for prediction of transverse shear stresses in a laminated shell". In: *International journal of solids and structures* 23.8 (1987), pp. 1145–1161.

[65] Wanji Chen and Junling Si. "A model of composite laminated beam based on the global–local theory and new modified couple-stress theory". In: *Composite Structures* 103 (2013), pp. 99–107.

[66] Wanji Chen and Zhen Wu. "A new higher-order shear deformation theory and refined beam element of composite laminates". In: *Acta Mechanica Sinica* 21.1 (2005), pp. 65–69.

[67] Claudia Chinosi, Lucia Della Croce, and Terenzio Scapolla. "Hierarchic finite elements for thin Naghdi shell model". In: *International Journal of Solids and Structures* 35.16 (1998), pp. 1863–1880.

[68] Maria Cinefra and Erasmo Carrera. "Shell finite elements with different through-the-thickness kinematics for the linear analysis of cylindrical multilayered structures". In: *International Journal for Numerical Methods in Engineering* 93.2 (2013), pp. 160–182.

[69] Maria Cinefra and Stefano Valvano. "A variable kinematic doubly-curved MITC9 shell element for the analysis of laminated composites". In: *Mechanics of Advanced Materials and Structures* 23.11 (2016), pp. 1312–1325.

[70] Maria Cinefra, Stefano Valvano, and Erasmo Carrera. "Heat conduction and Thermal Stress Analysis of laminated composites by a variable kinematic MITC9 shell element". In: *Curved and Layered Structures* 1 (2015), pp. 301–320.

[71] Maria Cinefra et al. "Axiomatic/asymptotic technique applied to refined theories for piezoelectric plates". In: *Mechanics of advanced materials and structures* 22.1-2 (2015), pp. 107–124.

[72] Maria Cinefra et al. "Best theory diagrams for multilayered plates considering multifield analysis". In: *Journal of Intelligent Material Systems and Structures* 28.16 (2017), pp. 2184–2205.

[73] Maria Cinefra et al. “Hygrothermal analysis of multilayered composite plates by variable kinematic finite elements”. In: *Journal of Thermal Stresses* 40.12 (2017), pp. 1502–1522.

[74] Maria Cinefra et al. “Variable kinematic shell elements for composite laminates accounting for hygrothermal effects”. In: *Journal of Thermal Stresses* 40.12 (2017), pp. 1523–1544.

[75] GR Cowper. “The shear coefficient in Timoshenko’s beam theory”. In: *Journal of applied mechanics* 33.2 (1966), pp. 335–340.

[76] Edward F Crawley and Eric H Anderson. “Detailed models of piezoceramic actuation of beams”. In: *Journal of Intelligent Material Systems and Structures* 1.1 (1990), pp. 4–25.

[77] Edward F Crawley and Javier De Luis. “Use of piezoelectric actuators as elements of intelligent structures”. In: *AIAA Journal* 25.10 (1987), pp. 1373–1385.

[78] M D’Ottavio et al. “Bending analysis of composite laminated and sandwich structures using sublaminate variable-kinematic Ritz models”. In: *Composite Structures* 155 (2016), pp. 45–62.

[79] YC Das and BK Rath. “Thermal bending of moderately thick rectangular plate.” In: *AIAA Journal* 10.10 (1972), pp. 1349–1351.

[80] Frédéric Dau, Olivier Polit, and Maurice Touratier. “C1 plate and shell finite elements for geometrically nonlinear analysis of multilayered structures”. In: *Computers & structures* 84.19-20 (2006), pp. 1264–1274.

[81] Lucia Della Croce and Terenzio Scapolla. “Hierarchic finite elements with selective and uniform reduced integration for Reissner-Mindlin plates”. In: *Computational Mechanics* 10.2 (1992), pp. 121–131.

[82] Hachmi Ben Dhia. “Multiscale mechanical problems: the Arlequin method”. In: *Comptes Rendus de l’Academie des Sciences Series IIB Mechanics Physics Astronomy* 12.326 (1998), pp. 899–904.

[83] Hashmi Ben Dhia and Guillaume Rateau. “The Arlequin method as a flexible engineering design tool”. In: *International Journal for Numerical Methods in Engineering* 62.11 (2005), pp. 1442–1462.

[84] MC Dökmeci. “Variational principles in piezoelectricity”. In: *Lettere al Nuovo Cimento (1971-1985)* 7.11 (1973), pp. 449–454.

[85] PC Dumir et al. “Improved efficient zigzag and third order theories for circular cylindrical shells under thermal loading”. In: *Journal of Thermal Stresses* 31.4 (2008), pp. 343–367.

[86] Alexander Düster, Henrike Bröker, and Ernst Rank. “The p-version of the finite element method for three-dimensional curved thin walled structures”. In: *International Journal for Numerical Methods in Engineering* 52.7 (2001), pp. 673–703.

[87] Eduardo N Dvorkin and Klaus-Jürgen Bathe. “A continuum mechanics based four-node shell element for general non-linear analysis”. In: *Engineering Computations* 1.1 (1984), pp. 77–88.

[88] Leonhard Euler. “Methodus inveniendi lineas curvas maximi minimive proprietate gaudentes, sive solutio problematis isoperimetrici lattissimo sensu accepti”. In: (1744).

[89] Carlos A Felippa. “Introduction to finite element methods”. In: *Course Notes, Department of Aerospace Engineeing Sciences, University of Colorado at Boulder, available at http://www. colorado. edu/engineering/Aerospace/CAS/courses. d/IFEM. d* (2004).

[90] AJM Ferreira, CMC Roque, and RMN Jorge. “Analysis of composite plates by trigonometric shear deformation theory and multiquadrics”. In: *Computers & structures* 83.27 (2005), pp. 2225–2237.

[91] AJM Ferreira et al. “Analysis of laminated shells by a sinusoidal shear deformation theory and radial basis functions collocation, accounting for through-the-thickness deformations”. In: *Composites Part B: Engineering* 42.5 (2011), pp. 1276–1284.

[92] AJM Ferreira et al. “Non-linear analysis of sandwich shells: the effect of core plasticity”. In: *Computers & Structures* 76.1-3 (2000), pp. 337–346.

[93] Adolph Fick. “V. On liquid diffusion”. In: *The London, Edinburgh, and Dublin Philosophical Magazine and Journal of Science* 10.63 (1855), pp. 30–39.

[94] Matteo Filippi et al. “Analysis of laminated composites and sandwich structures by trigonometric, exponential and miscellaneous polynomials and a MITC9 plate element”. In: *Composite Structures* 150 (2016), pp. 103–114.

[95] M Filippi et al. “Static and free vibration analysis of laminated beams by refined theory based on Chebyshev polynomials”. In: *Composite Structures* 132 (2015), pp. 1248–1259.

[96] J Fish. “The s-version of the finite element method”. In: *Computers & Structures* 43.3 (1992), pp. 539–547.

[97] J Fish and S Markolefas. “The s-version of the finite element method for multilayer laminates”. In: *International Journal for Numerical Methods in Engineering* 33.5 (1992), pp. 1081–1105.

[98] Joseph Fourier. *Theorie analytique de la chaleur, par M. Fourier.* Chez Firmin Didot, père et fils, 1822.

[99] Randall M Hauch. “Industrial approach to static and dynamic finite element modeling of composite structures with embedded actuators”. In: *Smart Structures & Materials’ 95.* International Society for Optics and Photonics. 1995, pp. 458–469.

[100] R Hauptmann and K Schweizerhof. "A systematic development of 'solid-shell' element formulations for linear and non-linear analyses employing only displacement degrees of freedom". In: *International Journal for Numerical Methods in Engineering* 42.1 (1998), pp. 49–69.

[101] QZ He et al. "Multi-scale modelling of sandwich structures using hierarchical kinematics". In: *Composite Structures* 93.9 (2011), pp. 2375–2383.

[102] Michael Thomas Hicks. *Design of a carbon fiber composite grid structure for the GLAST spacecraft using a novel manufacturing technique.* Tech. rep. SLAC, 2001.

[103] FB Hildebrand, E Reissner, and GB Thomas. "Notes on the foundations of the theory of small displacements of orthotropic shells". In: (1949).

[104] Nicholas John Hoff and Lawrence W Rehfield. "Buckling of axially compressed circular cylindrical shells at stresses smaller than the classical critical value". In: *Journal of Applied Mechanics* 32.3 (1965), pp. 542–546.

[105] Heng Hu et al. "Multi-scale nonlinear modelling of sandwich structures using the Arlequin method". In: *Composite Structures* 92.2 (2010), pp. 515–522.

[106] Heng Hu, Salim Belouettar, Michel Potier-Ferry, et al. "Multi-scale modelling of sandwich structures using the Arlequin method Part I: Linear modelling". In: *Finite Elements in Analysis and Design* 45.1 (2008), pp. 37–51.

[107] Jin H Huang and Tsung-Lin Wu. "Analysis of hybrid multilayered piezoelectric plates". In: *International Journal of Engineering Science* 34.2 (1996), pp. 171–181.

[108] Thomas JR Hughes, Martin Cohen, and Medhat Haroun. "Reduced and selective integration techniques in the finite element analysis of plates". In: *Nuclear Engineering and Design* 46.1 (1978), pp. 203–222.

[109] Thomas JR Hughes and TEi Tezduyar. "Finite elements based upon Mindlin plate theory with particular reference to the four-node bilinear isoparametric element". In: *Journal of applied mechanics* 48.3 (1981), pp. 587–596.

[110] Woo-Seok Hwang and Hyun C Park. "Finite element modeling of piezoelectric sensors and actuators". In: *AIAA journal* 31.5 (1993), pp. 930–937.

[111] MW Hyer et al. "Temperature dependence of mechanical and thermal expansion properties of T300/5208 graphite/epoxy". In: *Composites* 14.3 (1983), pp. 276–280.

[112] Takurō Ikeda. *Fundamentals of piezoelectricity.* Oxford university press, 1996.

[113] Frédéric Jacquemin and Alain Vautrin. "A closed-form solution for the internal stresses in thick composite cylinders induced by cyclical environmental conditions". In: *Composite Structures* 58.1 (2002), pp. 1–9.

[114] Robert Millard Jones. *Mechanics of Composite Materials.* CRC Press, 1998.

[115] R Jones et al. “Analysis of multi-layer laminates using three-dimensional super-elements”. In: *International Journal for Numerical Methods in Engineering* 20.3 (1984), pp. 583–587.

[116] KD Jonnalagadda, GE Blandford, and TR Tauchert. “Piezothermoelastic composite plate analysis using first-order shear deformation theory”. In: *Computers & structures* 51.1 (1994), pp. 79–89.

[117] T Kant and RK Khare. “Finite element thermal stress analysis of composite laminates using a higher-order theory”. In: *Journal of Thermal Stresses* 17.2 (1994), pp. 229–255.

[118] T Kant and JR Kommineni. “Large amplitude free vibration analysis of cross-ply composite and sandwich laminates with a refined theory and C° finite elements”. In: *Computers & structures* 50.1 (1994), pp. 123–134.

[119] T Kant and BS Manjunatha. “Higher-order theories for symmetric and unsymmetric fiber reinforced composite beams with C0 finite elements”. In: *Finite Elements in Analysis and Design* 6.4 (1990), pp. 303–320.

[120] T Kant, DRJ Owen, and OC Zienkiewicz. “A refined higher-order C plate bending element”. In: *Computers & Structures* 15.2 (1982), pp. 177–183.

[121] Rakesh K Kapania and Stefano Raciti. “Recent advances in analysis of laminated beams and plates, Part I: Shear effects and buckling”. In: *AIAA Journal* 27.7 (1989), pp. 923–935.

[122] Rakesh K Kapania and Stefano Raciti. “Recent advances in analysis of laminated beams and plates, Part II: Vibrations and wave propagation”. In: *AIAA Journal* 27.7 (1989), pp. 935–946.

[123] S Kapuria. “A coupled zig-zag third-order theory for piezoelectric hybrid cross-ply plates”. In: *Transactions, American Society of Mechanical Engineers* 71.5 (2004), pp. 604–614.

[124] S Kapuria, P Kumari, and JK Nath. “Efficient modeling of smart piezoelectric composite laminates: a review”. In: *Acta Mechanica* 214.1-2 (2010), pp. 31–48.

[125] Santosh Kapuria. “An efficient coupled theory for multilayered beams with embedded piezoelectric sensory and active layers”. In: *International Journal of Solids and Structures* 38.50 (2001), pp. 9179–9199.

[126] Santosh Kapuria and Peter Hagedorn. “Unified efficient layerwise theory for smart beams with segmented extension/shear mode, piezoelectric actuators and sensors”. In: *Journal of Mechanics of Materials and Structures* 2.7 (2007), pp. 1267–1298.

[127] Santosh Kapuria and Poonam Kumari. “Boundary layer effects in Levy-type rectangular piezoelectric composite plates using a coupled efficient layerwise theory”. In: *European Journal of Mechanics-A/Solids* 36 (2012), pp. 122–140.

[128] M Karama, KS Afaq, and S Mistou. “A refinement of Ambartsumian multi-layer beam theory”. In: *Computers & Structures* 86.9 (2008), pp. 839–849.

[129] M Karama, KS Afaq, and S Mistou. “Mechanical behaviour of laminated composite beam by the new multi-layered laminated composite structures model with transverse shear stress continuity”. In: *International Journal of solids and structures* 40.6 (2003), pp. 1525–1546.

[130] LJTM Kempers. “A comprehensive thermodynamic theory of the Soret effect in a multicomponent gas, liquid, or solid”. In: *The Journal of Chemical Physics* 115.14 (2001), pp. 6330–6341.

[131] SMR Khalili, M Shariyat, and I Rajabi. “A finite element based global–local theory for static analysis of rectangular sandwich and laminated composite plates”. In: *Composite Structures* 107 (2014), pp. 177–189.

[132] Rakesh Kumar Khare, Tarun Kant, and Ajay Kumar Garg. “Closed-form thermo-mechanical solutions of higher-order theories of cross-ply laminated shallow shells”. In: *Composite Structures* 59.3 (2003), pp. 313–340.

[133] A A Khdeir, M D Rajab, and J N Reddy. “Thermal effects on the response of cross-ply laminated shallow shells”. In: *International Journal of Solids and Structures* 29.5 (1992), pp. 653–667.

[134] AA Khdeir. “Thermoelastic analysis of cross-ply laminated circular cylindrical shells”. In: *International Journal of Solids and Structures* 33.27 (1996), pp. 4007–4017.

[135] AA Khdeir and JN Reddy. “Thermal stresses and deflections of cross-ply laminated plates using refined plate theories”. In: *Journal of Thermal Stresses* 14.4 (1991), pp. 419–438.

[136] Yeongbin Ko, Phill-Seung Lee, and Klaus-Jürgen Bathe. “A new 4-node MITC element for analysis of two-dimensional solids and its formulation in a shell element”. In: *Computers & Structures* 192 (2017), pp. 34–49.

[137] Yeongbin Ko, Phill-Seung Lee, and Klaus-Jürgen Bathe. “The MITC4+ shell element and its performance”. In: *Computers & Structures* 169 (2016), pp. 57–68.

[138] Fessal Kpeky et al. “Linear and quadratic solid–shell finite elements SHB8PSE and SHB20E for the modeling of piezoelectric sandwich structures”. In: *Mechanics of Advanced Materials and Structures* 25.7 (2018), pp. 559–578.

[139] Gennady M Kulikov and SV Plotnikova. “Advanced formulation for laminated composite shells: 3D stress analysis and rigid-body motions”. In: *Composite Structures* 95 (2013), pp. 236–246.

[140] Gennady M Kulikov and SV Plotnikova. “Exact 3D stress analysis of laminated composite plates by sampling surfaces method”. In: *Composite Structures* 94.12 (2012), pp. 3654–3663.

[141] Gennady M Kulikov and SV Plotnikova. “Three-dimensional exact analysis of piezoelectric laminated plates via a sampling surfaces method”. In: *International Journal of Solids and Structures* 50.11 (2013), pp. 1916–1929.

[142] GM Kulikov and SV Plotnikova. “A sampling surfaces method and its implementation for 3D thermal stress analysis of functionally graded plates”. In: *Composite Structures* 120 (2015), pp. 315–325.

[143] P Kumari and S Kapuria. “Boundary layer effects in rectangular cross-ply Levy-type plates using zigzag theory”. In: *ZAMM-Journal of Applied Mathematics and Mechanics/Zeitschrift für Angewandte Mathematik und Mechanik* 91.7 (2011), pp. 565–580.

[144] CK Lee. “Theory of laminated piezoelectric plates for the design of distributed sensors/actuators. Part I: Governing equations and reciprocal relationships”. In: *The Journal of the Acoustical Society of America* 87.3 (1990), pp. 1144–1158.

[145] Arthur W Leissa. *Vibration of shells.* Vol. 288. Scientific, Technical Information Office, National Aeronautics, and Space Administration Washington, 1973.

[146] M Lezgy-Nazargah, SB Beheshti-Aval, and M Shariyat. “A refined mixed global–local finite element model for bending analysis of multi-layered rectangular composite beams with small widths”. In: *Thin-Walled Structures* 49.2 (2011), pp. 351–362.

[147] G Li et al. “An adaptable refinement approach for shell finite element models based on node-dependent kinematics”. In: *Composite Structures* 210 (2019), pp. 1–19.

[148] Xiaoyu Li and Dahsin Liu. “A laminate theory based on global–local superposition”. In: *International Journal for Numerical Methods in Biomedical Engineering* 11.8 (1995), pp. 633–641.

[149] Xiaoyu Li and Dahsin Liu. “Generalized laminate theories based on double superposition hypothesis”. In: *International Journal for Numerical Methods in Engineering* 40.7 (1997), pp. 1197–1212.

[150] SH Lo et al. “Hygrothermal effects on multilayered composite plates using a refined higher order theory”. In: *Composite Structures* 92.3 (2010), pp. 633–646.

[151] Alexandre Loredo. “Exact 3D solution for static and damped harmonic response of simply supported general laminates”. In: *Composite Structures* 108 (2014), pp. 625–634.

[152] Augustus Edward Hough Love. “The small free vibrations and deformation of a thin elastic shell”. In: *Philosophical Transactions of the Royal Society of London. A* 179 (1888), pp. 491–546.

[153] J L Mantari, A S Oktem, and C Guedes Soares. “Bending response of functionally graded plates by using a new higher order shear deformation theory”. In: *Composite Structures* 94.2 (2012), pp. 714–723.

[154] JL Mantari, EM Bonilla, and C Guedes Soares. “A new tangential-exponential higher order shear deformation theory for advanced composite plates”. In: *Composites Part B: Engineering* 60 (2014), pp. 319–328.

[155] JL Mantari, AS Oktem, and C Guedes Soares. “A new trigonometric shear deformation theory for isotropic, laminated composite and sandwich plates”. In: *International Journal of Solids and Structures* 49.1 (2012), pp. 43–53.

[156] KM Mao and CT Sun. “A refined global-local finite element analysis method”. In: *International Journal for Numerical Methods in Engineering* 32.1 (1991), pp. 29–43.

[157] Peter Marti. *Theory of structures: fundamentals, framed structures, plates and shells.* John Wiley & Sons, 2013.

[158] AS Mawenya and JD Davies. “Finite element bending analysis of multilayer plates”. In: *International Journal for Numerical Methods in Engineering* 8.2 (1974), pp. 215–225.

[159] F Miglioretti and E Carrera. “Application of a refined multi-field beam model for the analysis of complex configurations”. In: *Mechanics of Advanced Materials and Structures* 22.1-2 (2015), pp. 52–66.

[160] F Miglioretti, E Carrera, and M Petrolo. “Variable kinematic beam elements for electro-mechanical analysis”. In: *Smart Structures and Systems* 13.4 (2014), pp. 517–546.

[161] Craig J Miller, TP Kicher, and WA Millavec. “Thermal stress analysis of layered cylindrical shells”. In: *AIAA Journal* 19.4 (1981), pp. 523–530.

[162] Raymond D Mindlin. “Influence of rotatory inertia and shear on flexural motions of isotropic, elastic plates”. In: *J. appl. Mech.* 18 (1951), pp. 31–38.

[163] JA Mitchell and JN Reddy. “A refined hybrid plate theory for composite laminates with piezoelectric laminae”. In: *International Journal of Solids and Structures* 32.16 (1995), pp. 2345–2367.

[164] Hashem M Mourad, Todd O Williams, and Francis L Addessio. “Finite element analysis of inelastic laminated plates using a global–local formulation with delamination”. In: *Computer Methods in Applied Mechanics and Engineering* 198.3 (2008), pp. 542–554.

[165] D Muheim Thompson and O Hayden Griffin JR. “2-D to 3-D global/local finite element analysis of cross-ply composite laminates”. In: *Journal of Reinforced Plastics and Composites* 9.5 (1990), pp. 492–502.

[166] H Murakami. “Laminated composite plate theory with improved in-plane responses”. In: *Journal of Applied Mechanics* 53.3 (1986), pp. 661–666.

[167] P Nali, E Carrera, and A Calvi. “Advanced fully coupled thermo-mechanical plate elements for multilayered structures subjected to mechanical and thermal loading”. In: *International Journal for Numerical Methods in Engineering* 85.7 (2011), pp. 896–919.

[168] Nhon Nguyen-Thanh et al. “An extended isogeometric thin shell analysis based on Kirchhoff–Love theory”. In: *Computer Methods in Applied Mechanics and Engineering* 284 (2015), pp. 265–291.

[169] Ali Mohammad Naserian Nik and Masoud Tahani. “Analytical solutions for bending analysis of rectangular laminated plates with arbitrary lamination and boundary conditions”. In: *Journal of Mechanical Science and Technology* 23.8 (2009), pp. 2253–2267.

[170] Ahmed K Noor and W Scott Burton. “Assessment of computational models for multilayered composite shells”. In: *Applied Mechanics Reviews* 43.4 (1990), pp. 67–97.

[171] Ahmed K Noor and W Scott Burton. “Three-dimensional solutions for antisymmetrically laminated anisotropic plates”. In: *Journal of Applied Mechanics* 57.1 (1990), pp. 182–188.

[172] John Frederick Nye. *Physical properties of crystals: their representation by tensors and matrices.* Oxford university press, 1985.

[173] J Tinsley Oden et al. “Toward a universal hp adaptive finite element strategy, Part 2. A posteriori error estimation”. In: *Computer Methods in Applied Mechanics and Engineering* 77.1-2 (1989), pp. 113–180.

[174] M Özakça, E Hinton, and NVR Rao. “Comparison of three-dimensional solid elements in the analysis of plates”. In: *Computers & Structures* 42.6 (1992), pp. 953–968.

[175] A Pagani, AG de Miguel, and E Carrera. “Cross-sectional mapping for refined beam elements with applications to shell-like structures”. In: *Computational Mechanics* 59.6 (2017), pp. 1031–1048.

[176] Alfonso Pagani et al. “Analysis of laminated beams via Unified Formulation and Legendre polynomial expansions”. In: *Composite Structures* 156 (2016). 70th Anniversary of Professor J. N. Reddy, pp. 78–92.

[177] NJ Pagano. “Exact solutions for rectangular bidirectional composites and sandwich plates”. In: *Journal of Composite Materials* 4.1 (1970), pp. 20–34.

[178] BP Patel, M Ganapathi, and DP Makhecha. “Hygrothermal effects on the structural behaviour of thick composite laminates using higher-order theory”. In: *Composite Structures* 56.1 (2002), pp. 25–34.

[179] Alberto Peano. “Hierarchies of conforming finite elements for plane elasticity and plate bending”. In: *Computers & Mathematics with Applications* 2.3-4 (1976), pp. 211–224.

[180] Marco Petrolo, Alessandro Lamberti, and Federico Miglioretti. “Best theory diagram for metallic and laminated composite plates”. In: *Mechanics of Advanced Materials and Structures* 23.9 (2016), pp. 1114–1130.

[181] Vincent Piefort. “Finite element modelling of piezoelectric active structures”. PhD thesis. Ph. D. thesis. Bruxelles, Belgium: Université Libre de Bruxelles, Department for Mechanical Engineering and Robotics, 2001.

[182] R Byron Pipes, Jack R Vinson, and Tsu Wei Chou. “On the Hygrothermal Response of Laminated Composite Systems”. In: *Journal of Composite Materials* 10.2 (1976), pp. 129–148.

[183] VG Piskunov et al. “Rational transverse shear deformation higher-order theory of anisotropic laminated plates and shells”. In: *International Journal of Solids and Structures* 38.36 (2001), pp. 6491–6523.

[184] O Polit and M Touratier. “A new laminated triangular finite element assuring interface continuity for displacements and stresses”. In: *Composite Structures* 38.1-4 (1997), pp. 37–44.

[185] William Prager. “Variational principles of linear elastostatics for discontinuous displacements, strains and stresses”. In: *Recent Progress in Applied Mechanics. The Folkey Odquist Volume. Stockholm: Almquist and Wiksell* (1967), pp. 463–474.

[186] Sai Sudha Ramesh et al. “Computation of stress resultants in plate bending problems using higher-order triangular elements”. In: *Engineering Structures* 30.10 (2008), pp. 2687–2706.

[187] Franz G Rammerstorfer, K Dorninger, and Alois Starlinger. “Composite and sandwich shells”. In: *Nonlinear analysis of shells by finite elements.* Springer, 1992, pp. 131–194.

[188] MC Ray. “Zeroth-order shear deformation theory for laminated composite plates”. In: *Journal of Applied Mechanics* 70.3 (2003), pp. 374–380.

[189] JN Reddy. “A general non-linear third-order theory of plates with moderate thickness”. In: *International Journal of Non-Linear Mechanics* 25.6 (1990), pp. 677–686.

[190] JN Reddy. “A simple higher-order theory for laminated composite plates”. In: *Journal of Applied Mechanics* 51.4 (1984), pp. 745–752.

[191] JN Reddy. “An evaluation of equivalent-single-layer and layerwise theories of composite laminates”. In: *Composite structures* 25.1-4 (1993), pp. 21–35.

[192] JN Reddy. *An introduction to the finite element method.* Vol. 2. 2.2. McGraw-Hill New York, 1993.

[193] JN Reddy. "Exact solutions of moderately thick laminated shells". In: *Journal of Engineering Mechanics* 110.5 (1984), pp. 794–809.

[194] JN Reddy. *Mechanics of laminated composite plates and shells: theory and analysis.* CRC Press, 2004.

[195] JN Reddy and CF Liu. "A higher-order shear deformation theory of laminated elastic shells". In: *International Journal of Engineering Science* 23.3 (1985), pp. 319–330.

[196] JN Reddy and DH Robbins. "Theories and computational models for composite laminates". In: *Applied Mechanics Reviews* 47.6 (1994), pp. 147–169.

[197] Junuthula Narasimha Reddy. *Energy and variational methods in applied mechanics: with an introduction to the finite element method.* Wiley New York, 1984.

[198] Eric Reissner. "The effect of transverse shear deformation on the bending of elastic plates". In: *J. appl. Mech.* (1945), A69–A77.

[199] JG Ren. "Bending of simply-supported, antisymmetrically laminated rectangular plate under transverse loading". In: *Composites Science and Technology* 28.3 (1987), pp. 231–243.

[200] A Robaldo and Erasmo Carrera. "Mixed finite elements for thermoelastic analysis of multilayered anisotropic plates". In: *Journal of Thermal Stresses* 30.2 (2007), pp. 165–194.

[201] DH Robbins and JN Reddy. "Analysis of piezoelectrically actuated beams using a layer-wise displacement theory". In: *Computers & Structures* 41.2 (1991), pp. 265–279.

[202] DH Robbins and JN Reddy. "Variable kinematic modelling of laminated composite plates". In: *International Journal for Numerical Methods in Engineering* 39.13 (1996), pp. 2283–2317.

[203] Nellya N Rogacheva. *The theory of piezoelectric shells and plates.* CRC press, 1994.

[204] R Rolfes and K Rohwer. "Improved transverse shear stresses in composite finite elements based on first order shear deformation theory". In: *International Journal for Numerical Methods in Engineering* 40.1 (1997), pp. 51–60.

[205] Dimitris A Saravanos and Paul R Heyliger. "Mechanics and computational models for laminated piezoelectric beams, plates, and shells". In: *Applied Mechanics Reviews* 52 (1999), pp. 305–320.

[206] M Savoia and JN Reddy. "A variational approach to three-dimensional elasticity solutions of laminated composite plates". In: *Journal of Applied Mechanics* 59.2S (1992), S166–S175.

[207] Terenzio Scapolla and Lucia Della Croce. “Combining hierarchic high order and mixed-interpolated finite elements for Reissner-Mindlin plate problems”. In: *Computer Methods in Applied Mechanics and Engineering* 116.1-4 (1994), pp. 185–192.

[208] Terenzio Scapolla and Lucia Della Croce. “Hierarchic and mixed-interpolated finite elements for Reissner-Mindlin problems”. In: *Communications in numerical methods in engineering* 11.7 (1995), pp. 549–562.

[209] Richardt Schardt. “Generalized beam theory—an adequate method for coupled stability problems”. In: *Thin-walled structures* 19.2-4 (1994), pp. 161–180.

[210] Ch Schwab. *P-and Hp-Finite Element Methods: Theory and Applications in Solid and Fluid Mechanics (Numerical Mathematics and Scientific Computation).* Oxford University Press, New York, 1999.

[211] Chi-Hung Shen and George S Springer. “Moisture absorption and desorption of composite materials”. In: *Journal of composite materials* 10.1 (1976), pp. 2–20.

[212] Rameshchandra P Shimpi and Yuwaraj M Ghugal. “A new layerwise trigonometric shear deformation theory for two-layered cross-ply beams”. In: *Composites Science and Technology* 61.9 (2001), pp. 1271–1283.

[213] GC Sih, MT Shih, and SC Chou. “Transient hygrothermal stresses in composites: coupling of moisture and heat with temperature varying diffusivity”. In: *International Journal of Engineering Science* 18.1 (1980), pp. 19–42.

[214] George C Sih, J Michopoulos, and Shang-Ching Chou. *Hygrothermoelasticity.* Springer Science & Business Media, 2012.

[215] W Smittakorn and PR Heyliger. “A discrete-layer model of laminated hygrothermopiezoelectric plates”. In: *Mechanics of Composite Materials and Structures* 7.1 (2000), pp. 79–104.

[216] Henryk Stolarski and Ted Belytschko. “Shear and membrane locking in curved C0 elements”. In: *Computer Methods in Applied Mechanics and Engineering* 41.3 (1983), pp. 279–296.

[217] A Suleman and VB Venkayya. “A simple finite element formulation for a laminated composite plate with piezoelectric layers”. In: *Journal of Intelligent Material Systems and Structures* 6.6 (1995), pp. 776–782.

[218] CT Sun and XD Zhang. “Use of thickness-shear mode in adaptive sandwich structures”. In: *Smart Materials and Structures* 4.3 (1995), p. 202.

[219] CK Sung and BS Thompson. “A variational principle for the hygrothermoelastodynamic analysis of mechanism systems”. In: *Journal of mechanisms, transmissions, and automation in design* 109.3 (1987), pp. 294–300.

[220] KS Surana et al. “On p-version hierarchical interpolation functions for higher-order continuity finite element models”. In: *International Journal of Computational Engineering Science* 2.04 (2001), pp. 653–673.

[221] Manil Suri. “Analytical and computational assessment of locking in the hp finite element method”. In: *Computer Methods in Applied Mechanics and Engineering* 133.3-4 (1996), pp. 347–371.

[222] Barna A Szabó. “Mesh design for the p-version of the finite element method”. In: *Computer Methods in Applied Mechanics and Engineering* 55.1-2 (1986), pp. 181–197.

[223] Barna A Szabó. “Some recent developments in finite element analysis”. In: *Computers & Mathematics with Applications* 5.2 (1979), pp. 99–115.

[224] Barna A Szabó and Ivo Babuška. *Finite element analysis.* John Wiley & Sons, 1991.

[225] Barna A Szabó and AK Mehta. “p-convergent finite element approximations in fracture mechanics”. In: *International Journal for Numerical Methods in Engineering* 12.3 (1978), pp. 551–560.

[226] Barna Szabó, Alexander Düster, and Ernst Rank. “The p-Version of the Finite Element Method”. In: Wiley Online Library, 2004.

[227] KY Sze, LQ Yao, and Sung Yi. “A hybrid stress ANS solid-shell element and its generalization for smart structure modelling. Part II—smart structure modelling”. In: *International Journal for Numerical Methods in Engineering* 48.4 (2000), pp. 565–582.

[228] A Szekeres. “Analogy between heat and moisture: Thermo-hygro-mechanical tailoring of composites by taking into account the second sound phenomenon”. In: *Computers & Structures* 76.1 (2000), pp. 145–152.

[229] Andras Szekeres and Jueri Engelbrecht. “Coupled thermal and moisture fields with application to composites”. In: *Periodica Polytechnica. Engineering. Mechanical Engineering* 41.2 (1997), p. 151.

[230] C Tahiani and L Lachance. “Linear and non-linear analysis of thin shallow shells by mixed finite elements”. In: *Computers & Structures* 5.2-3 (1975), pp. 167–177.

[231] Yoram Tambour. “On local temperature overshoots due to transport coupling of heat and moisture in composite materials”. In: *Journal of composite materials* 18.5 (1984), pp. 478–494.

[232] Alexander Tessler. “A higher-order plate theory with ideal finite element suitability”. In: *Computer methods in applied mechanics and engineering* 85.2 (1991), pp. 183–205.

[233] SP Timoshenko. “On the transverse vibrations of bars of uniform cross-section”. In: *The London, Edinburgh, and Dublin Philosophical Magazine and Journal of Science* 43.253 (1922), pp. 125–131.

[234] Stephen P Timoshenko. “LXVI. On the correction for shear of the differential equation for transverse vibrations of prismatic bars”. In: *The London, Edinburgh, and Dublin Philosophical Magazine and Journal of Science* 41.245 (1921), pp. 744–746.

[235] Francesco Tornabene and Erasmo Viola. “Static analysis of functionally graded doubly-curved shells and panels of revolution”. In: *Meccanica* 48.4 (2013), pp. 901–930.

[236] A Tounsi and EA Adda Bedia. “Simplified method for prediction of transient hygroscopic stresses in polymer matrix composites with symmetric environmental conditions”. In: *Applied Composite Materials* 10.1 (2003), pp. 1–18.

[237] A Tounsi, M Bouazza, and E Adda Bedia. “Computation of transient hygroscopic stresses in unidirectional laminated composite plates with cyclic and asymmetrical environmental conditions”. In: *International Journal of Mechanics and Materials in Design* 1.3 (2004), pp. 271–286.

[238] Stephen W Tsai. *Composites design.* Vol. 5. Think composites Dayton, OH, 1988.

[239] VB Tungikar and Koganti M Rao. “Three dimensional exact solution of thermal stresses in rectangular composite laminate”. In: *Composite Structures* 27.4 (1994), pp. 419–430.

[240] HS Tzou and M Gadre. “Theoretical analysis of a multi-layered thin shell coupled with piezoelectric shell actuators for distributed vibration controls”. In: *Journal of Sound and Vibration* 132.3 (1989), pp. 433–450.

[241] HS Tzou and R Ye. “Analysis of piezoelastic structures with laminated piezoelectric triangle shell elements”. In: *AIAA journal* 34.1 (1996), pp. 110–115.

[242] Stefano Valvano and Erasmo Carrera. “Multilayered plate elements with node-dependent kinematics for the analysis of composite and sandwich structures”. In: *Facta Universitatis, Series: Mechanical Engineering* 15.1 (2017), pp. 1–30.

[243] Martinus T Van Genuchten, George F Pinder, and Emil O Frind. “Simulation of two-dimensional contaminant transport with isoparametric Hermitian finite elements”. In: *Water Resources Research* 13.2 (1977), pp. 451–458.

[244] TK Varadan and K Bhaskar. “Bending of laminated orthotropic cylindrical shells—an elasticity approach”. In: *Composite Structures* 17.2 (1991), pp. 141–156.

[245] Senthil S Vel and RC Batra. “Analysis of piezoelectric bimorphs and plates with segmented actuators”. In: *Thin-Walled Structures* 39.1 (2001), pp. 23–44.

[246] Daniele Versino, Hashem M Mourad, and Todd O Williams. “A global–local discontinuous Galerkin shell finite element for small-deformation analysis of multi-layered composites”. In: *Computer Methods in Applied Mechanics and Engineering* 271 (2014), pp. 269–295.

[247] Daniele Versino et al. “A global–local discontinuous Galerkin finite element for finite-deformation analysis of multilayered shells”. In: *Computer Methods in Applied Mechanics and Engineering* 283 (2015), pp. 1401–1424.

[248] P Vidal and O Polit. “A family of sinus finite elements for the analysis of rectangular laminated beams”. In: *Composite Structures* 84.1 (2008), pp. 56–72.

[249] P Vidal and O Polit. “A sine finite element using a zig-zag function for the analysis of laminated composite beams”. In: *Composites Part B: Engineering* 42.6 (2011), pp. 1671–1682.

[250] Vasiliĭ Zakharovich Vlasov. *Thin-walled elastic beams*. National Technical Information Service, 1984.

[251] Bor-Tsuen Wang and Craig A Rogers. “Laminate plate theory for spatially distributed induced strain actuators”. In: *Journal of Composite Materials* 25.4 (1991), pp. 433–452.

[252] Ji Wang and Jiashi Yang. “Higher-order theories of piezoelectric plates and applications”. In: *Applied Mechanics Reviews* 53.4 (2000), pp. 87–99.

[253] C Wenzel et al. “Coupling of heterogeneous kinematics and Finite Element approximations applied to composite beam structures”. In: *Composite Structures* 116 (2014), pp. 177–192.

[254] John D Whitcomb and Kyeongsik Woo. “Application of iterative global/local finite-element analysis. Part 1: Linear analysis”. In: *International Journal for Numerical Methods in Biomedical Engineering* 9.9 (1993), pp. 745–756.

[255] John D Whitcomb and Kyeongsik Woo. “Application of iterative global/local finite-element analysis. Part 2: Geometrically non-linear analysis”. In: *International Journal for Numerical Methods in Biomedical Engineering* 9.9 (1993), pp. 757–766.

[256] James M Whitney. “Analysis of interlaminar mode II bending specimens using a higher order beam theory”. In: *Journal of Reinforced Plastics and Composites* 9.6 (1990), pp. 522–536.

[257] James M Whitney. “Bending-extensional coupling in laminated plates under transverse loading”. In: *Journal of Composite Materials* 3.1 (1969), pp. 20–28.

[258] James M Whitney and Arthur W Leissa. “Analysis of heterogeneous anisotropic plates”. In: *Journal of Applied Mechanics* 36.2 (1969), pp. 261–266.

[259] Todd O Williams. “A generalized multilength scale nonlinear composite plate theory with delamination”. In: *International Journal of Solids and Structures* 36.20 (1999), pp. 3015–3050.

[260] Jiashi Yang. *An introduction to the theory of piezoelectricity*. Vol. 9. Springer Science & Business Media, 2004.

[261] J Yarasca et al. “Multiobjective Best Theory Diagrams for cross-ply composite plates employing polynomial, zig-zag, trigonometric and exponential thickness expansions”. In: *Composite Structures* 176 (2017), pp. 860–876.

[262] Fuh-Gwo Yuan and Robert E Miller. “A higher order finite element for laminated beams”. In: *Composite structures* 14.2 (1990), pp. 125–150.

[263] Enrico Zappino et al. “Global-local analysis of laminated plates by node-dependent kinematic finite elements with variable ESL/LW capabilities”. In: *Composite Structures* 172 (2017), pp. 1–14.

[264] Enrico Zappino et al. “Numerical analyses of piezoceramic actuators for high temperature applications”. In: *Composite Structures* 151 (2016), pp. 36–46.

[265] XD Zhang and CT Sun. “Formulation of an adaptive sandwich beam”. In: *Smart Materials and Structures* 5.6 (1996), p. 814.

[266] JZ Zhu and OC Zienkiewicz. “Adaptive techniques in the finite element method”. In: *International Journal for Numerical Methods in Biomedical Engineering* 4.2 (1988), pp. 197–204.

[267] OC Zienkiewicz, JP De SR Gago, and Don W Kelly. “The hierarchical concept in finite element analysis”. In: *Computers & Structures* 16.1 (1983), pp. 53–65.

[268] OC Zienkiewicz and S Nakazawa. “On variational formulation and its modifications for numerical solution”. In: *Computers & Structures* 19.1-2 (1984), pp. 303–313.

[269] OC Zienkiewicz, RL Taylor, and JM Too. “Reduced integration technique in general analysis of plates and shells”. In: *International Journal for Numerical Methods in Engineering* 3.2 (1971), pp. 275–290.

[270] OC Zienkiewicz and Jian Z Zhu. “A simple error estimator and adaptive procedure for practical engineerng analysis”. In: *International Journal for Numerical Methods in Engineering* 24.2 (1987), pp. 337–357.

[271] OC Zienkiewicz, JZ Zhu, and NG Gong. “Effective and practical h–p-version adaptive analysis procedures for the finite element method”. In: *International Journal for Numerical Methods in Engineering* 28.4 (1989), pp. 879–891.

[272] Olek C Zienkiewicz and Robert L Taylor. *The finite element method for solid and structural mechanics*. Elsevier, 2005.

[273] Hao Zuo et al. “Analysis of laminated composite plates using wavelet finite element method and higher-order plate theory”. In: *Composite Structures* 131 (2015), pp. 248–258.